# Chemical Vapor Deposition of Polysilicon on a Morphous Materials

Michel Pietrantonio

A Thesis
in
The Faculty
of
Engineering

Presented in Partial Fulfillment of the Requirements
for the Degree of Master of Engineering
Concordia University
Montreal, Quebec, Canada

March, 1983

© Michel Pietrantonio, 1983

# ACKNOWLEDGEMENT

ACKNOWLEDGEMENT

I would like to express my sincere thanks to my research supervisor, Dr. B.A. Lombos for his cooperation and long discussions during the course of this project.

I would also like to thank Dr. M. Averous for his help and opinions on the Hall effect measurements; Dr. R.C. Sharma for reviewing the manuscript and for his valuable comments. Dr. I. Dickson of the Ecole Polytechnique of Montreal for the X-ray diffraction work; Dr. C.M. Mitchell of the Energy, Mines and Resources for the S.E.M. cross sectional pictures and Dr. J.C. Bresse of the Universite des Sciences et Technique du Languedoc for the S.E.M. pictures.

ABSTRACT

ABSTRACT

CHEMICAL VAPOR DEPOSITION OF POLYSILICON
ON AMORPHOUS MATERIALS

Michel Pietrantonio

In this investigation polysilicon films have been grown by the thermal decomposition of silane in a resistance heated furnace on fused silica, graphite and thermally grown $SiO_2$ substrates.

The crystallinity and transport properties are investigated as functions of deposition conditions and doping levels of the grown films.

The effect of the grain boundaries, characterizing the polycrystals, are examined using a model based on deep lying levels in the band gap. The concept of impurity band conduction is attempted to be related to the mobility minimum observed at a given carrier concentration in the case of polysilicon. The conditions of increased power conversion efficiency of polysilicon solar cells are examined, based on the obtained experimental data and on the results of the analysis of the deep lying impurity model.

TABLE OF CONTENTS

# TABLE OF CONTENTS

| | PAGE |
|---|---|
| TABLE OF CONTENTS .............................. | |
| LIST OF FIGURES ................................ | |
| LIST OF TABLES ................................. | |
| INTRODUCTION | 1 |
| CHAPTER 1 - EXPERIMENTAL PROCEDURE ................ | 3 |
| 1.1 Decomposition Apparatus ................ | 4 |
| CHAPTER 2 - INTRODUCTION | 16 |
| 2.1 C.V.D. of Silicon on Fused Silica ... | 17 |
| 2.2 C.V.D. of Silicon on Graphite | 44 |
| Introduction ........................ | 44 |
| 2.2.1. Poly-Silicon on Graphite ..... | 44 |
| CHAPTER 3 - HALL EFFECT ........................... | 74 |
| Introduction to Hall Effect ................... | 74 |
| 3.1 Hall effect Setup ..................... | 80 |
| 3.2 Elimination of the Secondary Galvanometric Effects related to Hall Effect ......................... | 85 |
| 3.3 Hall Effect Sample Preparation ...... | 88 |
| 3.4 Measured Transport Properties - Experimental Results ................ | 94 |

PAGE

3.4.1 Gas-Phase Molar Ratio .............. 94

3.4.2 Hall Mobility of Polysilicon ....... 108

3.4.3 Sample Resistivity ................ 104

3.4.4 Electrical Properties of Polysilicon as a Function of Annealin Time .......... 114

CHAPTER 4 PHOTOVOLTAIC EFFECT ...................... 117

4.1 Optical Absorption in a semiconductor ..... 118

4.2 Fabrication of a Photovoltaic Device ...... 124

4.2.1 Sample Preparation ................ 124

4.2.2 Contacts .......................... 124

4.2.3 Alloying .......................... 124

4.2.4 Sun Simulation .................... 125

CHAPTER 5 DISCUSSION ............................ 127

CHAPTER 6 CONCLUSION ............................ 141

REFERENCE ........................................ 145

APPENDIX A ....................................... 149

APPENDIX B ....................................... 158

APPENDIX C ....................................... 170

APPENDIX D ....................................... 172

APPENDIX E-A ..................................... 189

APPENDIX E-B ..................................... 197

APPENDIX F ....................................... 203

# LIST OF FIGURES

## LIST OF FIGURES

PAGE

Fig. 1 - Tellysurf measurement of the oxide thickness .................... 5

Fig. 2 - Chemical Vapour Deposition System for Silicon ................. 6

Fig. 3 - Graphite Substrate Holder ........... 8

Fig. 4 - Chemical Vapor Deposition System for silicon with water cooled gas mixture system inlet ........... 10

Fig. 5 - Water cooled gas mixture inlet system made of fused silica ......... 12

Fig. 6 - Gas exhaust system ................. 13

Fig. 7 - Power system resistance heater furnace ............................. 14

Fig. 8 - Amorphous Silicon, T = 500°C ......... 21

Fig. 8A - X-Ray Diffraction of amorphous Silicon at 500°C .................... 22

Fig. 9 - Amorphous Silicon, T = 550°C ........ 23

Fig. 9A - X-Ray Diffraction of amorphous Silicon at 550°C .................... 24

Fig. 10 - Scanning electron micrograph of the as-grown surface of a silicon layer deposited on a fused silica substrate at 680°C by the pyrolisis of silane at flow rates of 0.55ℓ/min of He and 20ℓ/min of $SiH_4$............ 25

Fig. 11 - Scanning electron micrograph of the as-grown surface of a silicon layer deposited on graphite substrate at 750°C by the pyrolysis of Silane at flow rates of 1.05ℓ/min of He and 2.0ℓ/min of $SiH_4$. .................. 26

Fig. 12 - Scanning electron micrograph of the as-grown surface of a silicon layer deposited on fused silica substrate . 28

PAGE

Fig. 12 (cont'd.) - at 796°C by the pyrolysis of silane at flow rates of 1.15ℓ/min of He and 2.0ℓ/min of Silane .................................. 28

Fig. 13 - Scanning electron micrography of the as-grown surface of a boron-doped film by growth deposited on fused silica substrate at 796°C by the pyrolysis of Silane at flow rates of 0.7ℓ/min of He 0.2ℓ/min of $B_2H_6$ (.05% by Vol. in $H_2$) and 2.0ℓ/min of $SiH_4$ ........................ 29

Fig. 14 - Scanning electron micrograph of the as-grown surface of a silicon layer deposited on fused silica substrate at T=825°C by the pyrolysis of silane at flow rates of 1.3ℓ/min of $SiH_4$ .......... 30

Fig. 15 - X-ray diffraction spectra of silicon deposited on fused silica at T=825°C...... 32

Fig. 16 - X-ray diffraction spectra of silicon deposited on fused silica at T=973°C...... 33

Fig. 17 - Scanning electron micrography of the as-grown surface of a silicon layer deposited on fused-silica substrate at 927°C by the pyrolysis of silane at flow rates of 1.3ℓ/min of He and 2.0ℓ of $SiH_4$ .................................. 35

Fig. 18 - Characteristic temperature as the function of time (sec) of fig. 17 and the expression characterizing this curve is given by

$T(K) = 1.2562 \times 10^3 (t)^{-7.5198\times10^{-3}}$ ........ 36

Fig. 19 - S.E.M. of the as-grown surface of a silicon layer deposited on fused silica substrate at 950°C by the pyrolysis of Silane at flow rates of 1.8ℓ/min of He and 2.0ℓ/min of Silane .................. 38

Fig. 20 - Characteristic temperature as the function of time (sec) of fig. 19 and the expression characterizing this curve is given by

$T(K) = 1.2624 \times 10^3 t^{-5.8228\times10^{-3}}$ ......... 39

Fig. 21 - Scanning electron micrograph of the as-grown surface of a silicon layer

PAGE

Fig. 21 (cont'd) - deposited on fused silica substrate at 973°C by the pyrolysis of silane at flow rates of 1.9ℓ/min of He and 2.7ℓ/min of $SiH_4$ .......... 40

Fig. 22 - Influence of deposition temperature on the growth rate of polycrystalline silicon films without and with additional doping of $B_2H_6$ .......... 43

Fig. 23 - Scanning electron micrograph (S.E.M.) of the as-grown surface of a boron-doped film by growth deposited on graphite substrate at T=936°C by the pyrolysis of Silane at flow rates of 0.25ℓ/min of He, 0.2ℓ/min of $B_2H_6$ and 2.7ℓ/min of $S_iH_4$ .......... 48

Fig. 23A - Cross sectional S.E.M. of a boron doped layer, deposited on graphite at T=936°C. The magnification is of 1200. The deposition conditions were of 0.25ℓ/min of He, 0.2ℓ/min of $B_2H_6$ and 2.7ℓ/min of $S_iH_4$ .......... 49

Fig. 24 - S.E.M. of the as-grown surface of a boron doped film by growth, deposited on graphite substrate at T=954°C. The magnification is of 1200. Here the deposition conditions were of 0.8ℓ/min of He, 0.7ℓ/min of $B_2H_6$ and 2.7ℓ of $SiH_4$ .......... 51

Fig. 24A - Cross sectional S.E.M. of Fig. 24. The magnification is of 1200. Here the deposition conditions were that of fig. 24.

Fig. 24B - Characteristic temperature as the function of time (sec) of figure 24 and 24-a and the expression characterizing this curve is given by $T(K) = 1.2604\times10^{3}(t)^{-7.673\times10^{-3}}$ .......... 52

Fig. 25 - S.E.M. of the as-grown surface of a boron-doped film by growth deposited on graphite substrate of T=967°C. The magnification is 1200. Here the deposition conditions were of 0.4ℓ/min of He, 0.7ℓ/min of $B_2H_6$ and 2.7ℓ/min of $SiH_4$ .......... 55

PAGE

Fig. 25A - The magnificent is of 1200. Deposition condition were that of Fig. 25 ........................ 56

Fig. 25B - Characteristic temperature as the function of time (sec) of figs. 25 and 25-a and the expression characterizing this curve is given by

$T(K) = 1.2615 \times 10^3 (t)^{-5.139 \times 10^{-3}}$ ... 57

Fig. 26 - The magnification is of 1200. Here the deposition conditions were of 0.7ℓ/min of He, 1.25ℓ/min of $B_2H_6$ and 2.7ℓ/min of $SiH_4$ .......... 58

Fig. 26A - The magnification is of 780. The deposition conditions were of 0.4ℓ/min of He, 1.25ℓ/Min of $B_2H_6$ and 2.7ℓ/min of $SiH_4$ .............................. 60

Fig. 26B - Characteristic temperature as the function of time (sec) of fig. 26 and 26-a and the expression characterizing this curve is given by

$T(K) = 1.2654 \times 10^3 (t)^{-5.2191 \times 10^{-3}}$ .. 61

Fig. 27 - The magnification is of 1540. Here the deposition conditions were 0.8ℓ/min of He, 0.7ℓ/min of $B_2H_6$ and 2.7ℓ/min of $SiH_4$ .................... 62

Fif. 28 - S.E.M. of a chemically etched section of a boron doped silicon on graphite at T=936°C. The magnification is of 1400. The deposition condition were 0.8ℓ/min of He, 0.7ℓ/min of $B_2H_6$ and 2.7ℓ/min of $SiH_4$ .................. 64

Fif. 29 - X-ray diffraction spectra of a boron-doped silicon layer deposited on a graphite substrate at 980°C ......... 66

PAGE

Fig. 30 - X-ray diffraction spectra of a boron-doped silicon layer deposited on graphite substrate at 967°C .............. 68

Fig. 31 - X-ray diffraction spectra of a boron-doped silicon layer deposited on a graphite substrate at 950°C .............. 69

Fig. 32 - X-ray diffraction spectra of a boron-doped silicon layer deposited on graphite substrate at 940°C .............. 70

Fig. 33 - X-ray diffraction spectra of a boron-doped silicon layer deposited on a graphite substrate at 926°C .............. 71

Fig. 34 - Influence of deposition temperature on the growth rate of polycrystalline silicon films with $B_2H_6$ as the dopants ... 73

Fig. 35 - Hall effect configuration at different sample orientations....................... 75

Fig. 36 - Schematic representation of a bridge type Hall sample electrical connections ....... 77

Fig. 37 - Electrical schematic and instrumentation for Hall effect measurements ............ 81

Fig. 38 - Hall Effect Cane (H.E.C.) ................ 82

Fig. 39 - Schematic drawing of the low temperature cryostat ................................ 83

Fig. 40 - Sign convention and related galvano-magnetic effects ......................... 86

Fig. 41 - Charge carrier concentration n and p $= (eR_H)^{-1}(cm^{-3})$; resistivity, $\rho_p$ and $\rho_n$ (ohm-cm); Hall mobility ($\mu_H = \mu_p$ and $\mu_H = \mu_n$) $= R_H\rho^{-1}$ ($cm^2\ v^{-1}\ sec^{-1}$) as the function of [B,P/Si] gas phase mollar ratio ............................. 104

Fig. 42 - Hall mobility, $\mu_H(cm^2v^{-1}sec^{-1})$ as a function of acceptor concentration ....... 105

Fig. 43 - Hall mobility, $\mu_H(cm^2v^{-1}sec^{-1})$ as a function of Donor Concentration .......... 107

PAGE


Fig. 44 - Hall mobility, $\mu_H(cm^2 v^{-1} sec^{-1})$ of Diborane-doped polycrystalline layers, as a function of an average film thickness ........................ 109

Fig. 45 - Hall mobility, $\mu_H(cm^2 v^{-1} sec^{-1})$ of phosphine-doped polycrystalline layer, as a function of an average thickness .............................. 110

Fig. 46 - Resistivity of polysilicon as a function of boron and phosphorous doping concentration .................. 113

Fig. 47 - Hall mobility, $\mu_H(cm^2 v^{-1} s^{-1})$, resistivity ρ (ohm-cm) and acceptor concentration, p(cm-3) as a function of annealing temperature is 1025°C ..... 115

Fig. 48 - Radiative Transition Levels of Electrons ............................. 119

Fig. 49 - Ideal characteristic of a Silicon Solar Cell both under dark and iluminated conditions .................. 121

Fig. 50 - Fermi energy, $E_f$(eV) as the function of donor $N_D$(cm-3) and acceptor, $N_A$(cm-3) concentrations. The position of deep donor-like and deep acceptor-like states are indicated ......................... 126

Fig. 51 - Resistivities ρ(ohm-cm) as the function of charge carriers concentrations (cm-3).. 138

# LIST OF TABLES

LIST OF TABLES

PAGE

Table 1 - Chemical Vapor Deposition (C.V.D.) of undoped & doped polysilicon on fused silica ........................... 19

Table 2 - C.V.D. of boron doped polysilicon on graphite ........................... 45

Table 3 - Deposition conditions of boron Doped polysilicon at T = 950°C ........... 90

Table 4 - Deposition conditions of phosphrous doped polysilicon at T = 950°C ........... 91

Table 5 - Hall effect sample dimensions ............ 92

Table 6 - Hall effect measured data of sample 1x at room temperature .................. 95

Table 7 - Calculated galvanomagnetic properties of samples (1x-6) at room temperature .... 96

Table 8 - Measured galvanometric properties of sample 2xa as a function of temperature ................................. 98

Table 9 - Calculated galvanometric properties of sample 2xa as a function of temperature ................................. 100

Table 10 - Power conversion efficiency of polycrystalline silicon solar cell as a function of doping (n on p type grown polysilicon) concentration and grain size ................................. 126

Table D1 Hall effect data of sample 1xa at room temperature ................................. 172

Table D2 Hall effect data of sample 2x at room temperature ................................. 173

Table D3 Hall effect data of sample 2xa at room temperature ........................... 174

Table D4 Hall effect measured data of sample 3x at room temperature .................... 175

PAGE


Table D5 Hall effect measured data of sample 3xa at room temperature ................. 176

Table D6 Hall effect measured data of sample A at room temperature ................. 177

Table D7 Hall effect measured data of sample B at room temperature ................. 178

Table D8 Hall effect measured data of sample C at room temperature ................. 179

Table D9 Hall effect measured data of sample D at room temperature ................. 180

Table D10 Hall effect measured data of sample E at room temperature ................. 181

Table D11 Hall effect measured data of sample F at room temperature ................. 182

Table D12 Hall effect measured data of sample 1 at room temperature ................. 183

Table D13 Hall effect measured data of sample 2 at room temperature ................. 184

Table D14 Hall effect measured data of sample 3 at room temperature ................. 185

Table D15 Hall effect measured data of sample 4 at room temperature ................. 186

Table D16 Hall effect measured data of sample 5 at room temperature ................. 187

Table D17 Hall effect measured data of sample 6 at room temperature ................. 188

# INTRODUCTION

# INTRODUCTION

Polycrystalline silicon has more and more device applications in solid state integrated circuits. Its properties were investigated from thermal (1) and electrical (2) point of view for field effect transistors (FET's) and for other solid state device applications (3). Due to its transport properties, perturbed by the poly-crystallinity of the films, its utility as active device is limited. However, for large area simple, low cost and large quantity active devices, such as the photovoltaic power converters, the polysilicon still might be considered of reasonable interest. Several investigators examined this system, using different substrate materials, such as steel (4), titanium (5), aluminum (6), different ceramics (7,8), tantalum (9) and graphite (10). These substrate materials were investigated from the point of view of chemical, electrical and thermal properties for solar cell application. It might be concluded that graphite is one of the best choices for polysilicon substrate material.

In this investigation, therefore, graphite, fused silica and thermally grown $SiO_2$ were examined as substrates for polysilicon grown by thermal decomposition of silane, in a resistance heated furnace. The structure of the deposited films as the function of growth conditions were investigated. The transport properties: resistivities, mobilities and charge carrier concentrations as functions of temperature, for the different films, were measured. They are correlated

to the characteristics of the prepared thin films regarding their dependence on deposition conditions. The obtained data are compared to the ones available in other literature (11, 12, 13).

In chapter 1 the experimental setup for the deposition of polysilicon on fused silica, graphite and thermally grown $SiO_2$ is described. A comparison between two Chemical Vapor Deposition (CVD) techniques is given from the point of view of gas flow rates and the grain size of the deposited polysilicon.

In chapter 2 CVD grown polysilicon films are discussed. The influence of reaction gas flow rates and deposition temperature are examined on the basis of the data obtained from scanning electron microscopy and x-ray diffraction. The activation energies of the silicon deposition reactions on fused silica and graphite substrate are evaluated.

In chapter 3 the measured electrical properties (resistivity, Hall coefficient and carrier mobility) as functions of temperature are given.

In chapter 4 the photovoltaic effect is discussed. The technology and the experimental results obtained from some fabricated solar cells are described. The results are related to the structure of the deposited polysilicon described in the previous chapters.

# CHAPTER 1

# EXPERIMENTAL PROCEDURE

CHAPTER 1

EXPERIMENTAL PROCEDURE

Silicon is deposited in a helium (He) and hydrogen ($H_2$) (99.9999 purity) atmosphere using silane diluted (0.5% vol $SIH_4$ in $H_2$) as the source of silicone. For doping of the deposited films, high purity diborane (0.05% vol $B_2H_6$ in $H_2$) and phosphine (0.05% vol $PH_3$ in $H_2$) were used. The deposition temperatures were 500-937°C.

Silicon in the range of 500 to 973°C is deposited on graphite, clear fused silica and $SiO_2$ films grown on silicon. The graphite substrates* were cut approximately 1.5 mm thick, lapped with 5μm alumina powder and mechanically polished to mirror finish with 1μm, 0.3μm and 0.5μm alumina powder. After polishing the graphite substrates, they were chemically degreased with trichloroethane and acetone in an ultrasonic rinse for 1 hour and further heat treated for out-gasing at 1050°C for 3 hours in $H_2$ and He ambient.

Silicon was deposited on clear fused Silica wafers** 2.5×2.5cm, 1 mm thick. Prior to silicon deposition at temperature of 500 to 973°C they were degreased with organic solvents, of trichloroethane, acetone and chemically etched in 10% hydrofluoric acid and rinsed in an ultrasonic bath

---

* Canadian Carborandum Niagara Falls, N.Y., and Pure Carbon Co. Inc., St. Marys, P.Q. 15857.

** Heraus Amersil, Sayre Ville, New Jersey, U.S.A.

with distilled water. Then they were heat treated at 1050°C to remove any moisture content.

Thermally grown $SiO_2$ samples were prepared as follows: p-type Si samples with a typical resistivity of 8 ohm cm were cut with a diamond saw to 1 mm thick slices, lapped with abrasive powder (50.0 μm grain size) and mechanically polished with 12, 5 and 1μm alumina powder respectively. They were then degreased in organic solvents (trichloroethane, acetone) and rinsed in an ultrasonic bath with distilled water. Then they were chemically polished in C-P4A (50cc $HNO_3$, 30cc HF, 30cc $CH_3CO_2H$) for 2 minutes according to the A.S.T.M. (14). The wafers were then oxidized in a fused silica tube furnace at 1100°C in nitrogen saturating with water vapor, by a heated water bath. The final oxide was measured using the Tellysurf and it was approximately 7μm thick. fig. 1.

## 1.1 DECOMPOSITION APPARATUS

In the first series of experiments the heterogenous film structures were grown in a resistance heated furnace. These were polysilicon on graphite, fused silica and thermally grown $SiO_2$ respectively. A schematic diagram of this furnace is shown in fig. 2 . Electronic grade graphite substrate holders (6 cm long by 4.5 cm in diameter) were cleaned as described above and degased at 1050°C for 3 hours. Thereafter the surface of the holder was coated

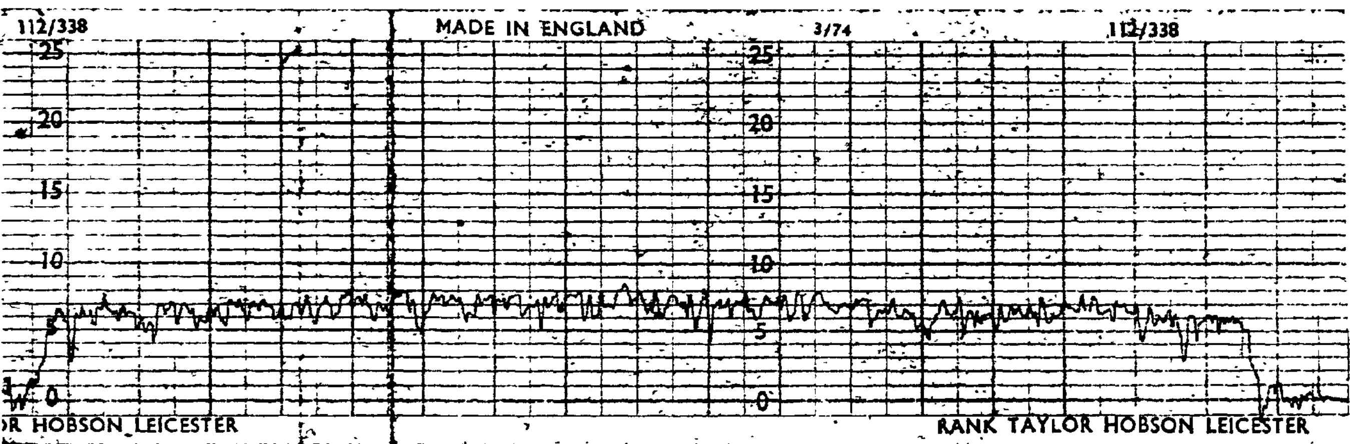


y(1 cm = 5μm vertical)

x(1 cm = $\frac{1}{20}$ cm horizontal)

Fig. 1 Tellysurf measurement of the oxide thickness

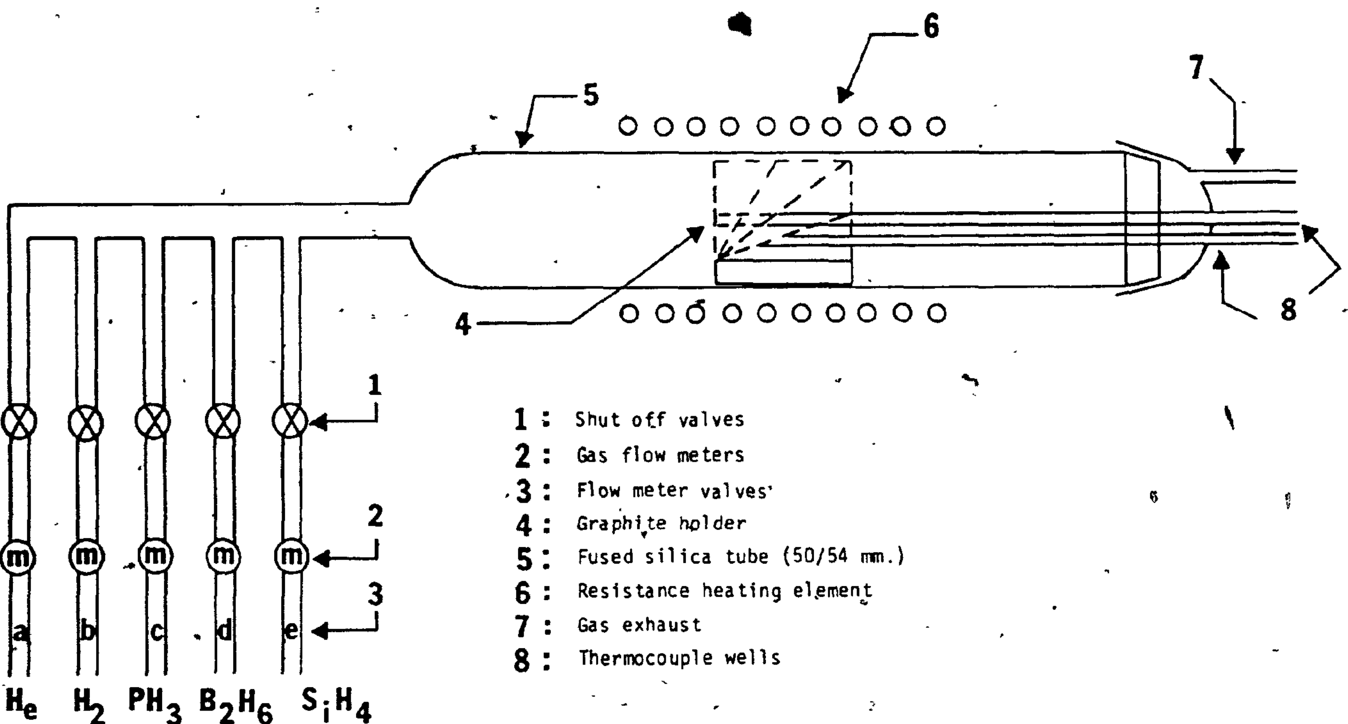


Fig. 2 Chemical Vapour Deposition System for Silicon.

with silicon to prevent any further out-gasing during the deposition of the polysilicon films. The substrate angle with respect to the deposition tube axis was varied gradually from a horizontal to vertical position, as it is shown in fig. 2 & 3. Then for a given deposition gas mixture concentration the angle dependence of the grain size was determined. This was to investigate the effects of gas flow direction on the grain sizes of the deposited films as will be discussed later.

Horizonal resistance heating furnace containing fused silica tube of 50-54 mm diameter and of 120 cm length was used for the experiment. Depositions on different substrates under different gas flow conditions were performed. For a given flow rate of the reactant gas, the largest grains were obtained when the substrate and its holder were perpendicular to the flow direction. Flow rates of carries gas mixture ranging from 7ℓ/min-27ℓ/min were used with silane gas mixtures flow rates of 0.5-3ℓ/min. The structure of the deposited films ranged from small size powder to polycristalline grain up to ≈ 1μm in size when examined under a 1000 x magnification of an optical microscope. The film thickness ranged from 0.5μm to ≈ 10μm and the time of depositions were from 45-60 mins. At flow rates of 27ℓ/min of $H_2$ and 3ℓ/min of $SiH_4$ mixture ($T=1023^0C$) clusters of silicon were deserved dispersed over the whole surface of the substrate. In some cases these clusters had dendritic formations. Since for solar cell application large (10 μm or more, ref. 6 )

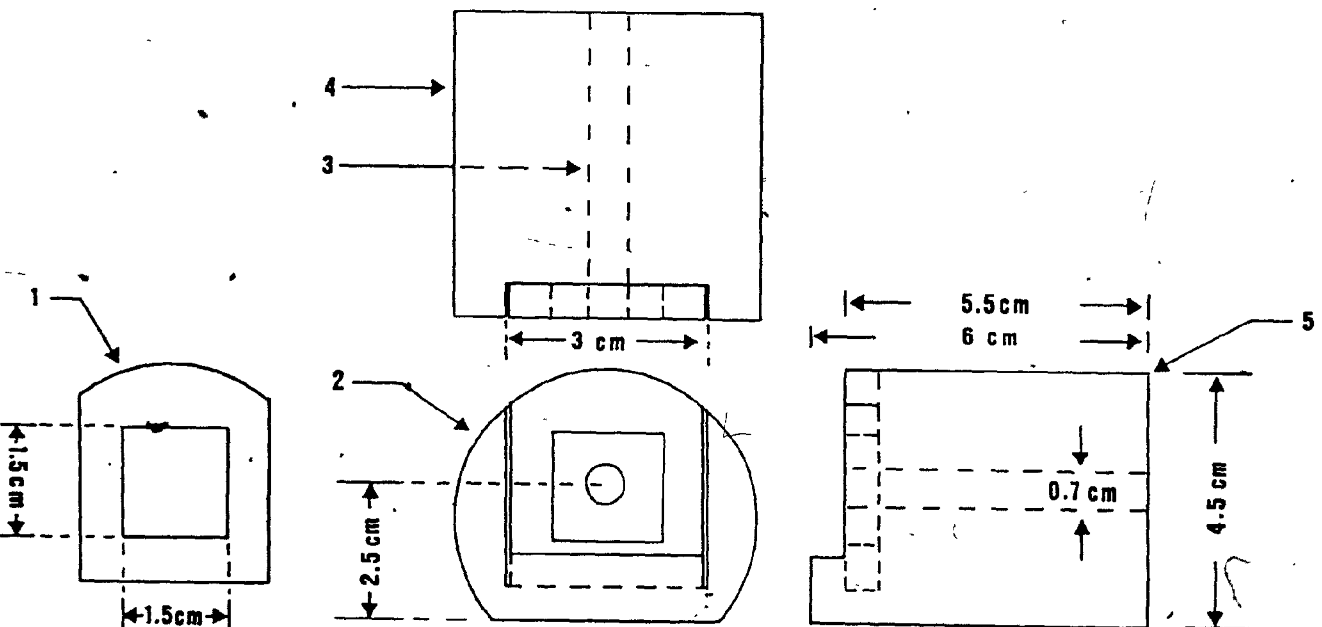


1 : Sample mask
2 : Front view
3 : Thermocouple well
4 : Top view
5 : Side view

Fig. 3 Graphite Substrate Holder

crystallites with columnar features are desired, the results obtained with this technique for growing polycrystalline silicon were found unsatisfactory. The main drawback of this system was the large degree of decomposition of silane before reaching the substrate materials. This was due to the silane's thermochemical instability even at room temperature. At temperatures above 650$^{o}$C its rate of decomposition largely increased. This thermal instability of silane tends to promote pyrolysis in the gas phase without surface activation. This thermal decomposition must be suppressed as much as possible before the gas reacts on surface of the substrate. This could be achieved by various ways such as low pressure deposition growths (15,16), high flow rates (10), both air and water cooled entry systems (17-19). In addition, the high consumption of ultra high purity gases "6-9" grade made the system uneconomical. To overcome these problems, pyrolysis of silane prior to deposition ought to be minimized as much as possible. This was achieved by applying a water cooled jacket around the gas inlet as shown in fig. 4. With this system, flow rates were dropped drastically from (26-27ℓ/min. to 2-6ℓ/min.). Distance from exit nozzle of the water cooled gas inlet to the substrate was 1.3-3.8 cm. The predecomposition of silane in the entering gas mixture was reduced, therefore the effective growth rates were largely increased and the morphology of the deposited films greatly improved. Furthermore as it will be seen in the next chapter, the size of the polysilicon grains have increased.

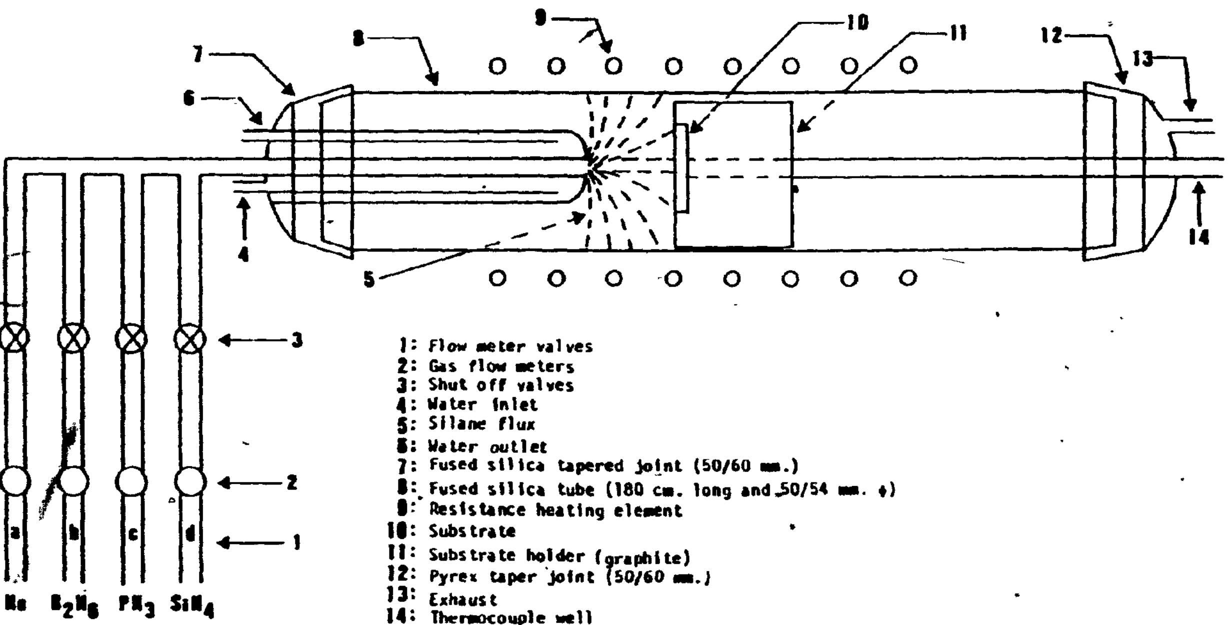


Fig. 4 Chemical Vapor Deposition system for silicon with water cooled gas mixture system inlet.

The water cooled gas inlet system is shown in fig. 5. It is made of fused silica, having a 7.0 mm diameter inner tube of 43 cm length. This is in a water jacket made of fused silica tubes of 18 and 28 mm outside diameter furnished with inlet and outlet nozzles. The system is mounted on a taper joint to be connected to the reaction tube. The amount of gas introduced into the system is controlled by Matheson metering values, type 603 and, the temperature in the system is controlled by a thermocouple placed through the substrate holder at the back of the substrate (see fig. 3-4). The actual temperature variation in the system were studied by placing the thermocouple exactly at the substrates position, under actual flow conditions. The gradients or temperature variations as a function of flow rates have been recorded on a Hewlett Packard Recorder (Model No. 7414A) (see fig. 18 & 20). To prevent any back flow in the system, the exhaust gases were passed through two pyrex traps, one empty, another half filled and finally burned. The liquid in the second trap was glycerol (fig. 6).

The schematic diagram of the resistance heated furnace is shown in fig. 7. It consists of a 50 cm. long three zone commercially available Kantal Al wire heater. It is connected through three transformers and two controllers. As is depicted in fig. 7, Chromel-Alumel thermocouples were used for adjusting and controlling the deposition temperature.

Temperature profiles of the furnace were determined as

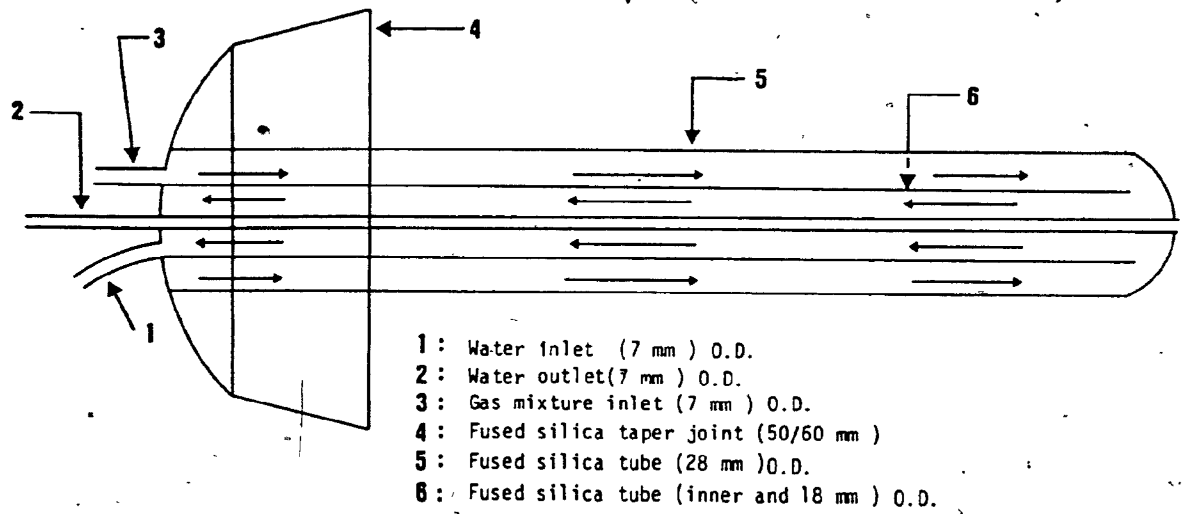


Fig. 5 Water cooled gas mixture inlet system made of fused silica.

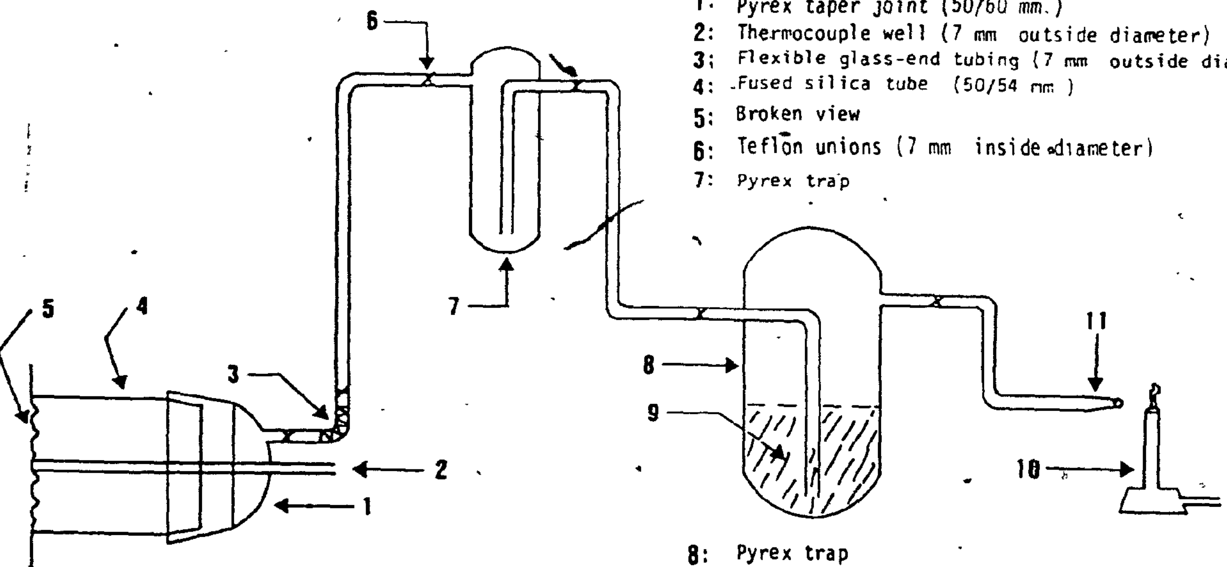


Fig. 6 Gas exhaust system

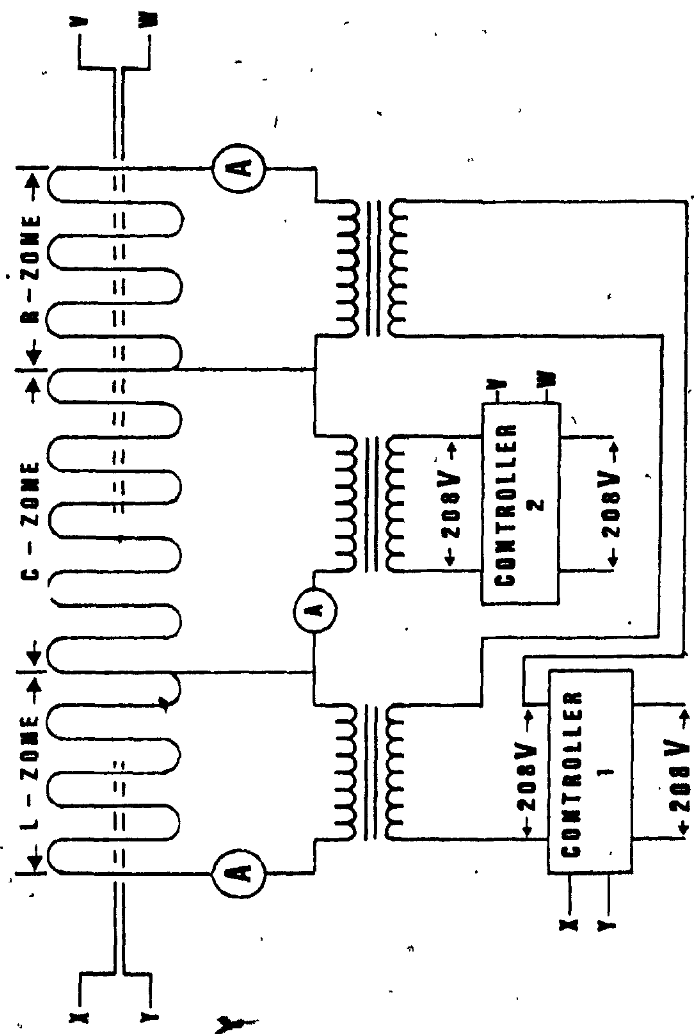


Fig. 7 Power system resistance heater furnace

follows: The Cromel-Alumel thermocouple wires (22 gauge) were inserted into a 6.3 mm outside diameter stainless steel 316 tubing of a length of 180 cm. The connector end of the thermocouple was then sealed with scaling wax and fitted through an ultra Torr Adapter* into the thermocouple well. The exposed junction of the thermocouple was placed at the position of the substrate and the temperature was recorded. These measurements were repeated at different substrate positions with respect to the nozzle of the water cooled gas inlet system. To simulate the growth temperature a combination of He and $H_2$ was used to replace the reactive gas mixtures. In attempt to actually measure the growth temperature as a function of reactive gas mixtures, it was noticed that by increasing the flow rate from 0.5 to 6$\ell$ $min^{-1}$ ($\simeq$ 6$\ell$/min) the temperature decreased from 990$^{o}$C to 920$^{o}$C. However, when the reactive gas mixture ($SiH_4$ in $H_2$) was introduced, after the initial temperature drop, as the decomposed silicon built up on the thermocouple, the temperature started to increase (see recording). This was due to the shielding effect of the deposited silicon, preventing the heat dissipation of the exposed thermocouple. Therefore this latter temperature corresponded closely to the substrate temperature of the gas flow.

---

* Laurentian Valve & Fittings, 96 Leacock-Point Claire, Que. H9R 1H1.

# CHAPTER 2

# CHEMICAL VAPOR DEPOSITION

## CHAPTER 2

## INTRODUCTION

The Chemical Vapor Deposition (C.V.D.) process is extensively used in the electronic industry for the fabrication of solid state devices and integrated circuits. This process consists of several physical and chemical steps. The exact path of the decomposition mechanism depends on the temperature of vapor phase, substrate and concentration of the reactant. Excellent account of this type of analysis is given by Hirth and Pound (20) and by Powell et al (21).

In the case of C.V.D. the reaction can either be surface rate or mass transfer controlled. In the first case the reaction rate, or in the case of Silane ($SiH_4$), the decomposition rate ($SiH_4 \rightarrow Si+2H_2$) would be the slowest, thus rate controlling process. This would manifest itself in a temperature dependence of the reaction rate according to the Arrhenieus equation ($\frac{dr}{dt} = Ae^{-E/RT}$) where

$\frac{dr}{dt}$ = growth rate (um/min)

E = activation energy of the reaction

R = Ideal Gas Constant

T = absolute temperature

However in the case of mass transfer control the reaction does not follow the above given rate law, since the slow process then would depend on the diffusion rate

of the reactant and products, to and from the surface, respectively. The temperature dependence of the reaction rate, then would only be notecable on the temperature dependence of the gas phase diffusion content. Therefore in the absence of equilibrium limitations, diffusion can be the rate limiting process in the C.V.D. of silicon but this manifests itself at temperatures well above 1000°C (22-23).

The most important steps involved in heterogeneous decomposition of $SiH_4$ are the diffusion rate of the reactant to the surface, decomposition of silane on the substrate which resolves into surface nucleation, and desorption of $H_2$. The slowest of these will be the rate controlling mechanism.

The thermal decomposition of silane to silicon and hydrogen was found to be a surface catalized reaction. This can be noticed since there is little indication of a gas phase parallel reaction. The thermal decomposition reaction, in contrast with the reduction type reaction of silicon halides is non reversible. Therefore the hydrogen desorption rate or its large excess in the gas phase, would not be a rate controlling mechanism.

## 2.1 C.V.D. OF SILICON ON FUSED SILICA

Deposition of polysilicon on fused silica slices have been performed as described previously in chapter 1 using the system shown in fig. 4.

Deposition of polysilicon were carried out from 500°C to 973°C. Experimental data related to growth rates as a

function of temperature and flow rates from 630°C to 950°C are collected in table 1. Plots of the growth rate as the function of reciprocal temperature were made and from the straight line so obtained, activation energy was calculated.

At deposition temperature of 500 [fig. 8] to 550°C [ fig. 9] the deposited silicon was found to be amorphous. This can be deduced from Laues' X-ray diffraction picture shown in fig. (8A and 9A). The lack of Laue's diffraction pattern indicates amorphous (disordered) structure. The deposited films of fig. (8-9) appear in various colours. These colours are due to the non uniform thickness of the deposited film.

At deposition temperature of 630° - 750°C the polycrystalline films were found to be practically smooth. These films are presented in fig. (10 and 11). The smoothness is due to the fact that the polycrystalline films are made up of very small crystallites with no preferred orientation. Higher growth temperature yielded larger crystallites and hence rougher surfaces. From the solar cell point of view this is advantageous since solar cells require large crystallites greater than 10μm or single crystal films are required. It can be noticed in fig. 10 and somewhat less in fig. 11, that faded white lines are propagating practically all over the surface. These cracks are the results of strains which are exhibited between the $SiO_2$ substrate and the deposited Si. This is due to their difference in coefficient of thermal expansions.

| DISTANCE from NOZZLE (cm) | TEMP. DET. (°C) | | MILLIVOLT SIGNAL (mV) | | GAS FLOW RATES | | | | | | GRAIN SIZE (μm) | GROWTH RATE (μm/min) |
|---|---|---|---|---|---|---|---|---|---|---|---|---|
| | no flow | with flow | no flow | with flow | He | | $B_2H_6$ | | $SiH_4$ | | | |
| | | | | | mm | L/min | mm | L/min | mm | L/min | | |
| UNDOPPED | | | | | | | | | | | | |
| 1" | 665 | 650 | 27.66 | 27.03 | 20 | 0.40 | - | - | 22 | 2.0 | 0.15 | 0.10 |
| " | 670 | 661 | 28.17 | 27.45 | 20 | 0.40 | - | - | 22 | 2.0 | 0.17 | 0.012 |
| " | 700 | 679 | 29.14 | 28.25 | 25 | 0.55 | - | - | 22 | 2.0 | 0.26 | 0.017 |
| " | 722 | 691 | 30.06 | 28.72 | 25 | 0.55 | - | - | 22 | 2.0 | 0.33 | 0.022 |
| " | 736 | 702 | 30.65 | 29.22 | 30 | 0.80 | - | - | 22 | 2.0 | 0.44 | 0.029 |
| " | 763 | 727 | 31.77 | 30.27 | 33 | 0.95 | - | - | 22 | 2.0 | 0.72 | 0.048 |
| " | 785 | 747 | 32.68 | 31.10 | 35 | 1.05 | - | - | 22 | 2.0 | 1.14 | 0.076 |
| " | 812 | 774 | 33.79 | 32.23 | 35 | 1.05 | - | - | 22 | 2.0 | 1.18 | 0.120 |
| " | 840 | 796 | 34.93 | 33.16 | 37 | 1.15 | - | - | 22 | 2.0 | 2.85 | 0.190 |
| " | 870 | 825 | 36.15 | 34.32 | 40 | 1.30 | - | - | 22 | 2.0 | 4.95 | 0.33 |
| | | | | | | | | | | | | |
| DOPPED | 650 | 630 | 27.03 | 26.19 | 10 | 0.20 | 5 | 0.20 | 22 | 2.0 | 0.15 | 0.010 |
| 1" | 665 | 648 | 27.66 | 26.95 | 10 | 0.20 | 5 | 0.20 | [illegible] | 2.0 | 0.23 | 0.015 |
| " | 678 | 661 | 28.21 | 27.49 | 13 | 0.17 | 5 | 0.20 | 22 | 2.0 | 0.32 | 0.021 |
| " | 702 | 679 | 29.22 | 28.25 | 15 | 0.25 | 5 | 0.20 | 22 | 2.0 | 0.45 | 0.03 |
| " | 723 | 691 | 30.10 | 28.72 | 15 | 0.25 | 5 | 0.20 | 22 | 2.0 | 0.60 | 0.04 |

Table 1: Chemical Vapor Deposition (C.V.D.) of undoped & doped polysilicon on fused silica. Growth temperature is from 630 to 973°C.

| DISTANCE from NOZZLE (cm) | TEMP. DET. (°C) | | MILLIVOLT SIGNAL (mV) | | GAS FLOW RATES | | | | | | GRAIN SIZE | GROWTH RATE | RECORDER SPEED |
|---|---|---|---|---|---|---|---|---|---|---|---|---|---|
| | | | | | He | | $B_2H_6$ | | $SiH_4$ | | | | |
| | no flow | with flow | no flow | with flow | mm | L/min | mm | L/min | mm | L/min | (μm) | (μm/min) | (mm/min) |
| DOPPED | 738 | 707 | 10.73 | 29.22 | 20 | 0.40 | 5 | 0.20 | 22 | 2.0 | 0.75 | 0.050 | |
| | 766 | 727 | 11.90 | 30.27 | 20 | 0.40 | 5 | 0.20 | 22 | 2.0 | 1.23 | 0.082 | |
| | 788 | 717 | 32.81 | 31.10 | 25 | 0.55 | 5 | 0.20 | 22 | 2.0 | 1.80 | 0.120 | |
| | 815 | 774 | 33.91 | 32.23 | 25 | 0.55 | 5 | 0.20 | 22 | 2.0 | 3.15 | 0.210 | |
| | 842 | 796 | 35.02 | 33.16 | 28 | 0.70 | 5 | 0.20 | 22 | 2.0 | 4.50 | 0.300 | |
| | 875 | 825 | 36.35 | 34.32 | 30 | 0.80 | 5 | 0.20 | 22 | 2.0 | 7.20 | 0.480 | |
| | | | | | | | | | | | | | |
| UNDOPPED | 985 | 927 | 40.73 | 38.44 | 20 | 0.40 | - | - | 32 | 3.0 | | | 10 |
| 1" | 985 | 927 | " | " | 35 | 1.05 | - | - | 25 | 2.5 | | | " |
| 1" | 985 | 927 | " | " | 30 | 0.80 | - | - | 27 | 2.5 | 6.2 | 0.41 | " |
| " | 955 | 927 | " | " | 40 | 1.30 | - | - | 22 | 2.0 | 7.65 | 0.51 | " |
| " | 990 | 950 | 40.92 | 39.35 | 30 | 0.80 | - | - | 30 | 2.7 | - | - | " |
| " | 990 | 950 | " | " | 50 | 1.80 | - | - | 22 | 2.0 | 10.5 | 0.70 | " |
| " | 1025 | 973 | 42.29 | 40.26 | 50 | 1.80 | - | - | 30 | 2.7 | | | " |
| | | | | | | | | | | | | | |
| | | | | | | | | | | | | | |
| | | | "Work discontinued" | | | | | | | | | | |

Table 1 (cont'd): Chemical Vapor Deposition (C.V.D.) of undoped & doped polysilicon on fused silica. Growth temperature is from 630 to 973°C.

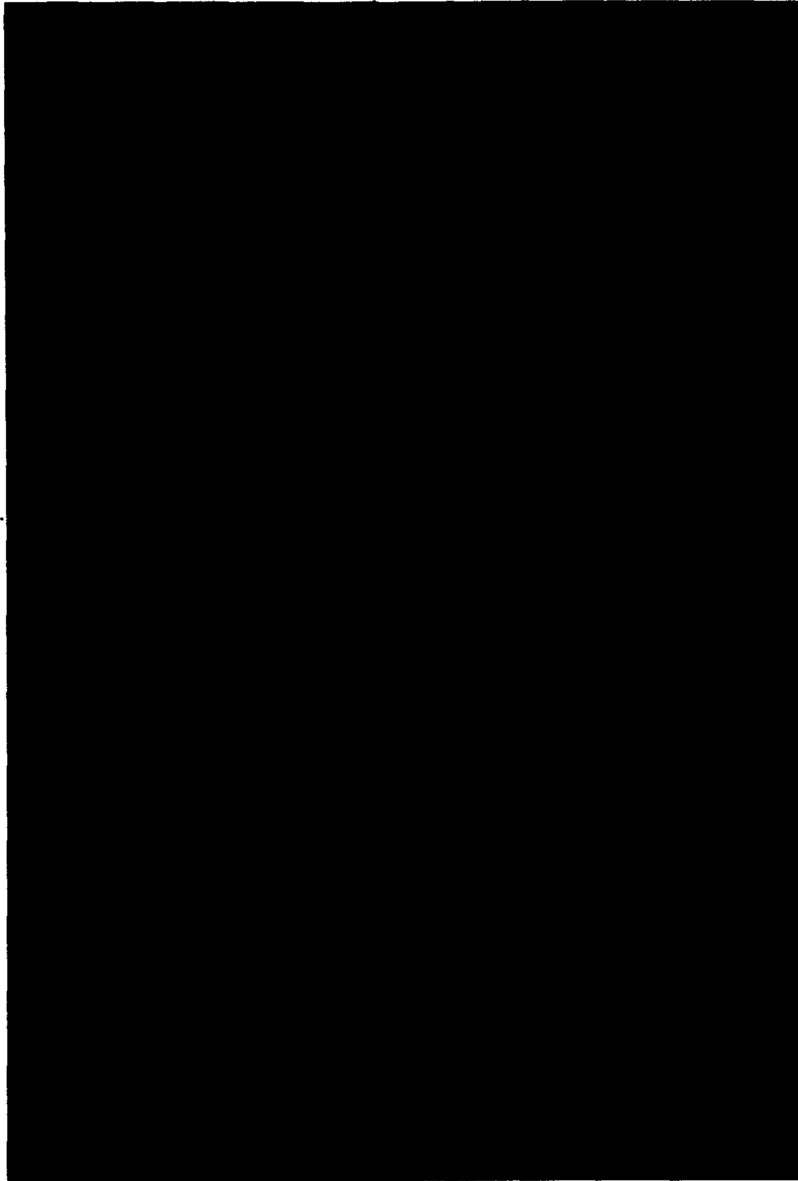

Figure 8: Amorphous Silicon ,T = 500°C

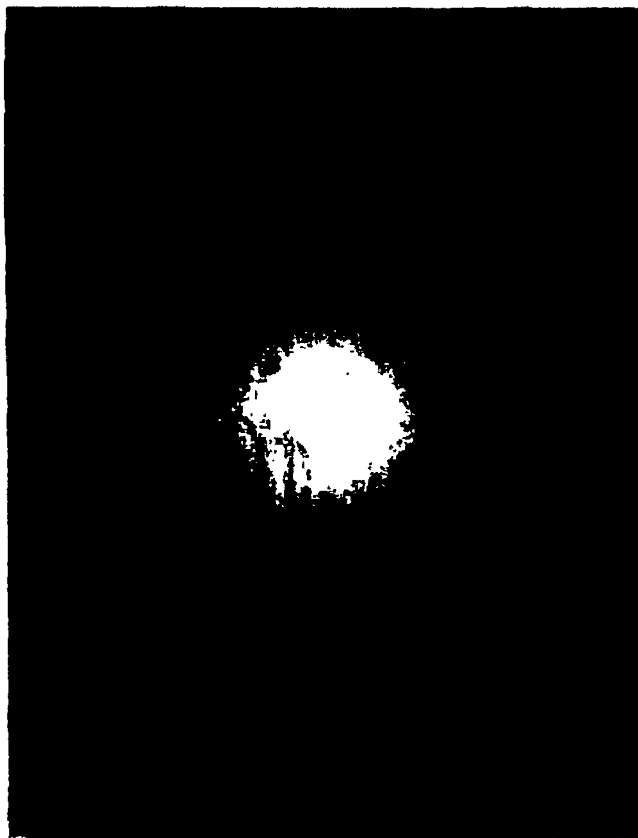

Figure 8A: X-Ray Difraction of amorphous Silicon at 500°C.

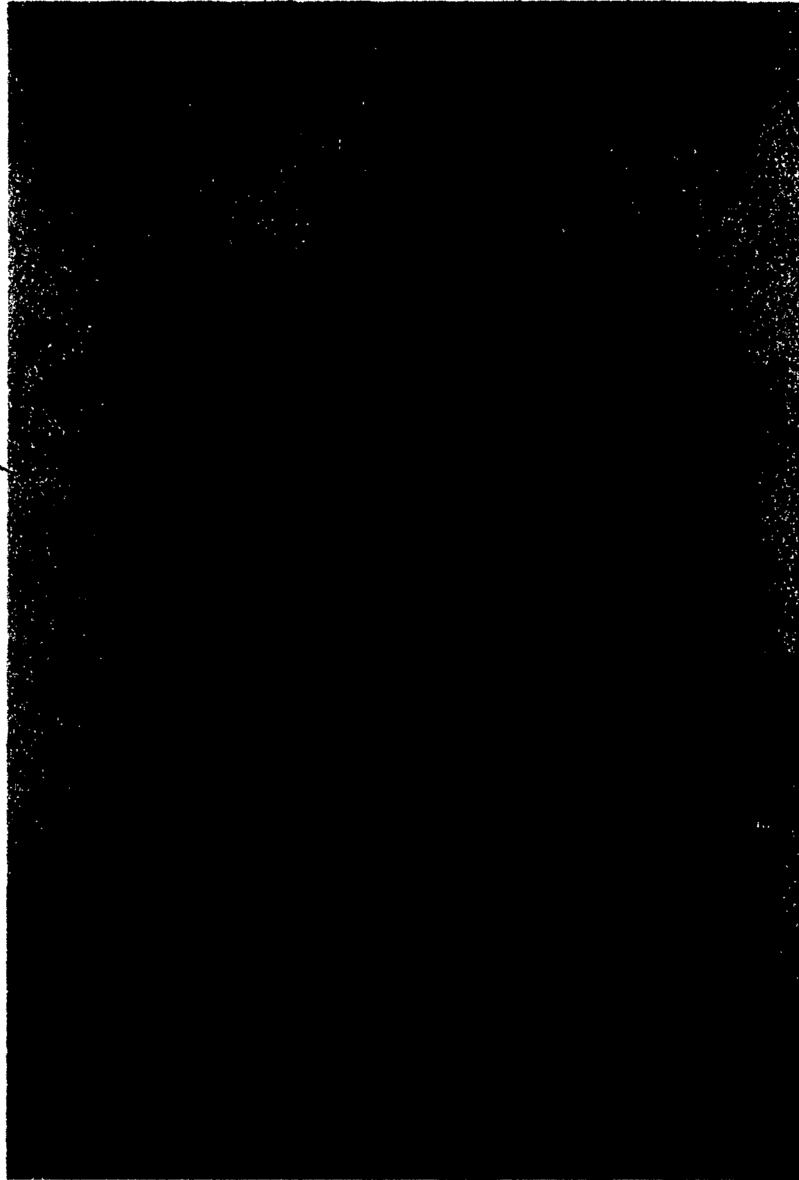

Figure 9: Amorphous Silicon, T = 550°C

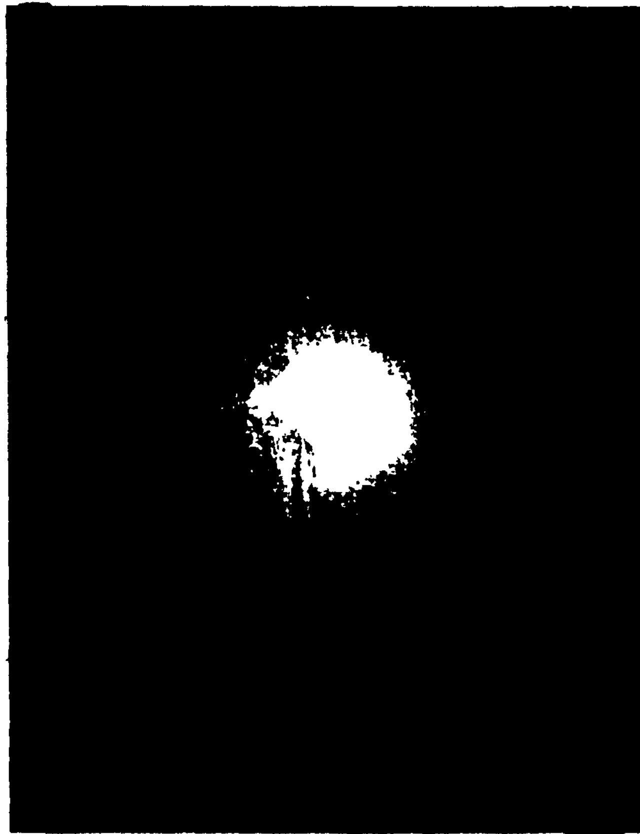

Figure 9A: X-Ray Diffraction of amorphous Silicon at 550°C.

Fig. 10: Scanning electron micrograph of the as-grown surface of a silicon layer deposited on a fused silica substrate at 680°C by the pyrolisis of silane at flow rates of 0.55ℓ/min of He and 20ℓ/min of $SiH_4$.

Fig. 11: Scanning electron micrograph of the as-grown surface of a silicon layer deposited on graphite substrate at 750°C by the pyrolysis of Silane at flow rates of 1.05ℓ/min of He and 2.0ℓ/min of $SiH_4$.

At approximately 800°C and above, the growth of preferred orientation of (110) was noticed. This was investigated on the other hand by the scanning electron microscopy (S.E.M.) pictures as they are shown in figs. (12,13,14) and by the x-ray diffraction recording as they are shown in figs. (15 and 16) (see appendix A).

Fig. 12 shows the S.E.M. picture of the of grown polysilicon film at T=796°C. The magnification is 1200, the deposition conditions where 1.15ℓ/min of He and 2ℓ/min of $SiH_4$.

Fig. 13 shows the S.E.M. picture of the boron doped silicon layer deposited at T=796°C. The gas phase molar ratio of boron to silicon [B/Si] was $3.7x10^{-3}$. Comparing fig. 13 to fig. 12 it can be noticed that by introducing diborane ($B_2H_6$) into the system the size of the crystallites at T=796°C have increased by a factor of about 1.8. This increase in grain size might be related to the effect of diborane in the reacting gas mixture. If the absorption rate of diborane is commensurable or greater than the one of silane, the two reactance might compete for the active-centers of the surface. Consequently the diborane field sites were not available to the silane to be nucleated on. Therefore a decreased surface nucleation concentration for silicon growth would result. This phenomenon could explain the increase size of the grains, forming the doped deposited film.

Fig. 14 is the S.E.M. picture of the as grown polysilicon film at T=825°C. The magnification is 1200, the desposition

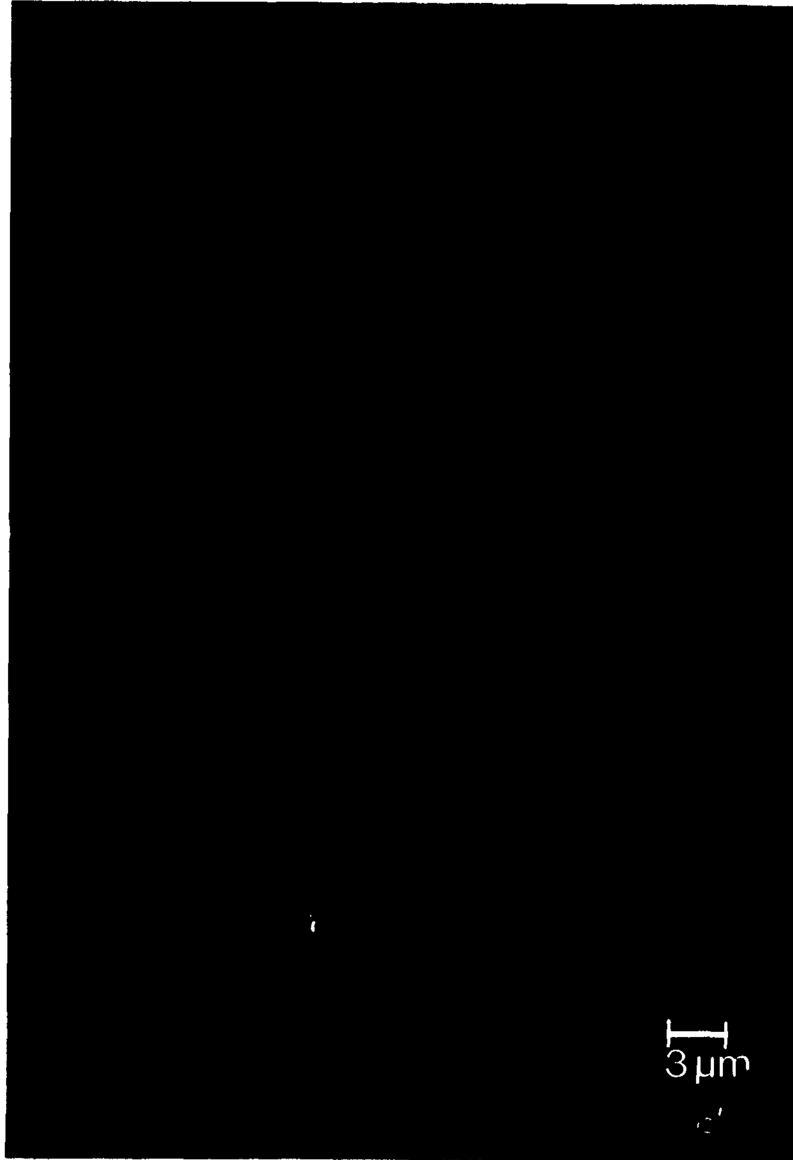


Fig. 12: Scanning electron micrograph of the as grown surface of a silicon layer deposited on fused silica substrate at 796°C by the pyrolysis of silane at flow rates of 1.15ℓ/min of He and 2.0ℓ/min of Silane.

Fig. 13: Scanning electron micrography of the as-grown surface of a boron-doped film by growth deposited on fused silica substrate at 796°C by the pyrolysis of Silane at flow rates of 0.7ℓ/min of He, 0.2ℓ/min of $B_2H_6$ .05% by Vol. in $H_2$ and 2.0ℓ/min of $SiH_4$.

Fig. 14 Scanning electron micrograph of the as-grown surface of a silicon layer deposited on fused silica substrate at T=825°C by the pyrolysis of silane at flow rates of 1.3ℓ/min of He and 2.0ℓ/min of $SiH_4$.

condition were as follows; 1.3ℓ/min of He and 2ℓ/min of $SiH_4$. It is noticed that at this temperature the deposited film is composed of large grains.This indicates the influence of the deposition temperature on the grain size of the polysilicon films.

The relative intensities (111), (220), (311), (400), (330) and (422) were measured to indicate the relative amounts of (111), (110), (311), (100), (331) and (211) planes present in the films. The relative intensities are depicted in figs. (15 and 16) for deposition temperatures of 825°C and 973°C. Comparing fig. 15 to fig. 16, it can be noticed that at 825°C the (220) texture dominates over the (111) and especially over the other orientations. The quality of the grown film at 825°C can be assessed from the (220)/(111) orientation intensity ratio. This was found to be equal to 2 indicating silicon crystallites of (110) orientation dominating over the (111).

As it can be deduced from fig. (16) at 973°C the (111) oriented crystallites dominate. The peaks of the (220) plane are also high but seem to be decreasing in intensity as the temperature is increasing. At this temperature the grown films exhibited a (111)/(220) intensity ratio of 1.09 ≈ 1.1 indicating that the silicon crystallites in this case show a weak (111) preferred orientation. The intensities of (220) or (110) texture are still greather than that shown in the A.S.T.M. card (24). The A.S.T.M. card contains recorded information on the amount of texture

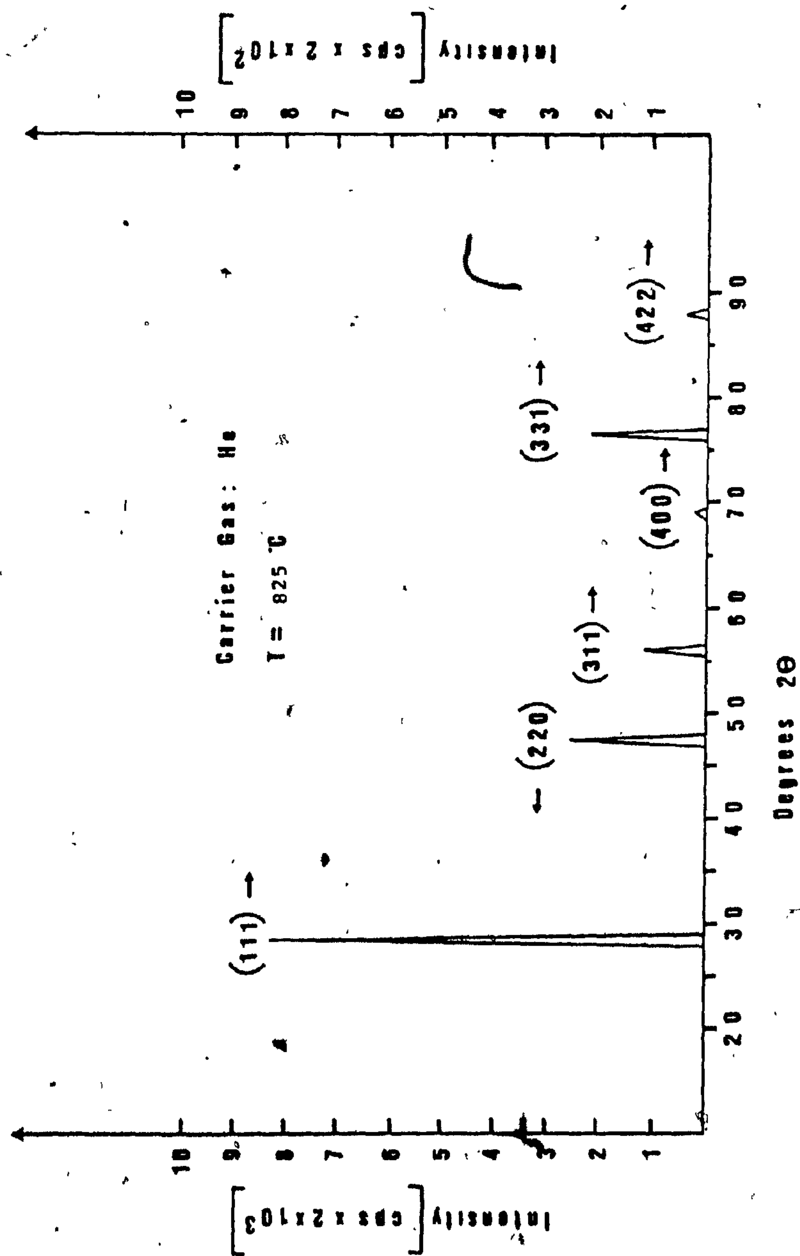


Fig. 15: X-ray diffraction spectra of polysilicon deposited on fused silica at T=825°C.

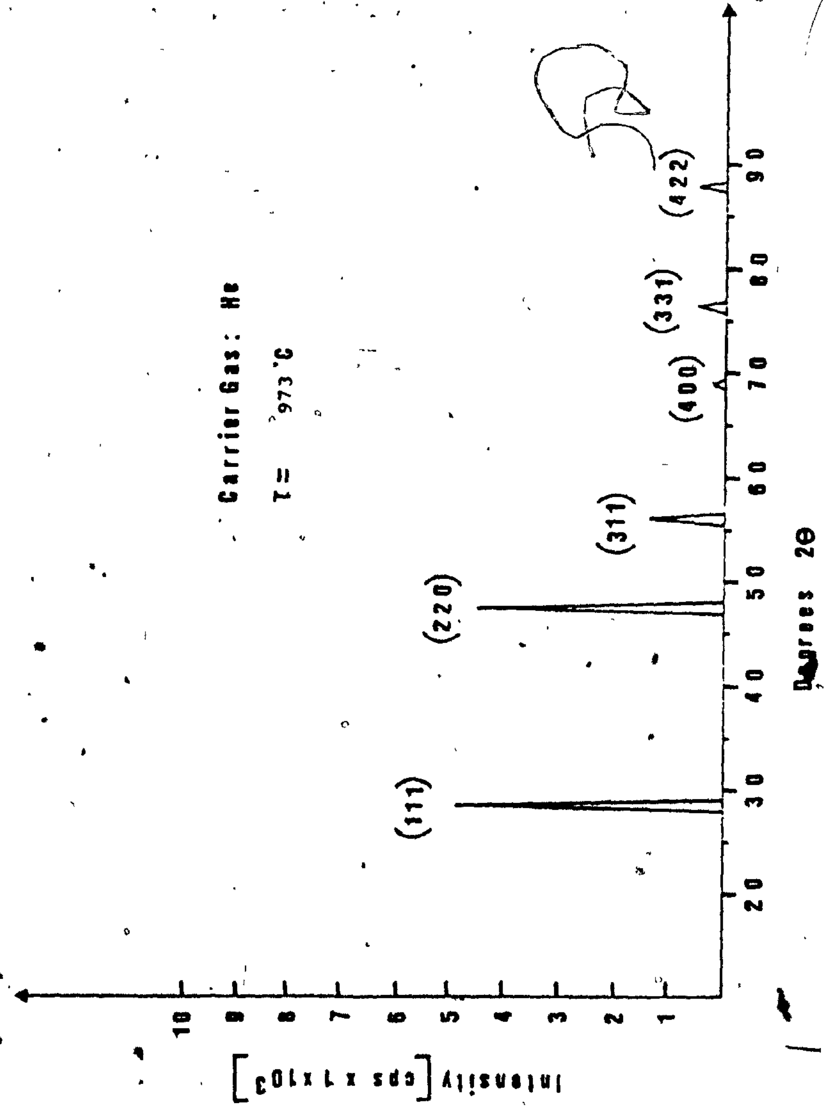


Fig. 16: X-Ray diffraction spectra of polysilicon deposited on fused silica at T=973°C.

present when single crystal silicon is in the form of a powder. The relative intensity ratios which one observes are based on the highest quantity of texture present. The highest intensity peak becomes a reference and the other peaks are compared to it on a percentage base, indicating the realtive amounts of planes present in the power. This is in good agreement with the published data (25,26) where the (111) orientation is dominating over (110) at temperatures above 1000°C.

Fig. 17 is the S.E.M. picutre of the as grown poly-silicon film at T=927°C. The magnification is 1200. The deposition condition were as follows; 1.3ℓ/min of He and 2ℓ/min of $SiH_4$. Under these conditions and temperature the silicon films appear to have taken some pyramidical form.

Fig. 18 depicts the characteristic temperature variation as a function of time (in seconds) related to the growth of film shown in fig. 17 starting from the onset of the gas flows, in the system.

An exponential decay which can be observed is due to the introduction of the gases into the reaction tube, causing the temperature in the system to drop. This occurs until the system attains steady state. The curve of fig. 20 was best fitted by the use of "power fitting" and the expression describing its behaviour can be given as $T(K) = at^b$ where

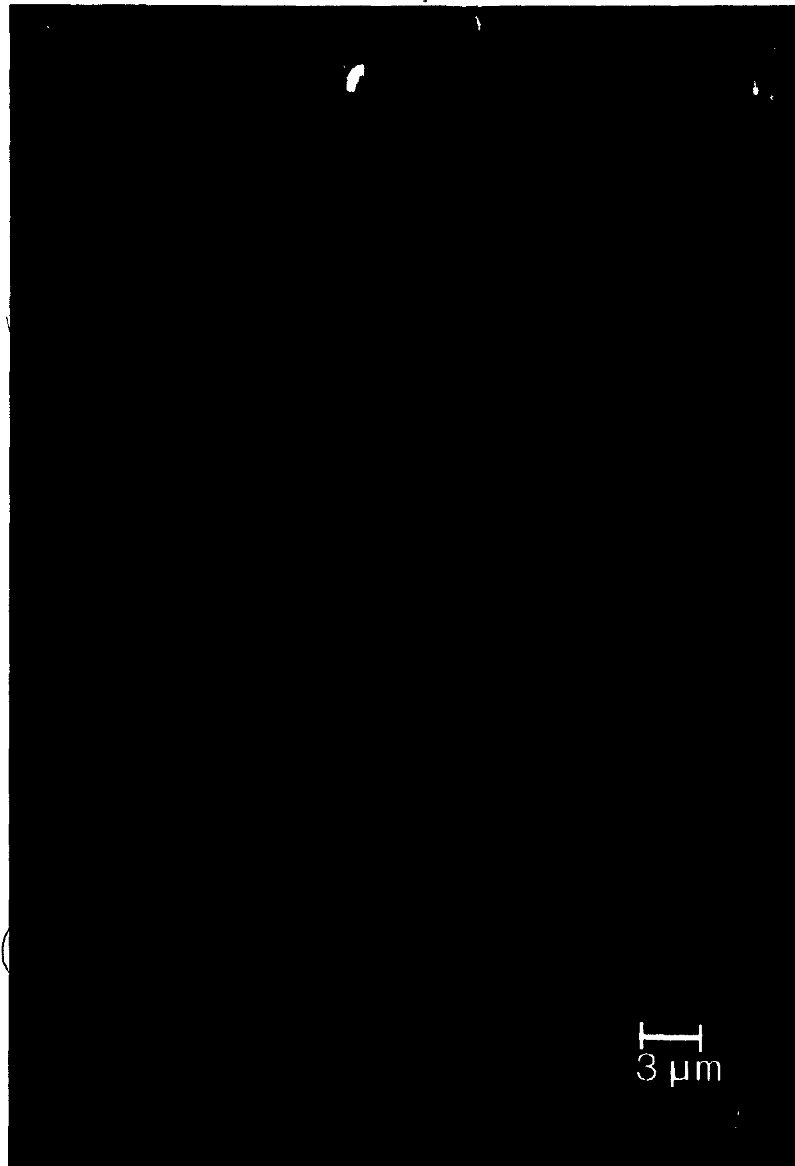


Fig. 17: Scanning electron micrograph of the as-grown surface of a silicon layer deposited on fused-silica substrate at 927°C by the pyrolysis of silane at flow rates of 1.3ℓ/min of He and 2.0ℓ of $SiH_4$.

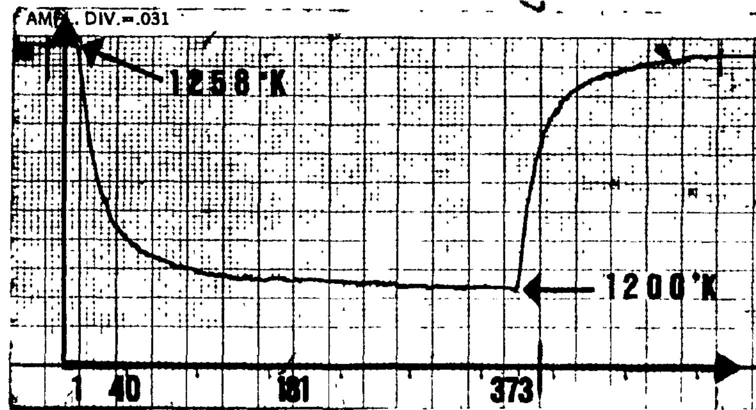


Fig. 18: Depicts the characteristic temperature as the function of time (sec) of fig. 17 and the expression characterizing this curve is given by $T(K) = 1.2562 \times 10^3 (t)^{-7.5198 \times 10^{-3}}$.

T(K) = temperature in degrees Kelvin

t = time (sec)

a and b = constants , given in the respective figures.

Fig. 19 is the S.E.M. picture of the grown polysilicon film at T=950°C. The magnification is 180: The deposition condition were 1.8ℓ/min of He and 2ℓ/min of $SiH_4$. At these deposition conditions and temperature, the grain size of the polysilicon has further increased. Comparing these pyramidical structures to that of fig. 17 it can be noticed that they have the same characteristics except the pyramids of fig. 19 are 2.7 times larger than those of fig. 17. Since the gas flow rates of the samples represented in fig. 17 and 19 were the same, the effect of increasing deposition temperature on the grain size can be noticed once more.

Fig. 20 depicts the characteristic temperature variation as the function of time for the sample related to the deposition of fig. 19.

Fig. 21 is the S.E.M. picutre of the grown polysilicon film at T=973°C. The magnificent is 180: The deposition condition were 1.8ℓ/min of He and 2.7ℓ/min of $SiH_4$. In this figure the reactant gas concentration was increased augmenting the flow rate from 2-2.7ℓ/min. This resulted in a decrease in the grain size of the deposited film (see fig. 21).

The average growth rate as a function of reciprocal growth temperature for undoped polysilicon (from 650°-825°C)

Fig. 19: S.E.M. of the as-grown surface of a silicon layer deposited on fused silica substrate at 950°C by the pyrolysis of Silane at flow rates of 1.8ℓ/min of He and 2.0ℓ/min of Silane.

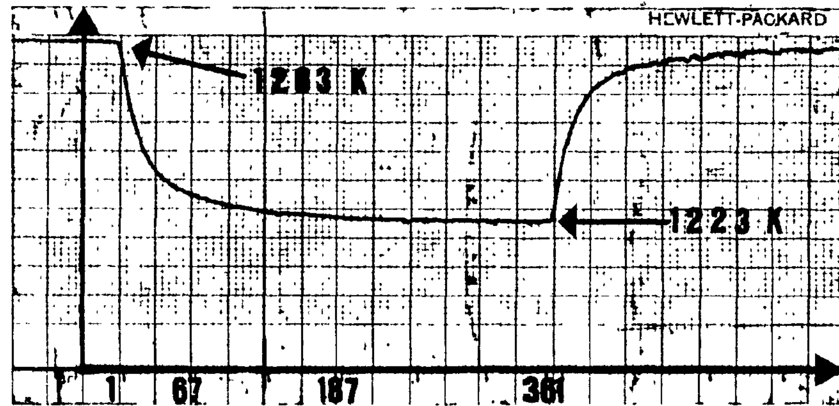


Fig. 20: Depicts the characteristic temperature as the function of time(sec) of fig. 19 and the expression characterizing this curve is given by

$$T(K) = 1.2624 \times 10^{3} t^{-5.8228 \times 10^{-3}}$$

Fig. 21: Scanning electron micrograph of the as-grown surface of a silicon layer deposited on fused silica substrate at 973°C by the pyrolysis of silane at flow rates of 1.9ℓ/min of He and 2.7ℓ/min of $SiH_4$.

and for $B_2H_6$ doped polysilicon (from 630°-825°C) with B/Si gas phase molar ration of $3.7x10^{-3}$ and undoped polysilicon (from 927°-950°C) were plotted on a semi-log graph as shown in fig. (22). From the obtained straight line the obtained activation energies can be calculated using the Arrhenieus equation as follows.

The theory of the Arrhenius equation is based upon the variation of the equilibrium constant with temperature given by the following expression.

$$\frac{d \ln K}{dt} = \frac{\Delta H}{RT^2} \quad (1)$$

The equilibrium constant K is given by $K=k/k'$ (2)

where

$k$ = represents the specific reaction rate in the forward direction

$k'$ = represents the specific reaction rate in the reverse direction

and

$\Delta H$ = change in enthalpy during the reaction.

Substituting equation 2 into equation (1) we obtain

$$\frac{d \ln k}{dt} - \frac{d \ln k'}{dt} = \frac{\Delta H}{RT^2} \quad (3)$$

where

$$\Delta H = \Delta H - \Delta H' = E - E' \quad (4)$$

$\Delta H + \Delta H'$ = are the forward and reverse reaction's enthalpies

$E$ & $E'$ = are the characteristic energies

From Eqn. 4 two separate expressions can be given.

$$\frac{d \ln k}{dT} = \frac{E}{RT^2} \tag{5}$$

$$\frac{d \ln k'}{dT} = \frac{E'}{RT^2} \tag{6}$$

Integrating one of the above expressions yields the Arrhenius equation.

$$k = A e^{-E/RT} \tag{7}$$

Using equation (7) a plot of ln k vs 1/T gives a straight line with a slope of -E/R.

The activation energy of the reaction (E) was interpreted by Arrhenius as the excess energy over the average energy that the reactants must possess in order for reaction to occur (27-28).

Maintaining the reactant gas flow rate constant (2ℓ/min) the growth of doped ($B_2H_6$ flow rate 0.2 ℓ/min) and undoped Silicon were determined. In the case of undoped and doped system the deposition temperature range was the same as the one mentioned above. The results are shown in fig. 22.

The experimentally determined temperature dependence of the growth rate resulted in activation energies of 41K cal/mole and 38 K cal/mole for the undoped and doped system, respectively.

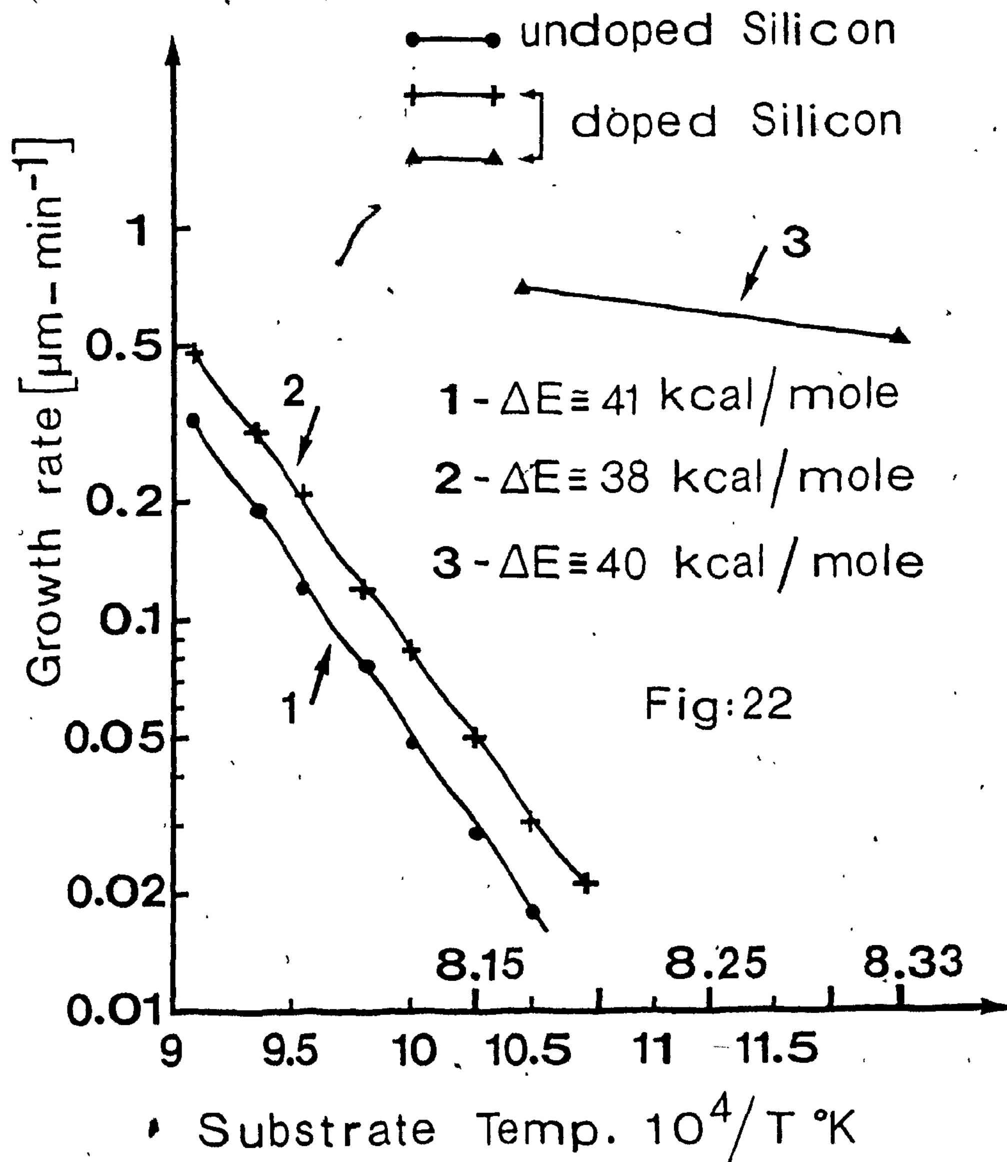


Fig. 22: Growth rate of polysilicon on fused silica as a function of temperature.

## 2.2 C.V.D. OF SILICON ON GRAPHITE

### Introduction

A chemical vapor deposition process treating the pyrolisis of $SiH_4$ was discussed in chapter 2.1. Due to the experimentally found evidence indicating that the silicon reacts with silica substrates causing it to peel off, further efforts were pursued to develop this type of solar energy converter. Consequently, polysilicon was deposited on graphite substrates as it has been outlined in the introduction.

### 2.2.1 Poly-Silicon on Graphite

Depositions of polysilicon on graphite have been performed as described previously in chapter 1 using the system as shown in fig. 4.

The substrate temperatures were in the range of 926° to 980°C.

Data related to the growth rate as a function of temperature, dopant ($B_2H_6$) and silane ($SiH_4$) flow rates are collected in Table 2. In all experiments, flow rates of the carrier (He) and dopant gases ($B_2H_6$) varied from (0.0-0.8ℓ/min and 0.2-1.25ℓ/min), respectively. The silane gas mixture flow rates varied from (1.75-3.7ℓ/min) to yield deposition rates in the range of (0.566-1.34μm/min). The concentration of silane was 0.5% vol in Hydrogen ($H_2$) in the reactant gas mixture.

The average deposition rate of silicon at 926-936°C

| DISTANCE from NOZZLE (cm) | TEMP. DET. (°C) | | MILLIVOLT SIGNAL (mV) | | GAS FLOW RATES | | | | | | GRAIN SIZE (μm) | GROWTH RATE (μm/min) | RECORDER SPEED (mm/min) |
|---|---|---|---|---|---|---|---|---|---|---|---|---|---|
| | | | | | He | | $B_2H_6$ | | $SiH_4$ | | | | |
| | no flow | with flow | no flow | with flow | mm | L/min | mm | L/min | mm | L/min | | | |
| 4/16 | 976 | 938 | 40.38 | 38.88 | 0 | 0 | 10 | 0.7 | 20 | 1.75 | | | |
| 4/16 | 976 | 931 | " | 38.60 | 20 | 0.4 | 10 | " | 20 | " | | | |
| 12/16 | 983 | 936 | 40.65 | 38.80 | 15 | 0.25 | 5 | 0.2 | 30 | 2.7 | 10 | 0.666 | |
| 12/16 | 983 | 926 | " | 38.40 | 20 | 0.4 | 10 | 0.7 | 30 | " | 12.34 | 0.823 | |
| 14/16 | 985 | 936 | 40.73 | 38.80 | 20 | 0.4 | 10 | 0.7 | " | " | 12.54 | 0.836 | |
| 14/16 | 985 | 923 | " | 38.28 | 20 | 0.4 | 15 | 1.25 | 30 | 2.7 | 12 | 0.800 | |
| 1" | 987 | 975 | 40.81 | 40.34 | 10 | 0.15 | 5 | 0.2 | 20 | 1.75 | | - | |
| 1" | 987 | 954 | " | 39.51 | 20 | 0.4 | 5 | 0.2 | 30 | 2.7 | 15.2 | 1.013 | |
| 1" | 987 | 948 | " | 39.27 | 10 | 0.15 | 10 | 0.7 | 30 | " | 14.6 | 0.973 | |
| 1" | 987 | 942 | " | 39.03 | 20 | 0.4 | 10 | 0.7 | 30 | " | 14 | 0.933 | |
| 1" | 987 | 932 | " | 38.64 | 30 | 0.8 | 10 | 0.7 | 30 | " | 13 | 0.866 | |
| 1" | 987 | 932 | " | " | 20 | 0.4 | 15 | 1.25 | 30 | " | 12.5 | 0.833 | |
| 1" | 987 | 922 | " | 38.24 | 20 | 0.4 | 10 | 0.7 | 40 | 3.7 | out | - | |
| 1 1/4 | 990 | 957 | 40.92 | 39.65 | 30 | 0.8 | 10 | 0.7 | 30 | 2.7 | 15.5-16 | 1.066 | |
| 1 1/4 | 1000 | 967 | 41.31 | 40.02 | 20 | 0.4 | 10 | 0.7 | 30 | " | 18.5 | 1.233 | |
| 1 1/4 | 1000 | 967 | 41.31 | 40.02 | 20 | " | 15 | 1.25 | 30 | " | 18.7 | 1.246 | |
| 1 1/4 | 1015 | 980 | 41.90 | 40.53 | 20 | " | 10 | " | 30 | " | 19.5-20 | 1.333 | |

Table 2: C.V.D. of boron-doped silicon on graphite. The deposition temperature is from 923-980°C.

was found to be about 0.833 and 0.666 μm/min respectively when the gas phase molar ratio of boron to silicon [B/Si] was of $3.7\times10^{-3}$ and $1.3\times10^{-2}$. At silane flow rates below 2.7ℓ/min the size of the crystalites became concentration dependent, as it is shown in Table 2. It is to be noted that in the deposition process of silicon on graphite, the size of the grains were found to depend on the amount of $B_2H_6$ present in the reactant system. For example (see Table 2) at T=936°C at a gas phase molar ratio [B/Si] $3.7\times10^{-3}$ the size of the grain was found to be approximately 10μm, but when the gas phase molar ratio [B/Si] was of $1.3\times10^{-2}$ the size of the grains were found to be on the average of 12.5 μm.

In the deposition temperature range of (T=927° to 980°C) it was found that the features of the crystallites remained the same when the B/Si molar ratio was between $3.7\times10^{-3}$ $-2.3\times10^{-2}$. Above or below this molar ratio the grain size of the crystallites decreased from about 20 - 15 μm (see Table 2).

Fig. 23 is a S.E.M. of a boron doped silicon layer deposited on graphite at T=936°C. The magnification is 1200. Here the deposition conditions were of 0.25ℓ/min of He, 0.2ℓ/min of $B_2H_6$ and 2.7ℓ/min of silane, resulting in a deposition rate of 0.3 μm/min. The size of the grains are 8 μm. The [B/Si] molar ratio was $3.7\times10^{-3}$.

Fig. 23-a shows a cross sectional S.E.M. picture of

a boron doped layer deposited on graphite at T=936°C. The magnification is 1200. The deposition conditions were that of the sample used for fig. 23. The cross section was obtained by simply breaking the graphite substrate. Large columns extending from the surface to the graphite substrate can be distinguished. They are having about the same size as the grains. It is noticeable, however, that at the silicon graphite interface the polynucleation introduces a less structured region. After about 10μm thickness the formation of the columns are dominating.

As it can be seen from the data collected in Tabe 2 the microstructure of the deposited polysilicon depends strongly on the substrate temperature and deposition rate. The silicon layers deposited at the temperatures of (923-980°C) and flow rates of (2.1 - 3.15 ℓ/min) consisted of crystallites with characteristic sizes of 10 - 20μm and with an average layer thickness ranging from 29 - 60μm (see fig. (24-26)).

From the S.E.M. picutres of figs. (24-26) it can be observed that large crystallites are mixed with smaller ones. The presence of these crystallites of different sizes might be due to the inhomogeneities present on the surface of the substrate affecting the nucleation sites and their distribution.

When the deposition rates were maintained between (0.866 - 1.3μm/min) and the temperature was varied from 926°C-980°C the structure of the crystallites remained the same

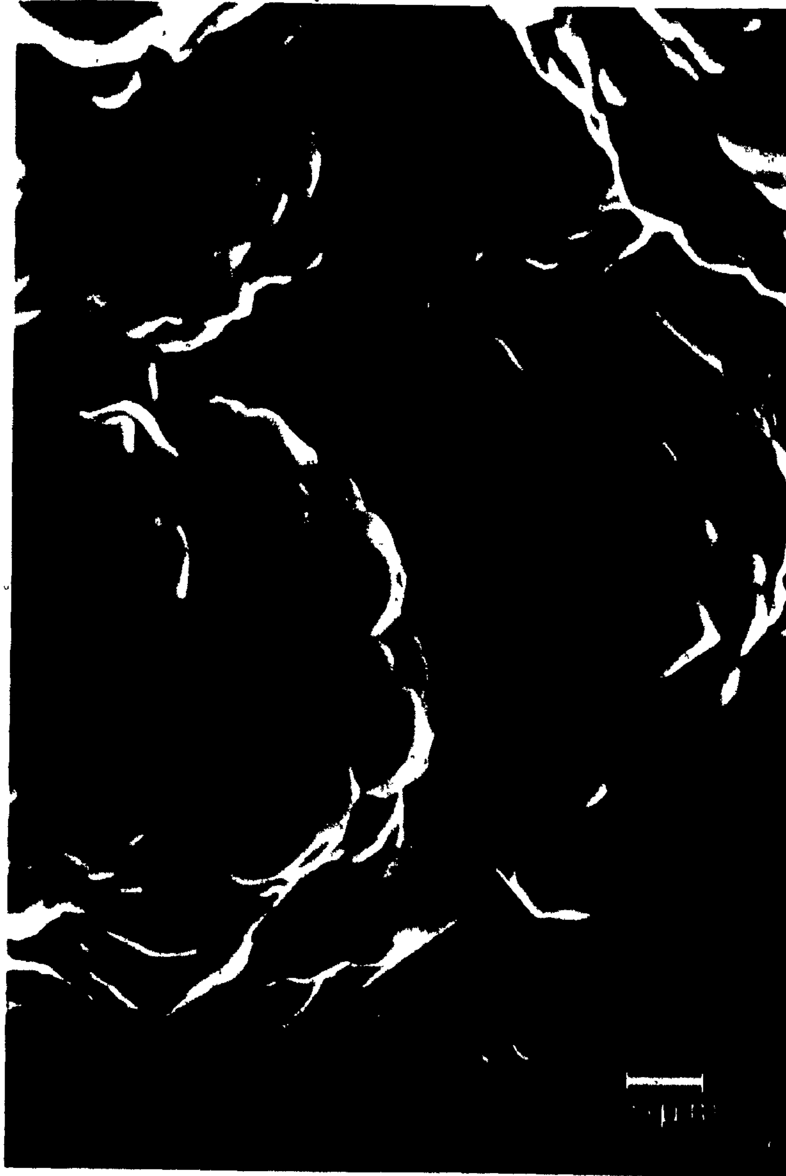

Fig. 23: Scanning electron micrograph (S.E.M.) of the as-grown surface of a boron-doped film by growth deposited on graphite substrate at T=936°C by the pyrolysis of Silane at flow rates of 0.25ℓ/min of He, 0.2ℓ/min. of $B_2H_6$ and 2.7ℓ/min of $S_iH_4$.

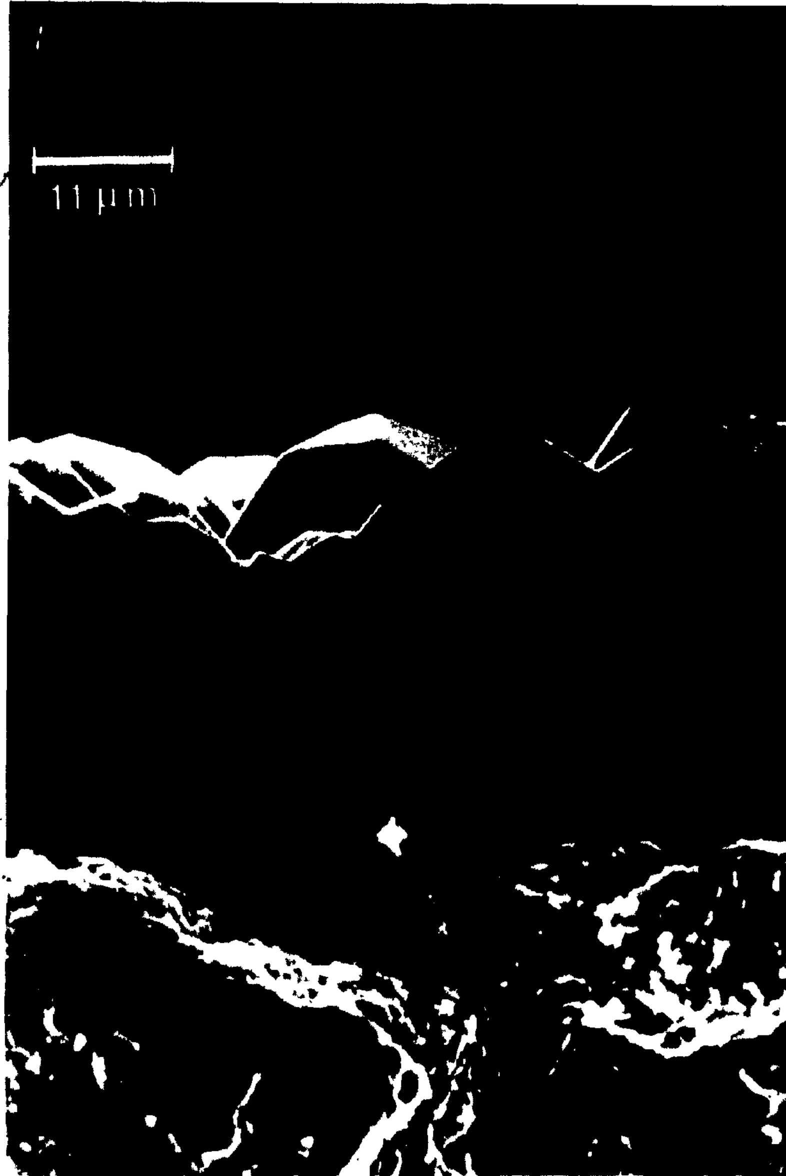


Fig. 23-a: Cross sectional S.E.M. of a boron doped layer, deposited on graphite at T=936°C. The magnification is 1200. The deposition conditions were of 0.25ℓ/min of He, 0.2ℓ/min of $B_2H_6$ and 2.7ℓ/min of $SiH_4$.

however their size increases with increasing temperature In fig. (24 a,b - 26 a,b) well defined columns extending from the graphite substrate across the deposited layer can be seen. The diameters of these columns and film thicknesses were in the range of 30 - 50μm thick.

Fig. 24 is a S.E.M. picture of a boron doped silicon layer deposited on graphite at T=954°C. The magnification is 1200. Here the deposition conditions were of 0.8ℓ/min of He 0.7ℓ/min of $B_2H_6$ and 2.7ℓ/min of $SiH_4$. The average size of the grains are 16μm. The [B/Si] gas molar ratio was $3.7\times10^{-3}$.

It can be noticed from fig. 24 that even though the deposition conditions were the same like the ones of fig. 23, the morophology or crystal structures has improved drastically, due to the increased deposition temperature (T=954°C). Fig. 24a is a cross section S.E.M. of Fig. 24. The magnification is of 1200. An increased layer uniformity can be observed in fig. 24a. Columns have homogenized in such a way that they appear as a continuous layer from the surface down to about 5μm from the silicon graphite interface.

Fig. 24-b depicts the characteristic temperature variation as the function of time (sec) related to the growth of the films shown in fig. 24 and 24a. The timing is from the onset of the gas flow in the system. This phenomenon was already discussed in Chapter 2 in relation to fig. 18.

Fig. 25 is a S.E.M. of doped silicon layer deposited

Fig. 24: S.E.M. of the as-grown surface of a boron doped film by growth, deposited on graphite substrate at T=954°C. The magnification is 1200. Here the deposition conditions were of 0.8ℓ/min of He, 0.7ℓ/min of $B_2H_6$ and 2.7ℓ of $SiH_4$.

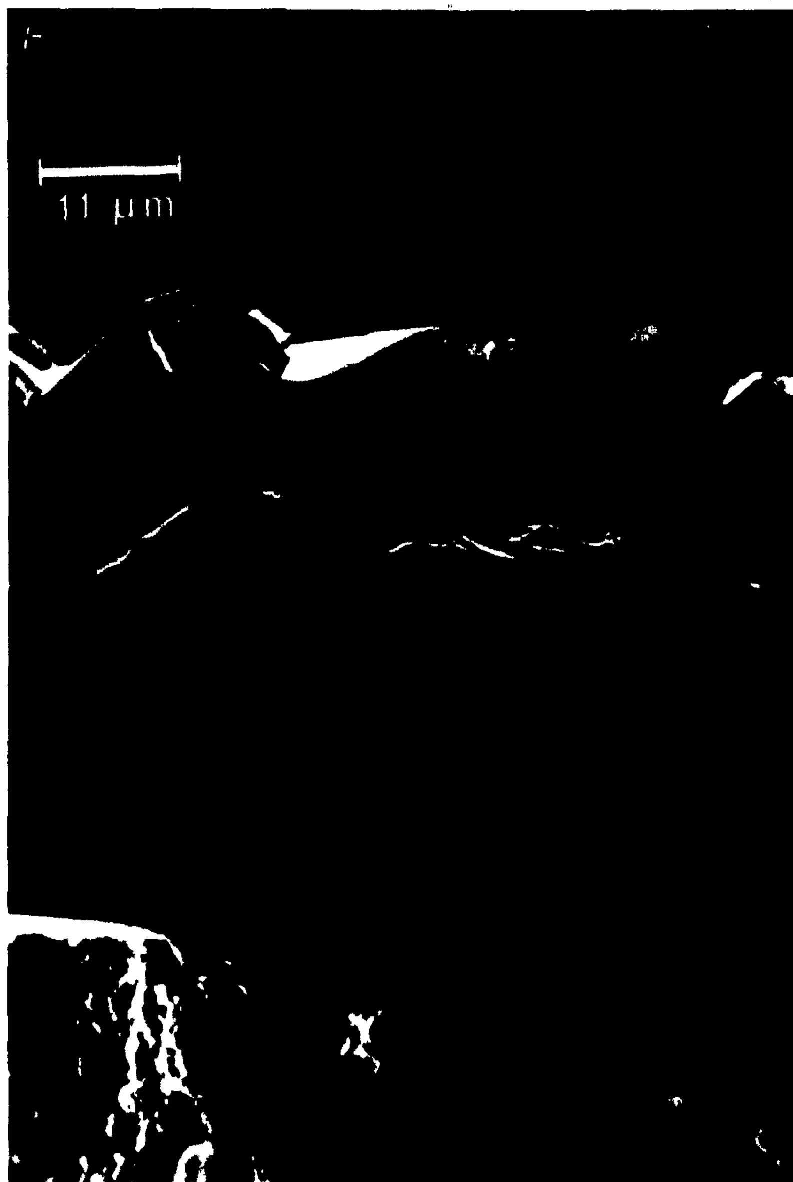


Fig. 24-a: Cross sectional S.E.M. of Fig. 24. The magnification is 1200. Here the deposition conditons were that of fig. 24.

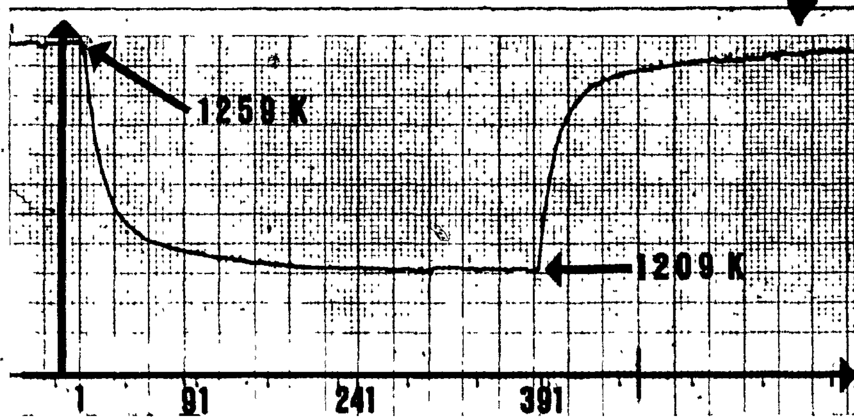


Fig. 24-b: Depicts the characteristic temperature as the function of time (sec) of figure 24 and 24-a, and the expression characterizing this curve is given by $T(K) = 1.2604\times10^{3}(t)^{-7.673\times10^{-3}}$.

on graphite at T = 967°C. The magnification is 1200. Here the deposition conditions were 0.4ℓ/min of He, 0.7ℓ/min of $B_2H_6$ and 2.7ℓ/min of $SiH_4$. The average size of the gain was 18.5μm. The [B/Si] gas phase molar ratio was $1.29\times10^{-2}$.

It can be seen again from fig. 25 that as the deposition temperature is increased, the structure of the deposited film remains the same while the size of the crystallites becomes about 1.2 times larger than the columns of fig. 24.

Fig. 25a is a cross sectional S.E.M. view of Fig. 25. The magnification is 1200. It can be seen that the morphology of the columns has improved. They extend from the silicon graphite interface to the surface with a thin (about 2μm) intermediary layer. At the right hand side of the photo one sees columns intermingled with other columns of different sizes. This indicates again the influence of heterogeneously distributed nucleation centers of the graphite substrate.

Fig. 25b depicts the characteristic temperature variation as the function of time (sec) related to the growth on the film shown in fig. 25 and 25a starting from the onset of the gas flow, in the system as it has been discussed previously.

Fig. 26 is a S.E.M. of a boron doped silicon layer deposited on graphite at T=967°C. The magnification is 1200. Here the deposition conditions were 0.4ℓ/min of He, 1.25ℓ/min of $B_2H_6$ and 2.7ℓ/min of $SiH_4$. The grain size was 18.7μm. The [B/Si] gas phase molar ratio was $2.3\times10^{-2}$. The condition of depositions were the same as the ones given in the case of fig. 25, however the doping concentration was

Fig. 25: S.E.M. of the as-grown surface of a boron-doped film by growth deposited on graphite substrate of T=967°C. The magnification is 1200. Here the deposition conditions were of 0.4ℓ/min of He, 0.7ℓ/min of $B_2H_6$ and 2.7ℓ/min of $SiH_4$.

Fig. 25-a: Cross sectional S.E.M. view of fig. 25. The magnification is 1200. Deposition condition were that of fig. 25.

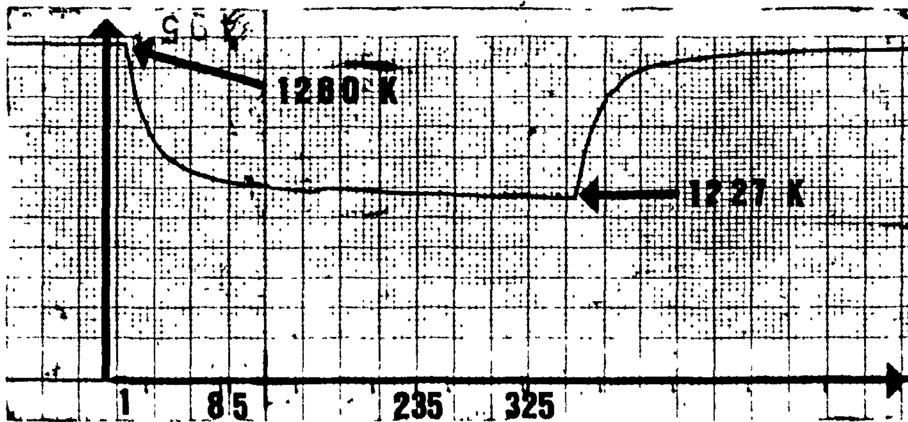


Fig. 25-b: Depicts the characteristic temperature as the function of time (sec) of figs. 25 and 25-a and the expression characterizing this curve is given by $T(K) = 1.2615\times10^{3}(t)^{-5.1395\times10^{-3}}$.

Fig. 26: S.E.M, of a boron doped silicon layer deposited on graphite at T=967°C. The magnification is 1200. Here the deposition conditions were of 0.7ℓ/min of He, 1.25ℓ/min of $B_2H_6$ and 2.7ℓ/min of $SiH_4$.

changed from $1.29\times10^{-2}$ to $2.3\times10^{-2}$ molar ratio of [B/Si].

Fig. 26a is a cross section S.E.M. of fig. 26. The magnification is 780. Here the temperature was maintained at 967°C, however the doping concentration was increased to $2.3\times10^{-2}$. This resulted in a more pronounced columnar structure of the grown layer. The average column diameters are about 20μm with a layer thickness of 49μm. Therefore, it can be seen that the growth of large columnar layers extending from the silicon/graphite interface to the surface can be realized at growth temperature starting at about 900°C.

Fig. 26b depicts the characteristic temperature variation as the function of time (sec) related to the growth of the film shown in fig. 26 and 26b starting from the onset of the gas flow in the system.

To obtain a better view of the microstructure or morphology of the films, a few samples were sent to Energy and Mining Resources of Canada to be analysed. Fig. 27 and 28 are the result of an etched sample. The etching solution was consisting of 30 parts of HNO3; 120 parts of acitic acid and 5 parts of hydroflouric acid. The etching time was one minute.

Fig. 27 is an S.E.M. of a boron doped and etched silicon layer deposited on graphite at T=936°C. The magnification is 1540. Here the deposition conditions were 0.8ℓ/min He, 0.7ℓ/min of $B_2H_6$ and 2.7ℓ/min of $SiH_4$, resulting in an average growth rate of 0.86μm/min. The grain diameters was about 13μm. The B/Si gas molar ratio was $1.29\times10^{-2}$. The grown surface of most of the crystallites

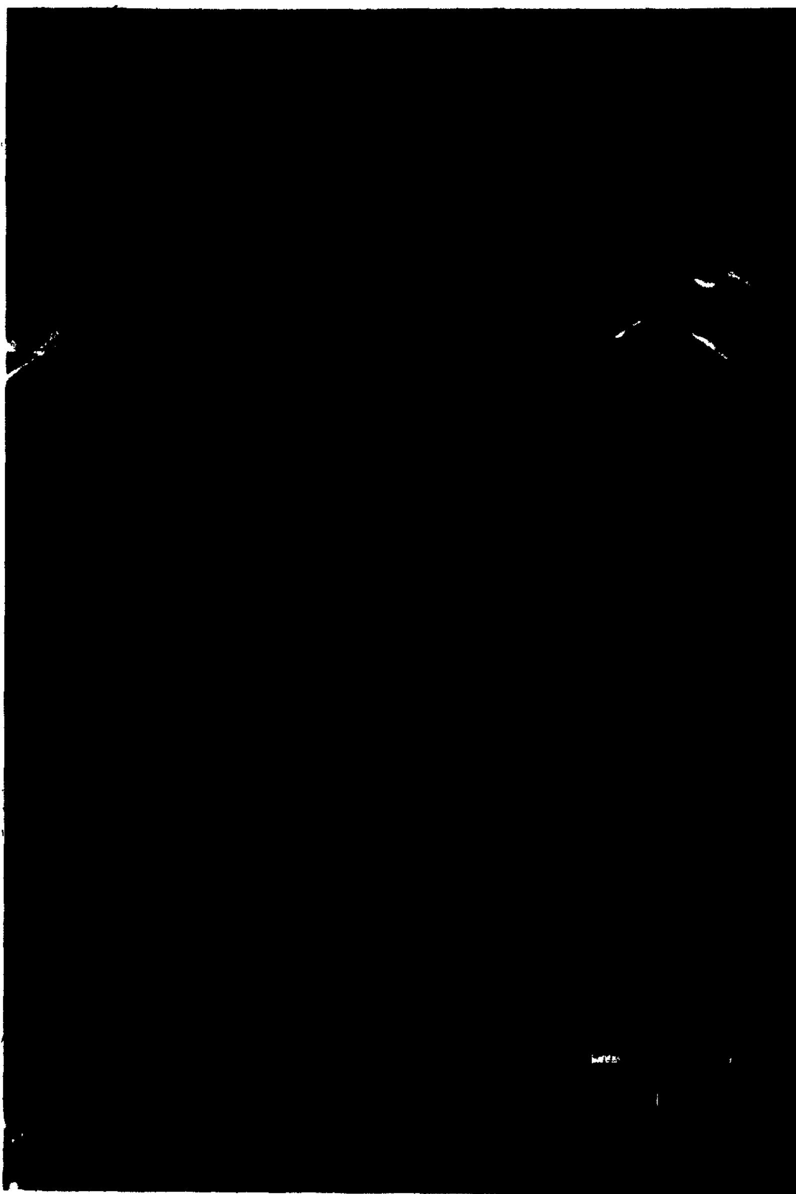

Fig. 26-a: Cross sectional S.E.M. of a boron doped layer deposited on graphite at T=967°C. The magnification is ~ 780. The deposition conditions were of 0.4ℓ/min of He, 1.25ℓ/min of $B_2H_6$ and 2.7ℓ/min of $SiH_4$.

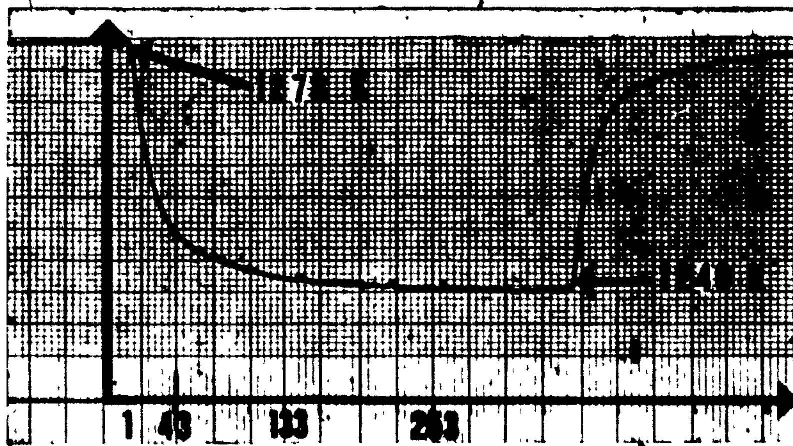


Fig. 26-b: Depicts the characteristic temperature as the function of time (sec) of fig. 26 and 26-a and the expression characterizing this curve is given by
$T(K) = 1.2654\times10^{3}(t)^{-5.2191\times10^{-3}}$

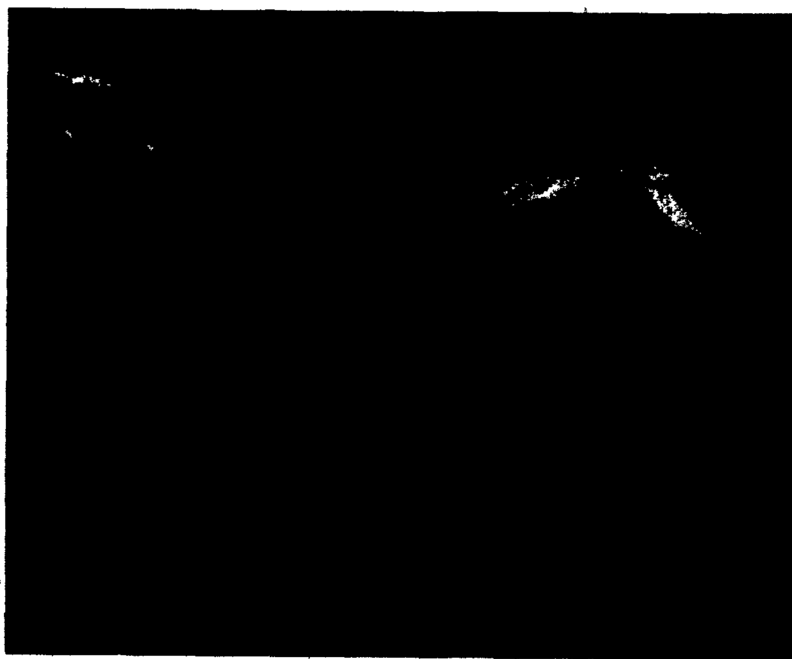

Fig. 27: S.E.M. of a boron doped and etched silicon layer deposited on graphite at T=936°C. The magnification is 1540. Here the deposition conditions were 0.8ℓ/min of He, 0.7ℓ/min of $B_2H_6$ and 2.7ℓ/min of $SiH_4$.

shows four sided pyramidical shape mixed with some triangular crystallites. It has been shown by x-ray diffractometry as it will be discussed in relation to figs. 29 to 33, that they are characterized by a preferential orientation in the (110) direction.

Fig. 28 shows the chemically etched section of a boron doped silicon on graphite deposited at 936°C. The magnification is 1400. The layer thickness was about 47μm. The gas molar ratio [B/Si] was that of fig. 27 It can be seen from fig. 28 that defined columns. extend from the silicon graphite interface to about 20μm.

The double layered columnar structure seen in fig. 28 may be related to the initial temperature drop at the onset of the gas flow, discussed previously (see figures 24b to 26b).

The crystallographic properties of a number of silicon layers deposited on graphite substrate by the CVD of silane, under a given range of substrate temperature, flow rates and dopant concentrations, were examined by x-ray diffraction scan using a Philips Mo. PW1130-60 difractometer with CuKα radiation source. A silicon powder of random orientation is known to have or show few strong diffraction peaks associated with (111), (220), (311),(331) and (422) crystallographic planes. These correspond to reflection angles of: 28.48°, 47.3°, 56.12°, 76.42° and 88.08° respectively. The relative intensities related to the respective orientation with their angles of reflection are:100, 60, 35, 13, 17 [see

Fig. 28: S.E.M. of a chemically etched section of a boron doped silicon on graphite at T=936°C. The magnification is of 1400. The deposition condition were 0.8ℓ/min of He, 0.7ℓ/min of $B_2H_6$ and 2.7ℓ/min of $SiH_4$.

appendix B].

The diffraction spectra of the silicon layer were obtained by scanning 2 θ in the range of 20°-90°. The dominant orientation of the deposited polysilicon was found to depend strongly on the substrate temperature and concentration of the reactants rather than the substrate itself. At the deposition temperature of 980°C the quality of grown layer is characterized by (111)/(220) intensity ratio of approximately 1.7. This indicates a strong (111) preferred orientation over the secondary preference of (220) orientation. This shows preferred orientation of (111) and (110). The ratio is found to decrease as the temperature decrease from 980°C. This effect of (111) orientation beginning to lead the (110) oriented crystallites was also observed on fused silica except the characteristic temperature was of 973°C. As the temperature of growth was further decreased the relative characteristics of the (111)/(110) is decreased. This decrease is also accompanied by the appearance of the higher index (331) and (311) planes.

Fig. 29 to 30 show the diffraction spectra of boron doped silicon layer on graphite at temperatures ranging from 926-980°C with growth rates ranging from 0.866-1.3μm/min.)

Fig. 29 is the x-ray diffraction spectrum of a boron doped silicon layer deposited on graphite substrate at 980°C by the pyrolysis of $SiH_4$ where the (111)/(220), (111)/(311),

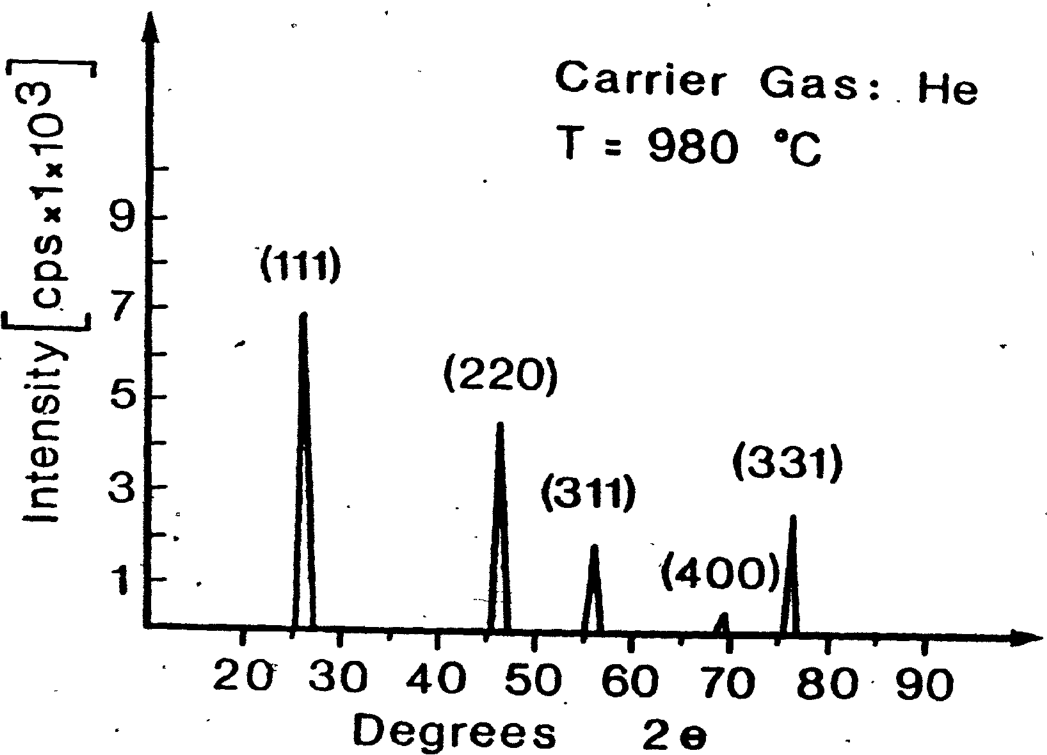


Fig. 29: X-ray diffraction spectra of a boron-doped silicon layer deposited on a graphite substrate at 980°C.

(111)/(400) and (111)/(331) intensity ratio are about 1.7, 4.3, 18.3, 2.2 respectively.

Fig. 30 is the diffraction spectrum of a boron doped silicon layer deposited on graphite substrate at 967°C where the (111)/(220), (111)/(311), (111)/(400), and (111)/(331), (111)/(422) intensity ratio are 0.14, 1.5, 18, 1.3, 3 respectively. If the intensity ratios are normalized to the highest peak, which in this case or at this temperature it is the (110), then the intensity ratio are of 7.0, 10, 123, 9 and 20 respectively.

Fig. 31 shows the diffraction spectrum of a boron doped silicon layer deposited on graphite substrate at T ≈ 950°C by the pyrolysis of $SiH_4$ where the relative (220)/(111), (220)/(311), (220)/(400), (220)/(331) and (220)/(422) intensity ratio are 16, 38, 900, 6, 64 respectively.

Fig. 32 shows the diffraction spectrum of a boron doped silicon layer deposited on a graphite substrate at T ≈ 942°C by the pyrolysis of SiH4 where the relative (220)/(111), (220)/(311), (220)/(400), (220)/(331) and (220)/(422) intensity ratios are 31, 47, 810, 10 and 114, respectively.

Fig. 33 shows the diffraction spectrum of a boron doped silicon layer deposited on a graphite substrate at T = 926°C by the pyrolysis of $SiH_4$ where the relative (220)/(111), (220)/(311), (220)/(400), (220)/(331) and

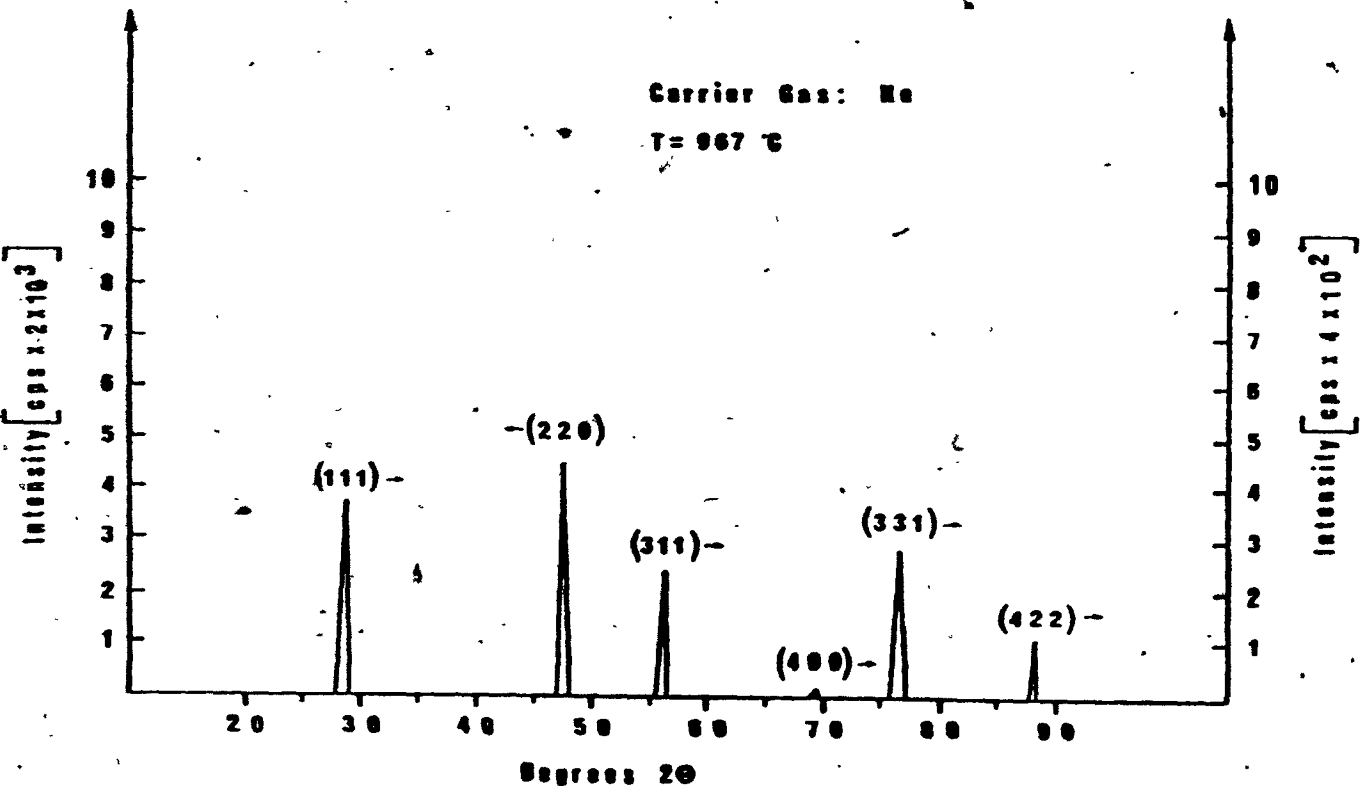


Fig. 30: X-ray diffraction spectra of a boron-doped silicon layer deposited on a graphite substrate at 967°C.

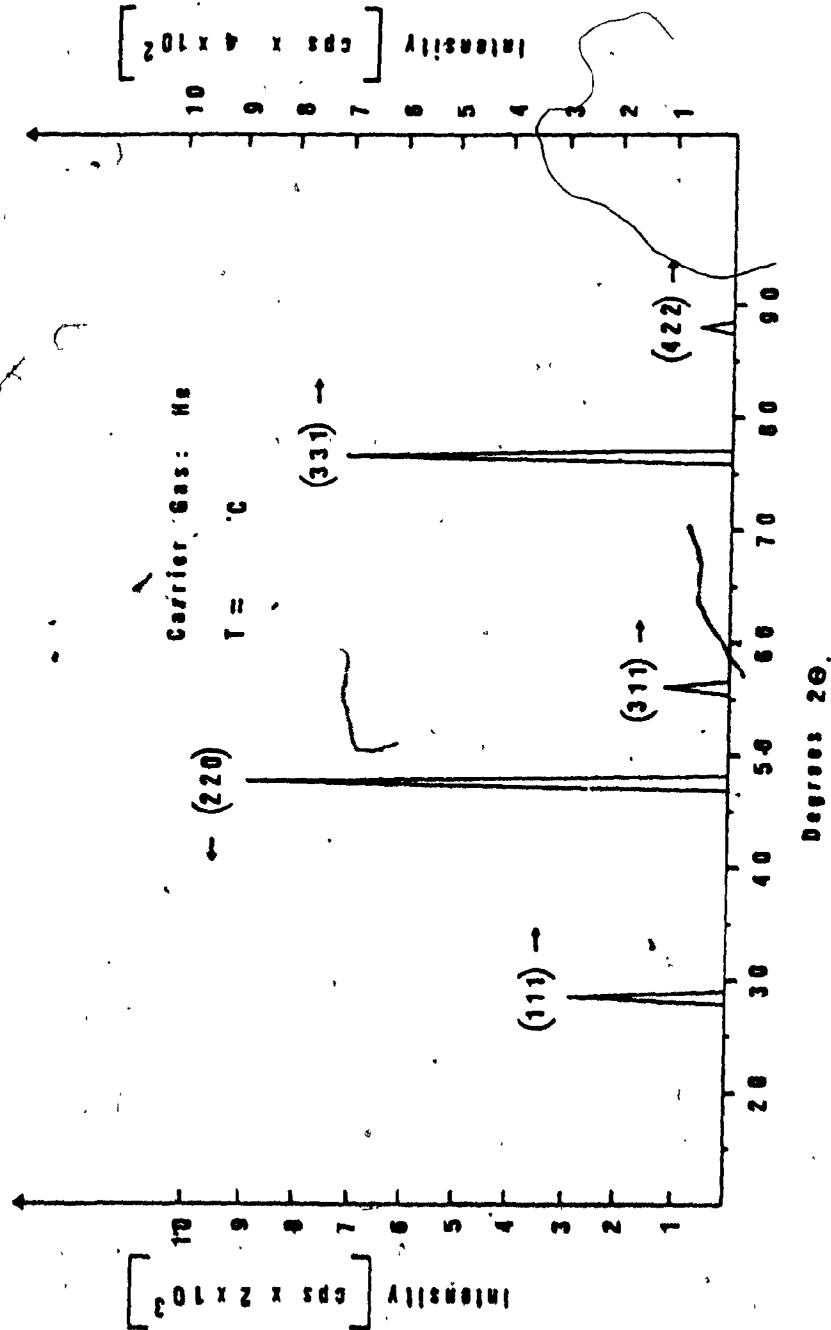


Fig. 31: X-ray diffraction spectra of a boron-doped silicon layer deposited on a graphite substrate at 950°C.

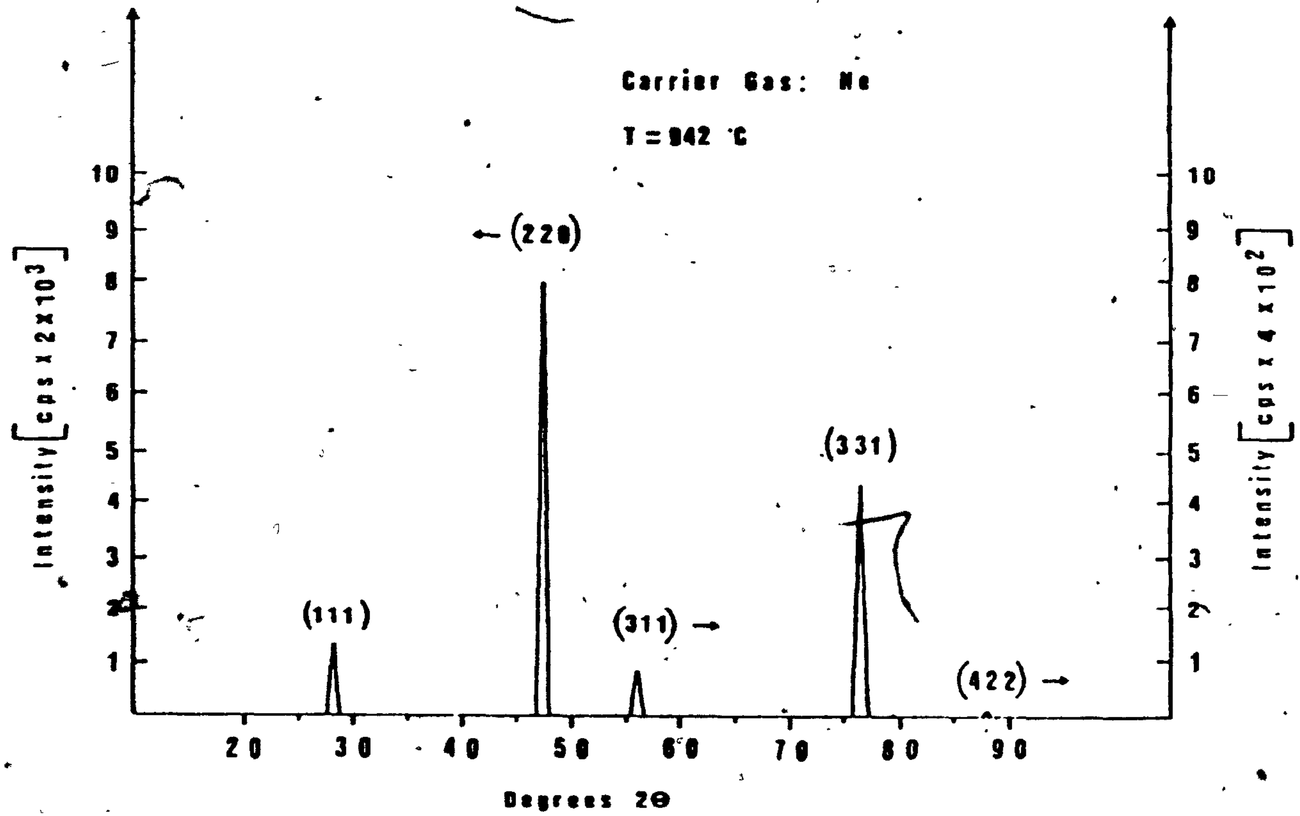


Fig. 32: X-ray diffraction spectra of a boron-doped silicon layer deposited on a graphite substrate at 940°C.

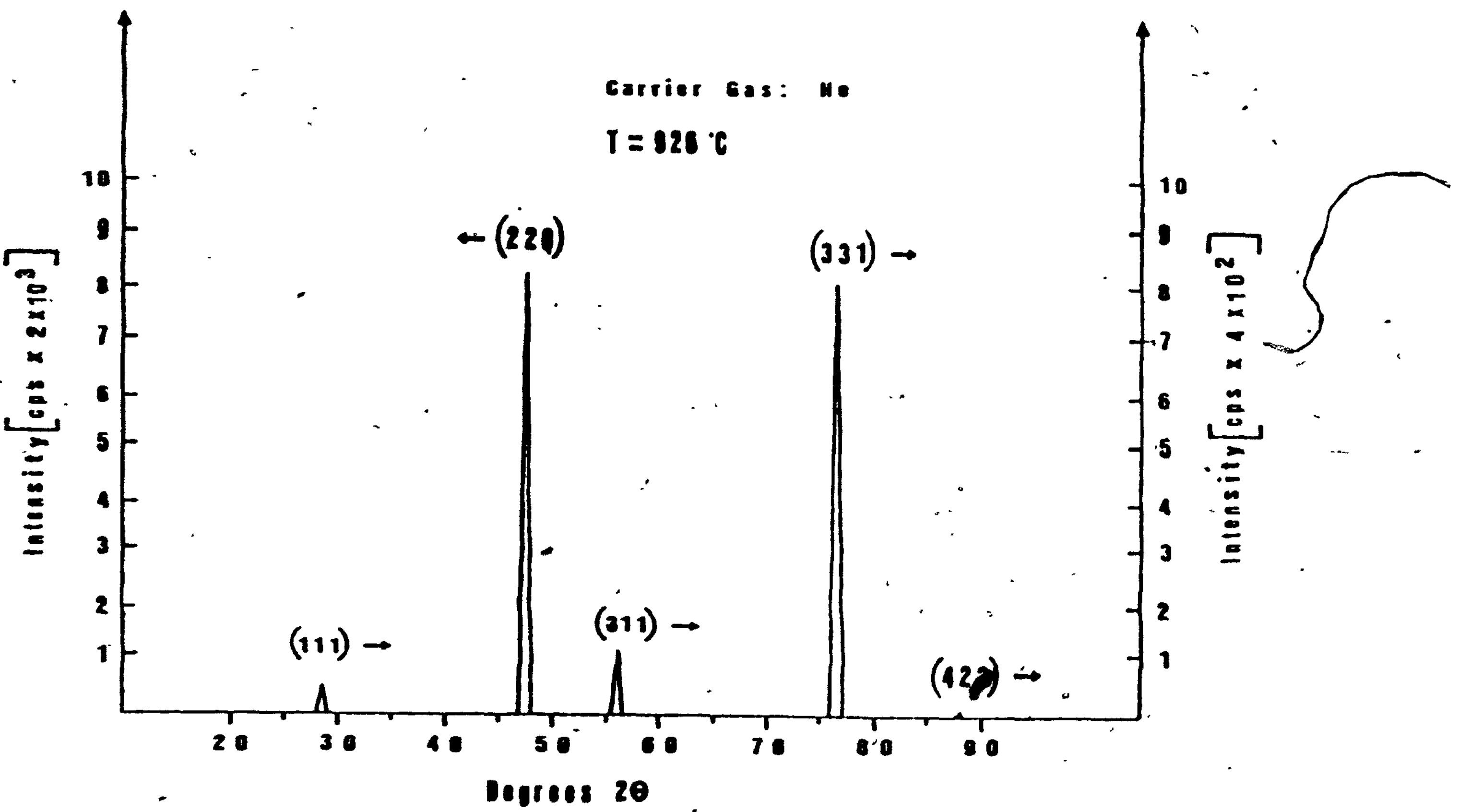


Fig. 33: X-ray diffraction spectra of a boron-doped silicon layer deposited on a graphite substrate at 926°C.

(220)/(422) intensity ratios are 101, 37, 8, 5 and 405 respectively.

It can be seen from fig. 29 to 33 that as the temperature decreases from 980°C the relative intensities of the (111), (311) (400) and (422) planes decrease while those of (220) and (331) planes increase.

From the data collected in Table 2 an Arrhenius plot of growth rate versus reciprocal temperature was plotted. The linear dependence of the growth rate with respect to the reciprocal of the growth temperature permitted the computation of an activation energy of 26 k cal/mole, as is depicted in fig. 34.

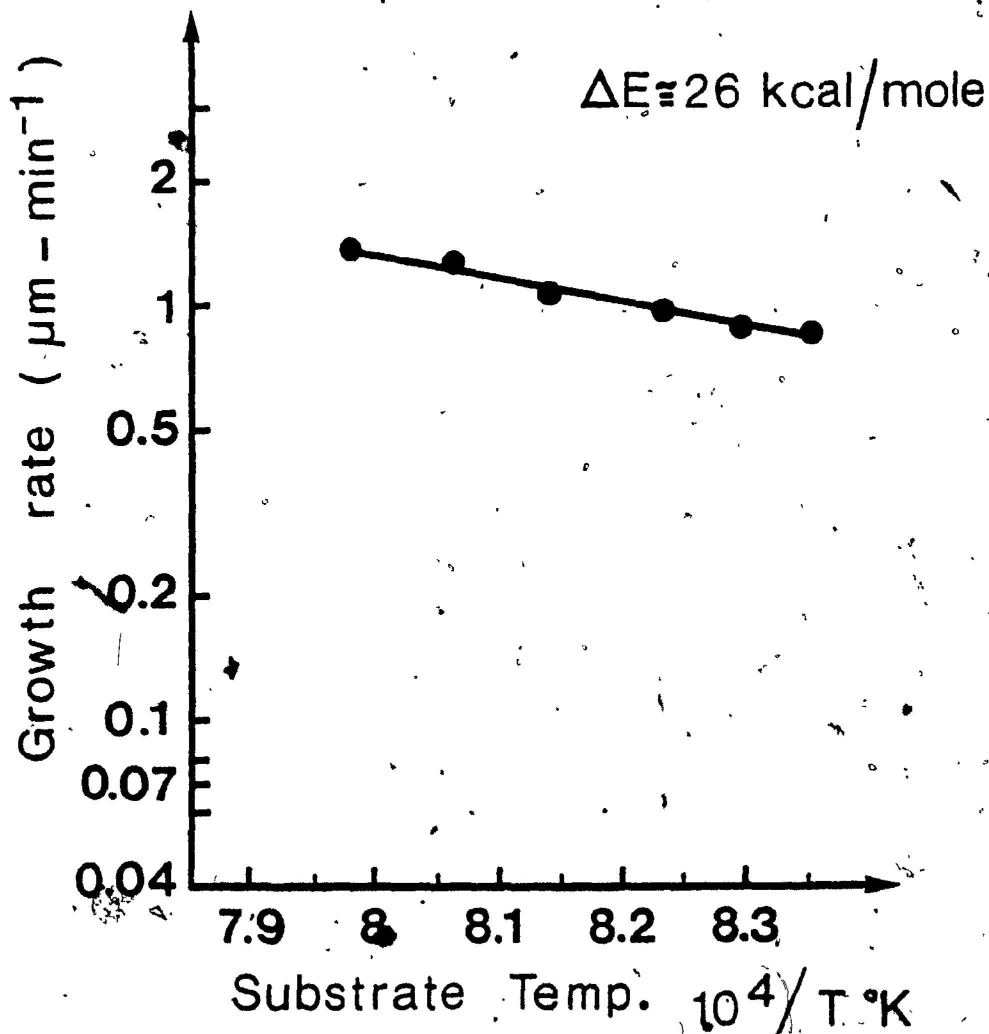


Fig. 34: Growth rate of polysilicon on graphite as a function of temperature (923 to 980°C). Flow rates of the carrier gas (He), dopant ($B_2H_6$) and silane are (0.15-0.8) ℓ/min of He, (0.2-1.25) ℓ/min of $B_2H_6$ and 2.7ℓ/min of $SiH_4$ respectively.

# CHAPTER 3

# HALL EFFECT

## CHAPTER 3

## HALL EFFECT

### Introduction to Hall Effect

The physical process underlying the Hall effect measurements (29,30) can be discussed with reference to fig. 35-35d.

In the above mentioned figures, it is assumed that an electrical current is flowing in the +ve x-direction, which means that the conducting electrons are drifting with a velocity $\vec{v}$ in the -ve x-direction (holes in a +ve x-direction). If a magnetic field is applied in the +ve z-direction a Lorentz force ($F = e(\vec{v}_x \times \vec{B}_z)$) comes into effect causing the path of the electrons to bend in the negative y-direction (for p-type semiconductor the path or deflection of holes is in the same direction) downward as shown in fig. 35-a. As a result, electron/holes accumulate at the lower surface producing a net -ve/+ve charge. Simultaneously a net +ve/-ve charge appears on the upper surface because of the deficiency of electrons/holes there. This combination of +ve and -ve charges create an electric field known as the Hall field which is measured as the Hall voltage, $V_H$ (31,32,33,34).

It is possible to determine the density and type of charge carrier in metals and semiconductor by measuring the Hall effect. The electron (fig. 35 or fig. 36) in the presence of a magnetic field of magnetic induction $B_z$ will be subjected to a Lorentz force F given by

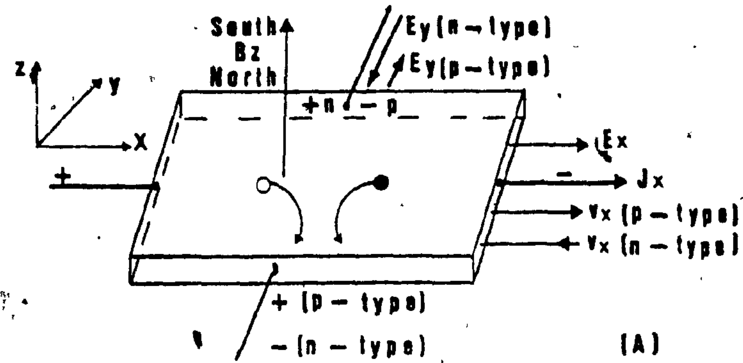


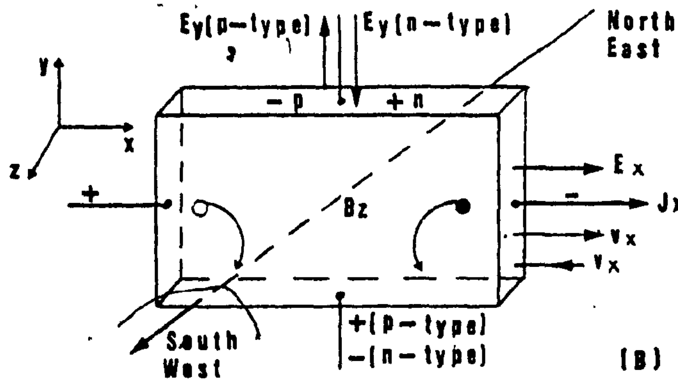


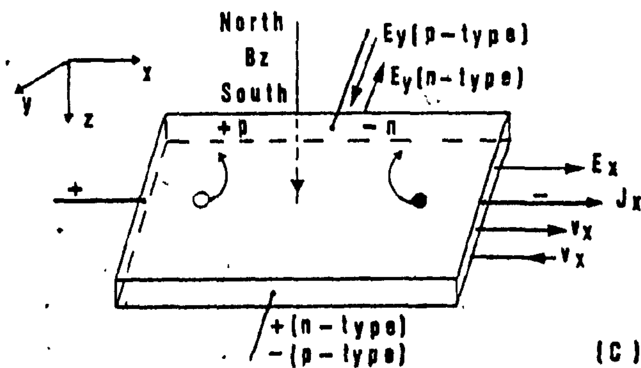


Fig. 35: Hall effect configurations at different sample orientations.

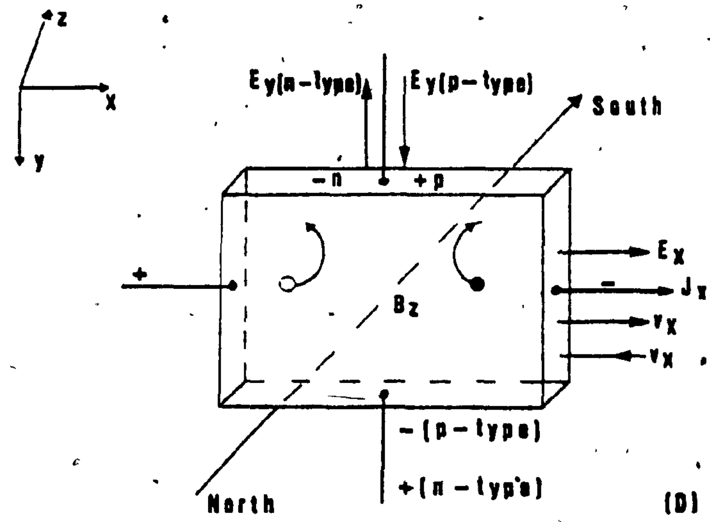


Fig. 35 (cont'd.): Hall effect configurations at different sample orientations.

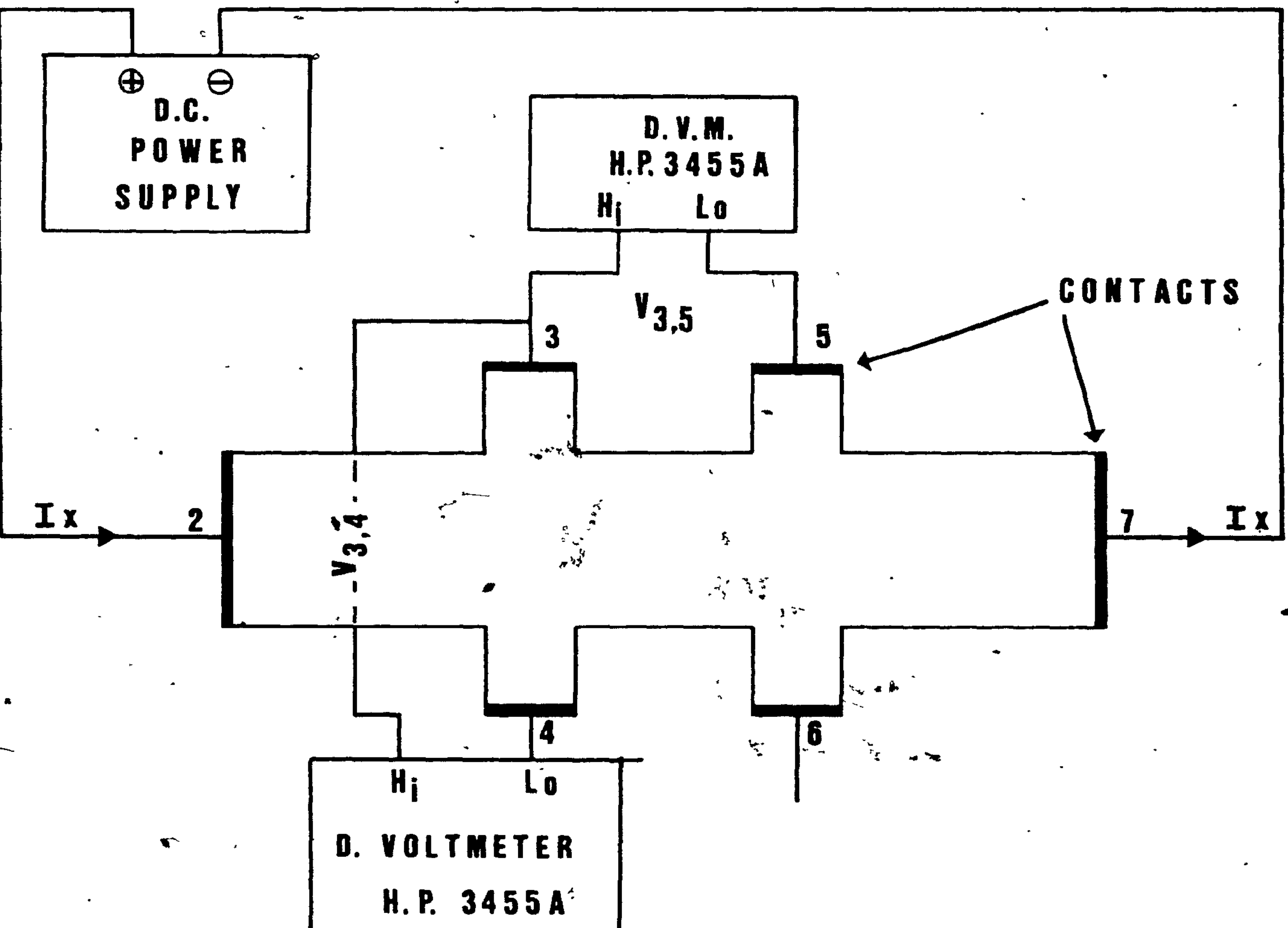


Fig. 36: Schematic representation of a bridge type Hall sample electrical connection.

$$F = e(v_x \times B_z) \qquad 3.1$$

where

$v_x$ = drift velocity of electrons

$e$ = electronic charge

$B_z$ = magnetic induction

$F$ = Lorentz force.

In the presence of an electric field $F_x$ the conduction electron will have a drift velocity $v_x$ superimposed on their random motion. The magnitude of $v_x$ is given by

$$v_x = \mu Ex \qquad 3.2$$

which defines the mobility $\mu$. Thus the Lorentz force F is in the y-directon and is of magnitude

$$F_y = - eB_z v_x + eE_y = 0 \qquad 3.3$$

The electrons are deflected toward the negative y face of the sample (see fig. 35-a) and produce a positive charge on the back face and a negative charge on the front face. Thus a potential difference, called the Hall potential, is built up between these faces; this voltage may be measured at leads three-four or five-six as it is shown also in fig. 36. If $E_y$ is the transverse field (equal to Voltage divided by the samples width), the transverse force -eEy on each electron must just balance the Lorentz Force. Hence,

$$E_y = B_z E_x \mu \qquad 3.4$$

The Hall coefficient $R_H$ then can be defined by

$$R_H = \frac{E_y}{B_z J_x} \qquad 3.5$$

or $E_y = R_H B_z j_x$

where $j_x = \sigma E_x$ is the current density in amperes per square meter in the x direction. Therefore, the Hall coefficient, $R_H$ can be determined experimentally. Since the conductivity is given by $\sigma = ne\mu$, where n is the number of charge carriers per unit volume, from above it follows that

$$R_H = -\frac{1}{en} \qquad 3.6$$

Thus if the charge carriers are electrons, the Hall coefficient will be negative and an experimental determination of $R_H$ gives the density of electrons. The polarity of the voltage measured across the Hall potential contacts is reversed if the charge carriers are holes, and again the density of carriers (the positively charge holes) may be determined.

For Hall effect measurements it is convenient to use specimens in the form of parallelipiped as shown in fig. 36 according to the ASTM specifications (14). If the width of the sample is w and the thickness t, a current $I_x$ can be passed through the sample and the conductivity is determined by measuring the voltage drop across pin three-five or four-six at a distance $\ell$:

$$\sigma = \frac{I}{V_{3,5 \text{ or } 4,6}} \cdot \frac{\ell}{w \cdot t} \text{ or } \rho = \frac{V_{3,5 \text{ or } 4,6}}{I} \cdot \frac{w \cdot t}{\ell} \qquad 3.7$$

If a voltage between the Hall probes (three-four or five-six) produced when a magnetic induction $B_z$ is applied is $V_H$, then equation 5 becomes

$$R_H = \frac{V_H}{B_z} \cdot \frac{t}{I} \qquad 3.8$$

If we multiply equation 7 with equation 8 we can obtain the Hall mobility ($\mu_H$).

$$\mu_H = R_H \sigma \qquad 3.9$$

## 3.1 HALL EFFECT SETUP

The schematic circuit diagram is shown in figs. (36) and (37). The actual measuring instrumentation used in this investigation consists of a field regulated magnetic power supply (Varian Associates Fieldial Mark I), regulated current source (Keithley 225 Current Source), regulated voltage supply (Anatek Electronics Ltd., Vancouver, Canada), digital voltmeter (Hewlett Pachard 3455A digital Voltmeter), Keithley 616 or 610C digital voltmeter, D.C. Differential Voltmeter (John Fluke MFG. Co. Inc., Model 881A), Hall effect cane (Concordia University, see fig. (38), Andonian Modular Liquid Helium Dewar fig. (39) (Andonian Associates, Inc. 26 Thayer Road Walthom, Massachussetts, Ivanhoe 4-0500), 2 mechanical pump and a diffusion pump (Varian Vacum Division).

The transport properties were measured using the circuit arrangement as shown in figure (36 and 37).

Fig. 36 shows the circuit arrangement related directly to the Hall sample. The Hall effect sample is provided with five pairs of contacts; 2-7 at the ends of the sample to enable a current to be passed through it, two

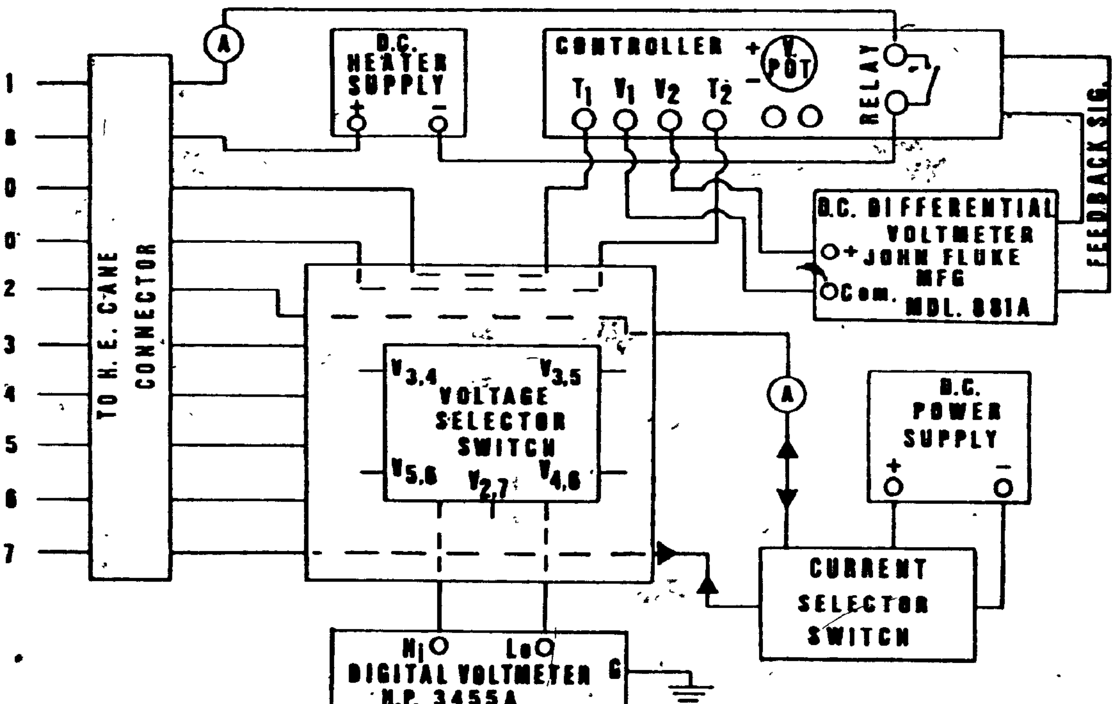


Fig. 37: Electrical schematic and instrumentation for Hall effect measurements.

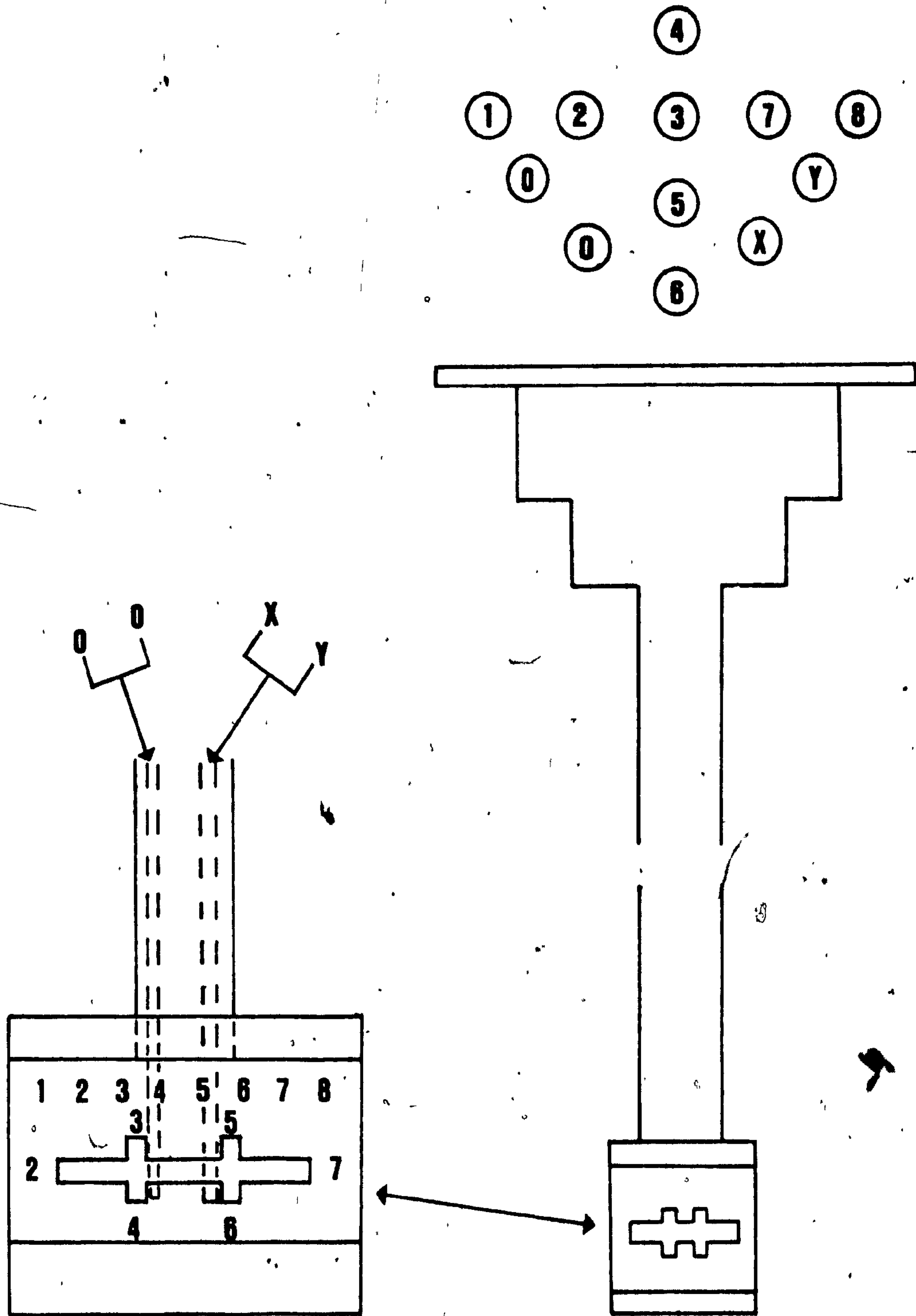


Fig. 38: Hall Effect Cane (H.E.C.).

LEGEND

A Electrical Connectors
B Off-Gas Line
C Helium Fill & Vent
D Insulation Line
E Nitrogen Vent
F Outer Shell
G Nitrogen Reservoir
H Helium Well
I Insulation Space
J Outer Tail Section
K Nitrogen Temperature Radiation Shield
L Sample Heater
M Exchange Gas Chamber
N Capillary
O Throttle Valve
P Sample Support Tube
Q Throttle-Valve Stem
R Nitrogen Fill
S Helium Gauge Port
T Throttle-Valve Top Works

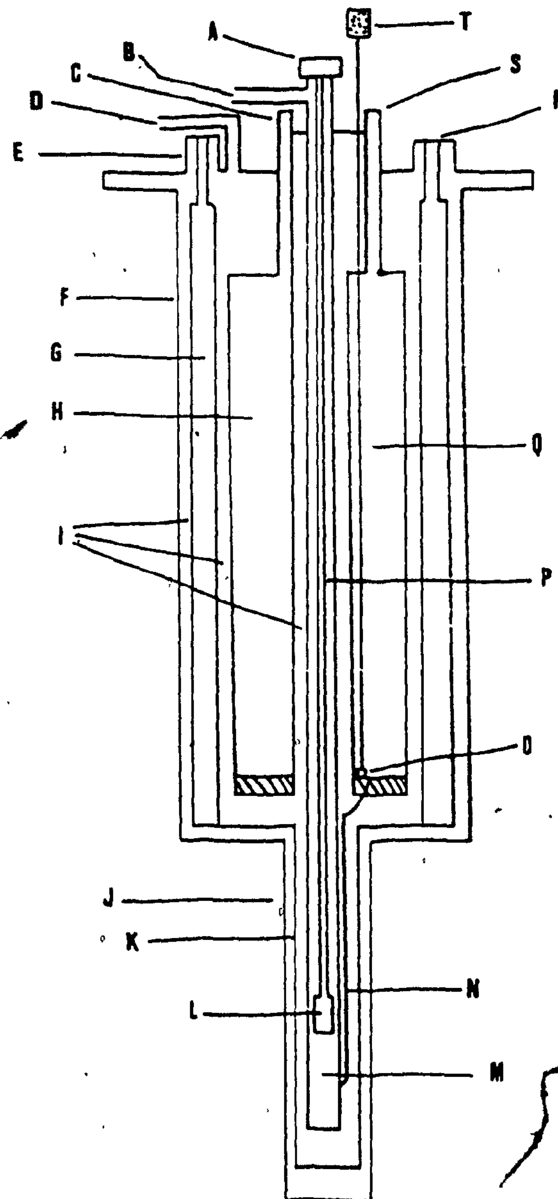


Fig. 39: Schematic drawing of the low temperature cryostat.

pairs of potential probes, 3-5, and 4-6 (this voltage is used to determine the resistivity of the sample at zero magnetic field) and two transverse pairs 3-4 and 5-6 (this voltage produced by the mutually perpendicular magnetic and electric fields known as the Hall voltage.

Fig. 37 shows the actual circuit arrangement used for measuring electrical transport properties of the semiconductor. It mainly consists of two direct current power supply. One is used for heating up the sample chamber from liquid Helium or nitrogen to room temperature ( D.C. Heater Power Supply). Another power supply (D.C. Power Supply) is used for introducing the sample current. The voltage selector switch permits the measurements of the different voltage by the H.P. digital Voltmeter. The Hall effect cane connector (H.E.C.C.) allows the link between the sample and the measuring instruments. The contact configuration of this cane is shown in fig. (37 and 38). Once the connections have been made to the Hall sample the Hall effect cane is inserted into the cryostat which is shown in fig. 39. It permits the controlled variation of the sample temperature between liquid He (4.2) and about 100$^{o}$C

The magnetic field required for the Hall effect measurements was supplied by a 12-inch Varian V-3900 electromagnet with 3 inch pole gap and a 9 inch pole face. By means of a temperature-controlled Hall effect crystal probe the magnetic field Intensity was maintained to 1% of the selected value. The field intensity was set by means of

a set of dials located in the control panel. A field reversing switch was also provided. The maximum field intensity available was 1 Tesla.

### 3.2 Elimination of the Secondary Galvanometric Effects Related to Hall Effect

In order to obtain accurate Hall voltage measurements certain associated effects which give rise to voltage drops at the Hall probes must be eliminated. As the physical size of the Hall sample is usually very small it is extremely difficult to align the Hall probes properly. Invariably, some misalignment is bound to occur. fig. 40B shows the equipotial lines along the sample when it is subjected to a current at its ends. Because of the misalignment the Hall probes A and B are at different potentials ($V_{IR}=V_A-V_B$). This potential drop across the probes is known as the IR drop. It is dependent on the direction of the current but is independent of the magnetic field.

The electrons which constitute the sample current do not move across the sample with the same velocity. The faster electrons will follow a different path from the slower ones when a magnetic field with intensity B is applied perpendicular to the sample. Hence more energy will be transported to one side of the sample than the other, resulting in a temperature difference as shown in Fig. 40C. This effect is known as the Ettingshausen effect. Since the Hall probes and the sample are of different materials, they

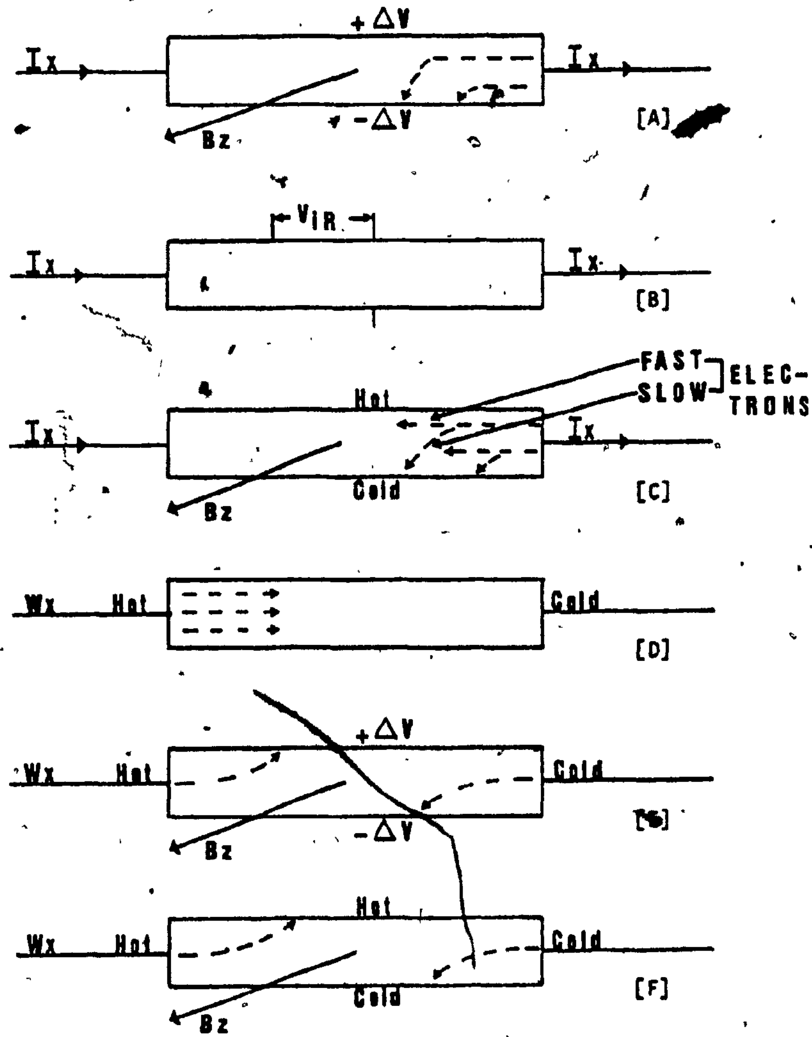


Fig. 40: Sign convention and related galvano-magnetic effects
[A] Hall; [B] IR drop [C] Ettingshausen;
[D-E] Nerst [D-F] Righi-Leduc (53)

form a thermocouple and thus generate a potential across the sample.

When the two ends of the Hall sample are subjected to a temperature difference, a thermal current will flow across the sample as shown in fig. 40D. This is the Nernst effect, (see fig. 40E) characterized by a potential $V_n$, will appear acorss the sample when a magnetic field is applied perpendicular to the sample. Under these same conditions a temperature difference across the sample is also produced. This is known as the Righi-Leduc effect (see fig. 40F).

Because of all these secondary effects the voltage measured across the Hall probe is a sum of $V_H$ (see fig. 40A) the Hall voltage; $V_{IR}$, the voltage due to probes misalignment; $V_E$, the voltage due to the Ettingshausen effect; $V_N$, the voltage due to the Nerst effect; and $V_{RL}$, the voltage due to the Righi-Leduc effect. All these voltages, with the exception of $V_E$, can be eliminated by taking a series of measurements with all possible combinations of currents, I, and magnetic field, B, directions. Noting that $V_H$ and $V_E$ are dependent on both I and B, $V_N$ and $V_{RL}$ are dependent only on B and $V_{IR}$ is dependent only on I, the measurements will give, for

+ve I and +ve B

$$V_1 = V_H + V_E + V_{IR} + V_N + V_{RL}$$

-ve I and +ve B

$$V_2 = -V_H - V_E - V_{IR} + V_N + V_{RL}$$

-ve I and -ve B

$$V_3 = V_H + V_E - V_{IR} - V_N - V_{RL}$$

+ve I and -ve B

$$V_4 = -V_H - V_E + V_{IR} - V_N - V_{RL}$$

Hence

$$\frac{(V_1-V_2) + (V_3-V_4)}{4} = V_H + V_E$$

The Ettingshausen effect can be minimized by immersing the Hall sample in a high thermal conductivity medium (isothermal environment). Under this condition $V_E$ is very small as compared to $V_H$ and it can be neglected (the mathematical analysis for eliminating these effects is shown in appendix C) (33,34).

## 3.3 Hall Effect Sample Preparation

Hall effect samples were made of polycrystalline silicon, with the geometrical shape of fig. 36 and were prepared as follows.

Polycrystalline silicon layers with a thickness of 17-85μm were deposited by C.V.D. as described above (see Chapter 1, fig. 4) on a 7μm thermally grown $SiO_2$, through a bridge shaped high purity graphite mask.

The high purity graphite mask was made out of 5 cm diameter graphite rod, circular wafers of approximately 2mm thick were cut. These wafers were then shaped into parallelograms (3.8 cm long, 2.5 cm wide) and lapped to a final

thickness of 1 mm. From these parallelograms Hall effect bridge masks were cut out with the dimensions specified by the A.S.T.M. standards (14) (15 mm x 3mm x 1mm). The masks were then cleaned in an ultrasonic bath in tricklor-oethane, acetone and methanol until no traces of graphite particles could be seen. They were degased for approximately 15 minutes at about 135°C and further heat treated for degasing at 1050°C for 1 hour in $H_2$ and He atmospheres.

To prevent the complete reduction of $SiO_2$ by depositing Si at about 950°C, a layer thickness of 7μm or more was required. This phenomenon was also observed by A.L. Fripp et al (35). After the deposition, the Hall samples were prepared for ohmic contacts. Ohmic contacts to these samples were made (see fig. 36) by evaporating gold through a contact mask under a vacuum of $10^{-6}$ mm of mercury (Hg). After the evaporation, the contacts were alloyed in the silicon at a eutetic temperature of Au/Si, at 370°C, for 5 minutes in an $H_2$ atmosphere. Wire leads to the six sides of the Hall samples were soldered with Indium-gold solder type 3, 5 and 13. The connections to the six sides of the sample were then tested with a curve tracer to verify whether the contacts were ohmic. Then, the samples were mounted on the Hall effect cane and measured. Details of the deposition conditions for these Hall samples are collected in Tables 3 and 4.

The precise Hall sample dimentions were measured with a Telysurf IV and are collected in Table 5.

| DISTANCE from NOZZLE (cm) | TEMP. DET. (°C) | | MILLIVOLT SIGNAL (mV) | | GAS FLOW RATES | | | | | | SAMPLE NO. | ANNEALING TIME hr |
|---|---|---|---|---|---|---|---|---|---|---|---|---|
| | no flow | with flow | no flow | with flow | He | | $B_2H_6$ | | $SiH_4$ | | | |
| | | | | | mm | L/min | mm | L/min | mm | L/min | | |
| 2.54 | | | | | 23 | 0.5 | 2 | 0.01 | 32 | 2.80 | 1x | |
| " | | | | | 21 | 0.4 | 4 | 0.10 | 32 | " | 1xA | |
| " | | | | | 22 | 0.45 | 8 | 0.40 | 32 | " | 2x | |
| " | | | | | 18 | 0.3 | 10 | 0.70 | 32 | " | 2xA | |
| " | | | | | 15 | 0.25 | 12 | 0.80 | 32 | " | 3x | |
| " | | | | | 10 | 0.15 | 15 | 1.10 | 32 | " | 3xA | |
| | | | | | | | | | | | | |
| " | | | | | 22 | 0.45 | 15 | 1.10 | 30 | 2.70 | A | 1 |
| " | | | | | 22 | " | 15 | " | 30 | " | B | 3 |
| " | | | | | 22 | " | 15 | " | 30 | " | C | 6 |
| " | | | | | 22 | " | 15 | " | 30 | " | D | 9 |
| " | | | | | 22 | " | 15 | " | 30 | " | E | 12 |
| " | | | | | 22 | " | 15 | " | 30 | " | F | 15 |
| | | | | | | | | | | | | |
| | | | | | | | | | | | | |
| | | | | | | | | | | | | |
| | | | | | | | | | | | | |

Table 3: Deposition Conditions of Boron doped polysilicon at T=950°C.

| DISTANCE from NOZZLE (cm) | TEMP. DET. (°C) | | MILLIVOLT SIGNAL (mV) | | GAS FLOW RATES | | | | | | SAMPLE NO. |
|---|---|---|---|---|---|---|---|---|---|---|---|
| | | | | | He | | $PH_3$ | | $SiH_4$ | | |
| | no flow | with flow | no flow | with flow | mm | L/min | mm | L/min | mm | L/min | |
| 2.54 | | | | | 22 | 0.45 | 10 | 0.70 | 32 | 2.80 | 1 |
| " | | | | | 27 | 0.65 | 5 | 0.15 | 32 | " | 2 |
| " | | | | | 31 | 0.85 | 1 | 0.022 | 35 | 3.15 | 3 |
| " | | | | | 20 | 0.38 | 1 | 0.022 | 40 | 3.6 | 4 |
| " | | | | | 20 | " | 1 | 0.022 | 40 | " | 5 |
| " | | | | | 20 | " | 5 | 0.15 | 40 | " | 6 |

Table 4: Deposition Conditons of Phosphorous doped polysilicon at T=950°C.

| SAMPLE DIMENSIONS | | | | |
|---|---|---|---|---|
| SAMPLE NO. | LENGTH L (mm) | LENGTH l (mm) | WIDTH w (mm) | AVE. THICKNESS t (μm) |
| 1X | 14.5 | 3.0 | 3.25 | 29 |
| 1XA | 15.0 | 3.0 | 3.27 | 35 |
| 2X | 16.0 | 3.5 | 3.10 | 21 |
| 2XA | 15.0 | 3.5 | 3.10 | 17 |
| 3X | 16.0 | 3.5 | 3.05 | 19 |
| 3XA | 15.5 | 3.5 | 3.10 | 24 |
| A | 15.0 | 3.2 | 3.30 | 19 |
| B | 15.2 | 3.2 | 3.30 | 26 |
| C | 15.6 | 3.4 | 3.28 | 17 |
| D | 15.6 | 3.2 | 3.32 | 23 |

Table 5: Hall effect sample dimensions

| SAMPLE NO. | SAMPLE DIMENSIONS | | | |
|---|---|---|---|---|
| | LENGTH L (mm) | LENGTH l (mm) | WIDTH w (mm) | AVE. THICKNESS t (μm) |
| E | 16.0 | 3.5 | 3.30 | 32.67 |
| F | 16.0 | 3.6 | 3.33 | 22.00 |
| 1 | 15.0 | 3.2 | 3.27 | 23.00 |
| 2 | 15.0 | 3.2 | 3.28 | 24.00 |
| 3 | 16.0 | 3.3 | 3.32 | 51.00 |
| 4 | 16.0 | 3.3 | 3.33 | 42.00 |
| 5 | 16.0 | 3.2 | 3.33 | 86.00 |
| 6 | 16.0 | 3.2 | 3.30 | 82.00 |
| U | 15.0 | 3.5 | 3.45 | 41.00 |
| P | | | | |

Table 5 Cont'd: Hall effect sample dimensions

## 3.4 Measured Transport Properties-Experimental Results

Hall effect and resistivity ($\rho$) measurements on sample 1x to 3xA, A-F and 1-6 have been performed. Their corresponding voltages for magnetic field variation from $1\times10^{-2}$ to 1 Tesla were recorded. A typical measurement of the Hall voltage is given in Table 6. All other measurements of the Hall voltages are given in table ($D_1$-$D_{17}$) in Appendix D. For each of the samples, resistivity $\rho$, (ohm cm), Hall coefficient $R_H$, ($cm^3 \rho^{-1}$), Hall mobility $\mu_H$, ($cm^2 v^{-1} s^{-1}$) and carrier concentrations p and n($cm^{-3}$) were calculated and the results are collected in Table 7.

To determine the transport properties of polycrystalline silicon as a function temperature, sample 2xA was measured from liquid nitrogen (77 K) to 373 K. It has been established that the Hall voltage coefficient become field independent at the range of temperature used in this investigation, for about 0.1 Tesla. Therefore all the measurements were performed at 0.5 Tesla. The results are collected in table 25. The corresponding $\rho$ (ohm cm) $R_H$ ($cm^3/C$), $\mu_H$ ($cm^2$ $volt^{-1}$ $sec^{-1}$) and p were calculated and are collected in Table 8-9.

The data obtained from the measured samples will be discussed later.

### 3.4.1 Gas-phase Molar Ratio

Sample 1x to 3x in table 3 were measured and the observed characteristics $\rho$ (ohm cm), $\mu_H$($cm^2$ $volt^{-1}$ $sec^{-1}$), p ($cm^{-3}$) as a function of doping concentration expressed

| B (Gauss) | $I^+$ | | $I^-$ | | $V_H$ ave. ($\mu V$) | $\frac{V_H \text{ ave.} (\mu V)}{B (\text{Gauss})}$ (nV) |
|---|---|---|---|---|---|---|
| | $V_H^+$ ($\mu V$) | $V_H^-$ ($\mu V$) | $V_H^+$ ($\mu V$) | $V_H^-$ ($\mu V$) | | |
| 0 | - 6906 | - 6907 | + 6907 | + 6908 | 0.50 | 2.50 |
| 400 | — | — | — | — | — | — |
| 700 | - 6904 | - 6909 | + 6900 | + 6911 | 4.00 | 5.71 |
| 1000 | - 6900 | - 6911 | + 6895 | + 6914 | 7.50 | 7.50 |
| 2000 | - 6887 | - 6930 | + 6883 | + 6927 | 21.75 | 10.88 |
| 3000 | - 6876 | - 6942 | + 6870 | + 6940 | 35.00 | 11.67 |
| 4000 | - 6863 | - 6954 | + 6858 | + 6953 | 46.50 | 11.63 |
| 5000 | - 6850 | - 6966 | + 6846 | + 6963 | 58.25 | 11.65 |
| 6000 | - 6838 | - 6977 | + 6833 | + 6974 | 70.00 | 11.67 |
| 7000 | - 6827 | - 6989 | + 6821 | + 6986 | 81.75 | 11.68 |
| 8000 | - 6815 | - 7000 | + 6808 | + 6997 | 93.50 | 11.69 |
| 9000 | - 6804 | - 7012 | + 6796 | + 7009 | 105.25 | 11.69 |
| 10000 | - 6792 | - 7024 | + 6784 | + 7020 | 117.00 | 11.70 |

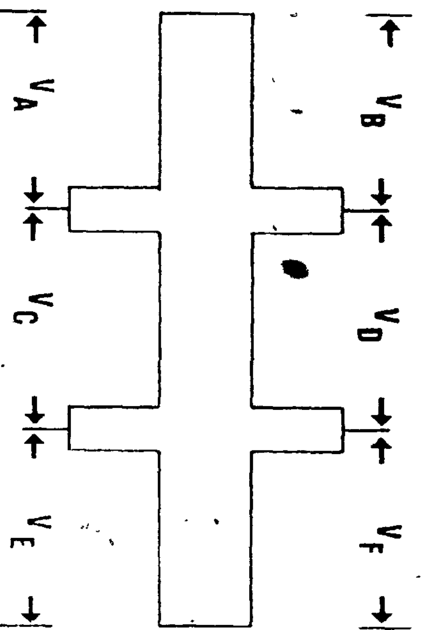


SAMPLE: 1X

$I$ = 5.0 mA

$V_A$ = mV
$V_B$ = mV
$V_C$ = 163.00 mV
$V_D$ = 166.00 mV
$V_E$ = mV
$V_F$ = mV

Table 6: Hall effect data of sample 1x at room temperature.

| HALL EFFECT EXPERIMENTAL RESULTS AT T = 300 °K | | | | |
|---|---|---|---|---|
| SAMPLE NO. | RESISTIVITY (ohm - cm) | H. COEFFICIENT $R_H$ ($cm^3$/coulomb) | H. MOBILITY $\mu_H$ ($cm^2$/volt·sec) | CARRIER CONCENTRATION n or p (atoms/$cm^3$) |
| 1X | $1.04 \times 10^{-1}$ | $+6.774 \times 10^{-1}$ | 6.5 | $9.22 \times 10^{18}$ |
| 1XA | $7.34 \times 10^{-3}$ | $+2.609 \times 10^{-1}$ | 35 | $2.39 \times 10^{19}$ |
| 2X | $6.70 \times 10^{-4}$ | $+2.850 \times 10^{-2}$ | 42 | $2.19 \times 10^{20}$ |
| 2XA | $5.57 \times 10^{-4}$ | $+2.38 \times 10^{-2}$ | 41 | $2.62 \times 10^{20}$ |
| 3X | $5.98 \times 10^{-4}$ | $+2.58 \times 10^{-2}$ | 46 | $2.42 \times 10^{20}$ |
| 3XA | | | | |
| A | $4.98 \times 10^{-4}$ | $+2.13 \times 10^{-2}$ | 43 | $2.93 \times 10^{20}$ |
| B | $5.72 \times 10^{-4}$ | $+2.60 \times 10^{-2}$ | 45 | $2.40 \times 10^{20}$ |
| C | $4.26 \times 10^{-4}$ | $+1.94 \times 10^{-2}$ | 45 | $3.22 \times 10^{20}$ |
| D | $5.22 \times 10^{-4}$ | $+2.21 \times 10^{-2}$ | 42 | $2.82 \times 10^{20}$ |

Table 7 : Calculated galvanomagnetic properties of samples (1x-6) at room temperature.

| HALL EFFECT EXPERIMENTAL RESULTS AT T = 300 °K | | | | |
|---|---|---|---|---|
| SAMPLE NO. | RESISTIVITY (ohm - cm) | H. COEFFICIENT $R_H$ ($cm^3$/coulomb) | H. MOBILITY $\mu_H$ ($cm^2$/volt-sec) | CARRIER CONCENTRATION n or p (atoms/$cm^3$) |
| E | $6.16 \times 10^{-4}$ | $+2.42 \times 10^{-2}$ | 39 | $2.58 \times 10^{20}$ |
| F | $5.45 \times 10^{-4}$ | $+1.98 \times 10^{-2}$ | 36 | $3.16 \times 10^{20}$ |
| 1 | $6.017 \times 10^{-2}$ | $-2.48 \times 10^{-1}$ | 4 | $2.51 \times 10^{19}$ |
| 2 | $4.60 \times 10^{-3}$ | $-2.39 \times 10^{-1}$ | 51 | $2.62 \times 10^{19}$ |
| 3 | $1.129 \times 10^{-2}$ | $-7.59 \times 10^{-1}$ | 67 | $8.23 \times 10^{19}$ |
| 4 | $6.018 \times 10^{-3}$ | $-4.90 \times 10^{-1}$ | 81 | $1.28 \times 10^{19}$ |
| 5 | $7.517 \times 10^{-3}$ | $-5.27 \times 10^{-1}$ | 70 | $1.18 \times 10^{19}$ |
| 6 | $6.596 \times 10^{-3}$ | $-4.59 \times 10^{-1}$ | 69 | $1.36 \times 10^{19}$ |
| U | | | | |

Table 7 (cont'd.): Calculated galvanomagnetic properties of samples (1x-6) at room temperature.

| TEMP. (°K) | MAGNETIC FIELD B(Gauss) | $I^+$ | | $I^-$ | | $V_H$ave. (μV) | VOLTAGE $V_D$ (μV) |
|---|---|---|---|---|---|---|---|
| | | $V_H^+$ (μV) | $V_H^-$ (μV) | $V_H^+$ (μV) | $V_H^-$ (μV) | | |
| 61.5 | 5000 | - 794 | - 869 | + 800 | + 874 | 37.25 | 14306 |
| 86 | 5000 | - 803 | - 876 | + 806 | + 881 | 37.00 | 14455 |
| 110 | 5000 | - 817 | - 890 | + 822 | + 896 | 36.75 | 14794 |
| 136 | 5000 | - 835 | - 909 | + 842 | + 914 | 36.50 | 15136 |
| 160 | 5000 | - 858 | - 931 | + 863 | + 935 | 36.25 | 15532 |
| 185 | 5000 | - 889 | - 962 | + 897 | + 968 | 36.00 | 16020 |
| 210 | 5000 | - 919 | - 989 | + 927 | + 1000 | 35.75 | 16558 |
| 235 | 5000 | - 949 | - 1020 | + 958 | + 1029 | 35.50 | 17085 |
| 260 | 5000 | - 980 | - 1051 | + 991 | + 1061 | 35.25 | 17689 |
| 284 | 5000 | - 1015 | - 1085 | + 1027 | + 1097 | 35.00 | 18338 |

Table 8 : Measured galvanometric properties of sample 2xa as a function of temperature.

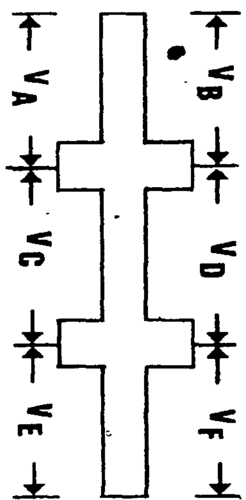


SAMPLE: 2XA

| TEMP. (°K) | MAGNETIC FIELD B(Gauss) | $I^+$ | | $I^-$ | | $V_H$ave. (μV) | VOLTAGE $V_D$ (μV) |
|---|---|---|---|---|---|---|---|
| | | $V_H^+$ (μV) | $V_H^-$ (μV) | $V_H^+$ (μV) | $V_H^-$ (μV) | | |
| 308 | 5000 | - 1052 | - 1124 | + 1063 | + 1130 | 34.75 | 19027 |
| 322 | 5000 | - 1092 | - 1160 | + 1100 | + 1170 | 34.50 | 19742 |
| 357 | 5000 | - 1130 | - 1200 | + 1143 | + 1210 | 34.25 | 20527 |
| 373 | 5000 | - 1150 | - 1219 | + 1163 | + 1230 | 34.00 | 20918 |

Table 8 cont'd: Measured galvanometric properties of sample 2xa as a function of temperature.

| HALL EFFECT EXP. RESULTS AS A FUNC. OF TEMP. | | | | |
|---|---|---|---|---|
| TEMP. °K | RESISTIVITY (ohm - cm) | H. COEFFICIENT $R_H$ ($cm^3$/coulomb) | H. MOBILITY $\mu_H$ ($cm^2$/volt·sec) | CARRIER CONCENTRATION p (atoms/$cm^3$) |
| 61.5 | $4.30 \times 10^{-4}$ | $+2.53 \times 10^{-2}$ | 59.0 | $2.47 \times 10^{20}$ |
| 86 | $4.35 \times 10^{-4}$ | $+2.52 \times 10^{-2}$ | 58.0 | $2.48 \times 10^{20}$ |
| 110 | $4.45 \times 10^{-4}$ | $+2.50 \times 10^{-2}$ | 56.0 | $2.50 \times 10^{20}$ |
| 136 | $4.55 \times 10^{-4}$ | $+2.48 \times 10^{-2}$ | 54.5 | $2.52 \times 10^{20}$ |
| 160 | $4.67 \times 10^{-4}$ | $+2.46 \times 10^{-2}$ | 53 | $2.53 \times 10^{20}$ |
| 185 | $4.82 \times 10^{-4}$ | $+2.45 \times 10^{-2}$ | 51 | $2.55 \times 10^{20}$ |
| 210 | $4.98 \times 10^{-4}$ | $+2.43 \times 10^{-2}$ | 49 | $2.57 \times 10^{20}$ |
| 235 | $5.14 \times 10^{-4}$ | $+2.41 \times 10^{-2}$ | 47 | $2.59 \times 10^{20}$ |
| 260 | $5.33 \times 10^{-4}$ | $+2.40 \times 10^{-2}$ | 45 | $2.61 \times 10^{20}$ |
| 284 | $5.52 \times 10^{-4}$ | $+2.38 \times 10^{-2}$ | 45 | $2.63 \times 10^{20}$ |

Table 9: Calculated galvanometric properties of sample 2xa as a function of temperature.

| HALL EFFECT EXP. RESULTS AS A FUNC. OF TEMP. | | | | |
|---|---|---|---|---|
| TEMP. °K | RESISTIVITY (ohm - cm) | H. COEFFICIENT $R_H$ ($cm^3$/coulomb) | H. MOBILITY $\mu_H$ ($cm^2$/volt·sec) | CARRIER CONCENTRATION p (atoms/$cm^3$) |
| 308 | $5.73 \times 10^{-4}$ | $+2.36 \times 10^{-2}$ | 41 | $2.64 \times 10^{20}$ |
| 322 | $5.94 \times 10^{-4}$ | $+2.35 \times 10^{-2}$ | 40 | $2.66 \times 10^{20}$ |
| 357 | $6.18 \times 10^{-4}$ | $+2.33 \times 10^{-2}$ | 38 | $2.68 \times 10^{20}$ |
| 373 | $6.30 \times 10^{-4}$ | $+2.31 \times 10^{-2}$ | 37 | $2.71 \times 10^{20}$ |

Table 9 cont'd: Calculated galvanometric properties of sample 2xa as a function of temperature.

in B/Si gas phase molar ratio have been plotted in Fig. 41. The acceptor concentration ($N_A$) values were obtained from Hall measurements. For high doping levels, $9\times10^{18}$ atom/cm$^3$ to $\approx 2.0\times10^{20}$ atom/cm$^3$, the acceptor concentration is proportional to the B/Si gas phase molar ratio. In the case of B/Si ratio of $1\times10^{-2}$ to $1.6\times10^{-1}$, the acceptor concentration remains constant at an approximate value of $3\times10^{20}$ atom/cm$^3$. This was the highest doping concentration obtained and was found to be close to the solid solubility (36) of boron in Si at this temperature of 950°C. This curve is in good agreement with Ref. (37). However, these authors (P. Rai-Choudhury and E.I. Salkowitz) (37) used single crystals silicon doped with $B_2H_6$, deposited from $SiCL_4$-$H_2$ mixture at 1500°K. At this temperature, the boron concentration reached a maximum of $7\times10^{20}$ atom/cm$^3$. This maximum is in agreement with the solid solubility of Boron into Silicon (36) at this deposition temperature. The behaviour below B/Si ratio of $1.7\times10^{-4}$ was not investigated in this work. In the literature (38) lower doping effects were reported. It was observed that decreasing the B/Si gas phase molar ratio to $5\times10^{-5}$ a sudden decrease in carrier concentration occurred. The extremely rapid decrease in $N_A$ below a B/Si ratio of $5\times10^{-5}$ was unprecendented as far as they knew in a $SiH_4$ system. Their reason for a sudden change was "In this range it was not possible to predict or control the values from $10^{14}$ atom/cm$^3$ to $5\times10^{18}$ atom/cm$^3$ by setting B/si vapor phase ratio".

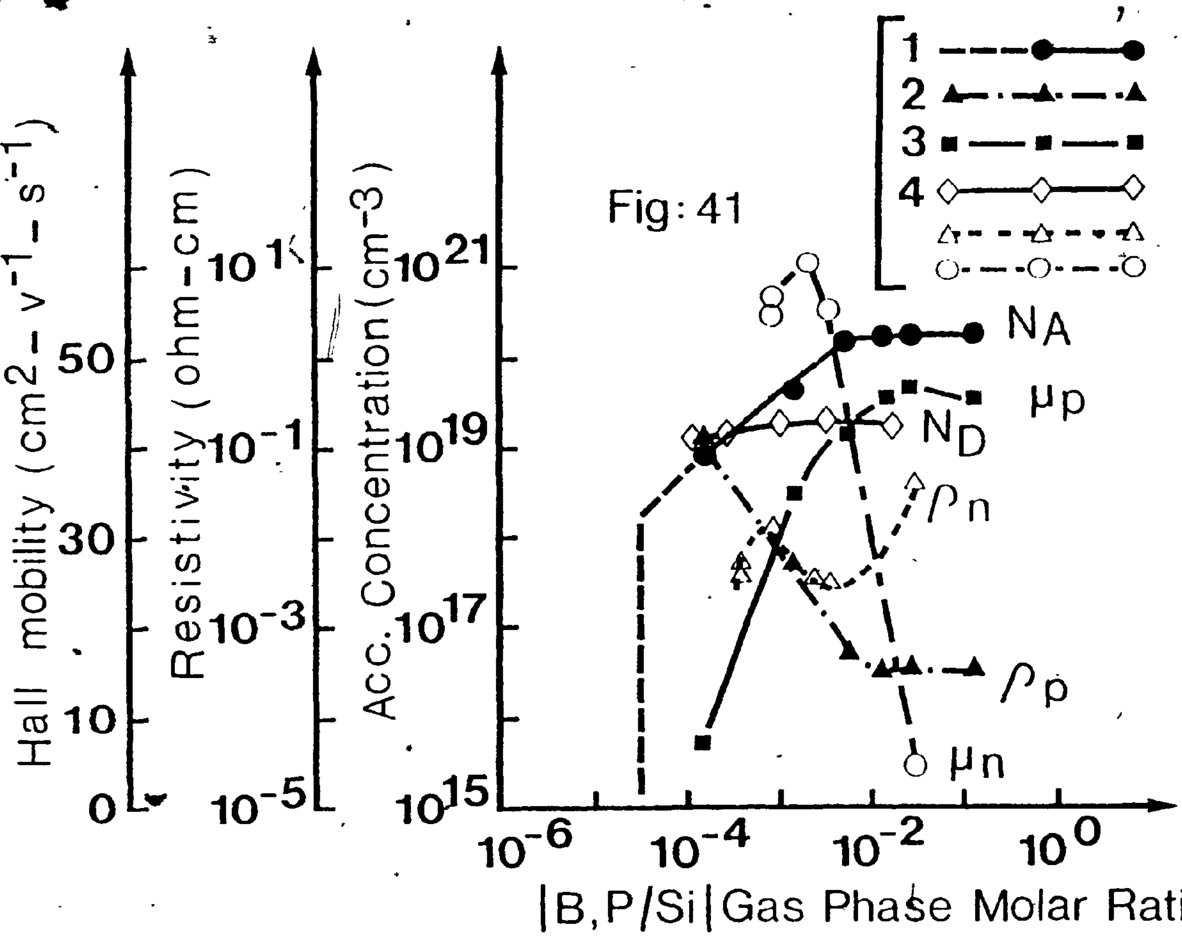


Fig. 41: Charge carrier concentration n and $p=(eR_H)^{-1}cm^{-3}$); resistivity, $\rho_p$ and $\rho_n$ (ohm cm); Hall mobility $\mu_p$ and $\mu_n=(R_H^{-1})$ ($cm^2 v^{-1} sec^{-1}$) as the function of [B,P/Si] gas phase molar ratio.

Fig. 41 also shows the variation of electrically active phophorous dopant or carrier concentration ($N_D$) of samples 1 to 6 (see table 4) deposited at T=950°C as a function of phosphorous to silicon ratio (P/Si) in the vapor. In a similar manner to the boron results, $1\times10^{19}$ atom/cm$^3$ to $3\times10^{19}$ atom/cm$^3$ is approximately proportional to P/si. The behaviour of carrier concentration above P/Si ratio of $1\times10^{-4}$ was not investigated. The maximum value of Nd observed was $3\times10^{19}$ atom/cm$^3$ and is in good agreement with the solid solubility limit of phosphorous in Si at this deposition temperature (36,39).

3.4.2 Hall Mobility of Polysilicon.

The Hall mobility ($\mu_H$) was determined from the ratio of the Hall coefficient ($R_H$) and the resisitvity ($\rho$) as measured at room temperature and it is shown for p and n-type samples in figs. 42 and 43.

Fig. 42 depicts the carrier mobility ($\mu_H$) for p-type polycrystalline silicon as a function dopant concentration ($N_A$). The hole mobility in single crystal silicon is also plotted for comparison. At the highest dopant concentration $2.5\text{-}3\times10^{19}$ cm$^{-3}$ the carriers have a mobility of approximately 45cm$^2$ v$^{-1}$ sec$^{-1}$. The mobility is about a half of the one in a single crystal silicon (90cm$^2$ v$^{-1}$ sec$^{-1}$). As the dopant concentration was decreased the mobility decreased sharply, and at a dopant concentration of $9\times10^{18}$ atom/cm$^3$ the mobility of the carrier reached a value

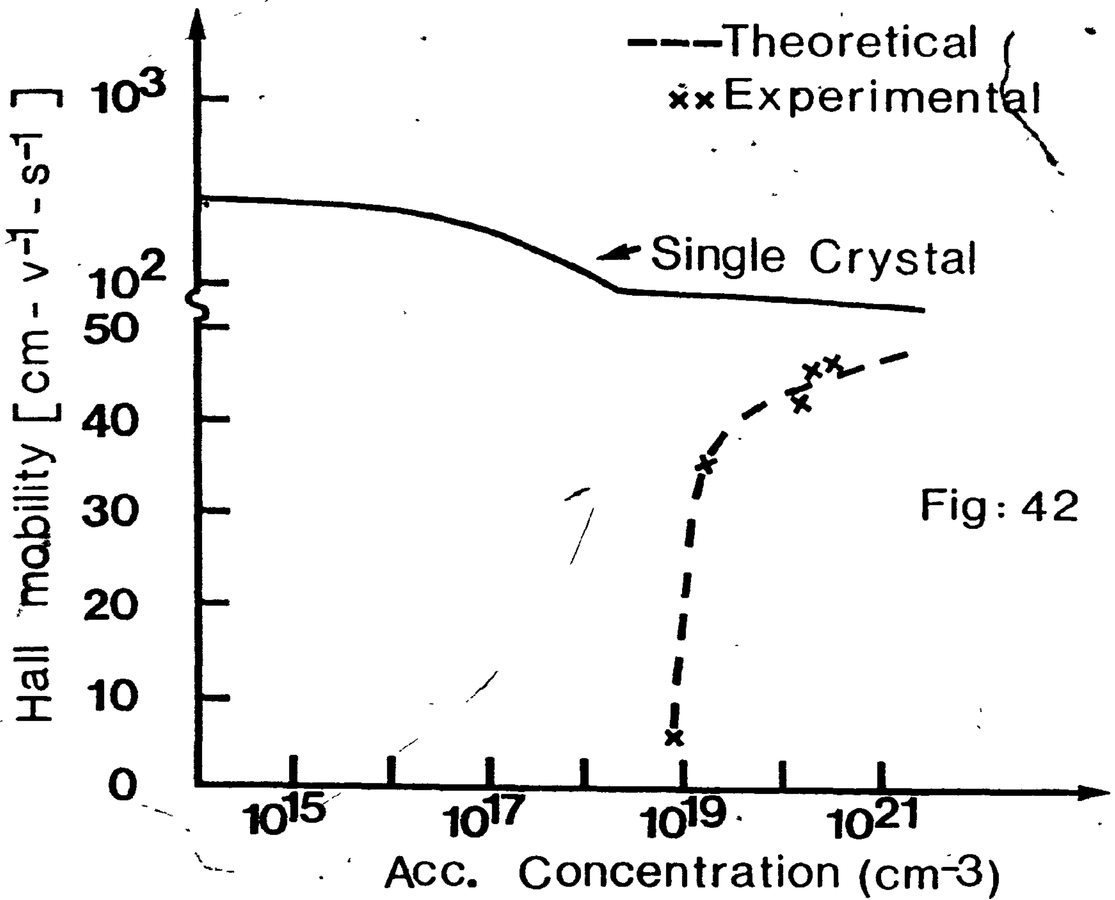


Fig. 42: Hall mobility $\mu_H (cm^2 v^{-1} s^{-1})$ as a function of acceptor concentration.

of approximately 7 $cm^2 v^{-1} sec^{-1}$. At this concentration the Hall mobility was 1/12 that of a single crystal silicon. There is no information regarding the Hall mobility below doping concentration of $9\times10^{18}$ atom/$cm^3$ since $\mu_H$ for p-type polysilicon was measured at high and medium dopant at high and medium dopant concentrations only.

Fig. 43 shows the variation of Hall mobility for an n-type polycrystalline silicon as a function of dopant concentration ($N_D$). The electron mobility in single crystal silicon is also plotted for comparison. In the case of a carrier concentration of $8.22\times10^{19}$ atom/$cm^3$ the mobility of n-type polysilicon was o.6 times that of the bulk mobility (110 $cm^2 v^{-1} sec^{-1}$) in n-type single crystal silicon. As the dopant concentration increased the $\mu_H$ reaches that of single crystal silicon. As the concentration of phosphorous was decreased from $4.5\times10^{19}$ $cm^{-7}$ to $4.5\times10^{19}$ atom/$cm^3$ the carrier mobility dropped to $\simeq$ 50 ($cm^2 v^{-1} sec^{-1}$). This mobility is 0.45 that of the single crystal silicon. As the dopant concentration was decreased the mobility decreased sharply and at a dopant concentration of $3\times10^{19}$ atom/$cm^{-3}$ the mobility of the carriers reached a minimum value of 4 ($cm^2 v^{-1} s^{-1}$) which corresponds to 1/27 or 0.04 times that of single crytal silicon. At carrier concentrations below $3\times10^{19}$ $cm^{-3}$ again the Hall mobility rises and at a carrier concentration of approximately $1.18\times10^{19}$ atom/$cm^3$ the Hall mobility reached 0.74 that of single crystal silicon. This phenomenon of decrease and increase of mobility has been observed by many other

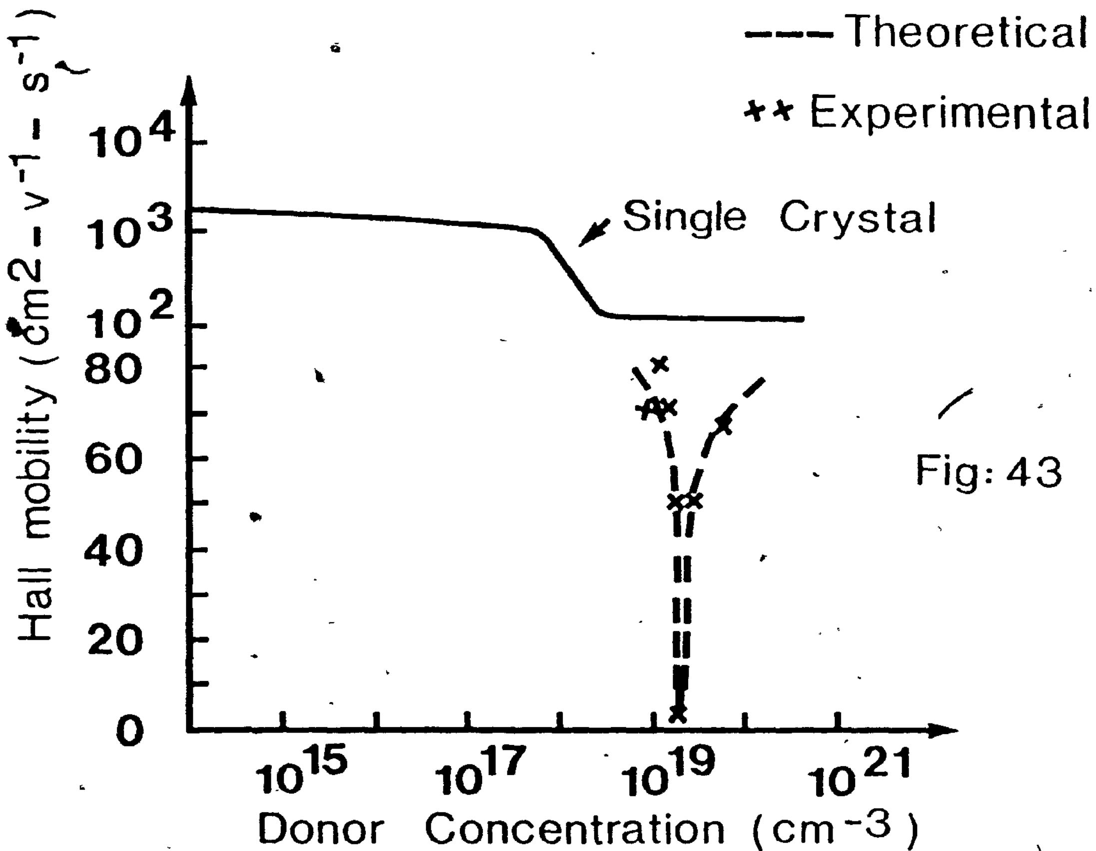


Fig. 43: Hall mobility, $\mu_H (cm^2 v^{-1} s^{-1})$ as a function of Donor Concentration.

researchers (11,13,38,40) and will be discussed later.

Fig. 44 shows the variation of Hall mobility for p-type polycrystalline silicon as a function of film thickness in the range of 17 to 32μm. Temperature of deposition was 950°C. The gas phase molar ratio was chosen to be of $5\times10^{-2}$ since as it is seen from fig. 41, as the B/Si gas ratio increases from $1\times10^{-2}$ to $5\times10^{-1}$, the impurity concentration remains constant. In the thickness range of 17μm to 32μm the Hall mobility remained approximately constant at an average value of $44 cm^2 v^{-1} sec^{-1}$, except for the thickness of 32μm where the mobility dropped to $39 cm^2 v^{-1} sec^{-1}$. This 8-9% change from the average value could be due to some changes in the doping concentration of the sample.

Fig. 45, similar to that of fig. 44 shows the variation of Hall mobility for n-type polycrystalline silicon as a function of film thickness. The gas phase molar ratio of P/Si was $2.5\times10^{-2}$. The sample thicknesses were in the range of 23μm to 86μm. In fig. 45 it can be noticed that the Hall mobility increased monotonically as the film thickness increases from 23μm to approximately 45μm. At thicknesses higher than 45μm, the Hall mobility becomes thickness independent.

### 3.4.3 Sample Resistivity

The average resistivity was calculated from the Hall effect data using the equation of $\rho = \frac{R.\omega.t}{\ell}$

where $\rho$ = resistivity of the sample (ohm-cm).

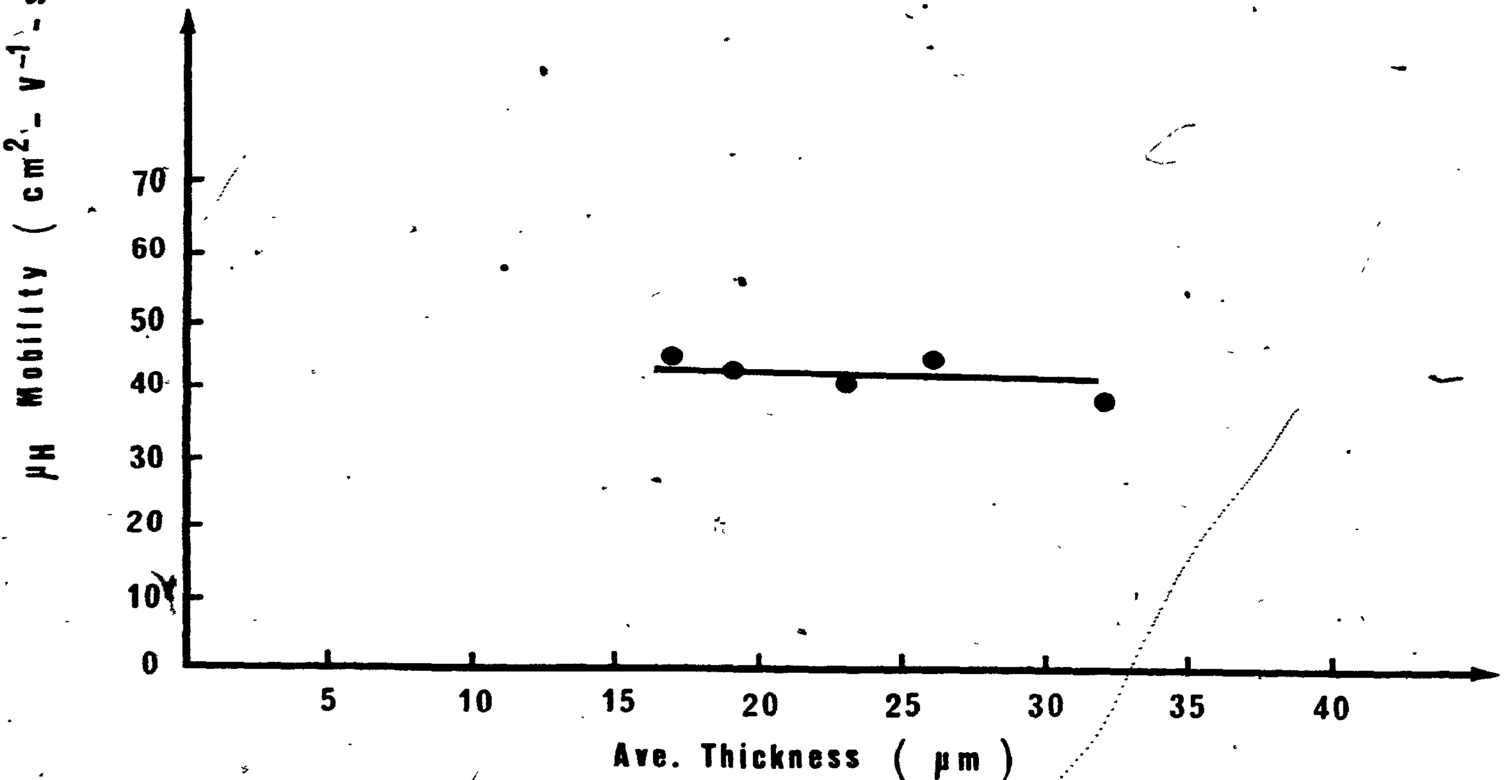


Fig. 44: Hall mobility, $\mu_H (cm^2 v^{-1} s^{-1})$ of boron-doped polycrystalline layers, as a function of some average film thickness.

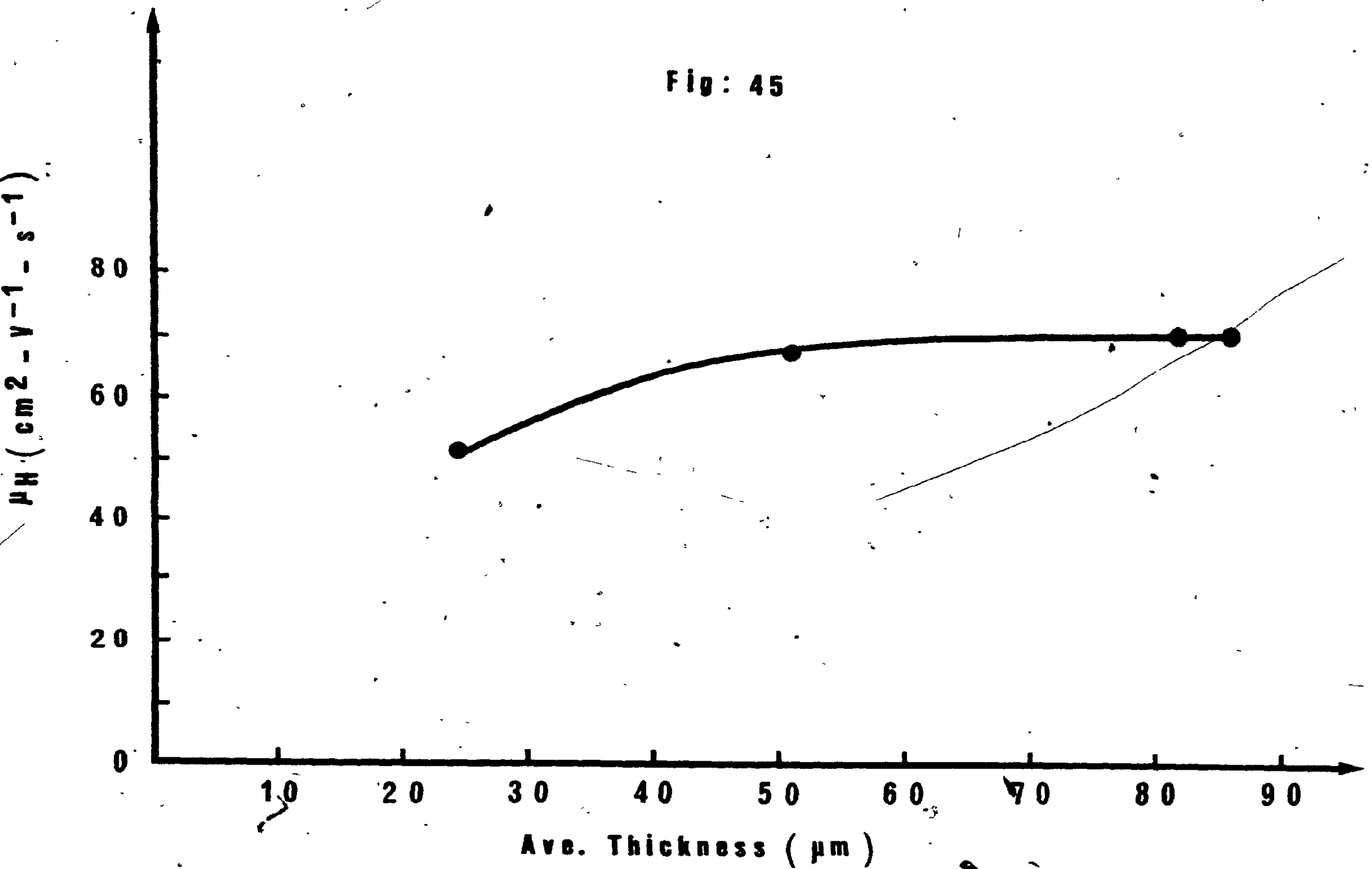


Fig. 45: Hall mobility, $\mu_H(cm^2 v^{-1} s^{-1})$ of phosphine-doped polycrystalline layers as a function of some average film thickness.

R = resistance of sample (ohms)

$\omega$ = average width ($\mu$m)

t = average thickness (cm)

$\ell$ = length between two hall probes (3-5 or 4-6, see fig. 36) (cm).

at room temperature.

Fig. 41 shows the variation of resistivity as a function of boron to silicon gas phase molar ratio. The temperature of deposition was at 950°C. The silane flow rates and that of the carrier gas were 2.8$\ell$/min and 0.25-0.5$\ell$/min respectively (see table 3).

For low ratios of gas phase dopant to silicon, the resistivity of the films decreased many-fold. At values of [B]/[Si] gas phase molar ratio of $1.6\times10^{-4}$ the resistivity was found to be of 0.1 ohm-cm and decreased linearly down to $9\times10^{-3}$. At values of [B]/[Si] greater than $1\times10^{-2}$ the resistivity of the films remained essentially constant at about $6-7\times10^{-4}$ ohm-cm (see table 24).

The resistivity of phosphorous-doped films is plotted as a function of the gas phase molar ratio of [P]/[Si] in fig. 41. At values of [P]/[Si] gas phase molar ratio of $1.4-1.6\times10^{-4}$ the resistivity was found to be $7\times10^{-2}$ ohms cm. It reached a minimum value of $4\times10^{-3}$ ohm-cm at [P]/[Si] of $5.5\times10^{-3}$ and then increased to about 0.065 ohm-cm at [P]/[Si] of $5\times10^{-2}$. From fig. 41 one also notices that at [P]/[Si] gas phase molar ratio of $1.4\times10^{-4}$ if the thickness of the deposited film is increased, the resistivity of the sample decreased.

For example at a film thickness of 23μm the resistivity was found to be $7\times10^{-2}$ ohm-cm but at a film thickness of 45μm the resistivity decreased to $6\times10^{-3}$ ohm-cm. The decreased is about an order of magnitude.

Fig. 46 shows the variation of resistivity with doping concentration of p- and n-type poly-silicon measured at room temperature. The undoped polycrystalline silicon layers, measured with an electronmeter resulted in resistivities greater than $6.2\times10^{6}$ ohm-cm. Although we have no data or information regarding the behaviour of the resistivity as a function of doping concentration up to $9\times10^{18}$ atom/cm$^3$ we presume that the behaviour of the resistivity follows a similar behaviour which was reported by Seto (13) up to this concentration. This author (13) also found resistivities in the order of $10^{6}$ and more when the impurity concentration was in the range of $10^{14}$-$10^{15}$ atoms/cm$^3$. As the concentration increased the resistivity decreased. As the impurity concentration was increased from approximately $2.5\times10^{18}$ atoms/cm$^3$, an abrupt resistivity drop of about five orders of magnitude was noticed (13). If we assume that the resistivity behaves in a similar manner up to our impurity concentration of $9\times10^{18}$ atom/cm$^3$, the resistivity at this point would correspond to a resistivity drop of 6-7 orders of magnitude in the case of this investigation. As the concentration is increased further from $9\times10^{18}$ to approximately $2.5\times10^{20}$ atoms/cm$^3$ the resistivity drops further but following an exponential function. This drop corresponds to another 2-3

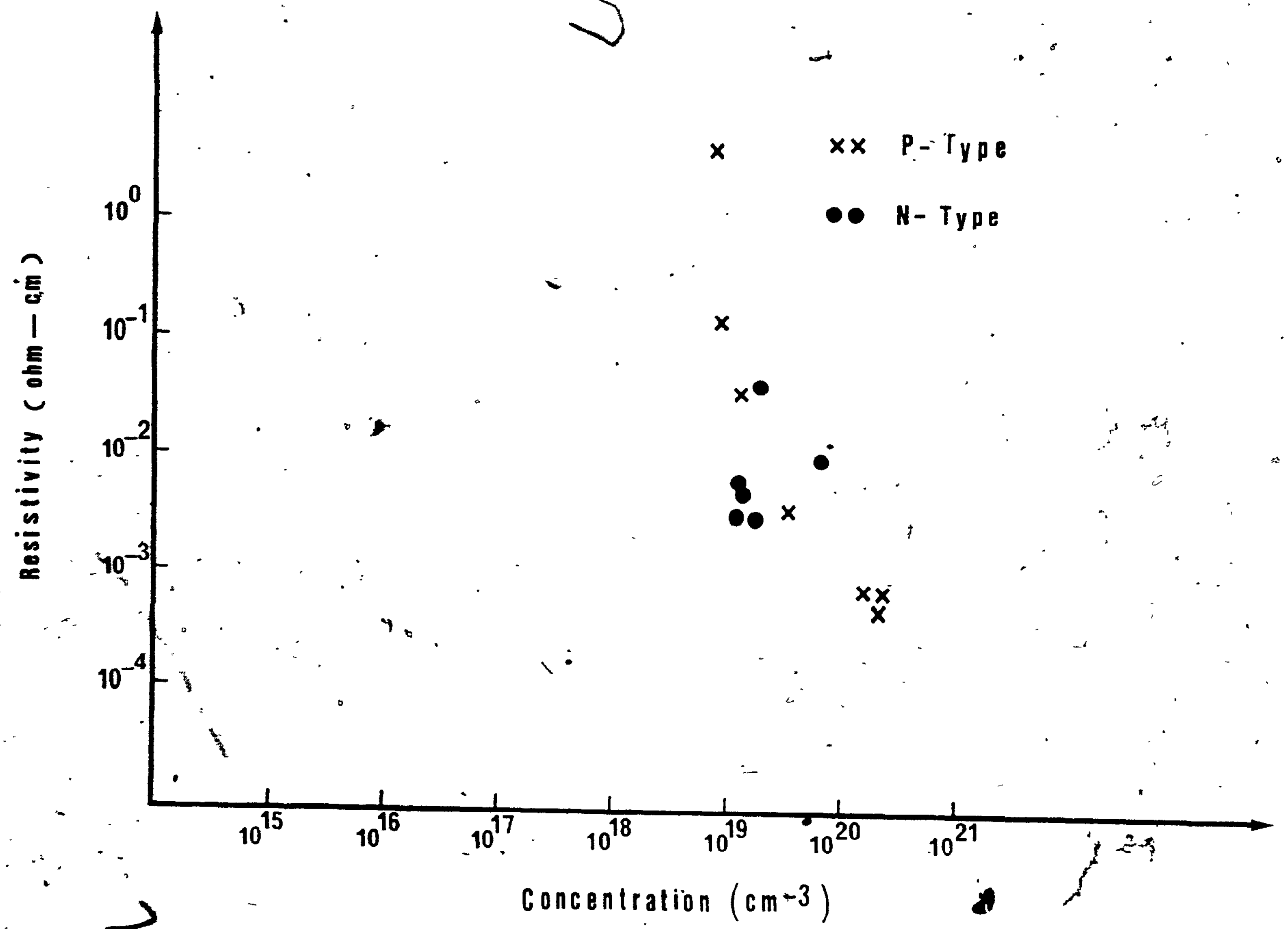


Fig. 46: Resistivity of Polysilicon as a function of Boron and Phosphorous doping concentration.

orders of magnitude.

As the impurity concentration is increased above the value of $2.5\times10^{20}$ atom/$cm^3$ the resistivity approaches a constant.

Fig. 46 also shows the variation of resistivitv with phosphorous doping concentration of the deposited poly-silicon. Here the behaviour of the resistivity as the function of doping concentration is different from the one depicted in Fig. 46. As the concentration decreases from $8.2\times10^{19}$ atom/$cm^3$ $2.5\times10^{19}$ atom/cm, the resistivity increases linearly then as the dopant concentration decreases further from $2.5\times10^{19}$ atom/$cm^3$ can be seen an abrupt decrease in resistivity and with a further decrease in concentration from $1\times10^{19}$ atoms/$cm^3$, resistivity begins to increase again. This behaviour will be discussed later.

3.4.4 Electrical Properties of Poly-Silicon as a Functional of Anneating Time

Fig. 47 shows the variation of acceptor concentration, reistivity and Hall mobility as a function of annealing time.

The resistivity of boron doped films (deposited at T=950°C) was not found to change when annealed at 1025°C. Similar results were observed by annealing in hydrogen or helium. For the boron doped films a slight increase in resistivity from $5\times10^{-4}$ to $6\times10^{-4}$ ohm-cm can be noted as the annealing time increases.

The apparent Hall mobility of boron doped films seems

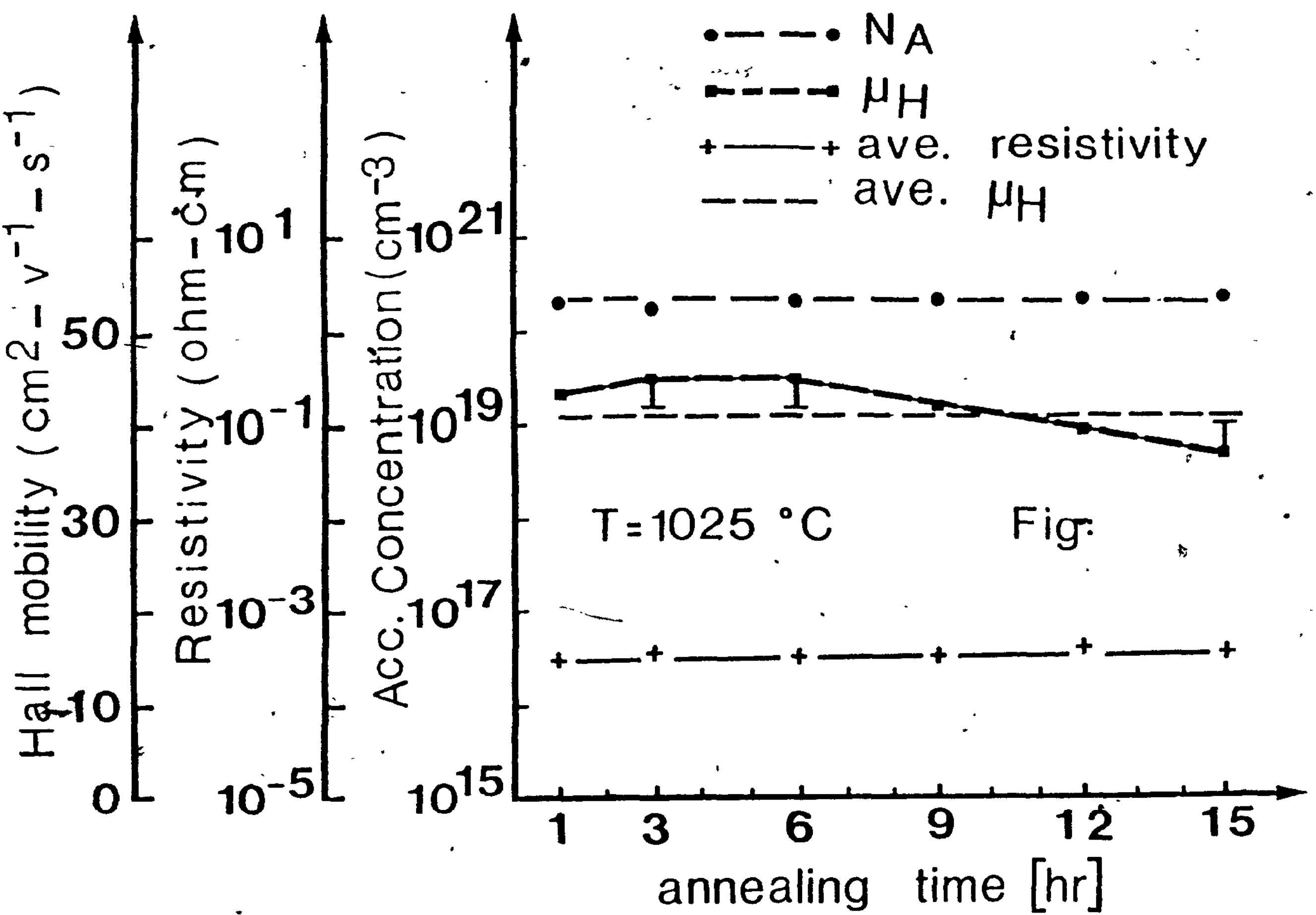


Fig. 47: Hall mobility, $\mu_H (cm^2 v^{-1} s^{-1})$, Resistivity $\rho$ (ohm cm) and Acceptor Concentration, $p(cm^{-3})$ as a function of annealing time. The annealing temperature is 1025°C.

to remain approximately constant up to 6hr of annealing and then as the annealing time increases the Hall mobility decreases in an linearly manner. This drop might be due to sample thickness variation. In fig. 47 the average mobility is depicted by a dashed line. The 10% error which can be seen, corresponds to a mobility difference of $4.5cm^2\ v^{-1}\ sec^{-1}$ from the average mobility. Therefore, it can be seen that the electrical properties of polysilicon remain constant at an annealing temperature of 1025°C.

# CHAPTER 4

# PHOTOVOLTAIC EFFECT

# CHAPTER 4

## INTRODUCTION TO PHOTOVOLTAIC EFFECT

### INTRODUCTION

The finite amount of available fossil fuel and continually increasing energy need of mankind dictate the need for development of alternate energy sources. Solar energy is one energy source that is abundantly available and can be harnessed by silicon solar cells. Production of polycrystalline silicon by the pyrolysis of silane has been touted as a promising method of reducing the present-day high cost of silicon cells.

The photovoltaic effect is the scientific word known to engineers as Solar Energy Conversion. It is a process by which a voltage is produced at the junction of two different materials ($S_i$ - Boron or Phosphorous) through an incident photon flux (to be explained in the next section). In a p-n junction, photons of sufficient energy, incident upon the semiconductor, produce hole-electron pairs. Some of these holes and electrons diffuse towards the junction and, if they are created sufficiently close to it, they will attain a high probability of reaching it before they recombine. At the junction they are separated by the barrier (electric field). If they are created at the p-side of the junction and diffuse towards the junction, the electrons will be swept across it into the n-side whereas the holes

will be blocked by the barrier. If the hole-electron pair diffuse in from the n-side of the junction, the holes are swept into the p-side by the barrier while the electrons are blocked.

The carriers which are swept across the barrier are the minority carriers in the region in which they are generated, and their flow through the barrier constitutes reverse current. If there are no exterior connections to the device (open circuit voltage), the charge which accumulates on either side of the junction reduces the barrier height. This reduction causes the forward current to increase. The forward current results from the passage of thermally produced majority carrier across the barrier. An equilibrium condition is quickly established, which results in an open-circuit voltage intermediate between zero and the full barrier voltage.

4.1 Optical Absorption in a Semiconductor

The unit of light, called a photon, is $h\nu$, where $\nu$ is the light frequency and h is plank's constant. The wavelength of light $\tau$ is related to frequency by

$$\tau = \frac{C}{\nu} = \frac{hC}{E_{ph}} = \frac{1.24}{E_{ph}(ev)} \ (nm) \qquad (4.1)$$

where

E = photon energy

hν = electron - volts

C = velocity of light

When a semiconductor is illuminated, photons may or maynot be absorbed, depending on the photon energy and the band-gap energy, $E_g$ . Photons with energy smaller than $E_g$ are not readily absorbed by the semiconductor beacuse there is no energy state available in the forbidden gap to accomodate an electron (fig. 48-a). Thus light is transmitted through and the material appears transparent. If $E_{ph} = E_g$, photons are absorbed to create electron-hole pairs, as shown in fig. 48-b . When photon energy is greater than $E_g$, an electron-hole pair is generated and in addition, the excess energy $E_{ph} - E_g$ is dissipated as heat fig. 48-c.

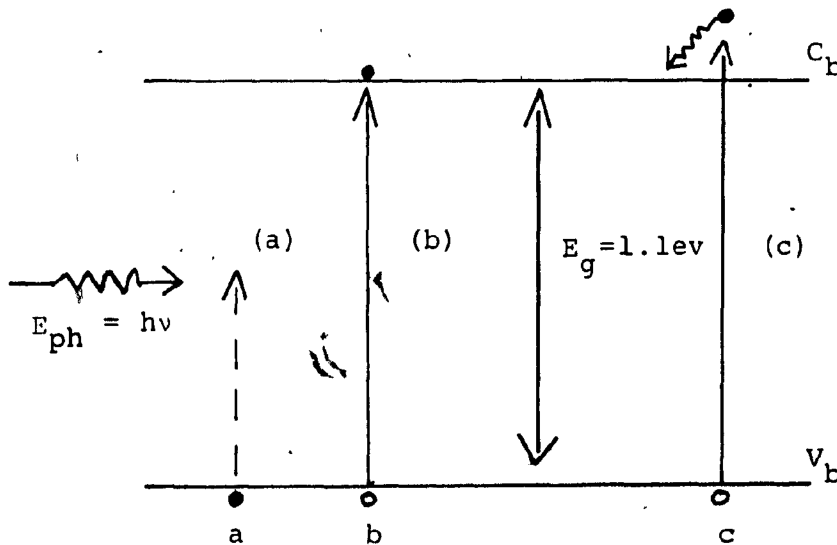


Fig. 48: Radiative Transition Levels of Electrons.

The total diode current under illumination is then given by

$$I = I_0 \, (E^{V/V_T} - 1) - Iph \qquad (4.2)$$

where

$I_0$ = saturation current.

$I_0 \, (e^{V/V_T} - 1)$ = reverse diode current.

$Iph$ = light penetrated current.

$V$ = Voltage

$V_T = \frac{kT}{q}$ = thermal equivalent voltage

$k$ = Boltzmann's constant.

$T$ = absolute terperature

$g$ = electronic charge ($1.6 \times 10^{-19}$C)

It is noted from fig. 49 that Iph is the current at zero voltage and thus equal to Isc. Setting $I = 0$ in Eq. 4.2, the open-circuited voltage obtained is

$$V_{oc} = V_T \ln \left(\frac{I_{ph}}{I_o} + 1\right) \qquad (4.3)$$

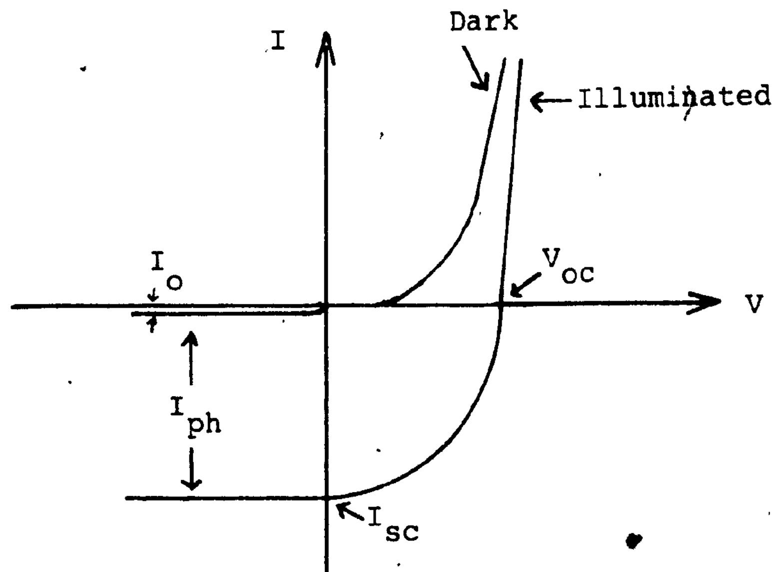


Fig. 49: Ideal characteristic of a Silicon Solar Cell both under dark and iluminated conditions.

Show the I-V characteristic of a solar cell both under dark and illuminated conditions. The characteristics in ideal when the series Resistance on both sides of the junction ($R_{sj}$) = 0, series resistance due to the contacts ($R_s$) = 0 shunt resistance ($R_{sh}$) of the junction = ∞ and resistance due to grain boundaries ($R_{gb}$) = 0.

The process of converting optical energy into electrical energy in a p-n junction can be summarized with the following basic steps:

a) Absorption of photons so that electron hole pairs are generated in both p and n side of the junction.

b) By diffusion, only those electron hole-pairs generated within a diffusion length (Ln+Lp) from the junction reach the space-charge region.

c) At the space-charge region, electron-hole pairs are separated by a strong electric field; electrons created on the p-side will slide down the potential to move to the n-side and holes created on the n-side move up to the p side (for holes join up the potential is analogous to rolling down for the electrons).

d) If the p-n junction diode is left open circuited, an accumulation of electrons and holes on the two side of junction will produce an open circuit voltage ($V_{oc}$).

e) If a load is connected to the diode, a current will flow.

f) Maximum current is realized when an electric short is placed across the diode terminals and it is called the short-circuit current ($I_{sc}$).

An equivalent circuit of the ideal solar-cell characteristic along with its deviation is given in Appendix E-A. While in Appendix E-B the realization of a practical solar cells is given, along with a detailed derivation of maximum power.

## 4.2 Fabrication of a Photovoltaic Device

The following subsections describe the fabricational procedure of a polycrystalline solar cell.

### 4.2.1 Sample Preparation

P-type doped layers of polycrystalline silicon were grown, as it was mentioned previously in Chapter 2 on graphite. On the p-doped polycrystalline layers n-type silicon layers were grown. The conditions of deposition of both p & n-type polysilicon layers are collected in Table 10.

Time of n on p deposition of polysilicon is from 2 to 5 min. which corresponds to a layer thickness of 1-5μm. The reason of shallow thickness is to create the junction close to the surface in order to increase the collection efficiency of the device.

### 4.2.2 Contacts

Contacts to n on p silicon are made as follows: the grown silicon layers are placed in an evaporator until the system reaches a vaccum of $10^{-6}$mmHg. Once at this vaccum gold is evaporated through a finger type mask.

### 4.2.3 Alloying

Alloying gold to silicon is performed at Eutetic temperature of 577°C in $H_2$ atmosphere for 5 min. The Eutectic point is that region of temperature where the two alloys combine. After alloying the samples, contacts are made to the top and bottom of the device. The device is now ready for measurements.

### 4.2.4 Sun Simulation

It is found that the amount of solar energy reaching the earth through the atmosphere on a clear day when the sun is at a zenith is $100mW/cm^2$. The AMI (Air Mass One) condition can be simulated by the use of an incondescent lamp, a beaker of water (to filter the I.R.) and a calibrated photo detector.

The incandescent lamp is placed in a back box (200 watts) (to eliminate any reflection) the light beam is then allowed to go through a water beaker through a 3mm hole onto the device. The device is positioned at the

distance of 4 cm. This distance corresponds to the power density of $100mW/cm^2$. The current-voltage characteristics of the device are then measured both in the dark (normal diode characteristic) and under illumination. The measured voltage and current values of the solar cells fabricated from various deposition conditions(n-type polysilicon deposited on p-type polysilicon) are reported in Table 10.

From Table 10 it is seen that the power conversion of the solar cell increases as the grain size of the p-type layer increases and when the n-type polysilicon layer is kept to a layer thickness of 1μm. Few samples were found to be resistive short, since the top contact of the n-type polysilicon layer was shorting the junction of the device to the p-type polysilicon layer. As the deposition of the n-type layer improved, the performance of the device approached that of a diode. Three samples were observed to behave like rectifiers (diodes) rather than solar cells. This was so, because the n-type polysilicon layer was to thick that it prevented (absorbed) the incoming light from reaching the junction were hole-electron pairs are generated. As the layer thickness of the n-type polysilicon was decreased to approximately 1μm and the series resistance of the cell was decreased, the devices were found to generate electricity. Also as the grain size of the p-type layer was increased the power converted by these cells increased.

| Gas Flow Rates | | | Layer Thickness | Gas Glow Rates | | | Grain Size | Temp | Current | Voltage |
|---|---|---|---|---|---|---|---|---|---|---|
| He | $PH_3$ | $SiH_4$ | | He | $B_2H_6$ | $SiH_4$ | | °C | μA | mV |
| mm | mm | mm | μm | mm | mm | mm | μm | | | |
| 25 | 1 | 35 | 7 | 15 | 5 | 30 | 10 | 935 | resistive | |
| 20 | 3 | 30 | 5 | 20 | 15 | 30 | 12 | 936 | resistive | |
| 20 | 3 | 30 | 2.7 | 20 | 15 | 30 | 12 | 936 | diode | |
| 20 | 5 | 35 | 2 | 20 | 10 | 30 | 12 | 942 | diode | |
| 20 | 7 | 30 | 1.6 | 30 | 10 | 30 | 14 | 942 | diode | |
| 20 | 1 | 30 | 1 | 30 | 10 | 30 | 15 | 957 | 40 | 20 |
| 20 | 10 | 35 | 1 | 20 | 10 | 30 | 15 | 967 | 100 | 43 |
| 20 | 10 | 30 | 1 | 20 | 10 | 30 | 18 | 967 | 150 | 75 |
| 20 | 10 | 30 | 1 | 20 | 10 | 30 | 20 | 980 | 300 | 120 |

**Table 10 : Measured power conversion of the solar cell as a function of n on p type polysilicon layer and grain size.**

# CHAPTER 5

# DISCUSSION

# CHAPTER 5

# DISCUSSION

Concerning the crystallinity of undoped samples the results show that at temperatures up to 500°C the deposited films on fused silica are amorphous. At deposition temperature of 630° ~ 750°C the polycrystalline films were found to be practically smooth. The smoothness was due to the fact that the polycrystalline films were made of very small crystallites with no preferred orientation. At temperatures higher than 750°C the smoothness of the films began to vanish. Of course the vanishing of the smooth films was due to the increase in grain size. At approximately 825°C a typical grain size of the undoped silicon films is 3μm.

Simultaneous, boron-doping during the growth of polycrystalline silicon films on fused silica by the thermal decomposition of $SiH_4$ has been found to enhance the growth rate and to lower the apparent activation energy for the growth. At a temperature of 800°C approximately the growth rate of doped as compared to undoped was found to be of 1.8 higher. Furthermore, microstructure of doped and undoped films depends on the growth temperature and doping level of boron.

At temperature well above 900°C the morphology of the deposited films improved. The average measured grain

size was found to be of 15μm. One drawback found for the deposition of polysilicon on fused silica was that the silicon reacted with the fused silica and due to the mismatch of the coefficient of thermal expansion cracking of the deposited films occured.

The preferred orientation of the silicon films deposited on fused silica by the pyrolytic decomposition of silane was found to be temperature dependent. Substrate temperature of approximately 970°C produced a strong (111) preferred orientation as compared to (110) planes. As the temperature decreased the preferred orientation of growth, reciprocates. This might be due to the different activation energies for different growth directions. At temperatures below 970°C the (110) oriented crystallites have more favorable growth conditions accompanied by {311} and {331}. The apparent activation energies of both undoped and doped were found to be 41 and 38 K cal/mole (1.77 and 1.64 eV) respectively.

Similarly boron-doping during the growth of polycrystalline silicon films on graphite by the thermal decomposition of $SiH_4$ has been found to enhance the growth by lowering the apparent activation energy. This is represented by the measured decrease in activation energy; 26 K cal/mole or 1.12 eV on graphite substrate as compared to the activation energy of Si on Si (37 K cal/mole or 1.6 eV). These results lead to a marked decrease in the required growth temperature, to a striking improvement in

the film morphology and to a better reproducibility of the film thickness.

The microstructure of the doped films depend on the growth temperature and doping level of boron in this case, as well. Boron doping promotes silicon growth. The structure remains the same (900-980°C), except the size of the crystallites increase. The silicon layers deposited at the temperatures of (923-980°C) and flow rates (2.1-3.15 ℓ/min) consist of crystallites with characteristic sizes of 10-20μm and with an average layer thickness ranging from 29-60μm. Large columns extending from the surface to the graphite substrate is realized. The average column diameter are about 20μm.

The preferred orientation of the silicon films deposited on graphite by the pyrolytic decomposition of silane is found to be temperature dependent. Substrate temperature of approximately 980°C produced a moderate (111) preferred orientation as compared to the (110) planes. Similarly as on fused silica, as the temperature decreased, the preferred orientation of growth reciprocates. At 926°C the (110) oriented crystallites have more favorable growth conditions. This growth condition is accompanied as well by (311) and (331) planes. The intensity ratio of (220)/(111) is found to be 101, indicating a very strong (110) preferred growth.

On a polycrystal, the effect of grain boundaries is of primary importance. These are separating, the single

crystal grains in the system. The properties of the grain boundaries have been studied by a number of investigators in germanium (41) and silicon as well (11,13,42). It was assumed that the grain boundaries consist of dangling bonds which are acting as trapping centers for electron as well as for holes. Using this concept Seto (13) analyzed the measured transport properties of polycrystalline silicon films. At low doping concentration a quasi instrinsic property of silicon was found. After a crystal carrier concentration, however the normal extrinsic behaviour of a single crystal silicon was approximated. The intrinsic domain, in the case of lightly doped samples, was characterized by an electrical activation energy of about half the energy gap value of single-crystal silicon. The most prominent feature of polysilicon was reported to be a mobility minimum as the function of carrier concentration; at about $N_A = 1.6\text{-}2\times10^{18}$ atom/cm$^3$ (11 & 13). A grain-boundary model including the trapping state was developed and carrier concentration and mobility as a function of doping concentration were calculated from the model. It has been deduced that the mobility exhibits a minimum when the impurity concentration, $N = Q_t/L$ where $Q_t$ is the density of traps per cm$^2$ ($Q_t=3.34\times10^{12}$ atom/cm $^2$ (13)) and L is the grain size in nm. The model treating the grain boundaries as a potential energy barrier was developed for small grained ($L \doteq 60$nm) polysilicon. In this investigation, however large grains ($L \doteq 20\mu$m) films

are to be treated. As it can be seen in fig. 42 and 43 a distinct mobility minimum as the function of impurity concentration is observed in this case, as well. Taking, however the key equation given by Seto for the position of the mobility minimum, and using the average grain size of the film of this investigation $L \doteq 10\mu m$, an impurity concentration of $3.3\times10^{15}$ atom/cm$^3$ is resulted from the condition of $N \doteq Q_t/L$. This is about three orders of magnitude below the one observed experimentally in large grained films (see figure 42 and 43).

Consequently a new model is introduced to analyze the transport properties of polysilicon. This model is based on the facts that the grain boundaries are disordered, therefore there are a large number of defects due to incomplete atomic bonding. This results in the formation of trapping states in complete agreement with the reasoning of Seto. It is also assumed that the impurity atom, as well, are randomly distributed in the lattice. Furthermore, it is assumed that the trapping states are located at 0.37 eV from the band edge in the energy gap, according to the literature (11 & 13). Then to explain the apparent intrinsic behaviour of polysilicon film it is assumed that these trapping states can be treated as deep lying "acceptor-like" and deep "donor-like" states. This concept was introduced by Marshal and Owern (43) when analyzing the transport properties of vitreous $As_2$ $Sc_3$. In this context the unusual feature of the band

structure suggested [43] is the proposition of traps introducing deep lying "acceptor-like" and "donor-like" states due to normal compensation mechanism by shallow lying impurities. The compensating donor and acceptor states are both necessary to explain the low conductivity of both p-type and n-type polycrystalline silicon films.

Then the electrical characteristics of the system can be analysed by computing the position of the Fermi level based on the always valid steady state neutrality condition

$$p^+ + \sum_i N_{di}{}^+ = n^- + \sum N_{ai}{}^- \tag{5.1}$$

where the mobile hole concentration, $p^+$, is given by the classical expression

$$p^+ = \left(\frac{2\pi m_h{}^* kT}{h^2}\right)^{3/2} \exp\left(\frac{-E_q}{RT}\right) \tag{5.2}$$

where $m_p{}^*$ is the density of state effective mass for the holes ($m_p{}^*/m_o$=0.5586), $m_o$ being the rest mass of the electron, k is the Boltzman constant, T is the absolute temperature and h is Planck's constant. The position of the Fermi energy, $E_f$, is taken from the top of the valence band. The ionized shallow donor concentration, $N_D$, by: (i=s)

$$N_{ds}{}^+ = N_D \left(1 - \frac{1}{1 + \frac{1}{2}\,\mathrm{ex}\left(\frac{E_g - E_d - E_f}{kT}\right)}\right) \tag{5.3}$$

where the Energy gap, Eg, is given by

$$Eg = [1.12 + (300-T) \times 1.3 \times 10^{-4}]\mathrm{eV} \tag{5.4}$$

Ed = 0.044 (eV) is the donor ionization potential in Si [44]. The compensating deep lying acceptor concentration, $N_{ad}^-$, (i=d) is given by the concentration of acceptor-like traps, $N_{at}$, as:

$$N_{ad}^- = N_{at}\left(1 - \frac{1}{1 + \frac{1}{2}\exp\left(\frac{E_f - E_g - E_t}{kT}\right)}\right) \qquad 5.5$$

where the trapping level is characterized by $E_t$=0.37eV, below the conduction band edge. The shallow ionized acceptor concentration introduced by boron doping concentration, $N_A(cm^{-3})$ is given by: (i=s)

$$N_{as}^- = N_A\left(1 - \frac{1}{1 + \frac{1}{4}\exp\left(\frac{E_f - E_a}{kT}\right)}\right) \qquad 5.6$$

where for boron in silicon $E_a$ = 0.045eV [44]. The factor $\frac{1}{4}$ takes into account the double degeneracy of the valence band and the spin of the electrons as well. The compensating deep lying donor-like trapping centers concentration $N_{dt}(cm^{-3})$ determines the ionized deep donor concentration as follows:

$$N_{dd}^+ = N_{dt}\left(1 - \frac{1}{1 + \frac{1}{2}\exp\left(\frac{E_t - E_q}{kT}\right)}\right) \qquad 5.7$$

Here it is assumed, as it was mentioned before that the trapping level acting as deep lying donor-like state, is $E_t$=0.37eV above the valence band edge, as it was proposed by Seto [13]. Finally, the mobile electron concentration, $n^-$, is given by the classical expression:

$$n^- = \left(\frac{2\pi m_n^* kT}{h^2}\right)^{3/2} \exp\left(\frac{E_f - E_g}{kT}\right) \qquad 5.8$$

where the density of state effective mass of the electrons was taken to be $m_n^*/m_o = 0.3271$ [44]. Then using the neutrality condition, equation 5.1 the position of the Fermi level can be determined graphically by scanning the Fermi energy from the top of the valence band, $E_f = 0$ to the bottom of the conduction band $E_f = E_g$. Then for any given impurity and trapping center concentration of a given temperature, the characteristic Fermi level will be given when the neutrality condition is satisfied. The results for an n-type polysilicon are shown in figs. 1-7 in Appendix F. Here the trapping concentration $N_{at} = 2.5\times10^{19}$ $(cm^{-3})$ was considered, based on the experimental value in fig. (43) and the donor concentration was varied from $N_{ds} = 1\times10^{15}$ $(cm^{-3})$ (sample #1) to $N_{ds} = 1\times10^{20}$ $(cm^{-3})$ (sample #7) by a factor of ten each time. It can be clearly seen that the Fermi level is at the center of the band gap when $N_{ds} < N_{at}$ and moves up in the direction of the conduction band as the shallow donor concentration is increasing.

When the condition of $N_{ds} \geq N_{at}$ is satisfied, the material becomes extrinsic indicated by the close proximity of the Fermi level to the conduction band (see sample #7).

Similar calculations were performed by the computer (H.P. Model No.: 9830A) in the case of p-type materials. Here the trapping concentration, introduced deep lying donor concentration required for compensation of the shallow

lying acceptor impurity is taken to be $N_{dt}=9\times10^{18}(cm^{-3})$ as indicated by the position of the mobility minimum observed experimentally (see fig. 42). The shallow impurity, thus the boron concentration was varied again from $N_{as} = 1\times10^{15}(cm^{-3})$ (sample #1) to $N_{as} = 5\times10^{20}(cm^{-3})$ (sample #9), as indicated in figs. 8-16 in Appendix F respectively. The behaviour of the Fermi level is similar to the one discussed in the case of the n-type polysilicon. If $N_{dt} >> N_A$ the Fermi level is close to the center of the band gap, indicating intrinsic, high resistivity materials. As the acceptor concentration is approaching the deep lying compensation donor concentration, the Fermi level drops in the direction of the valence band, showing more and more p-type character of the material (see sample #1 to #6). When the boron concentration, $N_A \geq N_{dt}$, the Fermi level is found to be in the proximity of the valence band (see sample #7,8,9) indicating extrinsic p-type materials.

The results for n- and p-type silicon of figs. 1-16 have been plotted in fig. 50. Where $N_{at}=2.5\times10^{19}(cm^{-3})$ and $N_{dt}=9\times10^{18}(cm^{-3})$ where taken corresponding to the position of the mobility minimum shown in fig. 42-43. It can be seen that the Fermi level remains close to the center of the energy gap, till the values of the shallow lying impurities are below the concentration of the corresponding deep-lying trapping center concentration. Then when this condition is reversed, the Fermi level approaches the corresponding band edge, indicating the transition from

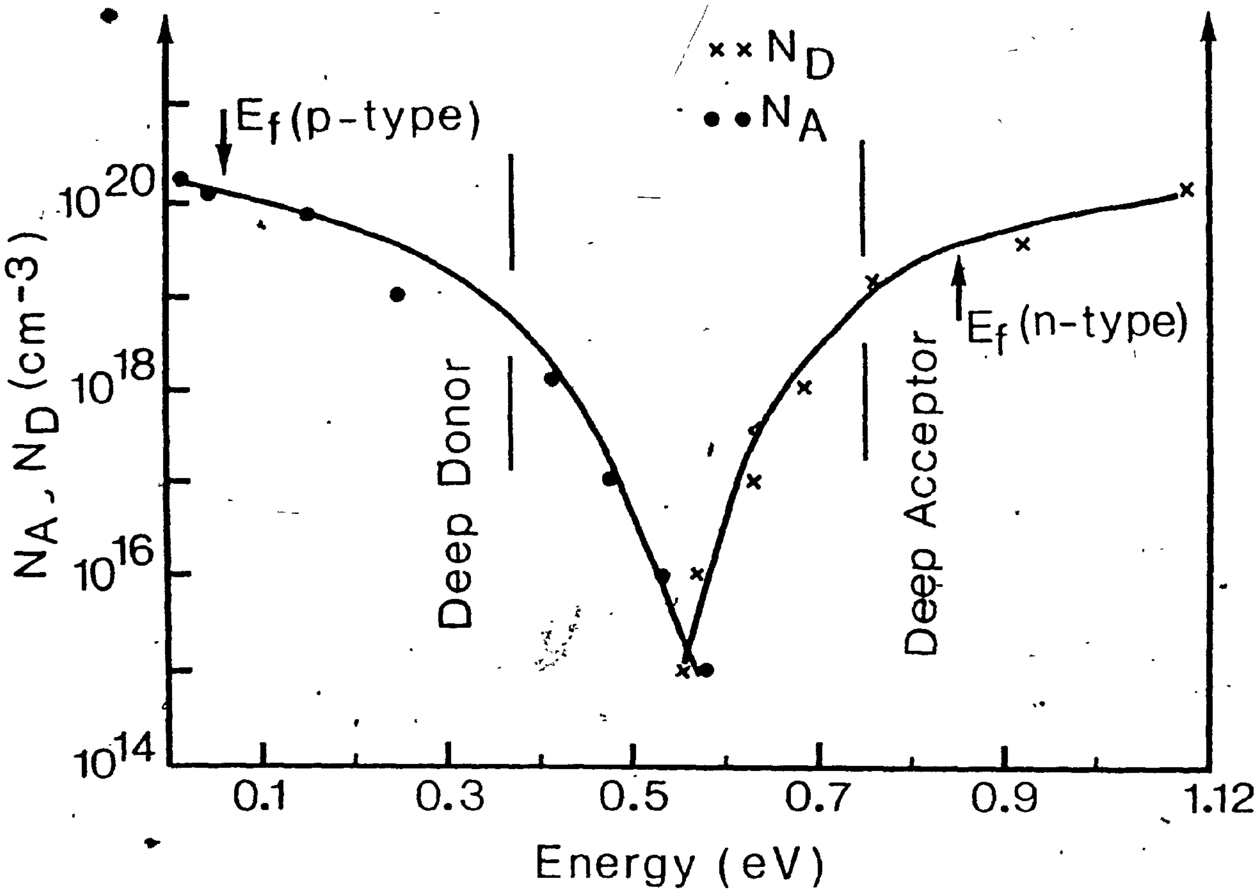


Fig. 50: Fermi energy, $E_f$(eV) as the function of donor $N_D(cm^{-3})$ and acceptor, $N_A(cm^{-3})$ concentrations. The position of deep donor-like and deep acceptor-like states are indicated.

intrinsic to extrinsic behaviour.

To compare this calculated characteristic, the resistivity of the material, as the function of doping concentration at a given deep-lying trapping center concentration for a given temperature, can be calculated. At the position of the Fermi level, characterizing each of the calculated cases, the mobile electron and hole concentration are given by equation 5.8 and 5.2 respectively. Then taking the electron and hole mobilities: $\mu_n$=1350 and $\mu_p$=480 ($cm^2v^{-1}s^{-1}$) respectively [44], the resistivity as the function of doping concentration can be calculated. The results (No. 3: p-type theoretical, No. 5: n-type theoretical) are shown in fig. 51 with the one obtained by Seto [13] (No. 1: p-type experimental, No. 2: p-type theoretical) and the experimental data (no. 4: experimental p-type) resulted from this investigation. A good agreement within these curves can be seen. This indicates the usefulness of the model developed in this investigation in the case of polysilicon, independent of the grain sizes.

There is a further consequence of treating the trapping centers as deep lying impurity-like compensating species. Assuming that these, as well as shallow impurities are randomly distributed in the system, then an average impurity seperation can be estimated by $R=(3/4\pi N_t)^{1/3}$, where $N_t$ is the ionized trapping impurity concentration, mentioned above. A characteristic Bohr radius, a*, represent-

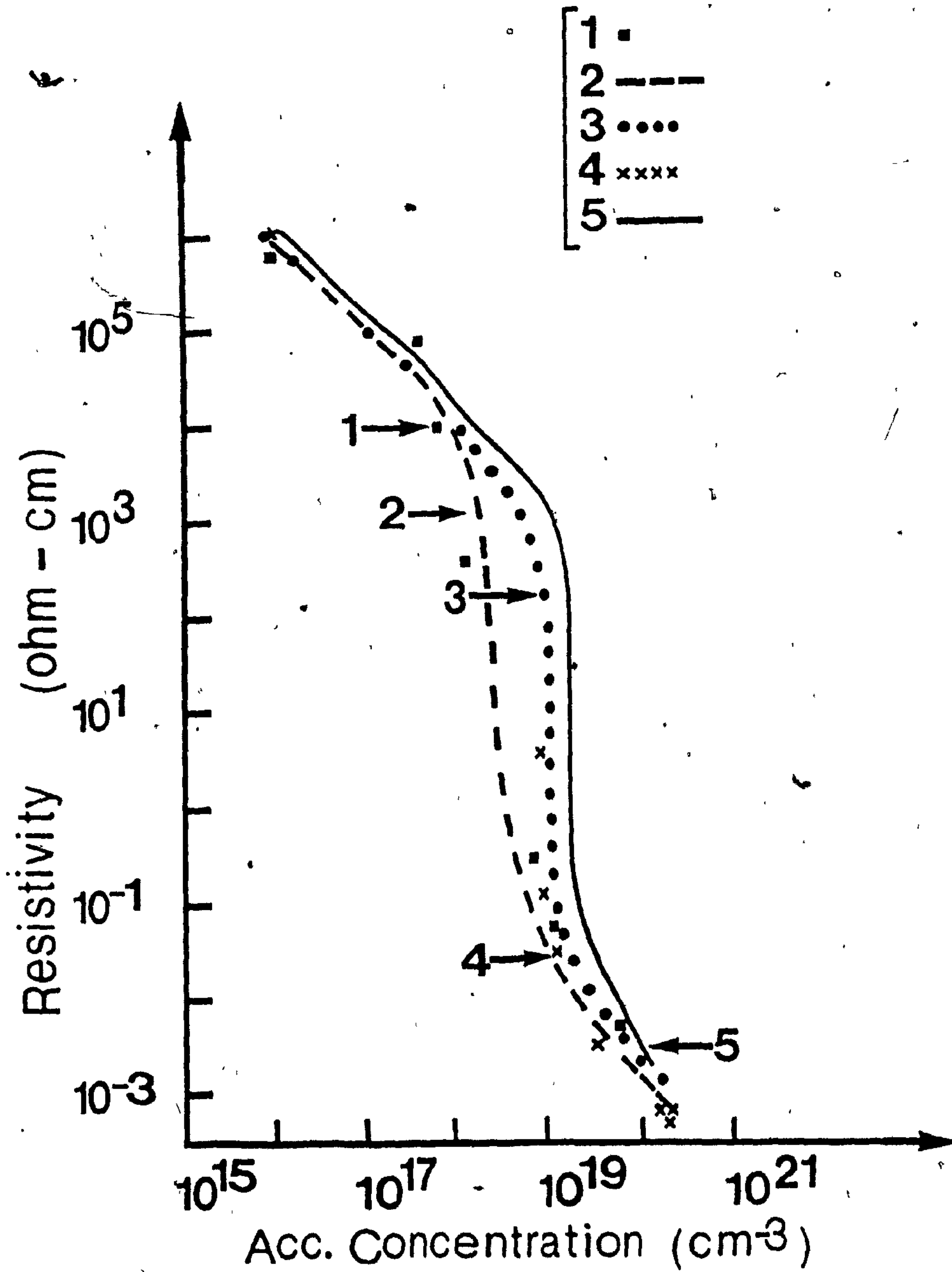


Fig. 51 : Resistivities $\rho$ (ohm-cm) as the function of charge carriers concentrations ($cm^{-3}$):
1: experimental points of Ref. 13
2: theoretical curves of Ref. 13
3: calculated curves for p-type film
4: experimental points of p-type film
5: calculated curve of n-type film.

ing these ionized deep-lying impurities can be also estimated by $a^* = \frac{4\pi\varepsilon\varepsilon_0 h^2}{m^* e^2}$ where $\varepsilon$ and $\varepsilon_o$ are the absolute and relative dielectric constants representing the system. In the n-type case, taking into consideration the above given deep-lying trapping centers introduced ionized acceptor-like states, $N_{ad}=2.5\times10^{19}(cm^{-3})$, a = 1.89nm and R=2.12mm can be determined. Then following the argument of Mott [46-47], if the average impurity separation, R, and the Bohr radius a* of these ionized impurities are commensurable, the formation of an impurity band can be assumed. In this case the overlapping wave functions of the ionized impurities, forming the impurity band, would reach through the grain boundaries, shorting their effect, when the Fermi level is in the impurity band. Then the propagation of the charge carriers can be regarded as a diffusion process in a random system. This type of transport property would be characterized by a low mobility, approximated by Mott [46] as:

$$\mu = \frac{2\pi R^2}{6n} \qquad 5.9$$

Taking into consideraiton the above calculated average impurity separation, R=2.12 nm, the electron mobility minimum, indicating the crossing of the impurity band by the Fermi level, would be $\mu=11.4(cm^2 volt^{-1} sec^{-1})$. The experimentally measured mobility (see fig. 43) at this minimum is $4(cm^2 volt^{-1} sec^{-1})$, which is about three times less than the impurity band mobility estimated by Mott [46].

Thus one can propose that the mobility minimum as the function of impurity concentration might be due to the crossing of the Fermi level, to the deep-lying impurity band. In this case the charge carriers would propagate in a random system, not influenced by the band structure of the solid, which is determined by the periodicity of the crystal lattice of the individual grains. Consequently, the density of state effective mass would loose its meaning and the rest mass of the electrons would characterize the conduction process. Therefore since

$$\mu = \frac{e\tau}{m^*} \qquad 5.10$$

an increase in electron mass, $m^*$ approaches $m_o$ would mean a decreased mobility, assuming that the relaxation time ($\tau$) would remain independent from the position of the Fermi level.

# CONCLUSION

CONCLUSION

The purpose of this chapter is to provide a summary of all the contributions made in this thesis and to indicate some future directions for producing and investigating depositions of polysilicon film.

In Chapter 1 a detailed description of the system (furnace, sample holder & etc.) was given and how it was used to grow polysilicon films. Also it has been shown as to how the flexibility of the water cooled jacket can be advantageous to the growth of polysilicon by retarding the pyrolysis of silane in particular at temperature of above $800^{o}C$.

In Chapter 2 we investigated in a systematic manner the growth of polysilicon as a function of temperature and doping conditions. At about $500^{o}C$ the films were amorphous. With increasing temperature the crystallinity of the chemical vapor deposited layers, increased. At around 800 to $825^{o}C$ the doped polysilicon crystals were 2 to 3 times larger than the undoped ones. At around $950^{o}C$ the grain size of the polycrystalline films averaged about 20μm on fused silica, graphite and thermally grown $SiO_2$ substrates. Plotting the growth rate as a function of the inverse temperature, the grown polycrystalline films on fused silica were found to be temperature dependent and are having activation energies 38 and 40K cal/mole

respectively. The films deposited on graphite instead were found to have an activation energy of 26K cal/mole. This implies that the films can be grown at lower temperatures. The thin films were characterized using scanning electron microscopy and x-ray diffraction. X-ray diffraction scan of the deposited films on graphite and fused silica both displayed a preferential growth in the [220] over the [111] orientation.

In Chapter 3 we discussed the experimental set up for Hall effect measurement and the relative Galvanometric effects related to Hall Effect measurements.

The transport properties were measured between 77K and 370K. It was found that the mobility went through a transition minimum and then suddenly the mobility increased, and approached the characteristic to that of simple crystal silicon (see fig. 42 & 43). To explain this experimentally obtained data, we derived a model based on deep lying impurity. In the model we assumed that the grain boundaries introduced dangling bonds and treated these dangling bonds as donor like and acceptor like deep lying compensating impurities. This model, accounting satisfactory for the measured transport properties, led to the recognition of the possible existence of impurity band conduction in polysilicon. These deep lying impurity bands could explain the experimentally osberved mobility minima, as the function of carrier concentration $N_A$ and $N_D$ were ploted

as a function of the Fermi level and found that the mobility minima coincided with the crossing of the Fermi level (see fig. 51) through the corresponding impurity band.

In Chapter 4 we spoke about the photovoltaic effect and showed how to produce solar cells by the chemical vapour deposition. The efficiencies of the actual built solar cells were found to exhibit low short circuit current and low open circuit voltage hence low efficiency (see table 10). The reason for such low efficiencies was attributed to

a) non uniformity of the n-type grown layer on the p-player.

b) Resistive short.

c) Resistive contact, (due to etching polysilicon at the polysilicon graphite interface.

e) Alloying of the top contact (metal diffusing through the grain boundaries to the p-type layer and as a result causing n-type polly layer to short with the p-type layer).

In summary well defined polysilicon layers have been grown on graphite with large crystallites and columnar features. The solar cells made from above depositions were found to exhibit low efficiencies in the order of 0.1 to 1% and this was merely due to the process (etchant, contacts, alloying etc.) rather than the grown polysilicon

layers. However by improving the process, solar cells having efficiencies of 6% and more can be made from this technique provided special attention is given to the fabrication aspect (contacts).

# REFERENCES

# REFERENCES

[1] K.E. Bean, N.P. Wentzschel, and D. Colman, J. Appl Phys. 40, 2358 (e) (1959); Paper 326 presented at Electrochem. Soc. Meeting, New York City, May 5-9, 1969.

[2] C.H. Fa and T.T. Jew, IEEE Trans. Electron Devices, ED-13, 290 (1966).

[3] T. Yoshihara, A. Yasuoka and H. Abe, J. Electrochem. Soc. 127, 1603 (1980).

[4] T.L. Chu, H.C. Mollenkopf, and Shirley S. Chu. J. Electrochem. Soc.: Solid State Science and Technology, 122, 1691 (1975).

[5] L.M. Ephrath, Journal of Electronic Materials, 4, 1207 (1975).

[6] P.H. Fang, L. Ephrath and W.B. Nowak, Applied Physic Letters, 25, 150 (1974).

[7] Terunori Warabisako and Tadashi Saitah, IEEE Transactions on Electron Devices, April 1977.

[8] J.D. Zook, R.B. Maciolek and J.D. Heaps, Jet Propulsion Laboratory, Contract No. 954356 and is part of the ERDA Low cost Silicon Solar array program.

[9] H.C. Theuerer, Purification of Silicon Bell Laboratories, Record, 327, Sept. (1955).

[10] T.L. Chu, H.C. Mollenkopf, and Shirley S. Chu, J. Electrochem. Soc: Solid State Science and Technology, 123, 106 (1976).

[11] T.I. Kamins, Journal of Applied Physics, 42, 4357 (1971).

[12] T.I. Kamins, J. Electrochem. Soc. Solid State Science and Technology, 127, 686 (1980).

[13] John Y.W. Seto, J. Appl. Phys. 46, 5247 (1975).

[14] American National Standard ANSI/ASTM, F76-F73, 349 (1975).

[15] R.J. Gieske and J.J. McMullen, Chemical Vapour Deposition, Proceedings of the Sixth International Conferences, p. 183, 1977.

[16] Roger E. Lagar, Michael T. Wauk and Richard S. Rosier, Chemical Vapour Deposition. Proceedings of the Sixth International Conference, p. 195, 1977.

[17] H.C. Theurer, J. Electrochem. Soc., 108, 649 (1961).

[18] G.W. Cullen, J.E. Corboy and R.T. Smith, J. of Crystal Growth, 31, 274, (1975).

[19] H. Splittgerber, M. Druminski, J. Herbst and C.H. Raetzel, Semiconductor Silicon; Proceeding of the Third International Symposium on Silicon Material Science and Technology, p. 256, 1977.

[20] J.P. Hirth and G.M. Pound, "Condensation and Evaporation", Progress in Material Science, Vol. 11B, Chalmers Editor, MacMillan, New York, 1963.

[21] C.F. Powell, J.H. Oxley and J.M. Blocker, Jr., Vapor Deposition, John Wiley and Sons, Inc., New York, 1966.

[22] B.A. Joyce and R.R. Bradley, J. Electrochem. Soc., 110, 1235 (1963).

[23] W.H. Shepherd, J. Electrochem. Soc., 112, 988, 1965.

[24] ASTM Card. No. 5-0565.

[25] F.M. Collins, Trans. Eight National Vacum Symposium, Vol. 2, 899 1961.

[26] Y. Katooka, J. Phys. Soc. Japan, 17, 967, (1962).

[27] O.A. Augen and K.M. Watson, Chemical Process Principle, John Wiley and Sons, Inc. New York p. 815-822, 1947.

[28] J.M. Smith, Chemical Engineering Kinetics, McGraw-Hill Book Company, Inc. New York, pp. 71-77, 1956.

[29] E.H. Hall, Amer. J. Math., 2, 287 (1897).

[30] E.H. Hall, The Hall Effect, Science, Vol. 5, p. 249, (1885).

[31] T.S. Hutchison and D.C. Baird, The Physics of Engineering Solids, John Wiley and Sons, Inc. New York, London, Sydney, p. 376, (1968).

[32] Shyh Wang, Solid State Electronics, McGraw-Hill Book Compnay, Inc. New York, p. 152-155, 243 (1966).

[33] R.H. Putley, The Hall Effect and Related Phenomena, Butterworth & Co. (Publishers) Ltd., p. 1-4, 23-64 (1960).

[34] R.B. Adler, A.C. Smith, R.L. Longini, Introduction to Semiconductor Physics, John Wiley & Sons, Inc., p. 55-57 (1964).

[35] A.L. Fripp, R.L. Stermer and A. Cotlin, J. Electrochem. Soc., Solid State Science, 117, 1569 (1970).

[36] E.S. Yong, Fundamentals of Semiconductor Devices, McGraw-Hill Book Company, p. 60 (1978).

[37] P.R. Choudhury and E.I. Salkowitz, J. Crystal Growth, 7, 361 (1970).

[38] M.E. Cowher and T.O. Sedgwick, J. Electrochem. Soc.; Solid State Science and Technology, 119, 1565 (1972).

[39] F.A. Trumbore, Bell Systems Tech. J., 39, 210 (1960).

[40] M.M. Mandurok, K.C. Saraswat and T.I. Kamis, J. Electrochem. Soc.; Solid State Science and Technology, 126, 1010 (1979).

[41] Y. Matukura, J. of Phys. Soc. Japan, 17, 1405 (1962).

[42] Y. Matukura, J. Appl. Phys., 2, 91 (1963).

[43] Marchal and Owens, Phil. Mag., 24, 1281 (1962).

[44] S.M. Sze, Physics of Semiconductors Devices, John Wiley and Sons, New York, London (1969).

[45] R.G. Chambers, Proc. Phys. Soc., London Sect. A., 65, 903 (1952).

[46] N.F. Mott, and W.D. Twose, Adv. Phys., 10, 107 (1961).

[47] N.F. Mott, Phil. Mag., 19, 835 (1969).

# APPENDIX A

## X-RAY DIFFRACTION OF POLYSILICON ON FUSED SILICA

5-0565 MINOR CORRECTION

| d | 3.14 | 1.92 | 1.64 | 3.139 | Si |
|---|---|---|---|---|---|
| $I/I_1$ | 100 | 60 | 35 | 100 | Silicon |

Rad. $CuK\alpha_1$ λ 1.5405 Filter Ni
Dia. Cut off Coll.
$I/I_1$ G. C. Diffractometer d corr. abs.?
Ref. Swanson and Fuyat, NBS Circular 539, Vol. II (1953)

Sys. Cubic S.G. $O_h^7$ - Fd3m
$a_0$ 5.4301 $b_0$ $c_0$ A C
α β γ Z 8
Ref. Ibid.

εα nωβ εγ Sign
2V D 2.328 mp Color
Ref.

Sample from Johnson Matthey Co. Spect anal.: <0.001% Cu, Ag, Zn, Sn, Mg, Fe.
X-ray pattern at 26°C.

Replaces 1-0787, 1-0791, 2-0561, 3-0517, 3-0529, 3-0534, 3-0544, 3-0549

| d Å | $I/I_1$ | hkl | d Å | $I/I_1$ | hkl |
|---|---|---|---|---|---|
| 3.138 | 100 | 111 | | | |
| 1.920 | 60 | 220 | | | |
| 1.638 | 35 | 311 | | | |
| 1.357 | 8 | 400 | | | |
| 1.246 | 13 | 331 | | | |
| 1.1083 | 17 | 422 | | | |
| 1.0450 | 9 | 511 | | | |
| 0.9599 | 5 | 440 | | | |
| .9178 | 11 | 531 | | | |
| .8586 | 9 | 620 | | | |
| .8281 | 5 | 533 | | | |
| .7836 | | 444 | | | |

1953

**SILICON REFLECTION ANGLES θ**

| 2θ | hkl | d(Å) | λ | MoK | CuK | NiK | CoK | FeK | CrK | λ | WL |
|---|---|---|---|---|---|---|---|---|---|---|---|
| | | | $\beta_1$ | 5.787 | 12.827 | 13.840 | 14.979 | 16.267 | 19.418 | $\beta_2$ | 11.447 |
| | | | $\alpha_1$ | 6.494 | 14.221 | 15.330 | 16.575 | 17.983 | 21.415 | $\beta_1$ | 11.794 |
| 28.48 | 111 | 3.1353 7 | $\alpha$ | 6.508 | 14.233 | 15.342 | 16.588 | 17.996 | 21.428 | $\alpha_1$ | 13.617 |
| | | | $\alpha_2$ | 6.534 | 14 257 | 15.366 | 16.613 | 18.021 | 21.454 | $\alpha_2$ | 13.721 |
| | | | $\beta_1$ | 9.477 | 21.256 | 22.995 | 24.965 | 27.221 | 32.882 | $\beta_2$ | 18.911 |
| | | | $\alpha_1$ | 10.644 | 23.651 | 25.577 | 27.766 | 30.275 | 36.602 | $\beta_1$ | 19.499 |
| 47.3 | 220 | 1.9200 1 | $\alpha$ | 10.[illegible]66 | 23.672 | 25.598 | 27.788 | 30.298 | 36.626 | $\alpha_1$ | 22.610 |
| | | | $\alpha_2$ | 10 709 | 23.714 | 25 641 | 27 831 | 30 343 | 36.674 | $\alpha_2$ | 22.789 |
| | | | $\beta_1$ | 11.132 | 25.158 | 27.263 | 29.664 | 32.438 | 39.540 | $\beta_2$ | 22.336 |
| | | | $\alpha_1$ | 12 508 | 28.061 | 30.414 | 33.111 | 36.240 | 44.360 | $\beta_1$ | 23.042 |
| 56.13 | 311 | 1.6373 9 | $\alpha$ | 12.534 | 28.087 | 30.440 | 33.138 | 36.269 | 44.391 | $\alpha_1$ | 26.796 |
| | | | $\alpha_2$ | 12.585 | 28.137 | 30.492 | 33.192 | 36.326 | 44.456 | $\alpha_2$ | 27.013 |
| | | | $\beta_1$ | 13.465 | 30.845 | 33.535 | 36.647 | 40.308 | 50.156 | $\beta_2$ | 27.280 |
| | | | $\alpha_1$ | 15.142 | 34.565 | 37.629 | 41.210 | 45.478 | 57.482 | $\beta_1$ | 28.167 |
| 69.16 | 400 | 1.3576 6 | $\alpha$ | 15.173 | 34.598 | 37.663 | 41.246 | 45.518 | 57.533 | $\alpha_1$ | 32.937 |
| | | | $\alpha_2$ | 15.235 | 34.663 | 37.732 | 41.319 | 45.597 | 57.636 | $\alpha_2$ | 33.215 |
| | | | $\beta_1$ | 14.699 | 33.967 | 37.015 | 40.575 | 44.825 | 56.791 | $\beta_2$ | 29.965 |
| | | | $\alpha_1$ | 16.538 | 38.188 | 41.708 | 45.884 | 50.983 | 66.763 | $\beta_1$ | 30.957 |
| 76.42 | 331 | 1.2458 7 | $\alpha$ | 16.572 | 38.226 | 41.747 | 45.927 | 51.031 | 66.838 | $\alpha_1$ | 36.334 |
| | | | $\alpha_2$ | 16.640 | 38.300 | 41.826 | 46.013 | 51.127 | 66.992 | $\alpha_2$ | 36.650 |
| | | | $\beta_1$ | 16.569 | 38.898 | 42.580 | 46.973 | 52.400 | 70.110 | $\beta_2$ | 34.149 |
| | | | $\alpha_1$ | 18.658 | 44.015 | 48.397 | 53.793 | 60.835 | | $\beta_1$ | 35.319 |
| 88.05 | 422 | 1.1085 2 | $\alpha$ | 18.697 | 44.062 | 48.447 | 53.850 | 60.906 | | $\alpha_1$ | 41.752 |
| | | | $\alpha_2$ | 18 774 | 44 153 | 48.547 | 53.963 | 61.045 | | $\alpha_2$ | 42.135 |
| | | | $\beta_1$ | 17 606 | 41 762 | 45.861 | 50.839 | 57.177 | 85.859 | $\beta_2$ | 36.541 |
| | | | $\alpha_1$ | 19.836 | 47.476 | 52.479 | 58.852 | 67.849 | | $\beta_1$ | 37.822 |
| | 511-333 | 1.0451 2 | $\alpha$ | 19.877 | 47.529 | 52.536 | 58.921 | 67.946 | | $\alpha_1$ | 44.935 |
| | | | $\alpha_2$ | 19.960 | 47.632 | 52.652 | 59.059 | 68.137 | | $\alpha_2$ | 45.364 |
| | | | $\beta_1$ | 19.226 | 46.476 | 51.378 | 57.578 | 66.186 | | $\beta_2$ | 40.406 |
| | | | $\alpha_1$ | 21.679 | 53.354 | 59.706 | 68.703 | | | $\beta_1$ | 41.880 |
| | 440 | .9600 1 | $\alpha$ | 21.725 | 53.419 | 58.781 | 68.810 | | | $\alpha_1$ | 50.257 |
| | | | $\alpha_2$ | 21.816 | 53.546 | 59.934 | 69.025 | | | $\alpha_2$ | 50.775 |
| | | | $\beta_1$ | 20.144 | 49.315 | 54.794 | 61.980 | 73.094 | | $\beta_1$ | 42.680 |
| | | | $\alpha_1$ | 22.726 | 57.046 | 64.557 | 77.010 | | | $\beta_1$ | 44.280 |
| | 531 | .9179 4 | $\alpha$ | 22.775 | 57.120 | 64.650 | 77.191 | | | $\alpha_1$ | 53.529 |
| | | | $\alpha_2$ | 22 871 | 57.267 | 64.838 | 77.561 | | | $\alpha_2$ | 54.113 |
| | | | $\beta_1$ | 21.602 | 54.161 | 60.868 | 70.693 | | | $\beta_2$ | 46.444 |
| | | | $\alpha_1$ | 24.394 | 63.772 | 74.876 | | | | $\beta_1$ | 48.277 |
| | 620 | .8586 6 | $\alpha$ | 24.447 | 63.870 | 75.039 | | | | $\alpha_1$ | 59.281 |
| | | | $\alpha_2$ | 24.551 | 64.063 | 75.376 | | | | $\alpha_2$ | 60.010 |

| hkl | d(Å) | λ | MoK | CuK | NiK | CoK | FeK | CrK | λ | WL |
|---|---|---|---|---|---|---|---|---|---|---|
| | | $\beta_1$ | 22.440 | 57.195 | 64.913 | 78.100 | | | $\beta_2$ | 48.711 |
| | | $\alpha_1$ | 25.354 | 68.446 | | | | | $\beta_1$ | 50.701 |
| 533 | .8281 6 | $\alpha$ | 25.409 | 68.569 | | | | | $\alpha_1$ | 63.042 |
| | | $\alpha_2$ | 25.518 | 68.811 | | | | | $\alpha_2$ | 63.896 |
| | | $\beta_1$ | 23.785 | 62.628 | 73.112 | | | | $\beta_2$ | 52.549 |
| | | $\alpha_1$ | 26.899 | 79 314 | | | | | $\beta_1$ | 54.846 |
| 444 | .7838 4 | $\alpha$ | 26.958 | 79.573 | | | | | $\alpha_1$ | 70:344 |
| | | $\alpha_2$ | 27.075 | 80.100 | | | | | $\alpha_2$ | 71.582 |
| | | $\beta_1$ | 24.564 | 66.259 | 80.514 | | | | $\beta_2$ | 54.915 |
| | | $\alpha_1$ | 27.798 | | | | | | $\beta_1$ | 57.434 |
| 711- | .7604 4 | $\alpha$ | 27.859 | | | | | | $\alpha_1$ | 76.100 |
| 551 | | $\alpha_2$ | 27.980 | | | | | | $\alpha_2$ | 77.952 |
| | | $\beta_1$ | 25.824 | 73.576 | | | | | $\beta_2$ | 59 035 |
| | | $\alpha_1$ | 29.254 | | | | | | $\beta_1$ | 62.021 |
| 642 | .7257 0 | $\alpha$ | 29.319 | | | | | | $\alpha_1$ | |
| | | $\alpha_2$ | 29.447 | | | | | | $\alpha_2$ | |
| | | $\beta_1$ | 26.560 | 79.916 | | | | | $\beta_2$ | 61.660 |
| | | $\alpha_1$ | 30.106 | | | | | | $\beta_1$ | 65.021 |
| 731- | .7070 1 | $\alpha$ | 30.173 | | | | | | $\alpha_1$ | |
| 553 | | $\alpha_2$ | 30.306 | | | | | | $\alpha_2$ | |
| | | $\beta_1$ | 27.755 | | | | | | $\beta_2$ | 66.446 |
| | | $\alpha_1$ | 31.494 | | | | | | $\beta_1$ | 70.750 |
| 800 | .6788 3 | $\alpha$ | 31.566 | | | | | | $\alpha_1$ | |
| | | $\alpha_2$ | 31.706 | | | | | | $\alpha_2$ | |
| | | $\beta_1$ | 28.456 | | | | | | $\beta_2$ | 69.705 |
| | | $\alpha_1$ | 32.311 | | | | | | $\beta_1$ | 75.009 |
| 733 | .6634 6 | $\alpha$ | 32.385 | | | | | | $\alpha_1$ | |
| | | $\alpha_2$ | 32.530 | | | | | | $\alpha_2$ | |
| | | $\beta_1$ | 29.600 | | | | | | $\beta_2$ | 76.480 |
| | | $\alpha_1$ | 33.649 | | | | | | $\beta_1$ | |
| 822- | .6400 1 | $\alpha$ | 33.727 | | | | | | $\alpha_1$ | |
| 660 | | $\alpha_2$ | 33.880 | | | | | | $\alpha_2$ | |
| | | $\beta_1$ | 30.273 | | | | | | $\beta_2$ | 82.903 |
| | | $\alpha_1$ | 34.439 | | | | | | $\beta_1$ | |
| 751 - | .6270 7 | $\alpha$ | 34.519 | | | | | | $\alpha_1$ | |
| 555 | | $\alpha_2$ | 34.677 | | | | | | $\alpha_2$ | |
| | | $\beta_1$ | 31.377 | | | | | | $\beta_2$ | |
| | | $\alpha_1$ | 35.738 | | | | | | $\beta_1$ | |
| 840 | .6071 6 | $\alpha$ | 35.822 | | | | | | $\alpha_1$ | |
| | | $\alpha_2$ | 35.987 | | | | | | $\alpha_2$ | |
| | | $\beta_1$ | 32.028 | | | | | | $\beta_2$ | |
| | | $\alpha_1$ | 36.508 | | | | | | $\beta_1$ | |
| 911- | .5960 9 | $\alpha$ | 36.594 | | | | | | $\alpha_1$ | |
| [illegible] | | [illegible] | [illegible] | | | | | | [illegible] | |

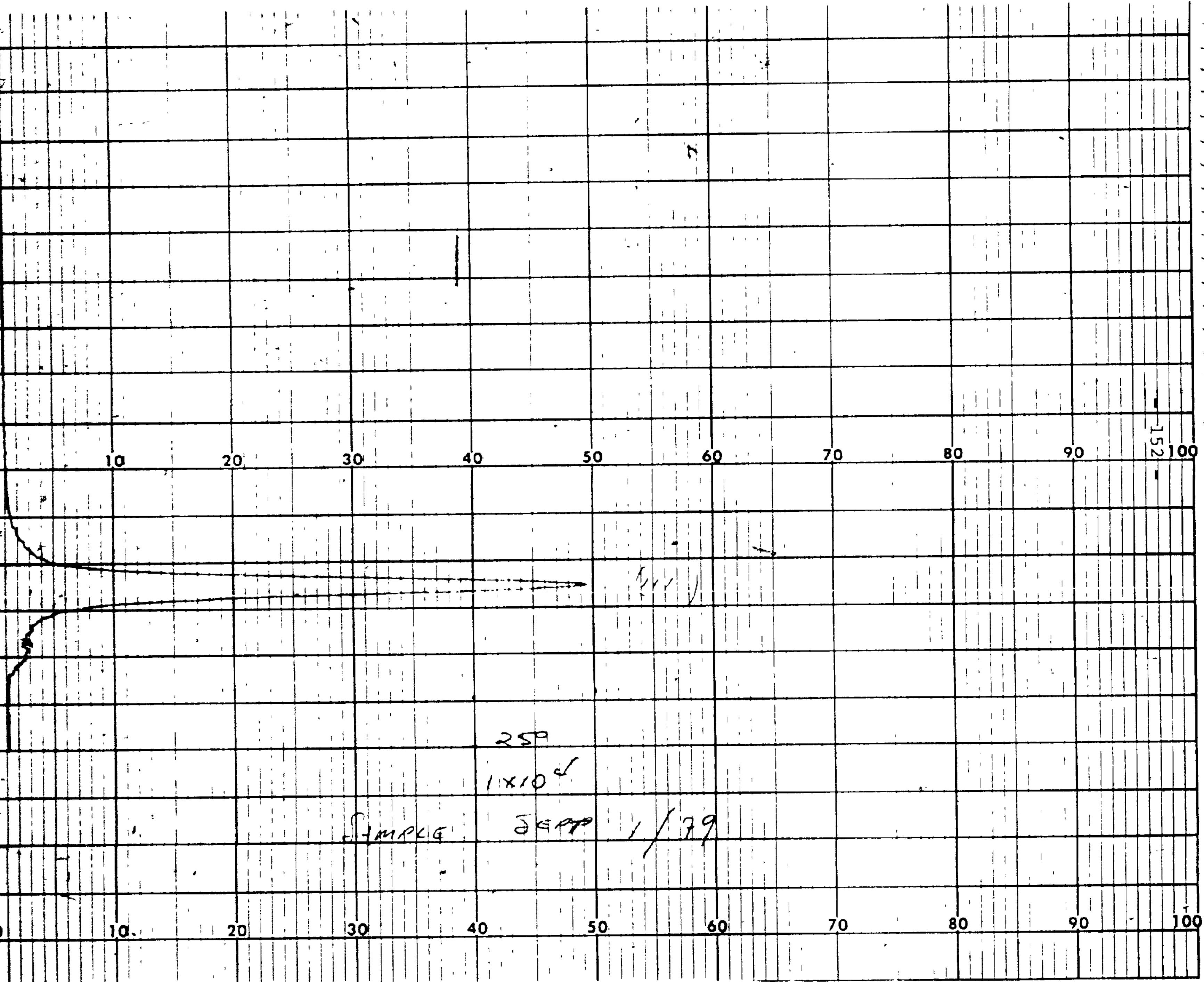

0
10
20
30
40
50
60
70
80
90
100
CHART NO. 4920/00
MADE IN CANADA

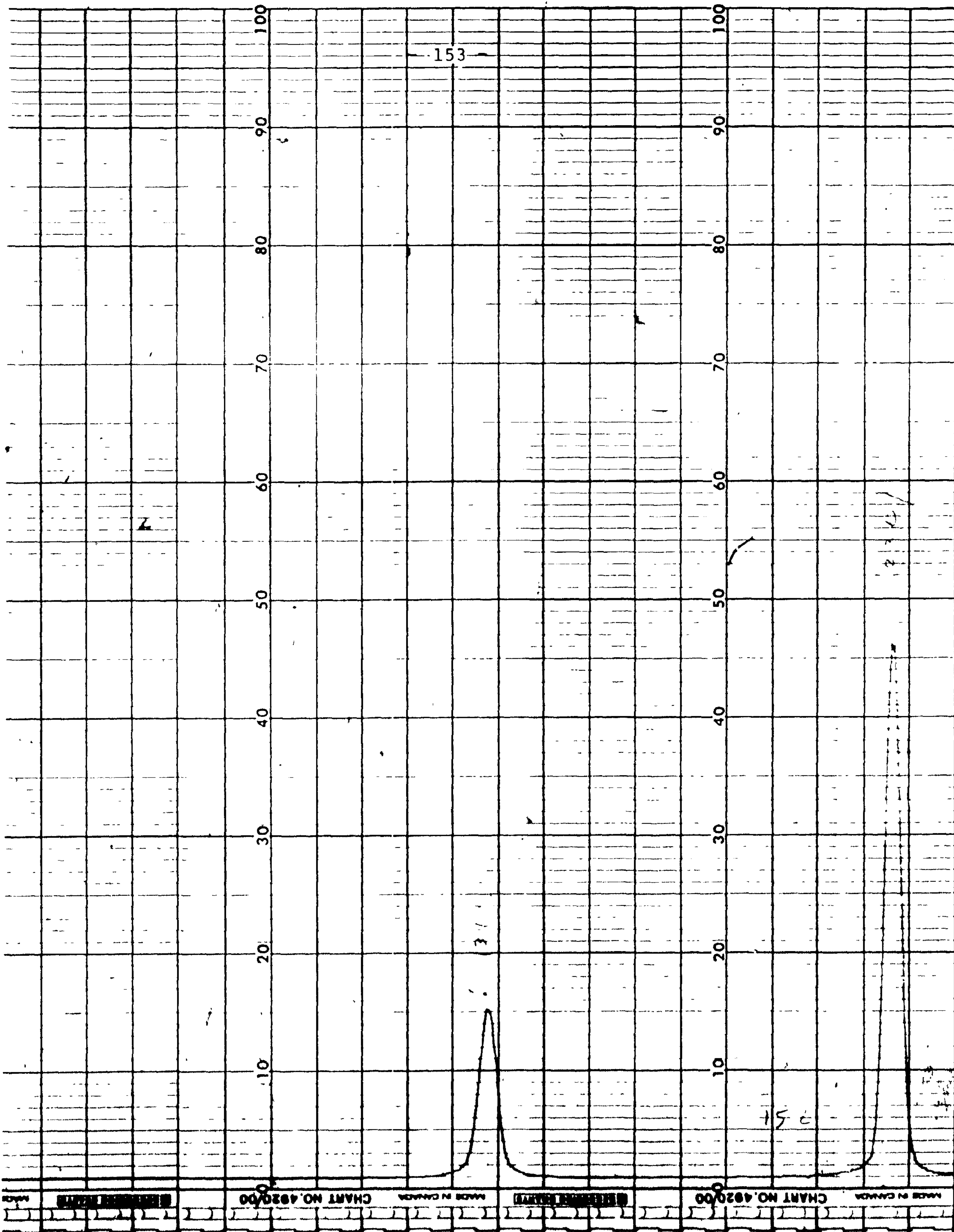

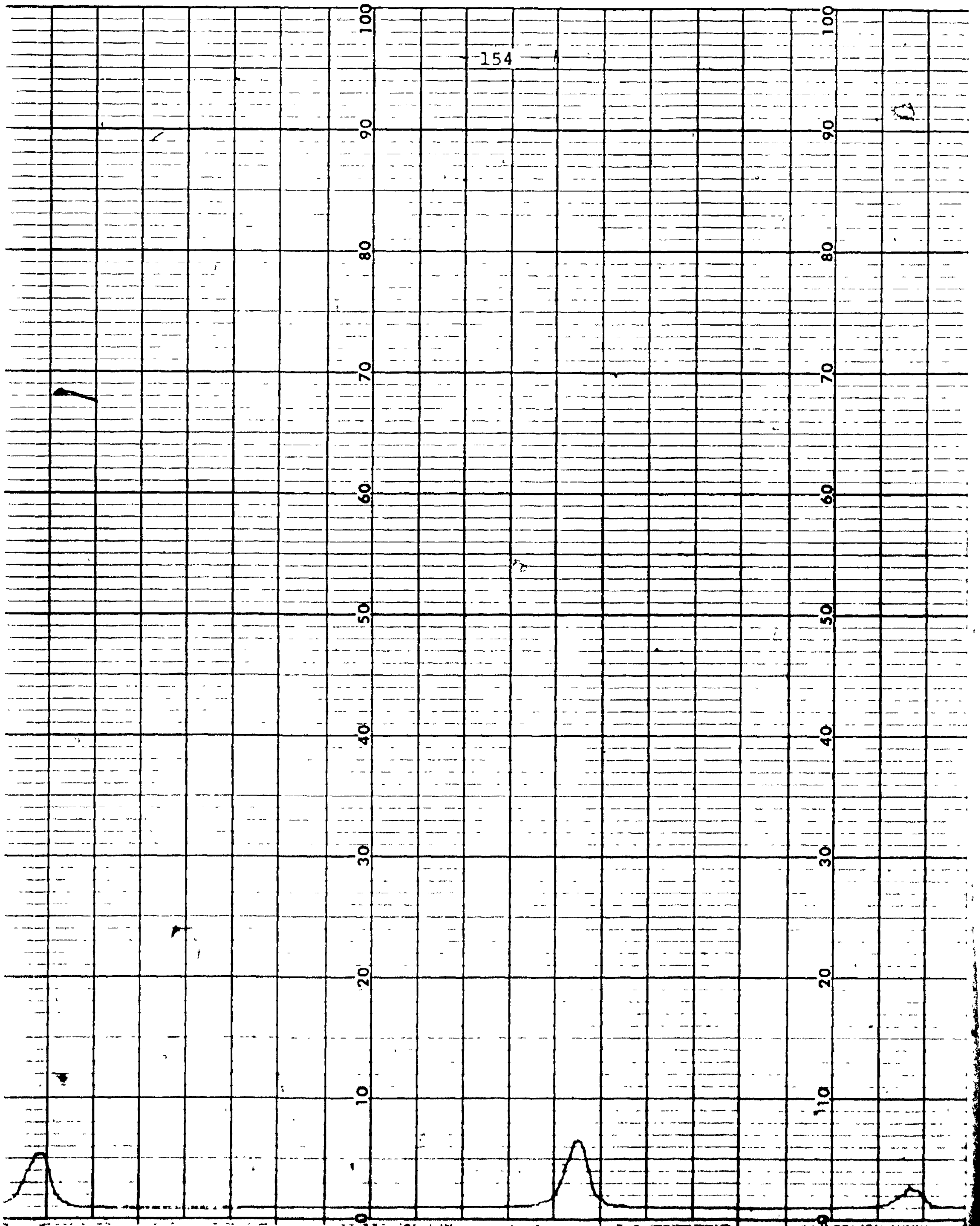
154
100
90
80
70
60
50
40
30
20
10
0
100
90
80
70
60
50
40
30
20
10
0

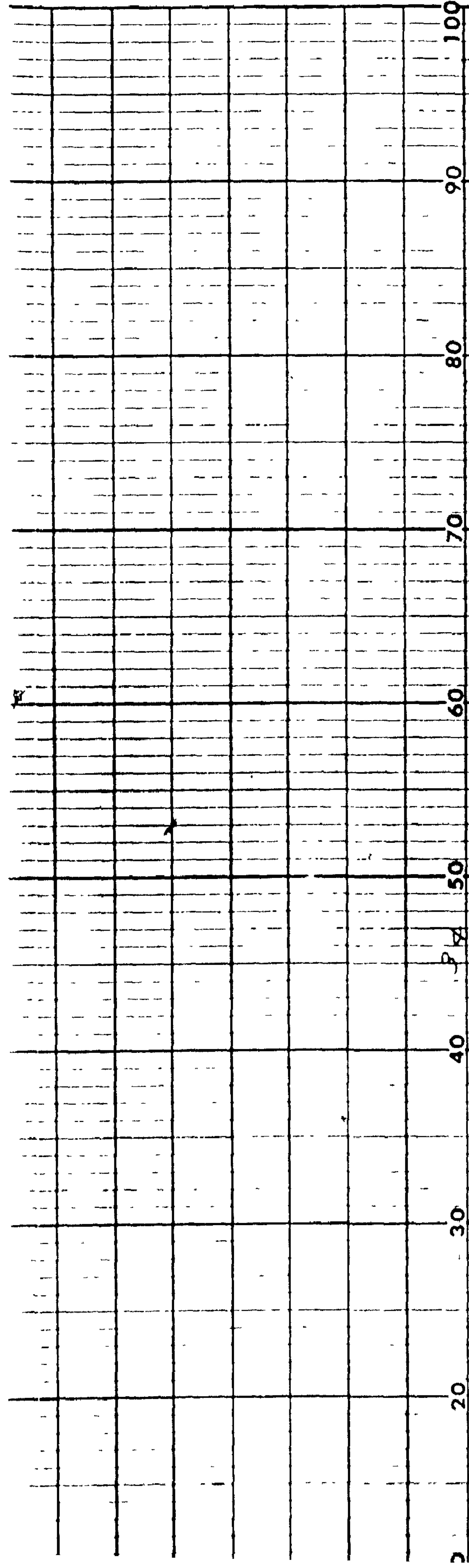

100 90 80 70 60 50 40 30 20

100 90 80 70 60 50 40 30 20 0

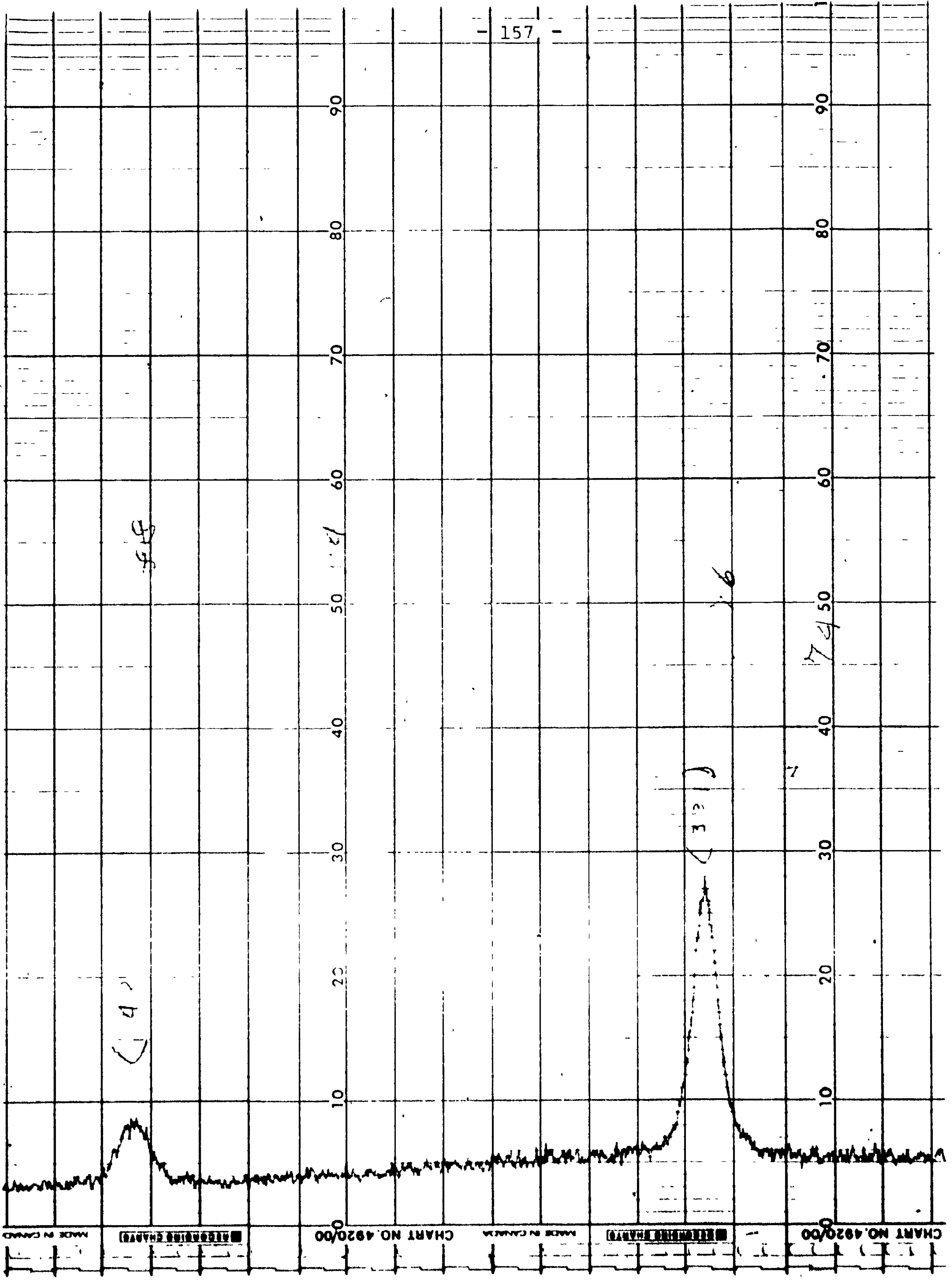

# APPENDIX B

## X-RAY DIFFRACTION OF POLYSILICON ON GRAPHITE

5-0565 MINOR CORRECTION

| d | 3.14 | 1.92 | 1.64 | 3.135 | Si |
|---|---|---|---|---|---|
| $I/I_1$ | 100 | 60 | 35 | 100 | SILICON |

Rad. $CuK\alpha_1$ λ 1.5405 Filter Ni
Dia. Cut off Coll.
$I/I_1$ G. C. DIFFRACTOMETER d corr. abs.?
Ref. SWANSON AND FUYAT, NBS CIRCULAR 539, VOL. II (1953)

Sys. CUBIC S.G. $O_h^7$ - Fd3m
$a_0$ 5.4301 $b_0$ $c_0$ A C
α β γ Z 8
Ref. IBID.

εα nωβ εγ Sign
2V D 2.328 mp Color
Ref.

SAMPLE FROM JOHNSON MATTHEY CO. SPECT ANAL.: <0.001% Cu, Ag, Zn, Sn, Mn, Fe.
X-RAY PATTERN AT 26°C.

REPLACES 1-0787, 1-0791, 2-0561, 3-0517, 3-0529, 3-0534, 3-0544, 3-0549

| d Å | $I/I_1$ | hkl | d Å | $I/I_1$ | hkl |
|---|---|---|---|---|---|
| 3.135 | 100 | 111 | | | |
| 1.920 | 60 | 220 | | | |
| 1.638 | 35 | 311 | | | |
| 1.357 | 8 | 400 | | | |
| 1.246 | 13 | 331 | | | |
| 1.1083 | 17 | 422 | | | |
| 1.0450 | 9 | 511 | | | |
| 0.9599 | 5 | 440 | | | |
| .9178 | 11 | 531 | | | |
| .8580 | 9 | 620 | | | |
| .8281 | 5 | 533 | | | |
| .7836 | | 444 | | | |

1955

## SILICON REFLECTION ANGLES θ

| 2θ (handwritten) | hkl | d(Å) | λ | MoK | CuK | NiK | CoK | FeK | CrK | λ | WL |
|---|---|---|---|---|---|---|---|---|---|---|---|
| | | | $\beta_1$ | 5.787 | 12.827 | 13.840 | 14.979 | 16.267 | 19.418 | $\beta_2$ | 11.447 |
| | | | $\alpha_1$ | 6.491 | 14 221 | 15.330 | 16.575 | 17 983 | 21.415 | $\beta_1$ | 11.794 |
| 28.48 | 111 | 3.1353 7 | $\alpha$ | 6.508 | 14.233 | 15.342 | 16.588 | 17.996 | 21.428 | $\alpha_1$ | 13.617 |
| | | | $\alpha_2$ | 6.534 | 14 257 | 15.366 | 16.613 | 18.021 | 21.454 | $\alpha_2$ | 13.721 |
| | | | $\beta_1$ | 9.477 | 21.256 | 22.995 | 24.965 | 27.221 | 32.862 | $\beta_2$ | 18.911 |
| | | | $\alpha_1$ | 10.644 | 23 651 | 25.577 | 27.766 | 30.275 | 36.602 | $\beta_1$ | 19.499 |
| 47.3 | 220 | 1 9200 1 | $\alpha$ | 10.666 | 23.672 | 25 598 | 27.788 | 30.298 | 36.626 | $\alpha_1$ | 22.610 |
| | | | $\alpha_2$ | 10 709 | 23.714 | 25 641 | 27.831 | 30.343 | 36.674 | $\alpha_2$ | 22.789 |
| | | | $\beta_1$ | 11.132 | 25.158 | 27.263 | 29.664 | 32.438 | 39.540 | $\beta_2$ | 22.336 |
| | | | $\alpha_1$ | 12 508 | 28.061 | 30.414 | 33 111 | 36.240 | 44.360 | $\beta_1$ | 23.042 |
| 56.13 | 311 | 1.6373 9 | $\alpha$ | 12.534 | 28.087 | 30.440 | 33.138 | 36.269 | 44.391 | $\alpha_1$ | 26.796 |
| | | | $\alpha_2$ | 12.585 | 28.137 | 30.492 | 33.192 | 36.326 | 44.456 | $\alpha_2$ | 27.013 |
| | | | $\beta_1$ | 13.465 | 30.845 | 33.535 | 36.647 | 40.308 | 50.156 | $\beta_2$ | 27.280 |
| | | | $\alpha_1$ | 15.142 | 34.565 | 37.629 | 41.210 | 45.478 | 57.482 | $\beta_1$ | 28.167 |
| 69.16 | 400 | 1.3576 6 | $\alpha$ | 15.173 | 34.598 | 37.663 | 41.246 | 45 518 | 57.533 | $\alpha_1$ | 32.937 |
| | | | $\alpha_2$ | 15.235 | 34.663 | 37.732 | 41.319 | 45.597 | 57.636 | $\alpha_2$ | 33.215 |
| | | | $\beta_1$ | 14.699 | 33.967 | 37.015 | 40.575 | 44.825 | 56.791 | $\beta_2$ | 29.965 |
| | | | $\alpha_1$ | 16.538 | 38.188 | 41.708 | 45.884 | 50.983 | 66.763 | $\beta_1$ | 30.957 |
| 76.42 | 331 | 1.2458 7 | $\alpha$ | 16.572 | 38.226 | 41.747 | 45.927 | 51.031 | 66.838 | $\alpha_1$ | 36.334 |
| | | | $\alpha_2$ | 16.640 | 38.300 | 41.826 | 46.013 | 51.127 | 66.992 | $\alpha_2$ | 36.650 |
| | | | $\beta_1$ | 16.569 | 38.898 | 42.580 | 46.973 | 52.400 | 70.110 | $\beta_2$ | 34.149 |
| | | | $\alpha_1$ | 18.658 | 44 015 | 48.397 | 53.793 | 60.835 | | $\beta_1$ | 35.319 |
| 88.03 | 422 | 1.1085 2 | $\alpha$ | 18.697 | 44.062 | 48.447 | 53.850 | 60.906 | | $\alpha_1$ | 41.752 |
| | | | $\alpha_2$ | 18.774 | 44.153 | 48.547 | 53.963 | 61.045 | | $\alpha_2$ | 42.135 |
| | | | $\beta_1$ | 17.606 | 41.762 | 45.861 | 50.839 | 57.177 | 85.859 | $\beta_2$ | 36.541 |
| | | | $\alpha_1$ | 19.835 | 47.476 | 52.479 | 58.852 | 67.849 | | $\beta_1$ | 37.822 |
| | 511-333 | 1.0451 2 | $\alpha$ | 19.877 | 47.529 | 52.536 | 58.921 | 67.946 | | $\alpha_1$ | 44.935 |
| | | | $\alpha_2$ | 19.960 | 47.632 | 52.652 | 59.059 | 68.137 | | $\alpha_2$ | 45.364 |
| | | | $\beta_1$ | 19.226 | 46.476 | 51.378 | 57.578 | 66.186 | | $\beta_2$ | 40.406 |
| | | | $\alpha_1$ | 21.679 | 53.354 | 59.706 | 68.703 | | | $\beta_1$ | 41.880 |
| | 440 | .9600 1 | $\alpha$ | 21.725 | 53.419 | 58.781 | 68.810 | | | $\alpha_1$ | 50.257 |
| | | | $\alpha_2$ | 21.816 | 53.546 | 59.934 | 69.025 | | | $\alpha_2$ | 50.775 |
| | | | $\beta_1$ | 20 144 | 49.315 | 54.794 | 61.980 | 73.094 | | $\beta_1$ | 42.680 |
| | | | $\alpha_1$ | 22.726 | 57.046 | 64.557 | 77.010 | | | $\beta_1$ | 44.280 |
| | 531 | .9179 4 | $\alpha$ | 22.775 | 57.120 | 64.650 | 77.191 | | | $\alpha_1$ | 53.529 |
| | | | $\alpha_2$ | 22.871 | 57.267 | 64.838 | 77.561 | | | $\alpha_2$ | 54.113 |
| | | | $\beta_1$ | 21.602 | 54.161 | 60.868 | 70.693 | | | $\beta_2$ | 46.444 |
| | | | $\alpha_1$ | 24.394 | 63.772 | 74.876 | | | | $\beta_1$ | 48.277 |
| | 620 | .8586 6 | $\alpha$ | 24.447 | 63.870 | 75.039 | | | | $\alpha_1$ | 59.281 |
| | | | $\alpha_2$ | 24.551 | 64.063 | 75.376 | | | | $\alpha_2$ | 60.010 |

| hkl | d(Å) | λ | MoK | CuK | NiK | CoK | FeK | CrK | λ | WL |
|---|---|---|---|---|---|---|---|---|---|---|
| | | $\beta_1$ | 22.440 | 57.195 | 64.913 | 78.100 | | | $\beta_2$ | 48.711 |
| | | $\alpha_1$ | 25.354 | 68.446 | | | | | $\beta_1$ | 50.701 |
| 533 | .8281 6 | $\alpha$ | 25.409 | 68.569 | | | | | $\alpha_1$ | 63.042 |
| | | $\alpha_2$ | 25.518 | 68.811 | | | | | $\alpha_2$ | 63.896 |
| | | $\beta_1$ | 23.785 | 62.628 | 73.112 | | | | $\beta_2$ | 52.549 |
| | | $\alpha_1$ | 26.899 | 79 314 | | | | | $\beta_1$ | 54.846 |
| 444 | .7838 4 | $\alpha$ | 26.958 | 79.573 | | | | | $\alpha_1$ | 70.344 |
| | | $\alpha_2$ | 27.075 | 80.100 | | | | | $\alpha_2$ | 71.582 |
| | | $\beta_1$ | 24.564 | 66.259 | 80.514 | | | | $\beta_2$ | 54.915 |
| | | $\alpha_1$ | 27.798 | | | | | | $\beta_1$ | 57.434 |
| 711- | .7604 4 | $\alpha$ | 27.859 | | | | | | $\alpha_1$ | 76.100 |
| 551 | | $\alpha_2$ | 27.980 | | | | | | $\alpha_2$ | 77.952 |
| | | $\beta_1$ | 25.824 | 73.576 | | | | | $\beta_2$ | 59 035 |
| | | $\alpha_1$ | 29.254 | | | | | | $\beta_1$ | 62.021 |
| 642 | .7257 0 | $\alpha$ | 29.319 | | | | | | $\alpha_1$ | |
| | | $\alpha_2$ | 29.447 | | | | | | $\alpha_2$ | |
| | | $\beta_1$ | 26.560 | 79.916 | | | | | $\beta_2$ | 61.660 |
| | | $\alpha_1$ | 30.106 | | | | | | $\beta_1$ | 65.021 |
| 731- | .7070 1 | $\alpha$ | 30.173 | | | | | | $\alpha_1$ | |
| 553 | | $\alpha_2$ | 30.306 | | | | | | $\alpha_2$ | |
| | | $\beta_1$ | 27.755 | | | | | | $\beta_2$ | 66.446 |
| | | $\alpha_1$ | 31.494 | | | | | | $\beta_1$ | 70.750 |
| 800 | .6788 3 | $\alpha$ | 31.566 | | | | | | $\alpha_1$ | |
| | | $\alpha_2$ | 31.706 | | | | | | $\alpha_2$ | |
| | | $\beta_1$ | 28.456 | | | | | | $\beta_2$ | 69.705 |
| | | $\alpha_1$ | 32.311 | | | | | | $\beta_1$ | 75.009 |
| 733 | .6634 6 | $\alpha$ | 32.385 | | | | | | $\alpha_1$ | |
| | | $\alpha_2$ | 32.530 | | | | | | $\alpha_2$ | |
| | | $\beta_1$ | 29.600 | | | | | | $\beta_2$ | 76.480 |
| | | $\alpha_1$ | 33.649 | | | | | | $\beta_1$ | |
| 822- | .6400 1 | $\alpha$ | 33.727 | | | | | | $\alpha_1$ | |
| 660 | | $\alpha_2$ | 33.880 | | | | | | $\alpha_2$ | |
| | | $\beta_1$ | 30.273 | | | | | | $\beta_2$ | 82.903 |
| | | $\alpha_1$ | 34.439 | | | | | | $\beta_1$ | |
| 751 - | .6270 7 | $\alpha$ | 34.519 | | | | | | $\alpha_1$ | |
| 555 | | $\alpha_2$ | 34.677 | | | | | | $\alpha_2$ | |
| | | $\beta_1$ | 31.377 | | | | | | $\beta_2$ | |
| | | $\alpha_1$ | 35.738 | | | | | | $\beta_1$ | |
| 840 | .6071 6 | $\alpha$ | 35.822 | | | | | | $\alpha_1$ | |
| | | $\alpha_2$ | 35.987 | | | | | | $\alpha_2$ | |
| | | $\beta_1$ | 32.028 | | | | | | $\beta_2$ | |
| | | $\alpha_1$ | 36.508 | | | | | | $\beta_1$ | |
| 911- | .5960 9 | $\alpha$ | 36.594 | | | | | | $\alpha_1$ | |
| 753 | | [illegible] | 36.76[illegible] | | | | | | [illegible] | |

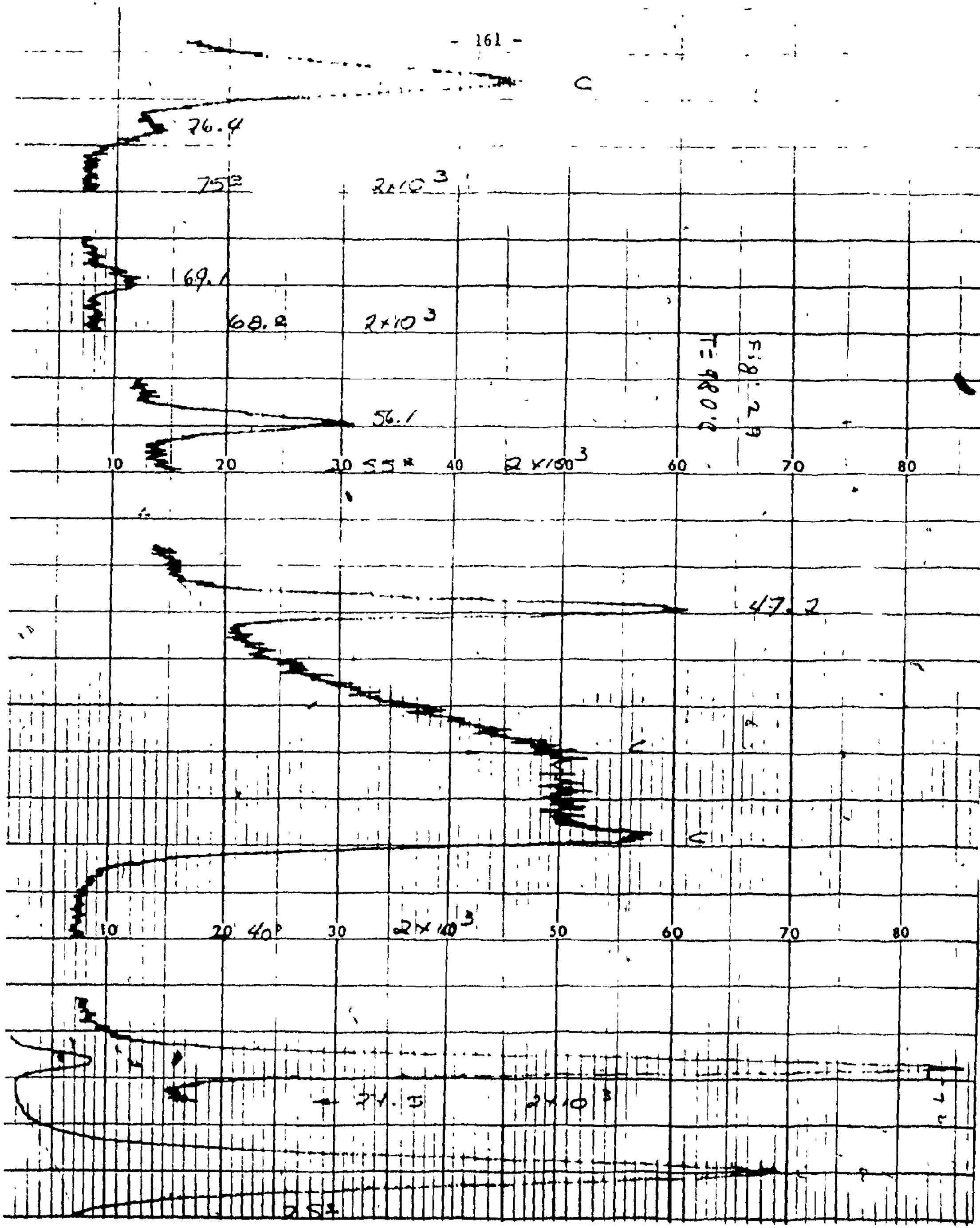

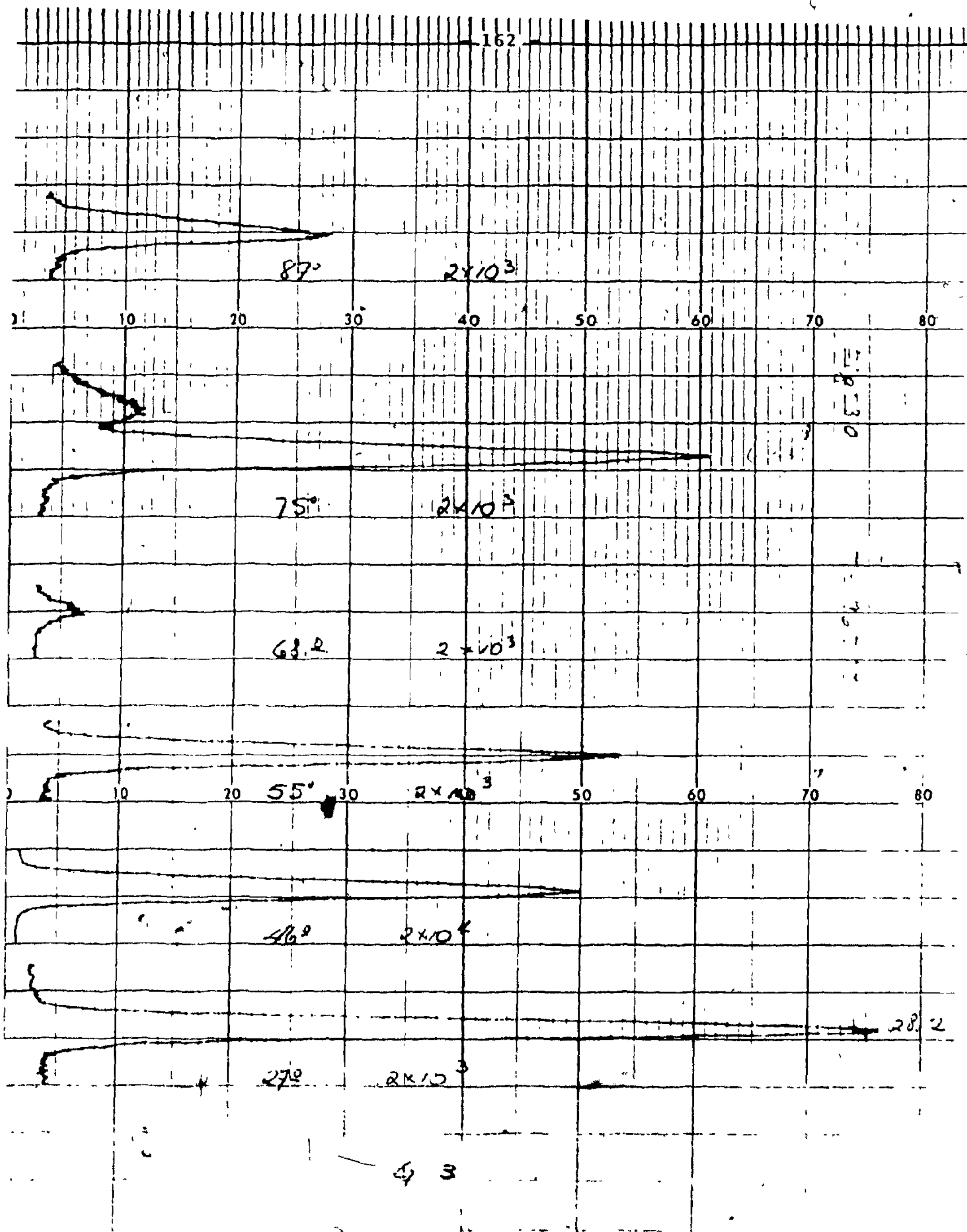

162
87°
2×10³
75°
2×10³
63.2
2×10³
55°
46°
2×10⁴
27°
2×10³
28.2

Fig 31 T= 954 C

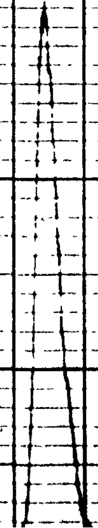

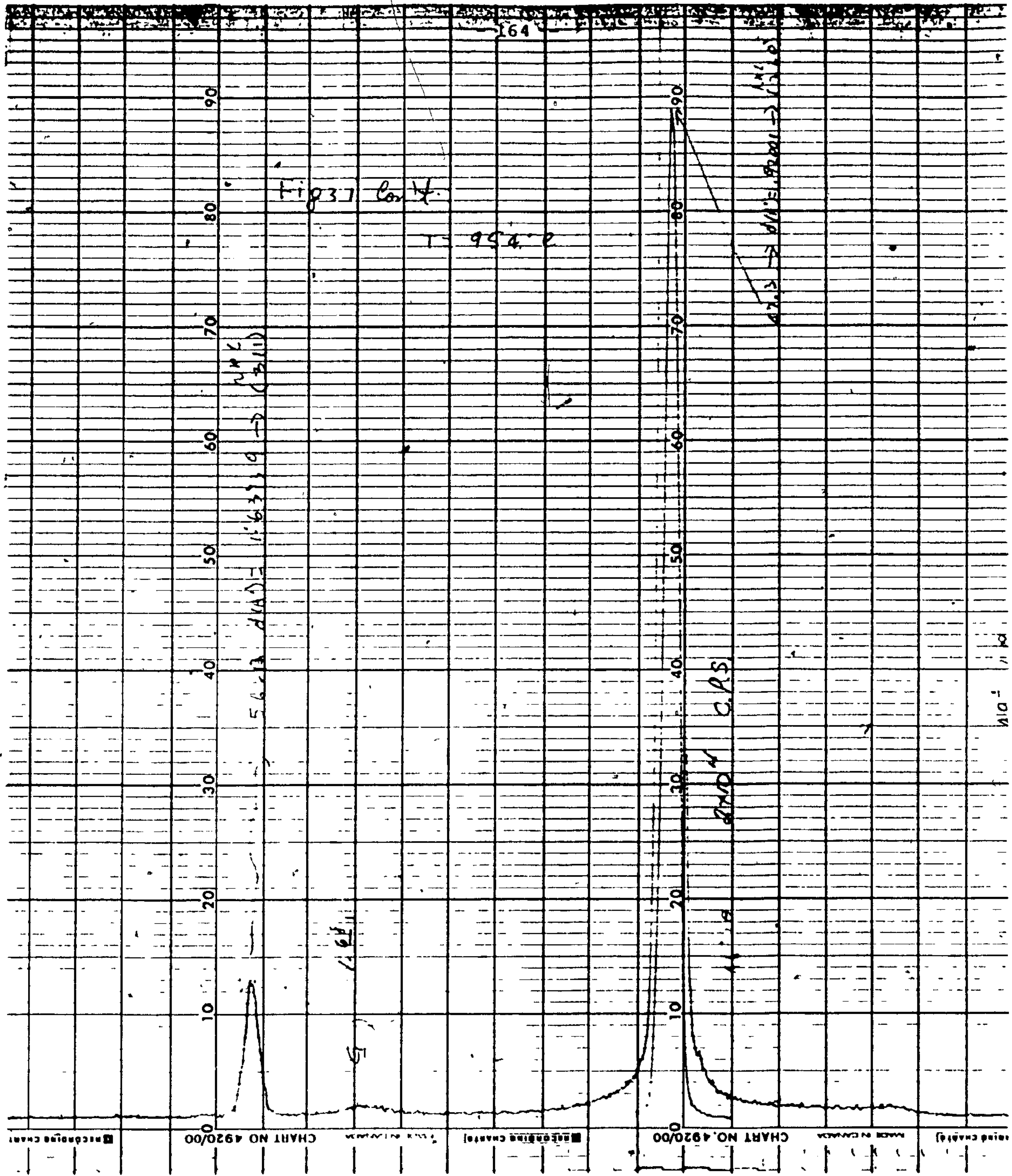

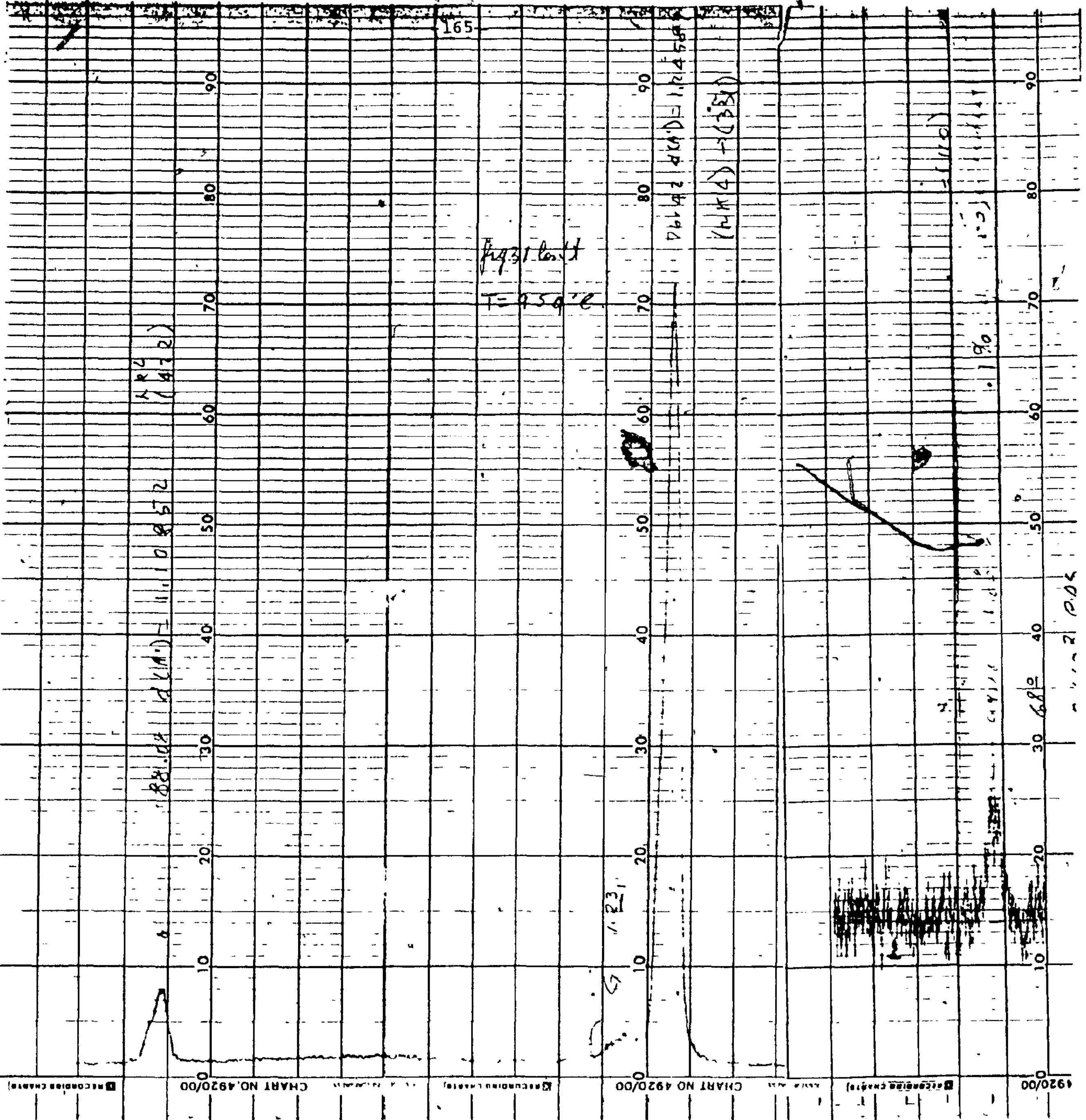

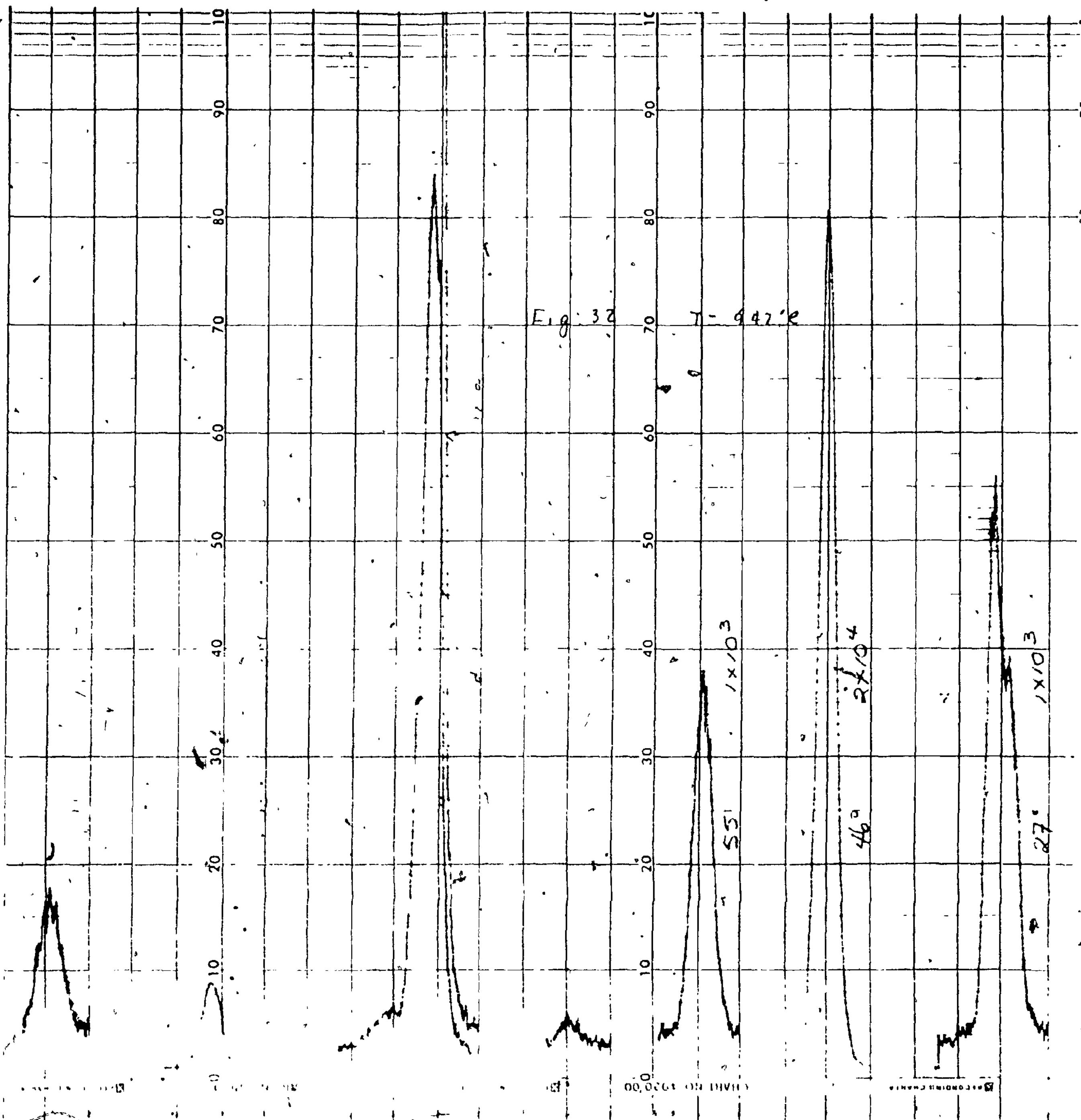

Fig. 32
1×10³
55'
2×10⁴
46°
1×10³
27°

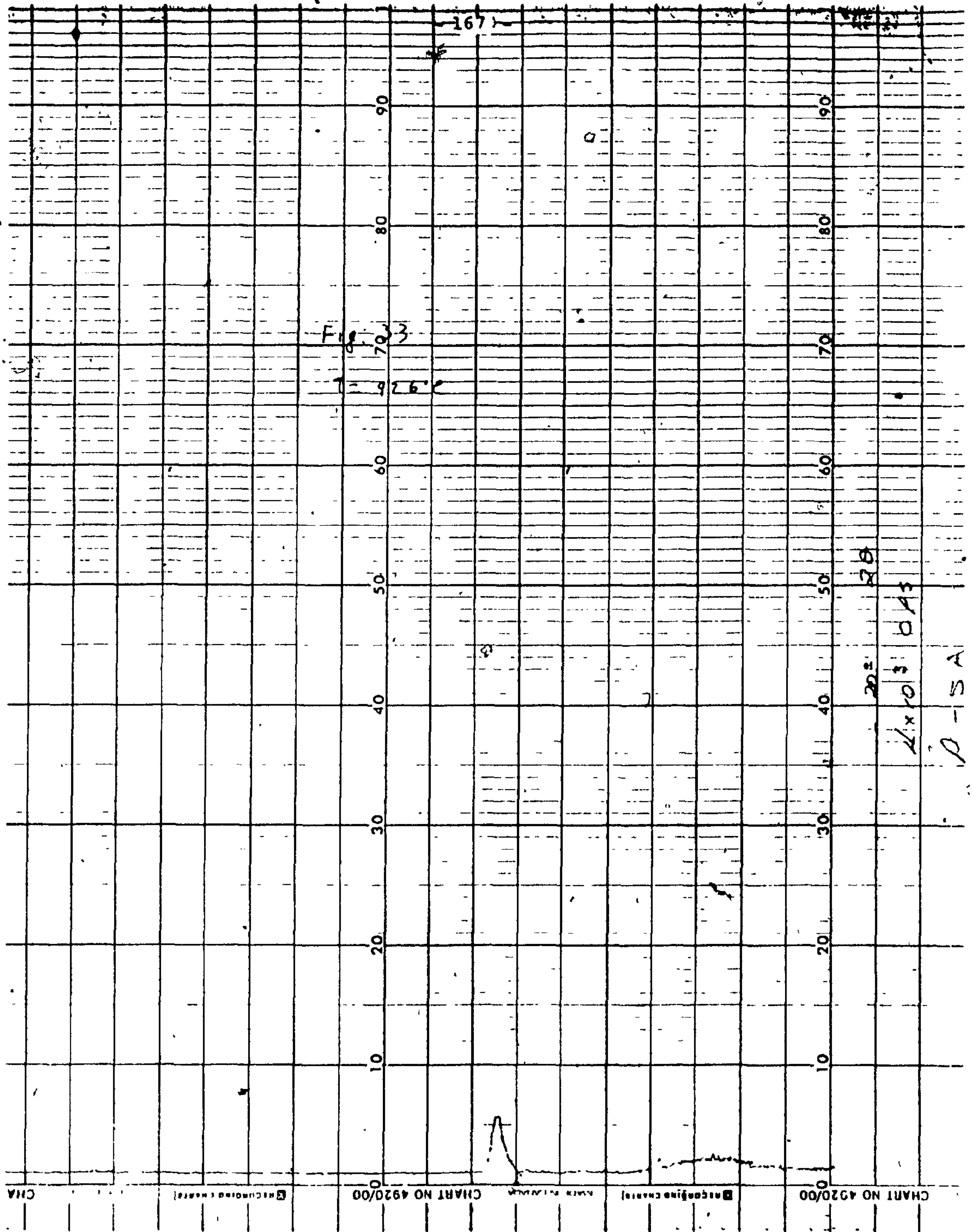
Fig. 33
T = 926°C

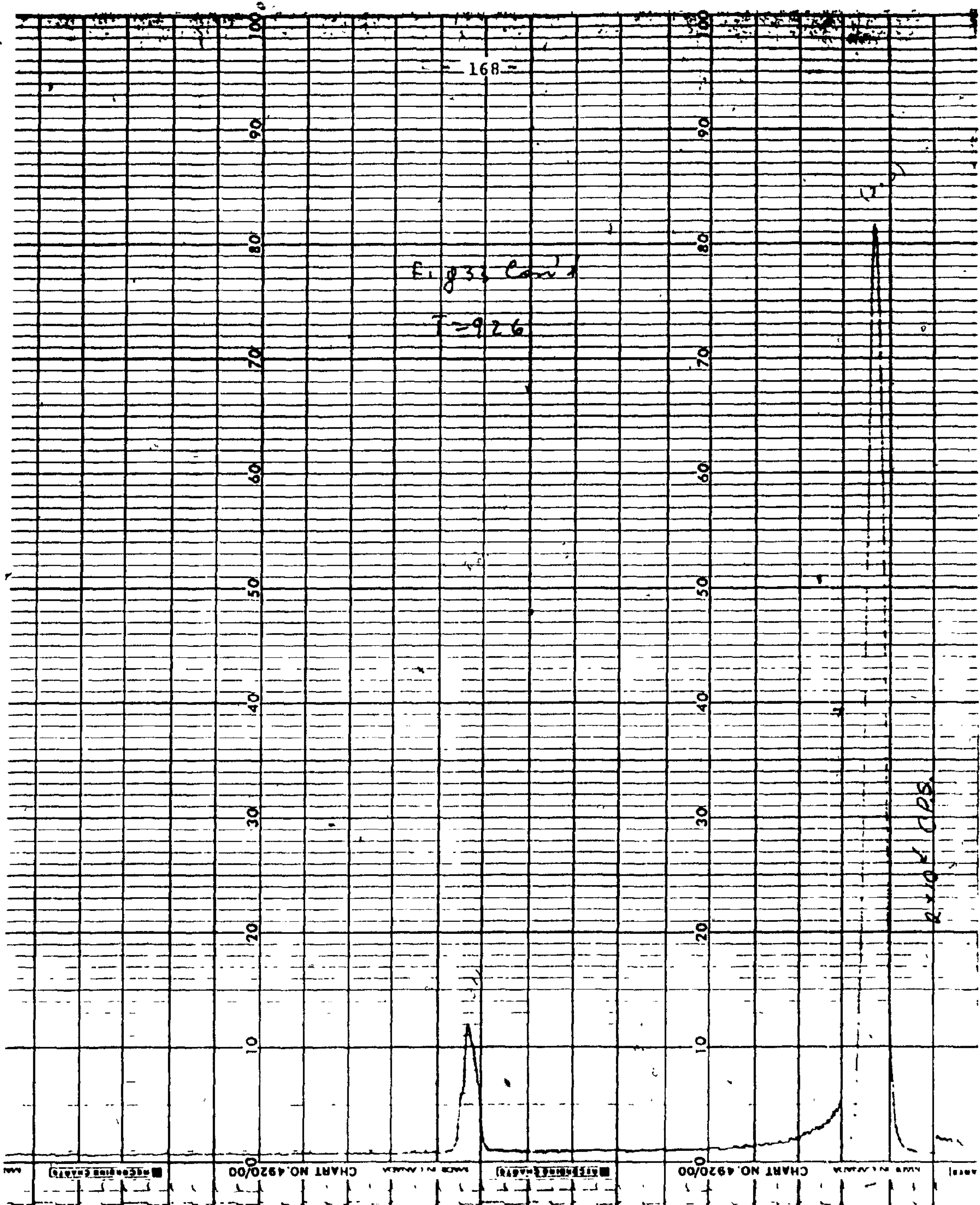

100
90
80
70
60
50
40
30
20
10
0
Fig 33 Cont'd
T=926
CHART NO. 4920/00

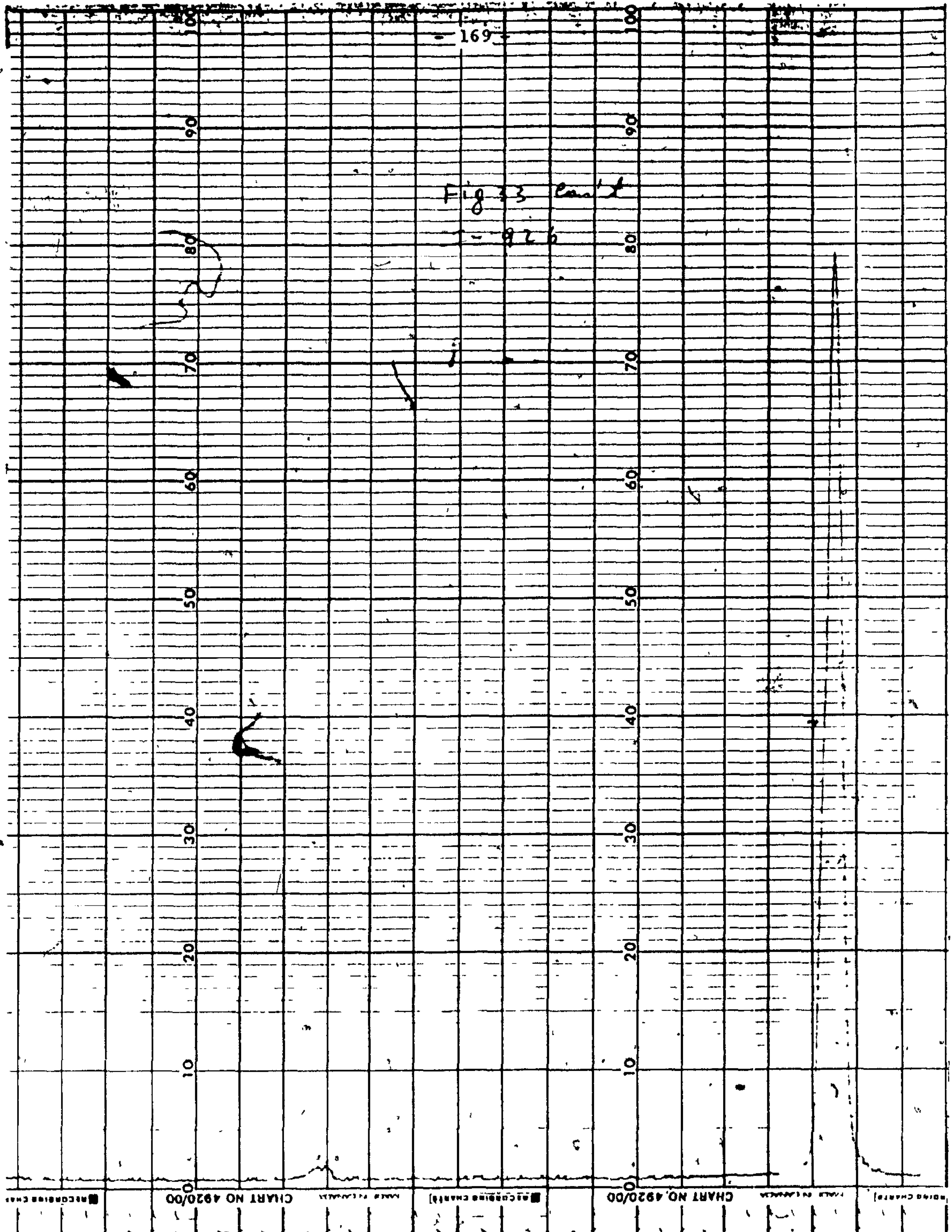
Fig 33 con't
100
90
80
70
60
50
40
30
20
10
0
CHART NO 4920/00

# APPENDIX C

## RELATED GALVANO-MAGNETIC EFFECTS

For;

+ve I and +ve B

$$V_1 = V_H + V_E + V_{IR} + V_N + V_{RL}$$

-ve I and +ve B

$$V_2 = -V_H - V_E - V_{IR} + V_N + V_{RL}$$

-ve I and -ve B

$$V_3 = V_H + V_E - V_{IR} - V_N - V_{RL}$$

+ve I and -ve B

$$V_4 = -V_H - V_E + V_{IR} - V_N - V_{RL}$$

Then;

$$V_{ave_1} = \frac{V_1 - V_2}{2} = V_H + V_E + V_{IR} + V_N + V_{RL} - (-V_H - V_E - V_{IR} + V_N + V_{RL})/2$$

$$= \frac{2V_H + 2V_E + 2V_{IR}}{2}$$

$$= \frac{2}{2}(V_H + V_E + V_{IR})$$

$$= V_H + V_E + V_{IR}$$

$$V_{ave_2} = \frac{V_3 - V_4}{2} = V_H + V_E - V_{IR} - V_N - V_{RL} - (-V_H - V_E + V_{IR} - V_N - V_{RL})/2$$

$$= \frac{2V_H + 2V_E - 2V_{IR}}{2} = \frac{2}{2}(V_H + V_E - V_{IR})$$

$$= V_H + V_E - V_{IR}$$

Hence;

$$V_{H\ ave} = \frac{V_{ave\ 1} + V_{ave\ 2}}{2} = \frac{2V_H + 2V_E + V_{IR} - V_{IR}}{2}$$

$$= \frac{2(V_H + V_E)}{2}$$

$$= V_H + V_E$$

# APPENDIX D

## MEASURED HALL VOLTAGES FOR SAMPLE 1XA-3X, A-F AND 1-6

| B (Gauss) | $I^+$ | | $I^-$ | | $V_H$ ave. (μV) | $V_H$ ave.(uV) / B(Gauss) (nV) |
|---|---|---|---|---|---|---|
| | $V_H^+$ (μV) | $V_H^-$ (μV) | $V_H^+$ (μV) | $V_H^-$ (μV) | | |
| 0 | - 243 | - 249 | + 241 | + 247 | 3.00 | 15.00 |
| 400 | — | — | — | — | — | — |
| 700 | - 235 | - 257 | + 234 | + 254 | 10.50 | 15.00 |
| 1000 | - 230 | - 261 | + 230 | + 259 | 15.00 | 15.00 |
| 2000 | - 216 | - 275 | + 213 | + 274 | 30.00 | 15.00 |
| 3000 | - 200 | - 290 | + 200 | + 289 | 44.75 | 14.92 |
| 4000 | - 185 | - 305 | + 185 | + 303 | 59.50 | 14.88 |
| 5000 | - 170 | - 320 | + 170 | + 318 | 74.50 | 14.90 |
| 6000 | - 155 | - 335 | + 155 | + 333 | 89.50 | 14.92 |
| 7000 | - 140 | - 350 | + 140 | + 348 | 104.50 | 14.93 |
| 8000 | - 125 | - 365 | + 125 | + 363 | 119.50 | 14.94 |
| 9000 | - 110 | - 380 | + 110 | + 378 | 134.50 | 14.94 |
| 10000 | - 95 | - 395 | + 95 | + 393 | 149.00 | 14.90 |

Table D1: Hall effect data of sample 1xa at room temperature.

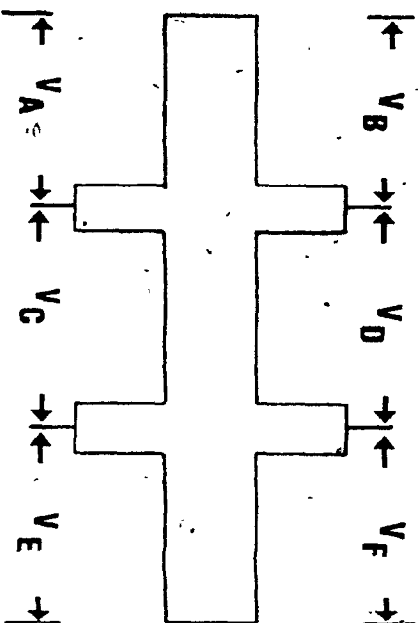


SAMPLE: 1XA

$I$ = 20 mA

$V_A$ = mV
$V_B$ = mV
$V_C$ = 38.43 mV
$V_D$ = 38.50 mV
$V_E$ = mV
$V_F$ = mV

| B (Gauss) | $I^+$ | | $I^-$ | | $V_H$ ave. (μV) | $\frac{V_H \text{ ave.} (\mu V)}{B (\text{Gauss})}$ (nV) |
|---|---|---|---|---|---|---|
| | $V_H^+$ (μV) | $V_H^-$ (μV) | $V_H^+$ (μV) | $V_H^-$ (μV) | | |
| 0 | + 218 | + 217 | - 216 | - 215 | 0.50 | 2.50 |
| 400 | + 220 | + 215 | - 218 | - 213 | 2.25 | 5.63 |
| 700 | + 222 | + 213 | - 220 | - 211 | 4.25 | 6.07 |
| 1000 | + 224 | + 210 | - 222 | - 209 | 6.75 | 6.75 |
| 2000 | + 231 | + 204 | - 230 | - 203 | 13.50 | 6.75 |
| 3000 | + 238 | + 197 | - 236 | - 195 | 20.25 | 6.75 |
| 4000 | + 245 | + 191 | - 243 | - 189 | 27.00 | 6.75 |
| 5000 | + 252 | + 184 | - 250 | - 183 | 33.75 | 6.75 |
| 6000 | + 259 | + 178 | - 257 | - 175 | 40.75 | 6.79 |
| 7000 | + 266 | + 172 | - 264 | - 168 | 47.50 | 6.79 |
| 8000 | + 274 | + 165 | - 271 | - 162 | 54.50 | 6.81 |
| 9000 | + 280 | + 158 | - 278 | - 155 | 61.25 | 6.81 |
| 10000 | + 286 | + 151 | - 285 | - 148 | 68.00 | 6.80 |

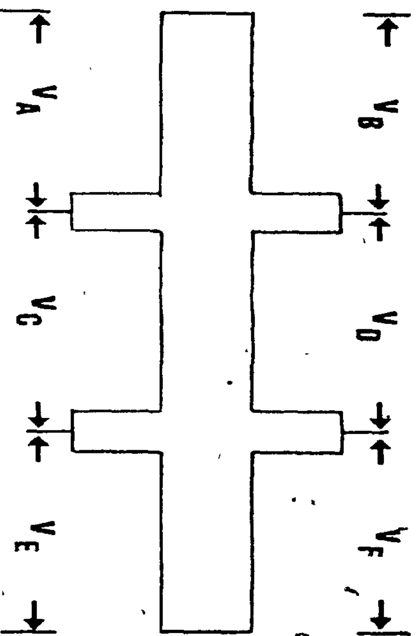


SAMPLE: 2X

$I$ = 50 mA

$V_A$ = 81.40 mV
$V_B$ = 81.00 mV
$V_C$ = 17.80 mV
$V_D$ = 18.60 mV
$V_E$ = 94.30 mV
$V_F$ = 94.00 mV

Table D2: Hall effect data of sample 2x at room temperature..

| B (Gauss) | $I^+$ $V_H^+$ (μV) | $I^+$ $V_H^-$ (μV) | $I^-$ $V_H^+$ (μV) | $I^-$ $V_H^-$ (μV) | $V_H$ ave. (μV) | $V_H$ ave.(dV) / B(Gauss) (nV) |
|---|---|---|---|---|---|---|
| 0 | + 1168 | + 1167 | - 1168 | - 1167 | 0.50 | 2.50 |
| 400 | + 1169 | + 1165 | - 1171 | - 1165 | 2.50 | 6.25 |
| 700 | + 1172 | + 1164 | - 1172 | - 1162 | 4.50 | 6.43 |
| 1000 | + 1174 | + 1162 | - 1175 | - 1160 | 6.75 | 6.75 |
| 2000 | + 1181 | + 1153 | - 1181 | - 1153 | 14.00 | 7.00 |
| 3000 | + 1188 | + 1145 | - 1187 | - 1146 | 21.25 | 7.00 |
| 4000 | + 1195 | + 1139 | - 1195 | - 1139 | 28.00 | 7.00 |
| 5000 | + 1202 | + 1132 | - 1202 | - 1132 | 35.00 | 7.00 |
| 6000 | + 1208 | + 1125 | - 1209 | - 1124 | 42.00 | 7.00 |
| 7000 | + 1216 | + 1118 | - 1216 | - 1117 | 49.25 | 7.04 |
| 8000 | + 1223 | + 1111 | - 1223 | - 1110 | 56.25 | 7.03 |
| 9000 | + 1230 | + 1104 | - 1230 | - 1103 | 63.25 | 7.03 |
| 10000 | + 1237 | + 1096 | - 1238 | - 1096 | 70.75 | 7.08 |

Table D3: Hall effect data of sample 2xa at room temperature.

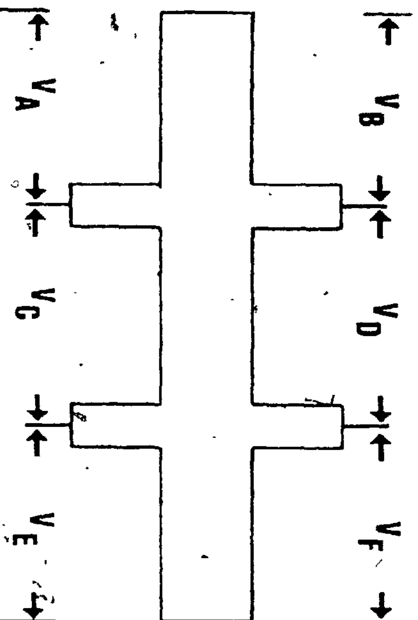


SAMPLE: 2XA

$I$ = 50 mA

$V_A$ = 58.56 mV
$V_B$ = 57.38 mV
$V_C$ = 18.52 mV
$V_D$ = 18.49 mV
$V_E$ = 89.34 mV
$V_F$ = 89.33 mV

| B (Gauss) | $I^+$ $V_H^+$ (μV) | $I^+$ $V_H^-$ (μV) | $I^-$ $V_H^+$ (μV) | $I^-$ $V_H^-$ (μV) | $V_H$ ave. (μV) | $V_H$ ave.(μV) / B(Gauss) nV |
|---|---|---|---|---|---|---|
| 0 | + 488 | + 487 | - 493 | - 492 | 0.50 | 2.50 |
| 400 | + 489 | + 486 | - 495 | - 490 | 2.00 | 5.00 |
| 700 | + 491 | + 483 | - 497 | - 488 | 4.25 | 6.07 |
| 1000 | + 495 | + 480 | - 498 | - 486 | 6.75 | 6.75 |
| 2000 | + 502 | + 475 | - 506 | - 479 | 13.50 | 6.75 |
| 3000 | + 509 | + 469 | - 513 | - 472 | 20.25 | 6.75 |
| 4000 | + 515 | + 461 | - 520 | - 466 | 27.00 | 6.75 |
| 5000 | + 521 | + 454 | - 526 | - 457 | 34.00 | 6.80 |
| 6000 | + 528 | + 445 | - 534 | - 454 | 40.75 | 6.79 |
| 7000 | + 534 | + 440 | - 540 | - 444 | 47.50 | 6.79 |
| 8000 | + 540 | + 432 | - 546 | - 437 | 54.25 | 6.78 |
| 9000 | + 548 | + 426 | - 552 | - 430 | 61.00 | 6.78 |
| 10000 | + 556 | + 428 | - 560 | - 424 | 68.00 | 6.80 |

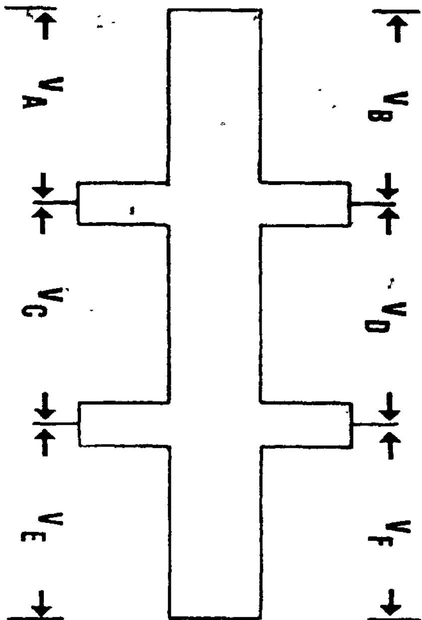


SAMPLE: 3X

$I$ = 50 mA

$V_A$ = mV
$V_B$ = mV
$V_C$ = 16.40 mV
$V_D$ = 16.20 mV
$V_E$ = mV
$V_F$ = mV

Table D4: Hall effect data of sample 3x at room temperature.

| B (Gauss) | $I^+$ | | $I^-$ | | $V_H$ ave. (μV) | $V_H$ ave.(uV) / B(Gauss) nV |
|---|---|---|---|---|---|---|
| | $V_H^+$ (μV) | $V_H^-$ (μV) | $V_H^+$ (μV) | $V_H^-$ (μV) | | |
| 0 | + 82 | + 82 | - 81 | - 78 | 0.75 | 3.75 |
| 400 | + 83 | + 81 | - 82 | - 77 | 1.75 | 4.38 |
| 700 | + 86 | + 79 | - 83 | - 76 | 3.50 | 5.00 |
| 1000 | + 88 | + 79 | - 85 | - 73 | 5.25 | 5.25 |
| 2000 | + 92 | + 72 | - 89 | - 76 | 10.75 | 5.38 |
| 3000 | + 98 | + 68 | - 95 | - 61 | 16.00 | 5.33 |
| 4000 | + 103 | + 62 | - 100 | - 56 | 21.25 | 5.31 |
| 5000 | + 109 | + 57 | - 105 | - 51 | 26.50 | 5.30 |
| 6000 | + 115 | + 51 | - 110 | - 46 | 32.00 | 5.33 |
| 7000 | + 120 | + 47 | - 116 | - 40 | 37.25 | 5.32 |
| 8000 | + 125 | + 42 | - 122 | - 34 | 42.75 | 5.34 |
| 9000 | + 130 | + 36 | - 128 | - 29 | 48.25 | 5.36 |
| 10000 | + 134 | + 30 | - 134 | - 24 | 53.50 | 5.35 |

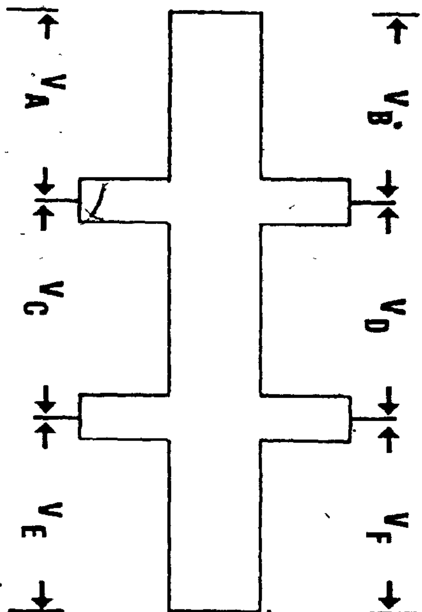


SAMPLE: 3XA

$I$ = 50 mA

$V_A$ = mV
$V_B$ = mV
$V_C$ = 14.30 mV
$V_D$ = 14.31 mV
$V_E$ = mV
$V_F$ = mV

Table D5: Hall effect data of sample 3xa at room temperature.

| B (Gauss) | $I^+$ | | $I^-$ | | $V_H$ ave. ($\mu V$) | $V_H$ ave.($\mu V$) / B(Gauss) (nV) |
|---|---|---|---|---|---|---|
| | $V_H^+$ ($\mu V$) | $V_H^-$ ($\mu V$) | $V_H^+$ ($\mu V$) | $V_H^-$ ($\mu V$) | | |
| 0 | + 343 | + 342 | - 338 | - 337 | 0.5 | 2.5 |
| 400 | + 344 | +341 | - 340 | - 336 | 1.75 | 4.38 |
| 700 | + 345 | + 340 | - 342 | - 334 | 3.25 | 4.64 |
| 1000 | + 348 | + 337 | - 343 | - 333 | 5.25 | 5.25 |
| 2000 | + 354 | + 333 | - 349 | - 327 | 10.75 | 5.38 |
| 3000 | + 358 | + 326 | - 355 | - 322 | 16.25 | 5.42 |
| 4000 | + 363 | + 321 | - 359 | - 315 | 21.50 | 5.38 |
| 5000 | + 369 | + 315 | - 364 | - 310 | 27.00 | 5.40 |
| 6000 | + 374 | + 310 | - 370 | - 305 | 32.25 | 5.38 |
| 7000 | + 381 | + 305 | - 375 | - 300 | 37.75 | 5.39 |
| 8000 | + 386 | + 299 | - 380 | - 295 | 43.00 | 5.38 |
| 9000 | + 391 | + 294 | - 386 | - 289 | 48.50 | 5.39 |
| 10000 | + 396 | + 288 | - 391 | - 284 | 53.75 | 5.38 |

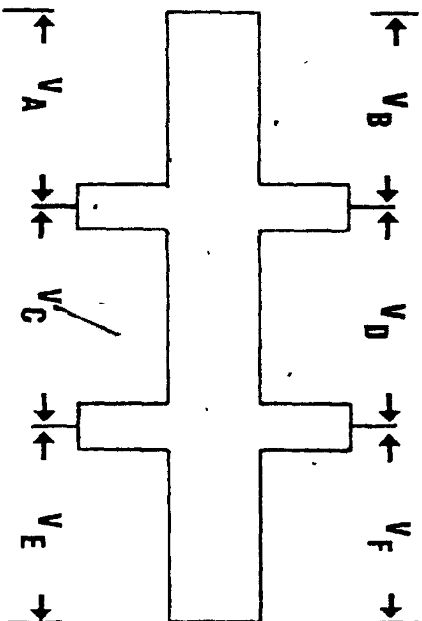


SAMPLE: A

$I$ = 50 mA

$V_A$ = 69.86 mV
$V_B$ = 69.49 mV
$V_C$ = 12.75 mV
$V_D$ = 12.70 mV
$V_E$ = 63.37 mV
$V_F$ = 62.84 mV

Table D6: Hall effect data of sample A at room temperature.

| B (Gauss) | $I^+$ | | $I^-$ | | $V_H$ ave. (μV) | $\frac{V_H \text{ ave.}(\mu V)}{B(\text{Gauss})}$ (nV) |
|---|---|---|---|---|---|---|
| | $V_H^+$ (μV) | $V_H^-$ (μV) | $V_H^+$ (μV) | $V_H^-$ (μV) | | |
| 0 | + 45 | + 44 | - 42 | - 41 | 0.5 | 2.50 |
| 400 | + 46 | + 43 | - 43 | - 40 | 1.5 | 3.75 |
| 700 | + 47 | + 41 | - 44 | - 38 | 3.0 | 4.28 |
| 1000 | +49 | + 39 | - 46 | - 36 | 5.0 | 5.00 |
| 2000 | + 54 | + 34 | - 51 | - 31 | 10.0 | 5.00 |
| 3000 | + 59 | + 29 | - 56 | - 26 | 15.0 | 5.00 |
| 4000 | + 64 | + 24 | - 61 | - 21 | 20.0 | 5.00 |
| 5000 | + 69 | + 18 | - 66 | - 15 | 25.5 | 5.10 |
| 6000 | + 74 | + 13 | - 71 | - 10 | 30.5 | 5.08 |
| 7000 | + 80 | + 9 | - 76 | - 5 | 35.5 | 5.07 |
| 8000 | + 85 | + 4 | - 81 | 0 | 40.5 | 5.06 |
| 9000 | + 91 | 0 | - 86 | + 5 | 45.5 | 5.06 |
| 10000 | + 96 | - 6 | - 92 | + 10 | 50.5 | 5.10 |

Table D7: Hall effect data of sample B at room temperature.

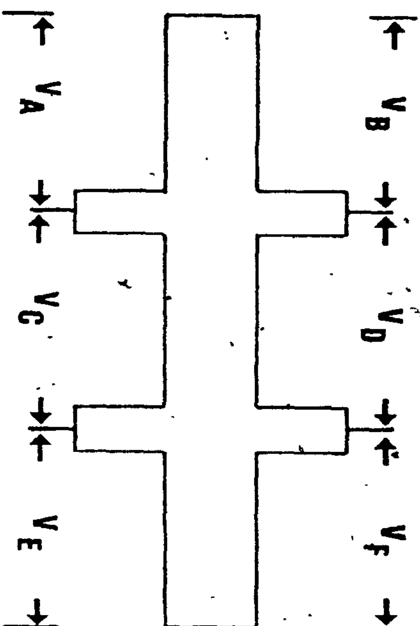


SAMPLE: B

$I$ = 50 mA

$V_A$ = 64.23 mV
$V_B$ = 63.94 mV
$V_C$ = 11.21 mV
$V_D$ = 11.11 mV
$V_E$ = 63.78 mV
$V_F$ = 64.17 mV

| B (Gauss) | $I^+$ | | $I^-$ | | $V_H$ ave. (μV) | $\frac{V_H \text{ ave. (uV)}}{B \text{ (Gauss)}}$ (nV) |
|---|---|---|---|---|---|---|
| | $V_H^+$ (μV) | $V_H^-$ (μV) | $V_H^+$ (μV) | $V_H^-$ (μV) | | |
| 0 | + 394 | + 393 | - 392 | - 391 | 0.50 | 2.50 |
| 400 | + 395 | + 392 | - 391 | - 389 | 1.50 | 3.75 |
| 700 | + 397 | + 390 | - 393 | - 387 | 3.25 | 4.64 |
| 1000 | + 399 | + 388 | - 396 | - 385 | 5.50 | 5.50 |
| 2000 | + 405 | + 382 | - 402 | - 380 | 11.25 | 5.63 |
| 3000 | + 410 | + 376 | - 408 | - 374 | 17.00 | 5.67 |
| 4000 | + 416 | + 370 | - 414 | - 369 | 22.75 | 5.69 |
| 5000 | + 421 | + 364 | - 419 | - 363 | 28.25 | 5.65 |
| 6000 | + 427 | + 358 | - 425 | - 358 | 34.00 | 5.67 |
| 7000 | + 432 | + 353 | - 431 | - 351 | 39.75 | 5.68 |
| 8000 | + 438 | + 347 | - 437 | - 346 | 45.50 | 5.69 |
| 9000 | + 444 | + 342 | - 443 | - 341 | 51.00 | 5.67 |
| 10000 | + 450 | + 336 | - 449 | - 336 | 56.75 | 5.68 |

Table D8: Hall effect data of sample C at room temperature.

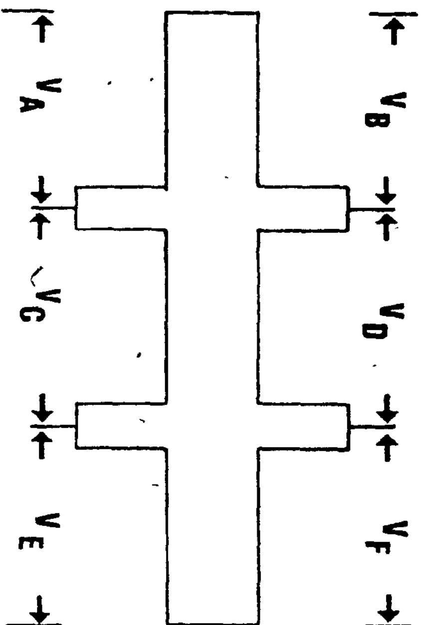


SAMPLE: C

$I$ = 50 mA

$V_A$ = 55.85 mV
$V_B$ = 55.75 mV
$V_C$ = 13.23 mV
$V_D$ = 13.27 mV
$V_E$ = 62.17 mV
$V_F$ = 62.15 mV

| B (Gauss) | $I^+$ | | $I^-$ | | $V_H$ ave. (μV) | $\frac{V_H \text{ ave.} (\mu V)}{B (\text{Gauss})}$ (nV) |
|---|---|---|---|---|---|---|
| | $V_H^+$ (μV) | $V_H^-$ (μV) | $V_H^+$ (μV) | $V_H^-$ (μV) | | |
| 0 | + 20 | + 20 | - 20 | - 19 | 0.25 | 1.25 |
| 400 | + 21 | + 18 | - 22 | - 18 | 1.75 | 4.38 |
| 700 | + 23 | + 16 | - 23 | - 17 | 3.25 | 4.64 |
| 1000 | + 24 | + 15 | - 24 | - 14 | 4.75 | 4.75 |
| 2000 | + 29 | + 10 | - 30 | - 10 | 9.75 | 4.88 |
| 3000 | + 34 | + 5 | - 35 | - 5 | 14.75 | 4.92 |
| 4000 | + 39 | 0 | - 40 | - 1 | 19.50 | 4.88 |
| 5000 | + 44 | - 5 | - 45 | + 4 | 24.50 | 4.90 |
| 6000 | + 49 | - 9 | - 49 | + 9 | 29.00 | 4.83 |
| 7000 | + 54 | - 14 | - 54 | + 14 | 34.00 | 4.85 |
| 8000 | + 59 | - 18 | - 59 | + 19 | 38.75 | 4.84 |
| 9000 | + 64 | - 23 | - 64 | + 24 | 43.75 | 4.86 |
| 10000 | + 69 | - 29 | - 69 | + 29 | 49.00 | 4.90 |

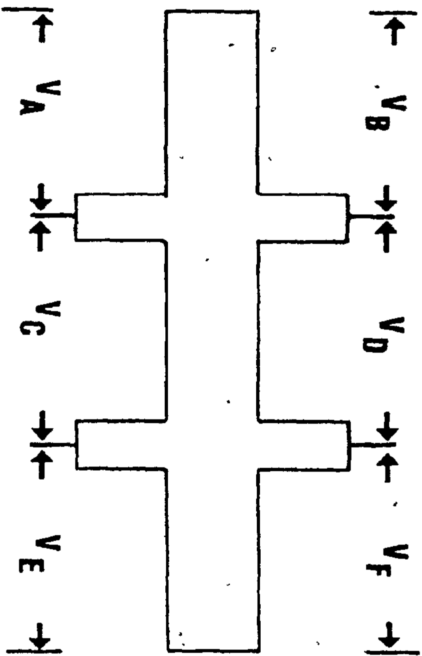


SAMPLE: D

$I = 50$ mA

$V_A = 54.00$ mV
$V_B = 53.02$ mV
$V_C = 11.50$ mV
$V_D = 12.00$ mV
$V_E = 54.05$ mV
$V_F = 53.55$ mV

Table D9: Hall effect data of sample D at room temperature.

| B (Gauss) | $I^+$ | | $I^-$ | | $V_H$ ave. (μV) | $V_H$ ave.(uV) / B(Gauss) (nV) |
|---|---|---|---|---|---|---|
| | $V_H^+$ (μV) | $V_H^-$ (μV) | $V_H^+$ (μV) | $V_H^-$ (μV) | | |
| 0 | + 141 | + 141 | - 142 | - 141 | 0.25 | 1.25 |
| 400 | + 142 | + 140 | - 143 | - 140 | 1.25 | 3.13 |
| 700 | + 144 | + 139 | - 144 | - 139 | 2.50 | 3.57 |
| 1000 | + 145 | + 138 | - 146 | - 138 | 3.75 | 3.75 |
| 2000 | + 149 | + 134 | - 150 | - 135 | 7.50 | 3.75 |
| 3000 | + 153 | + 130 | - 153 | - 131 | 11.25 | 3.75 |
| 4000 | + 156 | + 126 | - 157 | - 127 | 15.00 | 3.75 |
| 5000 | + 159 | + 122 | - 161 | - 124 | 18.50 | 3.70 |
| 6000 | + 163 | + 118 | - 164 | - 120 | 22.25 | 3.71 |
| 7000 | + 167 | + 115 | - 168 | - 116 | 26.00 | 3.71 |
| 8000 | + 171 | + 112 | - 172 | - 112 | 29.75 | 3.72 |
| 9000 | + 175 | + 118 | - 175 | - 108 | 33.50 | 3.72 |
| 10000 | + 179 | + 105 | - 179 | - 104 | 37.25 | 3.73 |

Table D10: Hall effect data of sample at E at room temperature.

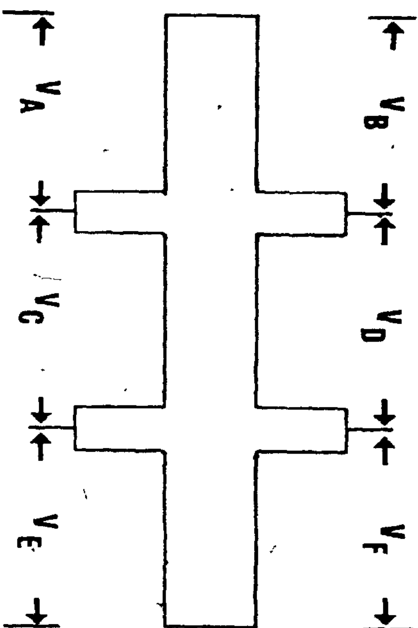


SAMPLE: E

$I$ = 50 mA

$V_A$ = 46.15 mV
$V_B$ = 46.22 mV
$V_C$ = 10.20 mV
$V_D$ = 10.30 mV
$V_E$ = 46.20 mV
$V_F$ = 46.31 mV

| B (Gauss) | $I^+$ | | $I^-$ | | $V_H$ ave. ($\mu V$) | $\frac{V_H \text{ ave.} (\mu V)}{B (\text{Gauss})}$ (nV) |
|---|---|---|---|---|---|---|
| | $V_H^+$ ($\mu V$) | $V_H^-$ ($\mu V$) | $V_H^+$ ($\mu V$) | $V_H^-$ ($\mu V$) | | |
| 0 | + 1033 | + 1032 | - 1030 | - 1030 | 0.25 | 1.25 |
| 400 | + 1034 | + 1031 | - 1031 | - 1029 | 1.25 | 3.13 |
| 700 | + 1035 | + 1029 | - 1033 | - 1028 | 2.75 | 3.93 |
| 1000 | + 1037 | + 1029 | - 1035 | - 1027 | 4.25 | 4.25 |
| 2000 | + 1041 | + 1024 | - 1040 | - 1021 | 9.00 | 4.50 |
| 3000 | + 1045 | + 1020 | - 1044 | - 1016 | 13.25 | 4.42 |
| 4000 | + 1050 | + 1015 | - 1048 | - 1011 | 18.00 | 4.50 |
| 5000 | + 1055 | + 1010 | - 1052 | - 1007 | 22.50 | 4.50 |
| 6000 | + 1060 | + 1005 | - 1056 | - 1003 | 27.00 | 4.50 |
| 7000 | + 1065 | + 1001 | - 1061 | - 999 | 31.50 | 4.50 |
| 8000 | + 1070 | + 997 | - 1066 | - 994 | 36.25 | 4.53 |
| 9000 | + 1074 | + 992 | - 1071 | - 989 | 41.00 | 4.55 |
| 10000 | + 1078 | + 987 | - 1075 | - 985 | 45.25 | 4.53 |

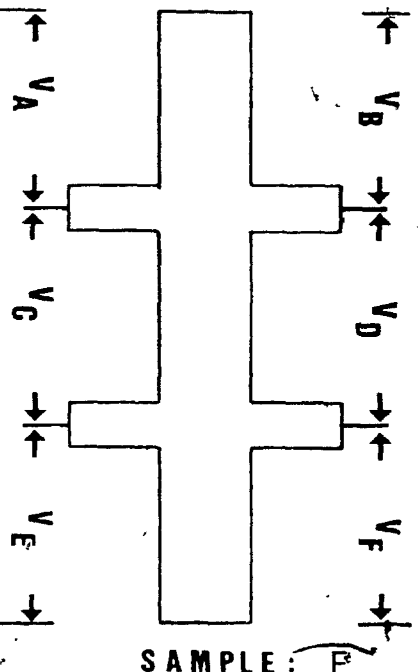


$I$ = 50 mA

$V_A$ = 72.90 mV
$V_B$ = 73.10 mV
$V_C$ = 14.01 mV
$V_D$ = 13.47 mV
$V_E$ = 73.12 mV
$V_F$ = 73.20 mV

Table D11: Hall effect data of sample F at room temperature.

| B (Gauss) | $I^+$ | | $I^-$ | | $V_H$ ave. ($\mu$V) | $\frac{V_H \text{ ave.}(\mu V)}{B(\text{Gauss})}$ (nV) |
|---|---|---|---|---|---|---|
| | $V_H^+$ ($\mu$V) | $V_H^-$ ($\mu$V) | $V_H^+$ ($\mu$V) | $V_H^-$ ($\mu$V) | | |
| 0 | - 33390 | - 33388 | + 33392 | + 33390 | 1.00 | 5.00 |
| 400 | — | — | — | — | — | — |
| 700 | - 33405 | - 33373 | + 33407 | + 33375 | 16.00 | 22.86 |
| 1000 | - 33412 | - 33363 | + 33432 | + 33373 | 27.00 | 27.00 |
| 2000 | - 33439 | - 33338 | + 33460 | + 33345 | 54.00 | 27.00 |
| 3000 | - 33466 | - 33312 | + 33489 | + 33319 | 81.00 | 27.00 |
| 4000 | - 33493 | - 33283 | + 33514 | + 33293 | 107.75 | 26.94 |
| 5000 | - 33521 | - 33257 | + 33542 | + 33266 | 135.00 | 27.00 |
| 6000 | - 33549 | - 33230 | + 33568 | + 33240 | 161.75 | 26.96 |
| 7000 | - 33577 | - 33201 | + 33595 | + 33214 | 189.25 | 27.04 |
| 8000 | - 33606 | - 33177 | + 33623 | + 33188 | 216.00 | 27.00 |
| 9000 | - 33634 | - 33151 | + 33653 | + 33161 | 243.75 | 27.08 |
| 10000 | - 33663 | - 33121 | + 33678 | + 33134 | 271.50 | 27.15 |

Table D12: Hall effect data of sample 1 at room temperature.

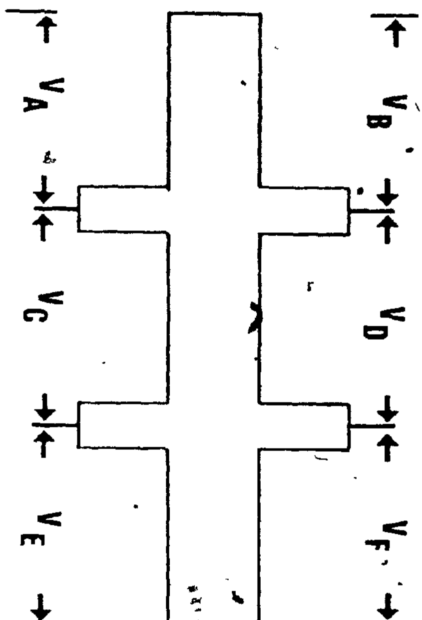


SAMPLE: 1

$I$ = .25 mA

$V_A$ = mV
$V_B$ = 218.50 mV
$V_C$ = 231.00 mV
$V_D$ = 231.60 mV
$V_E$ = 217.70 mV
$V_F$ = 399.30 mV

| B (Gauss) | $I^+$ $V_H^+$ (μV) | $I^+$ $V_H^-$ (μV) | $I^-$ $V_H^+$ (μV) | $I^-$ $V_H^-$ (μV) | $V_H$ ave. (μV) | $V_H$ ave.(μV) / B(Gauss) (nV) |
|---|---|---|---|---|---|---|
| 0 | + 1050 | + 1053 | - 1051 | - 1054 | 1.50 | 7.50 |
| 400 | — | — | — | — | — | — |
| 700 | + 1041 | + 1063 | - 1040 | - 1064 | 11.50 | 16.43 |
| 1000 | + 1030 | + 1070 | - 1030 | - 1069 | 19.75 | 19.75 |
| 2000 | + 1009 | + 1089 | - 1010 | - 1089 | 39.75 | 19.88 |
| 3000 | + 989 | + 1109 | - 990 | - 1109 | 59.75 | 19.92 |
| 4000 | + 970 | + 1129 | - 970 | - 1129 | 79.50 | 19.88 |
| 5000 | + 949 | + 1148 | - 950 | - 1149 | 99.50 | 19.90 |
| 6000 | + 929 | + 1168 | - 930 | - 1169 | 119.50 | 19.92 |
| 7000 | + 909 | + 1188 | - 910 | - 1189 | 139.50 | 19.93 |
| 8000 | + 889 | + 1208 | - 890 | - 1208 | 159.25 | 19.91 |
| 9000 | + 869 | + 1228 | - 870 | - 1228 | 179.25 | 19.92 |
| 10000 | + 849 | + 1248 | - 850 | - 1248 | 199.25 | 19.93 |

Table D13: Hall effect data of sample 2 at room temperature.

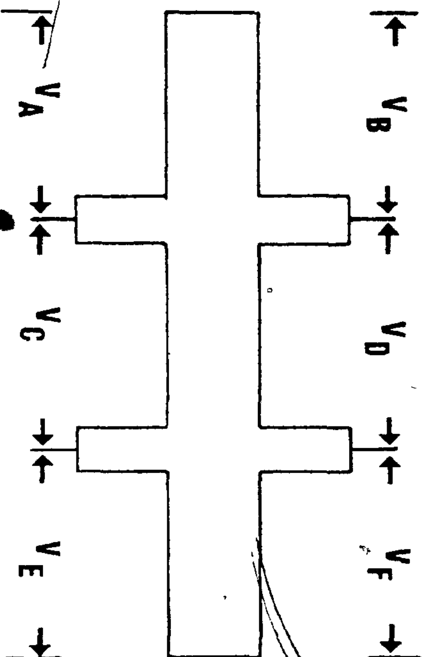


SAMPLE: 2

$I$ = 20 mA

$V_A$ = mV
$V_B$ = 93.60 mV
$V_C$ = 37.35 mV
$V_D$ = 37.40 mV
$V_E$ = 93.45 mV
$V_F$ = mV

| B (Gauss) | $I^+$ | | $I^-$ | | $V_H$ ave. (μV) | $\frac{V_H \text{ ave.} (\mu V)}{B (\text{Gauss})}$ (nV) |
|---|---|---|---|---|---|---|
| | $V_H^+$ (μV) | $V_H^-$ (μV) | $V_H^+$ (μV) | $V_H^-$ (μV) | | |
| 0 | - 560 | - 558 | + 561 | + 560 | 0.75 | 3.75 |
| 400 | — | — | — | — | — | — |
| 700 | - 575 | - 546 | + 576 | + 547 | 14.50 | 20.71 |
| 1000 | - 589 | - 530 | + 592 | + 532 | 29.75 | 29.75 |
| 2000 | - 619 | - 500 | + 621 | + 502 | 59.50 | 29.75 |
| 3000 | - 649 | - 470 | + 651 | + 473 | 89.25 | 29.75 |
| 4000 | - 678 | - 440 | + 681 | + 443 | 119.00 | 29.75 |
| 5000 | - 709 | - 411 | + 710 | + 413 | 148.75 | 29.75 |
| 6000 | - 739 | - 382 | + 740 | + 383 | 178.50 | 29.75 |
| 7000 | - 769 | - 353 | + 770 | + 353 | 208.25 | 29.75 |
| 8000 | - 799 | - 323 | + 800 | + 324 | 238.00 | 29.75 |
| 9000 | - 829 | - 293 | + 830 | + 294 | 268.00 | 29.78 |
| 10000 | - 859 | - 263 | + 860 | + 264 | 298.00 | 29.80 |

Table D14: Hall effect data of sample 3 at room temperature.

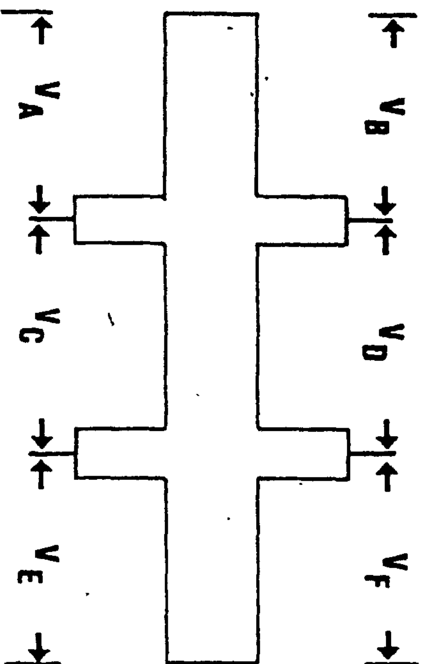


SAMPLE: 3

$I$ = 20 mA

$V_A$ = mV
$V_B$ = 223.00 mV
$V_C$ = 44.00 mV
$V_D$ = 44.04 mV
$V_E$ = mV
$V_F$ = 136.96 mV

| B (Gauss) | $I^+$ |  | $I^-$ |  | $V_H$ ave. ($\mu V$) | $\frac{V_H \text{ ave.} (\mu V)}{B (\text{Gauss})}$ (nV) |
|---|---|---|---|---|---|---|
|  | $V_H^+$ ($\mu V$) | $V_H^-$ ($\mu V$) | $V_H^+$ ($\mu V$) | $V_H^-$ ($\mu V$) |  |  |
| 0 | - 2031 | - 2030 | + 2030 | + 2029 | 0.50 | 2.50 |
| 400 | — | — | — | — | — | — |
| 700 | - 2045 | - 2019 | + 2044 | + 2017 | 13.25 | 18.93 |
| 1000 | - 2058 | - 2013 | + 2058 | + 2010 | 23.25 | 23.25 |
| 2000 | - 2081 | - 1988 | + 2080 | + 1987 | 46.50 | 23.25 |
| 3000 | - 2105 | - 1965 | + 2104 | + 1965 | 69.75 | 23.25 |
| 4000 | - 2129 | - 1942 | + 2127 | + 1942 | 93.00 | 23.25 |
| 5000 | - 2151 | - 1918 | + 2151 | + 1919 | 116.25 | 23.25 |
| 6000 | - 2175 | - 1894 | + 2174 | + 1895 | 140.00 | 23.33 |
| 7000 | - 2198 | - 1870 | + 2197 | + 1872 | 163.25 | 23.32 |
| 8000 | - 2222 | - 1847 | + 2221 | + 1849 | 186.75 | 23.34 |
| 9000 | - 2245 | - 1824 | + 2245 | + 1826 | 210.00 | 23.33 |
| 10000 | - 2269 | - 1802 | + 2270 | + 1802 | 233.75 | 23.38 |

Table D15. Hall effect data of sample 4 at room temperature .

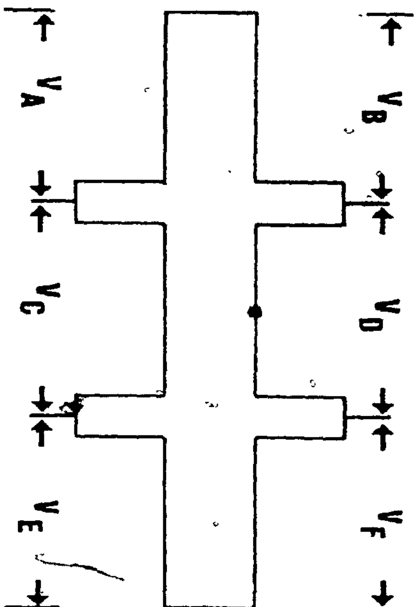


SAMPLE: 4

$I$ = 20 mA

$V_A$ = mV
$V_B$ = 163.60 mV
$V_C$ = 28.39 mV
$V_D$ = 28.40 mV
$V_E$ = mV
$V_F$ = 209.80 mV

| B (Gauss) | $I^+$ | | $I^-$ | | $V_H$ ave. (μV) | $V_H$ ave.(μV) / B(Gauss) (nV) |
|---|---|---|---|---|---|---|
| | $V_H^+$ (μV) | $V_H^-$ (μV) | $V_H^+$ (μV) | $V_H^-$ (μV) | | |
| 0 | + 748 | + 749 | - 740 | - 742 | 0.75 | 3.75 |
| 400 | — | — | — | — | — | — |
| 700 | + 742 | + 753 | - 733 | - 744 | 5.50 | 7.86 |
| 1000 | + 736 | + 760 | - 727 | - 751 | 12.00 | 12.00 |
| 2000 | + 724 | + 773 | - 715 | - 764 | 24.50 | 12.25 |
| 3000 | + 712 | + 786 | - 703 | - 776 | 36.75 | 12.25 |
| 4000 | + 700 | + 798 | - 690 | - 788 | 49.00 | 12.25 |
| 5000 | + 688 | + 810 | - 677 | - 800 | 61.25 | 12.25 |
| 6000 | + 676 | + 822 | - 665 | - 813 | 73.50 | 12.25 |
| 7000 | + 663 | + 834 | - 653 | - 825 | 85.75 | 12.25 |
| 8000 | + 650 | + 846 | - 641 | - 837 | 98.00 | 12.25 |
| 9000 | + 638 | + 859 | - 628 | - 850 | 110.75 | 12.31 |
| 10000 | + 625 | + 871 | - 616 | - 862 | 123.00 | 12.30 |

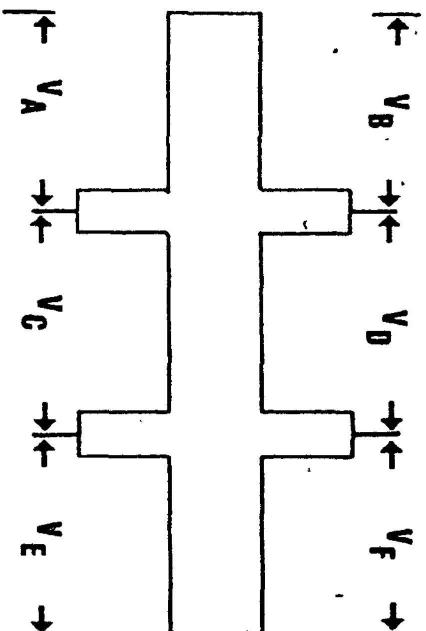


SAMPLE: 5

I = 20 mA

$V_A$ = mV
$V_B$ = mV
$V_C$ = 17.05 mV
$V_D$ = 16.80 mV
$V_E$ = mV
$V_F$ = mV

Table D16: Hall effect data of sample 5 at room temperature.

| B (Gauss) | $I^+$ $V_H^+$ ($\mu V$) | $I^+$ $V_H^-$ ($\mu V$) | $I^-$ $V_H^+$ ($\mu V$) | $I^-$ $V_H^-$ ($\mu V$) | $V_H$ ave. ($\mu V$) | $V_H$ ave.($\mu V$) / B(Gauss) (nV) |
|---|---|---|---|---|---|---|
| 0 | + 930 | + 932 | - 931 | - 933 | 1.00 | 5.00 |
| 400 | — | — | — | — | — | — |
| 700 | + 922 | + 940 | - 923 | - 942 | 9.25 | 13.21 |
| 1000 | + 918 | + 945 | - 918 | - 947 | 14.00 | 14.00 |
| 2000 | + 904 | + 959 | - 904 | - 961 | 28.00 | 14.00 |
| 3000 | + 890 | + 972 | - 889 | - 975 | 42.00 | 14.00 |
| 4000 | + 877 | + 987 | - 875 | - 989 | 56.00 | 14.00 |
| 5000 | + 863 | + 1001 | - 862 | - 1003 | 69.75 | 13.95 |
| 6000 | + 849 | + 1015 | - 848 | - 1017 | 83.75 | 13.96 |
| 7000 | + 835 | + 1030 | - 834 | - 1031 | 98.00 | 14.00 |
| 8000 | + 820 | + 1043 | - 820 | - 1045 | 112.00 | 14.00 |
| 9000 | + 805 | + 1058 | - 806 | - 1059 | 126.50 | 14.06 |
| 10000 | + 791 | + 1073 | - 791 | - 1073 | 141.00 | 14.10 |

Table D17: Hall effect data of sample 6 at room temperature.

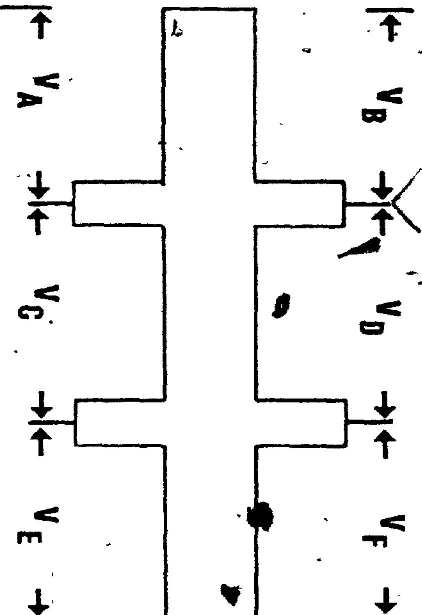


SAMPLE: 6

$I$ = 25 mA

$V_A$ = 0 mV
$V_B$ = mV
$V_C$ = 19.51 mV
$V_D$ = 19.52 mV
$V_E$ = mV
$V_F$ = mV

# APPENDIX E-A

## MODEL AND DERIVATION OF AN IDEAL SOLAR-CELL

The solar cell may best be defined by considering the case of an ideal p-n junction with a constant current source is parallel with it (see fig. A). The constant

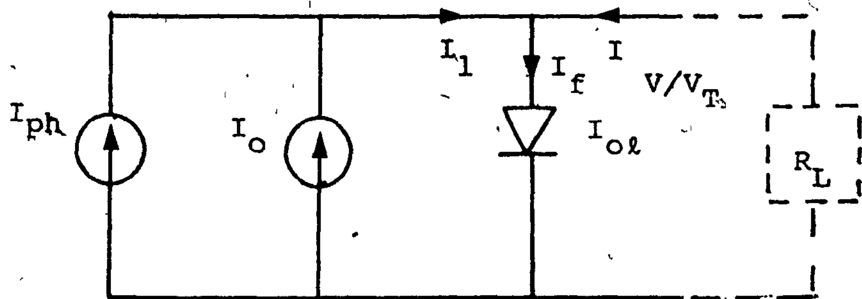


Fig. A

current source, $I_{ph}$ results from the excitation of excess carriers by solar radiation. This generated current is in the same direction to that of the reverse saturation current $I_0$. The total diode current under illumination is determined by solving for I as follows;

$$I_1 = I_{ph} + I_0 \qquad \text{(EA-1)}$$

$$I_f = I_1 + 1 \qquad \text{(EA-2)}$$

but $$I_f = I_0 e^{V/V_T} \qquad \text{(EA-3)}$$

where $V_T = kT/q$

then from equation EA-1 to EA-3, I is

$$I = I_0(e^{V/V_T} - 1) - I_{ph} \qquad \text{(EA-4)}$$

where $I_0$ = reverse saturation current of an ideal junction; q = charge of the electron, k = Boltzmann's constant, T = absolute temperature, $I_{ph}$ = strength of a constant current source and $V_T$ = thermal voltage = kT/q

The I-V characteristic of such a device is given by Eq. EA-4 and is plotted in fig. B. It is seen that the photovoltaic cell is a diode that operates in the fourth quadrant of the irradiated diode I-V characteristics.

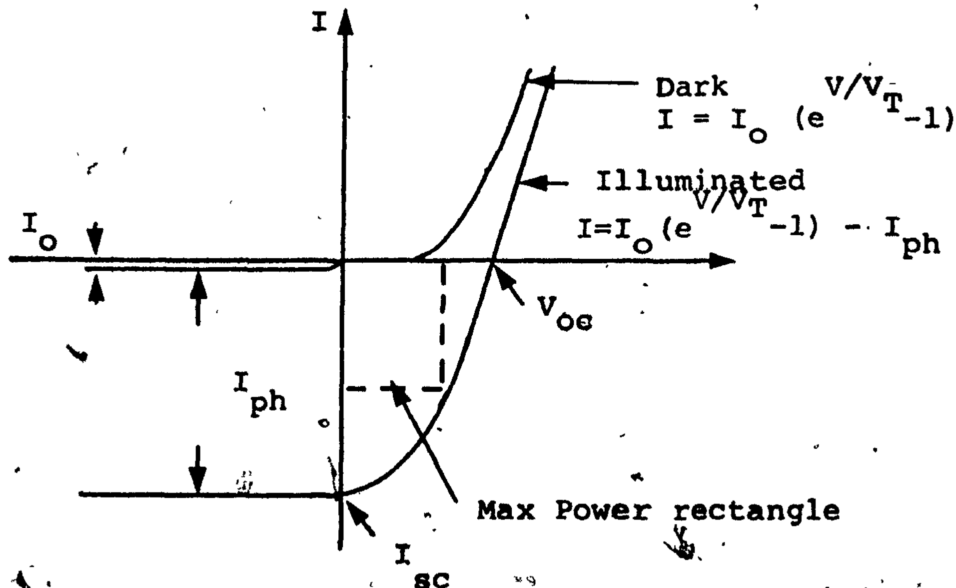


Fig. B

From Fig. B one notices that $I_{ph}$ is nothing but $I_{sc}$ (short circuit current). When the output voltage which equals the diode voltage, is about zero.

If the circuit of the external cell is left open, i.e., $R_L = \infty$, then $I = 0$. The open circuit voltage appearing across the contacts is by EA-4 equal to

$$V = V_{OC} = V_T \ln \left(\frac{I_{ph}}{I_0} + 1\right) \qquad \text{(EA-5)}$$

where we have an open-circuited voltage or electric power source which supplies a current if an external load is connected across it. The conversion of optical to electrical energy is thus realized.

Let us now calculate the maximum power that can be obtained from a solar energy converter (exclusive of losses by recombination, series, shunt and grain boundaries resistances) of Fig. A.

The power delivered to the load is given by

$$P = VI = V[I_0(e^{V/V_T}-1) - I_{ph}] \qquad \text{(EA-6)}$$

The voltage corresponding to the maximum power delivery $V_m$ is obtained by taking $\frac{\partial P}{\partial V}$ and set it = 0. Therefore

$$0 = I_0 e^{V/V_T}\left(\frac{V}{V_T} + 1\right) - I_0 - I_{ph} \qquad \text{(EA-7)}$$

$$\frac{I_{ph}}{I_0} + 1 = e^{V/V_T}(V/V_T + 1) \qquad \text{(EA-8)}$$

∴ The voltage corresponding to the maximum power is $V_m$. Then equation EA-8 can be written as

$$\frac{I_{ph}}{I_0} + 1 = e^{V_m/V_T}(V_m/V_T + 1) \qquad \text{(EA-9)}$$

From equation EA-4 and EA-7 we can now solve for $I_m$. Where $I_m$ is the current corresponding to the maximum power. From equation EA-7 we have said that

$$\frac{\partial P}{\partial V} = 0 = I_0 e^{V_m/V_T} + I_0 \frac{V_m}{V_T} e^{V_m/V_T} - I_0 - I_{ph}$$

but from equation EA-4, $I = I_m = I_0(e^{V_m/V_T} - 1) - I_{ph}$ then substituting equation EA-4 into equation EA-7 we obtain,

$$I_m = I_0 \frac{V_m}{V_T} e^{V_m/V_T} \qquad \text{(EA-10)}$$

Equation EA-10 can also be written in terms of the short circuit current $I_{ph} = I_{sc}$ simply by substituting in equation EA-10 or $e^{V_m/V_T}$. Therefore from equation EA-9 we can solve as follows for $e^{V_m/V_T}$ and substitute it into equation EA-10 yields,

$$I_m = I_0 \frac{V_m}{V_T} \frac{1}{(\frac{V_m}{V_T} + 1)} (\frac{I_{ph}}{I_0} + 1) \qquad \text{(EA-11)}$$

$I_m$ can now be written in terms of $I_{ph}$ if we multiply equation EA-11 by $I_0$ $I_{ph}$ . Then it becomes a "1"

$$I_m = I_{ph} \cdot \frac{V_m}{V_T} \cdot \frac{}{(\frac{V_m}{V_T} + 1)} (1 + \frac{I_0}{I_{ph}}) \qquad \text{(EA-12)}$$

The maximum current and maximum voltage achievable in a solar cell are $I_{ph} = I_{sc}$ and $V_{oc}$ respectively. To optimize the solar converter, we should have large $I_m$ and $V_m$ . This $I_m$ & $V_m$ represents the largest attainable power rectangle see fig. E-B. The ratio of $V_m I_m/I_{ph} V_{oc}$ is a useful source of measurement to realize the power from an I-V curve. This is called the fill factor and is well between 0.7 and 0.8 for a well-made cell.

The efficiency of solar energy conversion is given by.

$$\eta = \frac{\text{maximum power output density}}{\text{power input density}}$$

$$= \frac{I_{mp} \, V_{mp}/cm^2}{P_{in}/cm^2} \qquad \text{(EA-13)}$$

where

$P_{in}/cm^2$ = is the solar power density at AMI (Air mass one ≈ 100m W/cm²)

The maximum power ($P_{max}$) is the product of maximum current ($I_m$) multiplied by maximum voltage ($V_m$). Substituting for $I_m$ from equation EA-12 yields

$$P_{max} = V_m \left[ I_{ph} \cdot \frac{V_m}{V_T} \cdot \frac{1}{(\frac{V_m}{V_T} + 1)} (1 + \frac{I_0}{I_{ph}}) \right] \qquad \text{(EA-14)}$$

Maximum Power density will be equal to EA-14 divided by the Area (A)

$$P_{max\ d} = \frac{P_{max}}{A} = \frac{1}{A} \left[ I_{ph} \cdot \frac{V_{mp}}{V_T}^2 \cdot \frac{1}{(\frac{V_{mp}}{V_T} + 1)} (1 + \frac{I_0}{I_{ph}}) \right.$$

(EA-15)

The optimum load impedance which one can utilize then will be given by

$$R_{Lmax} = \frac{V_m}{I_m} \qquad \text{(EA-16)}$$

substituting for $I_m$ in equation EA-16.

$$R_{Lmax} = \frac{V_T \cdot (\frac{V_m}{V_T} + 1)}{Iph\ (1 + \frac{I_o}{Iph})} \qquad \text{(EA-17)}$$

Until now we have neglected the series resistance $R_{sj}$ on the n-p side of the junction, shunt resistance $R_{sh}$ of the junction, resistance due to grain boundaries $R_{gb}$ and series resistance $R_s$ due to the contacts. But if all of the above are taken into account the (I,V) characteristics will lie below the ideal characteristics of a solar cell ($R_{sj} = 0, R_{sh} \neq \infty$, $R_{gb} = 0$ and $R_s = 0$). These series resistances thus reduces the efficiency of the device, drastically and for the reason they should be kept as small as possible. Also to obtain a large open circuit voltage ($V_{oc}$) one should use a semiconductor with a large energy gap, low resistivity material with low mobility and high lifetime and long diffusion length.

Up to the present discussion only ideal junctions has been considered. Let us now consider a practical unit such that it has a shunt resistance, $R_{sh}$ and certainly some series resistance, $R_{gb}$, $R_{sj}$ and $R_s$. The model showing

all of these effects can be represented as shown in fig. A (see Appendix E-B). The analysis of this model is in Appendix E-B.

# APPENDIX E-B

## MODEL AND DERIVATION OF A PRACTICAL SOLAR-CELL

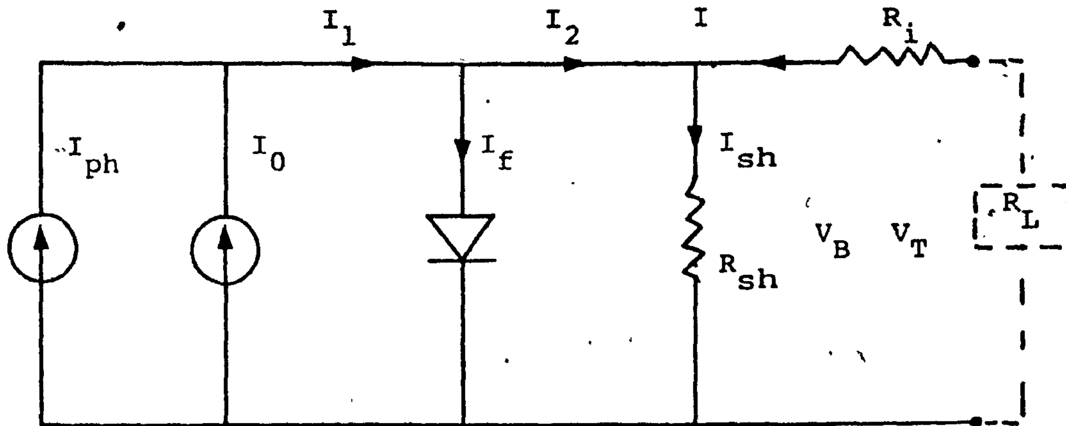


Fig. A

From the solar cells model

$$I_1 = I_{ph} + I_0 \qquad \text{(EB-1)}$$

$$I_2 = I_1 - I_f \qquad \text{(EB-2)}$$

$$I_{sh} - I = I_{ph} + I_0 - I_f \qquad \text{(EB-3a)}$$

or

$$I = -I_0 + I_f - I_{ph} - I_{sh} \qquad \text{(EB-3b)}$$

but

$$I_f = I_0 \, e^{\frac{qV}{kT}} \qquad \text{(EB-4)}$$

From equation (EB-1) to (EB-4), I is obtained as

$$I = I_0 \left(e^{\frac{qV}{kT}} - 1\right) - I_{ph} + I_{sh} \quad \text{(EB-5)}$$

where

$I$ = total diode current that would flow if a load was connected to th external of the cell

$I_{sh}$ = shunt current of the diode

$I_f$ = diffusion current of the diode

$I_{ph}$ = photon generated current

$V_B$ = diode built in potential

$V_t$ = output voltage

$R_i$ = total series resistances of the device (n-side, p-side, grains and grain boundaries, contact).

$R_{sh}$ = shunt resistance of the space charge region.

Note that in Figure EB-A if there exist no $R_i$ then

$$V_t = V_B = V_{oc} \quad \text{(EB-6)}$$

But in reality there exists $R_i$, therefore the output voltage $V_t$ is comprised fo the built in voltage ($V_B$) of the diode minus the voltage drops due to the resistance which exist. Hence the output voltage is given by

$$V_t = V_B - V_{Ri} \qquad \text{(EB-7)}$$

From equation EB-5 (assuming a very small load) I becomes,

$$I = I_0 \left(e^{\frac{q}{KT}(V_B - IR_i)} - 1\right) - I_{ph} + I_{sh} \qquad \text{(EB-8)}$$

Substituting for $I_{sh}$, $V_t/R_{sh}$ in equation (EB-8), the following is obtained.

$$\frac{I+I_{ph}}{I_0} - \frac{V_t}{I_0 R_{sh}} + 1 = e^{\frac{q(V_B - IR_i)}{kT}} \qquad \text{(EB-9)}$$

Taking the natural logarythm on both sides of equation (EB-9) yields an expression of the I-V characteristics as such

$$\ln\left(\frac{I+I_{ph}}{I_0} - \frac{V_B - IR_i}{I_0 R_{sh}} + 1\right) = \frac{q(V_B - IR_i)}{kT} \qquad \text{(EB-10)}$$

Rerranging eauation (EB-10), open circuit voltage ($V_{oc} = V_B$) is obtained as

$$V_{oc} = \frac{kT}{g} [\ell n (\frac{I+I_{ph}}{I_0} - \frac{V-IR_i}{I_0 R_{sh}} + 1) + IR_i]$$

(EB-11)

Power delivered to the load is given by

$$P = VI \quad \text{(EB-12)}$$

substituting I from equation EB-5,

$$P = V[I_0 (e^{\frac{qV_t}{kT}} - 1) - I_{ph} + I_{sh}] \quad \text{(EB-13)}$$

Maximum power output is obtained by taking the first derivative of equation (EB-13) with respect to $V_B$ and equating it to zero.

$$0 = I_o e^{\frac{qV_t}{kT}} (\frac{qV_t}{kt} + 1) - I_0 - I_{ph} + I_{sh} \quad \text{(EB-14)}$$

Rearranging equation (EB-14) lead to

$$\frac{I_{ph}-I_{sh}}{I_0} + 1 = e^{\frac{qV_t}{kT}} (\frac{qV_t}{kT} + 1) \quad \text{(EB-15)}$$

The maximum $V_B$ obtained from equation EB-15 is represented a $V_m$ and equation EB-15 can be written as

$$1 + \frac{I_{ph} - I_{sh} + 1}{I_0} = e^{\frac{q(V_m - IR_i)}{kT}} \left(\frac{qV_m}{kT} + 1\right) \qquad \text{(EB-16)}$$

Substituting equation (EB-5) into (EB-14), $I = I_m$ can be solved

$$I_m = I_0 \frac{qV_m}{KT} e^{\frac{qV_t}{kT}} \qquad \text{(EB-17)}$$

where

$I_m$ = current at max power

The efficiency of the solar energy converter is given by EA-15)

$$\eta = \frac{\text{max power output density}}{\text{power input density}} = \frac{I_m \cdot V_m / cm^2}{P_{in} / cm^2} \qquad \text{(EB-18)}$$

Substituting for $I_m$ from equation EB-17 and eliminating the exponential term by manipulating equation (EB-15), the final result is obtained. Hence the max power ($P_{max}$)

and efficiency of the system are;

$$P_{max} = \frac{I_m V_m}{A} = \frac{1}{A} \left[I_{ph} \cdot \frac{qV_t}{kT} \cdot \frac{V_m}{\left(\frac{qV_t}{kT} + 1\right)} \left(1 + \frac{I_0}{I_{ph}} - \frac{I_{sh}}{I_{ph}}\right)\right]$$

(EB-19)

$$\eta = \frac{1}{A} \left[I_{ph} \cdot \frac{qV_t}{kT} \cdot \frac{V_m}{\left(\frac{qV_t}{kT} + 1\right)} \left(1 + \frac{I_0}{I_{ph}} - \frac{I_{sh}}{I_{ph}}\right)\right] \cdot \frac{1}{P_{in}}$$

(EB-20)

where

$P_{in}$ = power density at air mass one (AM-1) and is equal to $\approx$ 100mW/cm$^2$

The optimum load impedance is then calculated as,

$$R_L = \frac{V_m}{I_m} = \frac{V_m}{I_{ph} \cdot \frac{qV_t}{kT} \left(\frac{qV_t}{kT} + 1\right) \left(1 + \frac{I_0}{I_{ph}} - \frac{I_{sh}}{I_{ph}}\right)}$$

(EB-21)

# APPENDIX F

## POSITION OF THE FERMI LEVEL AS A FUNCTION OF CHARGE DENSITY FOR VARIOUS IMPURITY CONCENTRATIONS

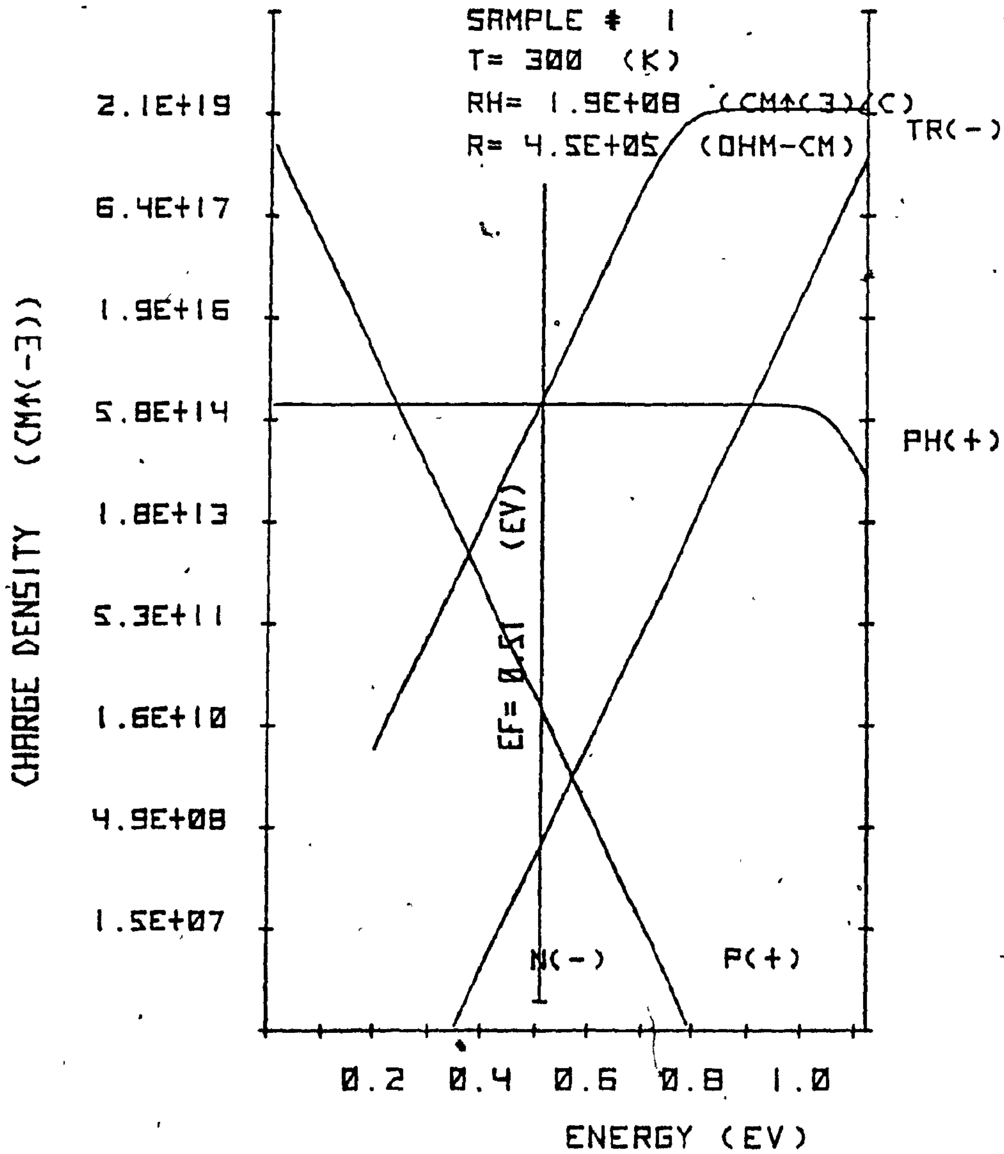


Fig 1: The calculated position of the Fermi level ($E_f$=0.51eV) of sample #1, with the electron n(-), hole p(+), ionized phosphorous PH(+) and deep acceptor traps TR(-) as the function of energy. At the Fermi level the concentrations in ($cm^{-3}$) are: n(-)=$2.7\times10^{8}$, p(+) = $2.8\times10^{10}$, PH(+)=$1\times10^{15}$, TR(-)=$1.2\times10^{15}$.

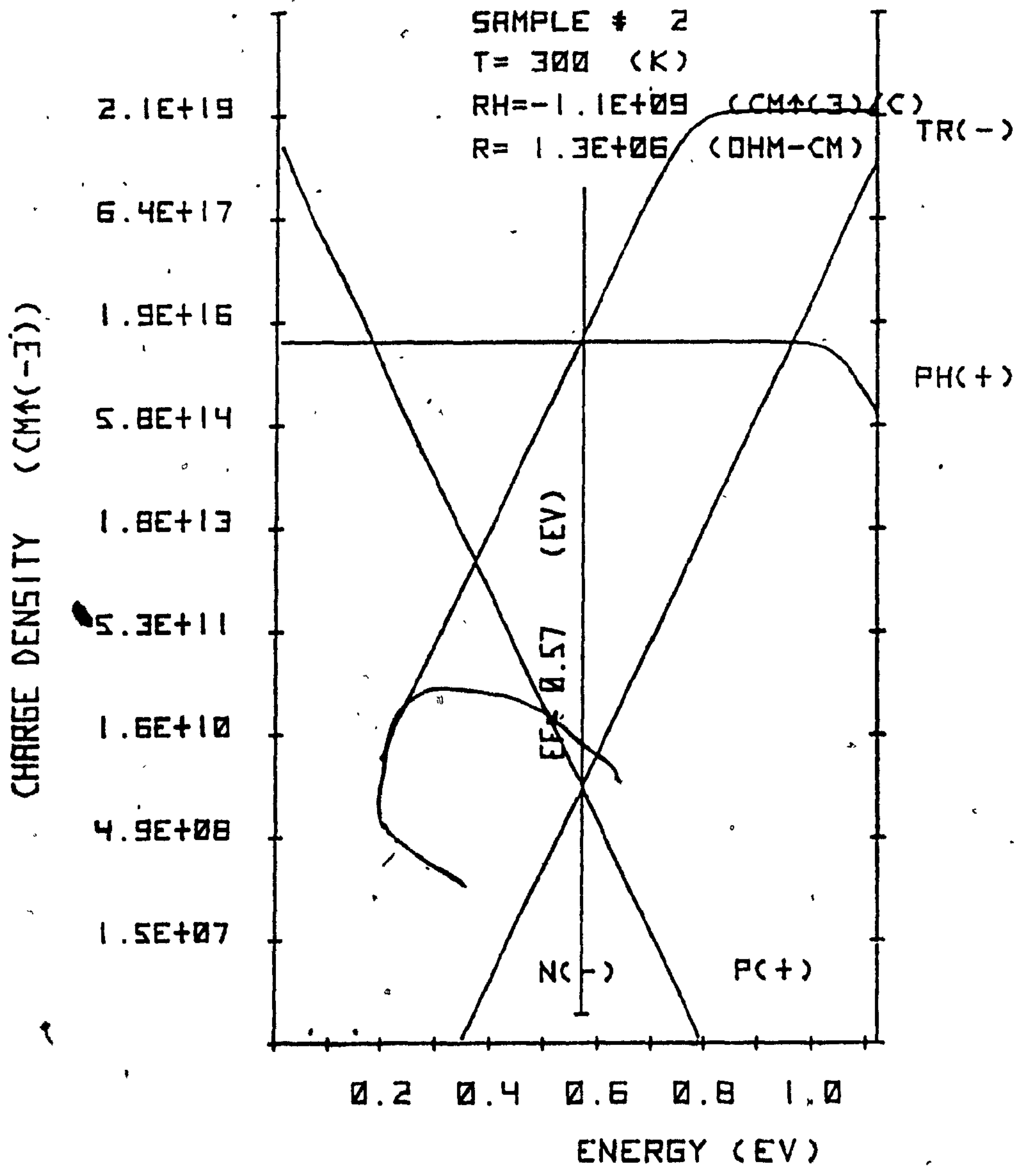


Fig. 2: The calculated position of the Fermi level of sample #2 ($E_f$=0.57) with the charge densities as in Fig. 1. At the Fermi level the concentrations in ($cm^{-3}$) are: n(-)=$2.7\times10^9$, p(+)=$2.8\times10^9$, PH(+)=$1.0\times10^{16}$, TR(-)=$1.2\times10^{16}$.

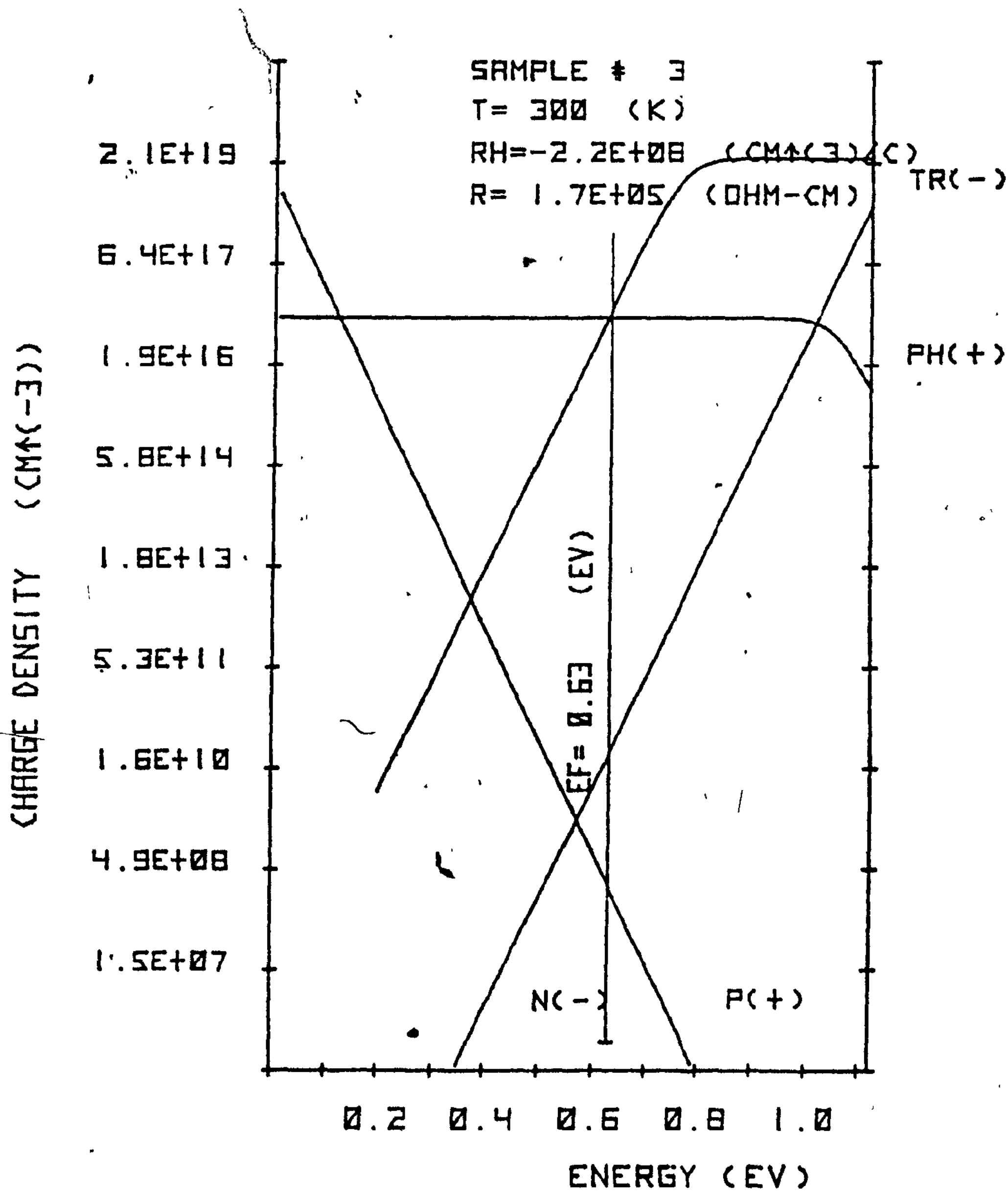


Fig. 3: The calculated position of the Fermi level ($E_f$=0.63) of sample #3 with the charge densities as in Fig. 1. At the Fermi level the concentrations in ($cm^{-3}$) are: n(-)=$2.8\times10^{10}$, p(+)=$2.7\times10^{8}$, PH(+)=$1.0\times10^{17}$, TR(-)=$1.2\times10^{17}$.

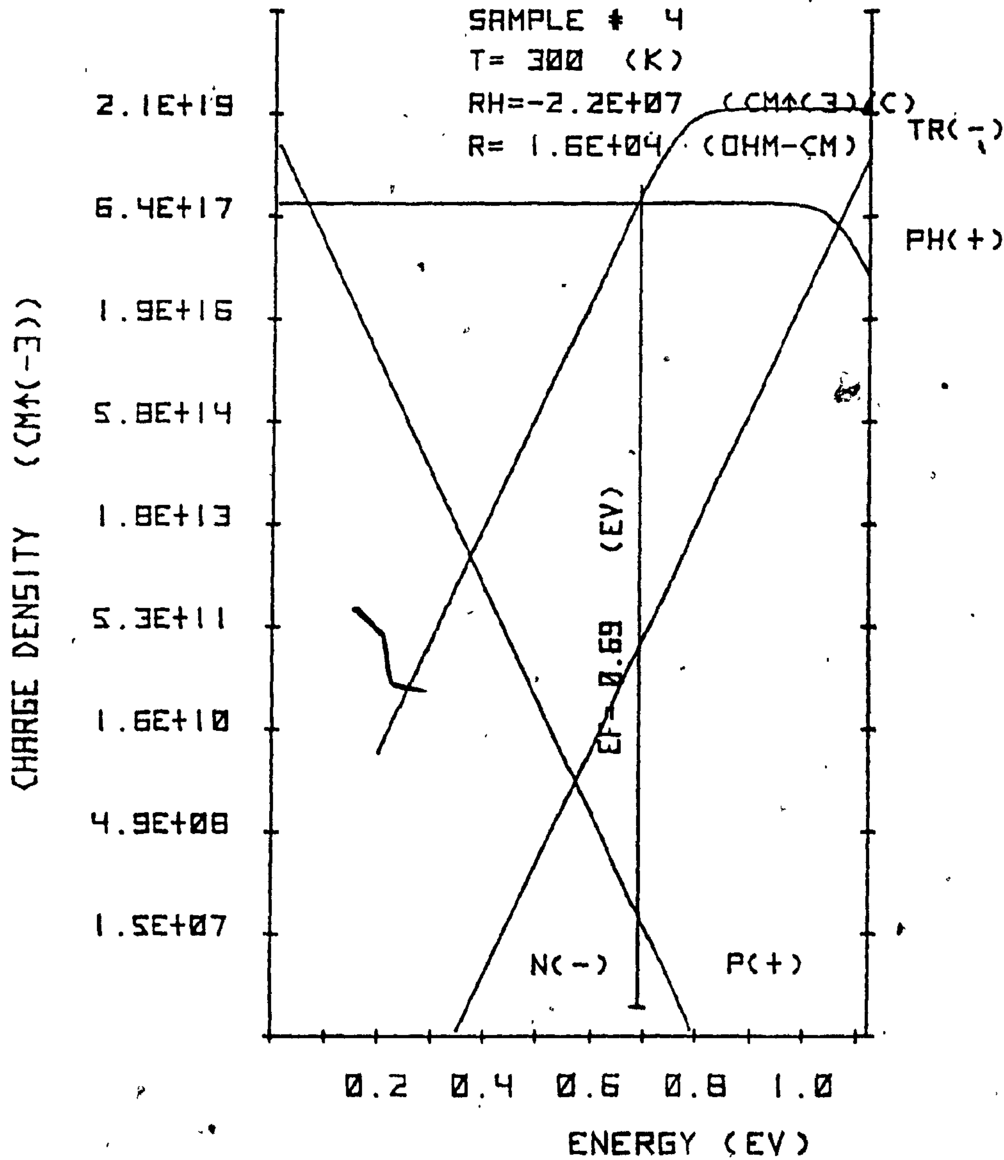


Fig. 4: The calculated position of the Fermi level ($E_f$=0.69eV) of sample #4 with the charge densities as in Fig. 1. At the Fermi level the concentrations in ($cm^{-3}$) are: n(-)=$2.8\times10^{11}$, p(+)=$2.7\times10^{7}$, PH(+)=$1.0\times10^{18}$, TR(-)=$1.2\times10^{18}$.

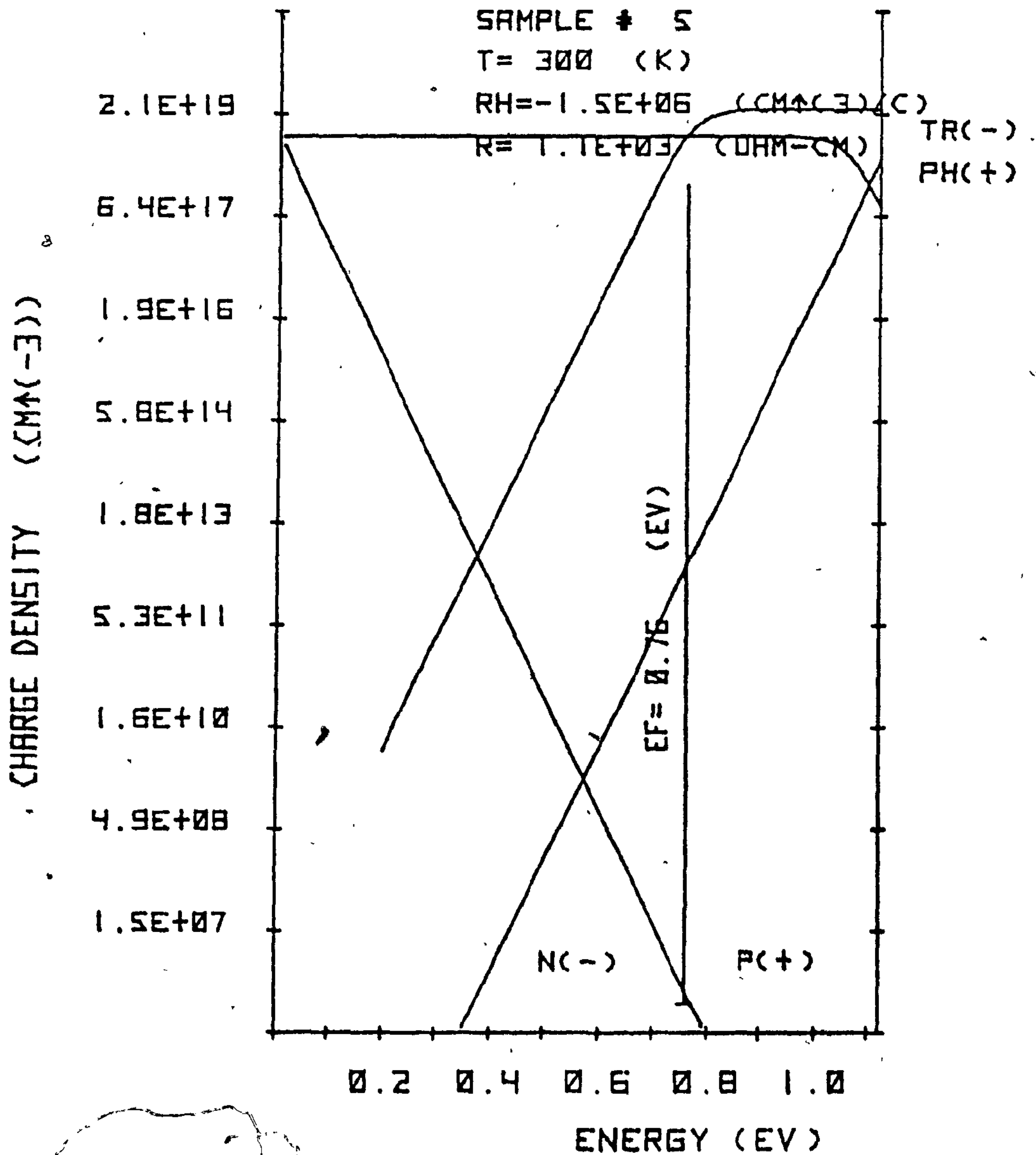


Fig. 5: The calculated position of the Fermi level ($E_f$=0.69eV) of sample #4 with the charge densities as in Fig. 1. At the Fermi level the concentrations in ($cm^{-3}$) are: $n(-)=2.8\times10^{11}$, $p(+)=2.7\times10^{7}$, $PH(+)=1.0\times10^{18}$, $TR(-)=1.2\times10^{18}$.

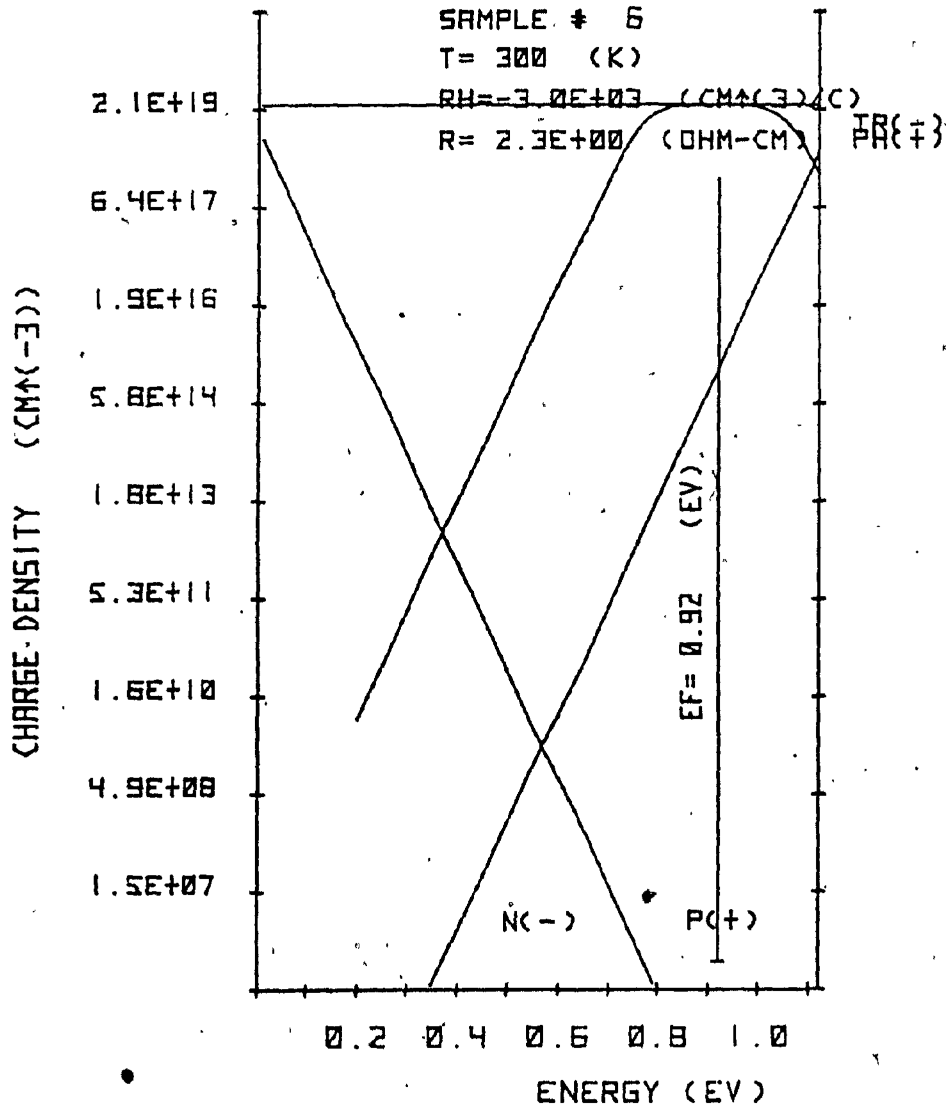


Fig. 6: The calculated position of the Fermi level ($E_f$=0.92eV) of sample #6 with the charge densities as in Fig. 1. At the Fermi level the concentrations in ($cm^{-3}$) are: $n(-)=2.0\times10^{15}$, $p(+)=3.7\times10^{3}$, $PH(+)=2.5\times10^{19}$, $TR(-)=2.5\times10^{19}$.

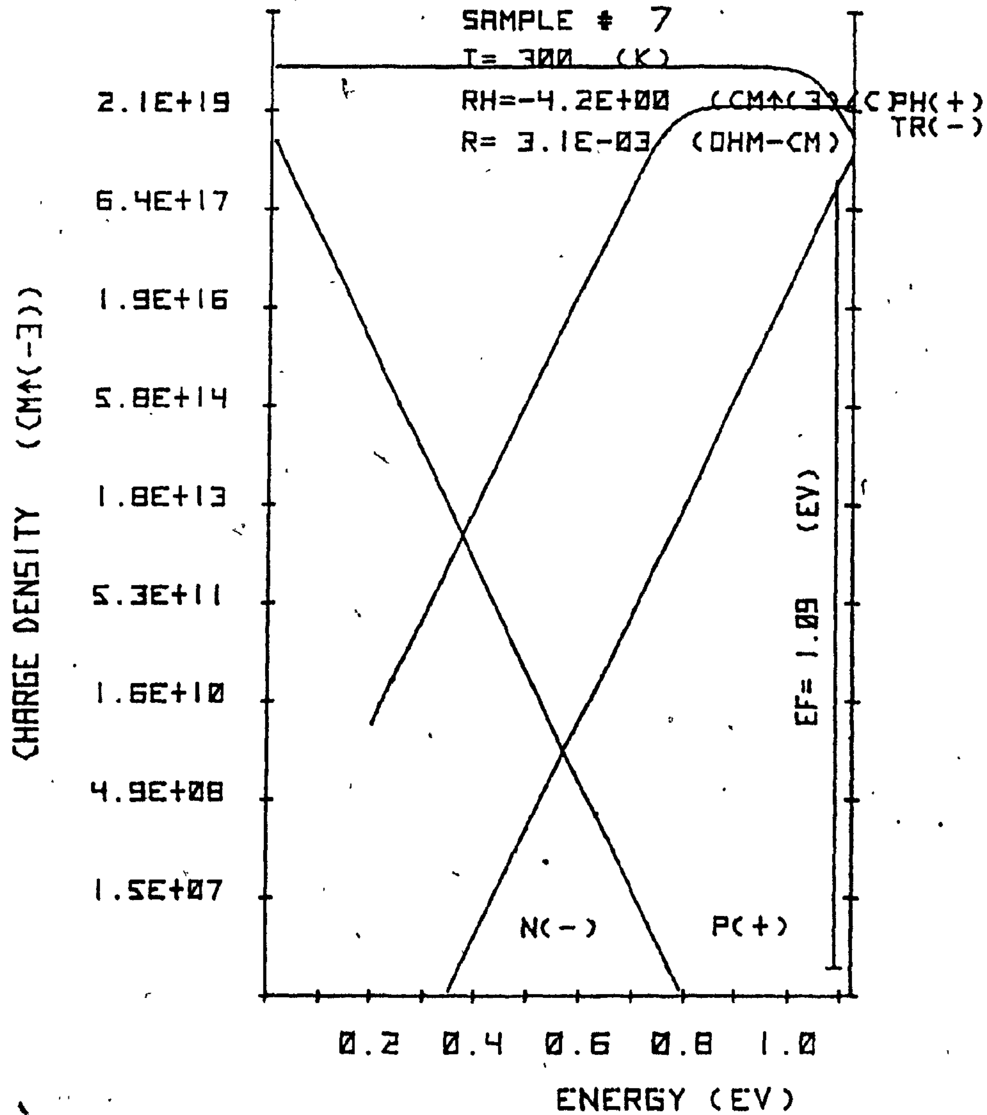


Fig. 7: The calculated position of the Fermi level ($E_f$=1.09eV) of sample #7 with the charge densities as in Fig. 1. At the Fermi level the concentration in ($cm^{-3}$) are: n(-)=$1.5\times10^{18}$, p(+)=$5.1\times10^{0}$ PH(+)=$2.3\times10^{19}$, TR(-)=$2.5\times10^{19}$.

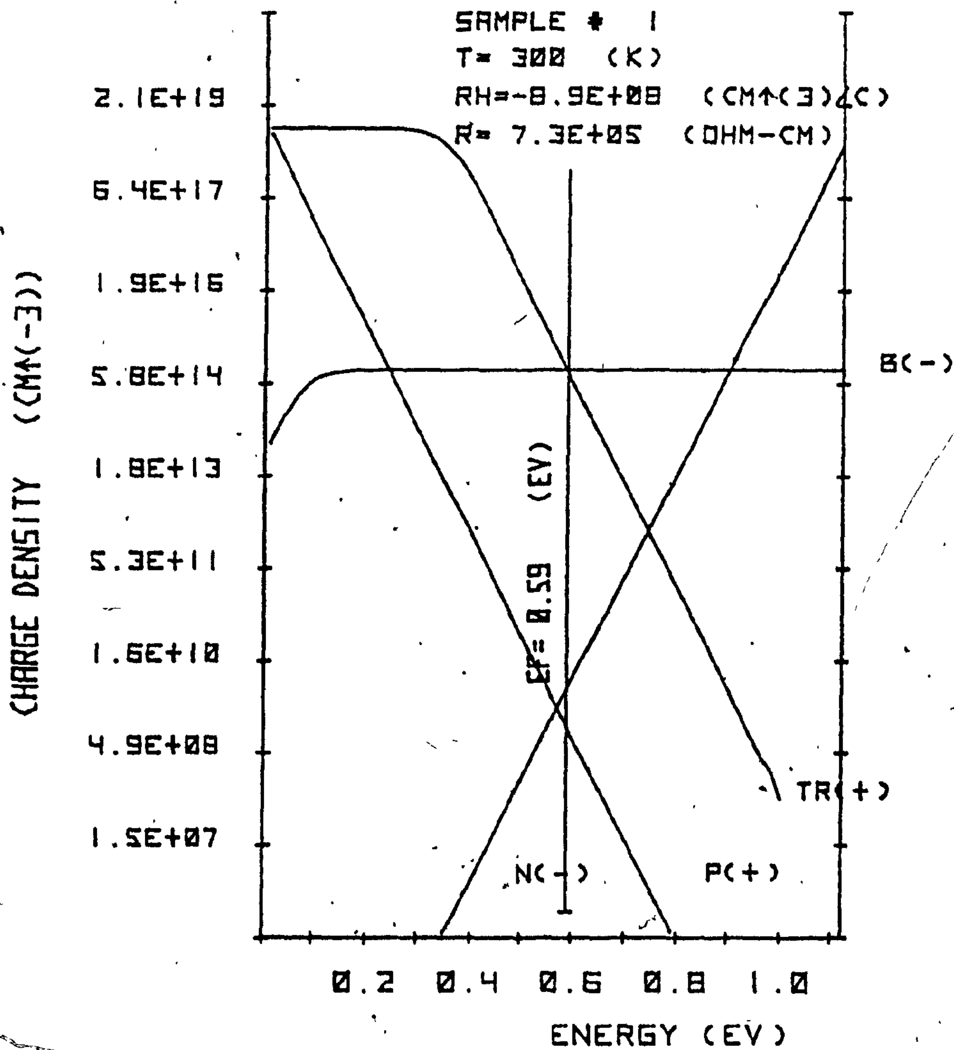


Fig. 8: The calculated position of the Fermi level ($E_f$-0.59eV) of sample #1, with electron n(-), hole p(+), ionized Boron B(-), and deep donor traps TR(+) as the function of Energy. At the Fermi level the concentrations in ($cm^{-3}$) are: n(-)=$5.9\times10^9$, p(+)=$1.3\times10^9$, B(-)=$1.0\times10^{15}$, TR(+)=$9.1\times10^{14}$.

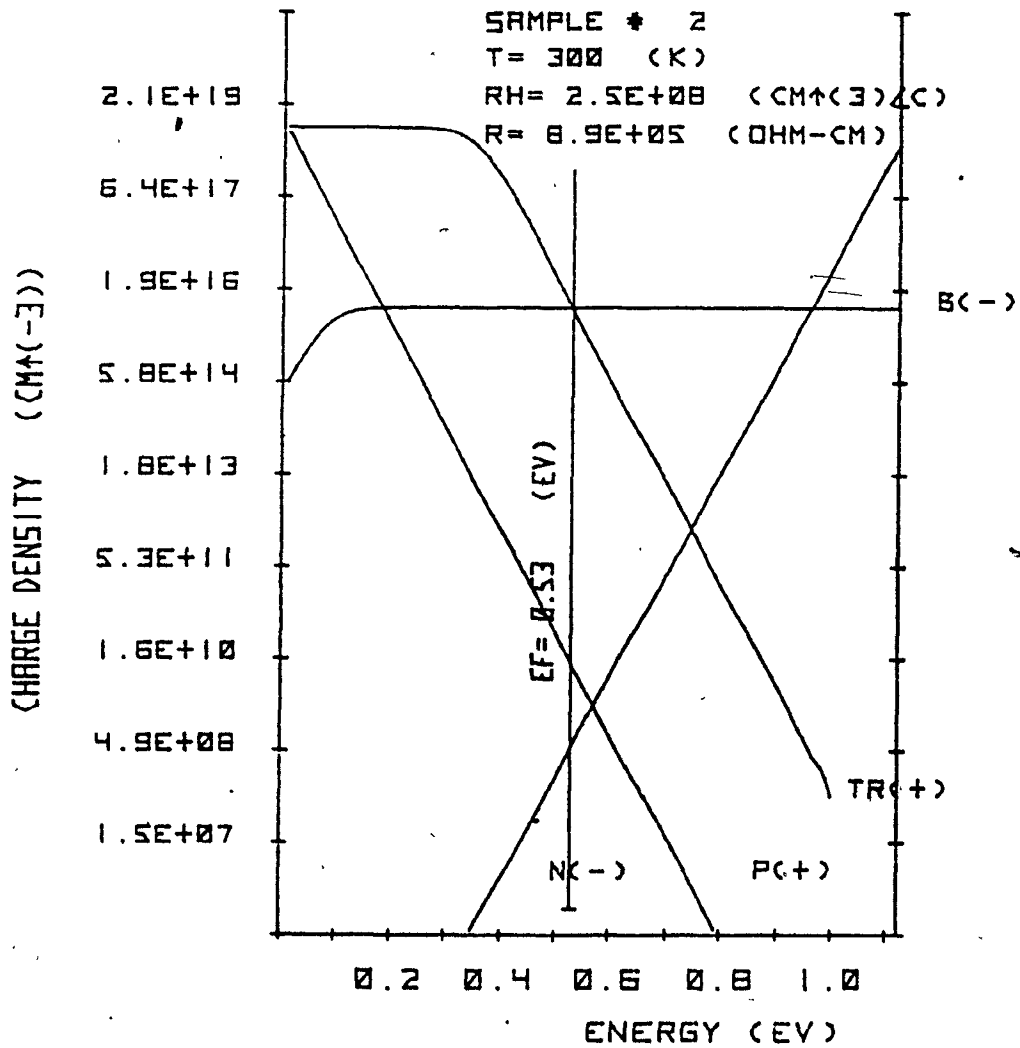


Fig. 9: The calculated position of the Fermi level ($E_f$=0.53eV) of sampel #2 with the charge densities as in fig. 8. At the Fermi level the concentration in ($cm^{-3}$) are: n(-)=$5.8\times10^{8}$, p(+)=$1.3\times10^{10}$, B(-)=$1.0\times10^{16}$, TR(+)=$9.2\times10^{15}$.

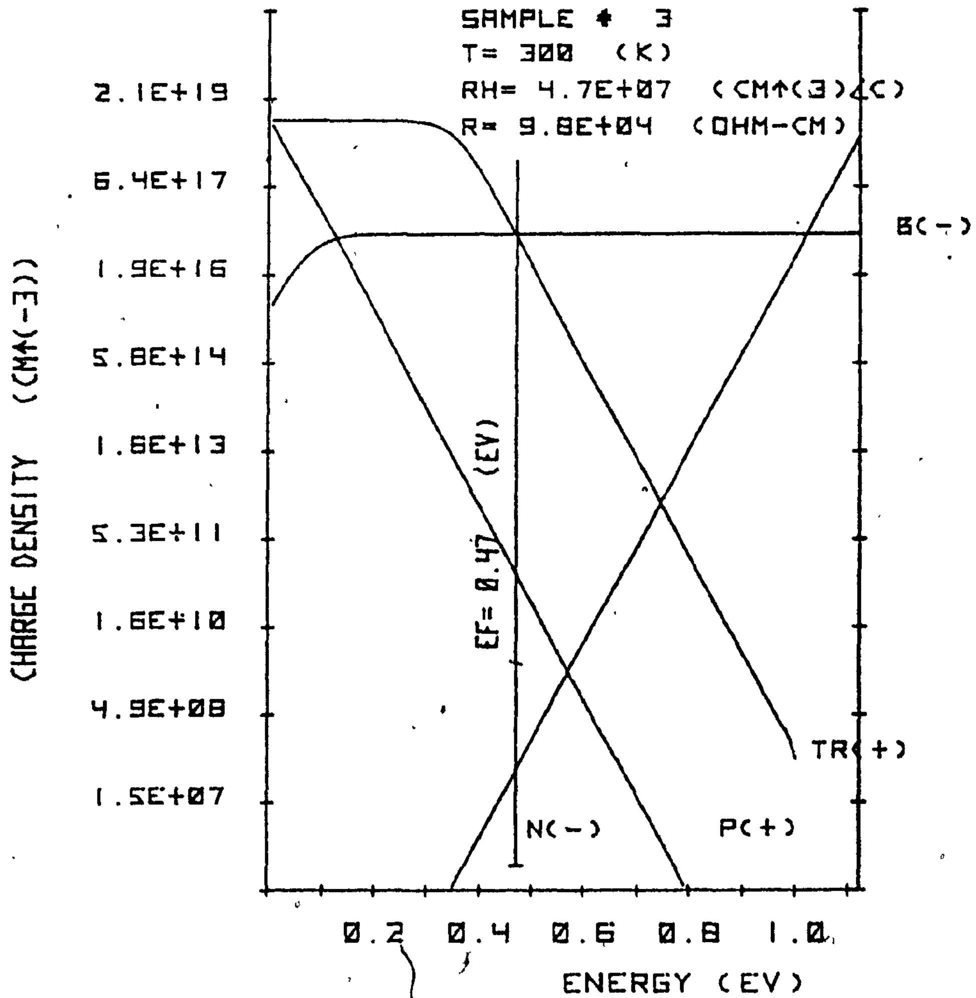


Fig. 10: The calculated position of the Fermi level ($E_f$=0.47eV) of sample #3 with the charge densities as in fig. 8. At the Fermi level the concentrations in ($cm^{-3}$) are: n(-)=$5.6\times10^{7}$, p(+)=$1.3\times10^{11}$, B(-)=$1.0\times10^{17}$, TR(+)=$9.3\times10^{16}$.

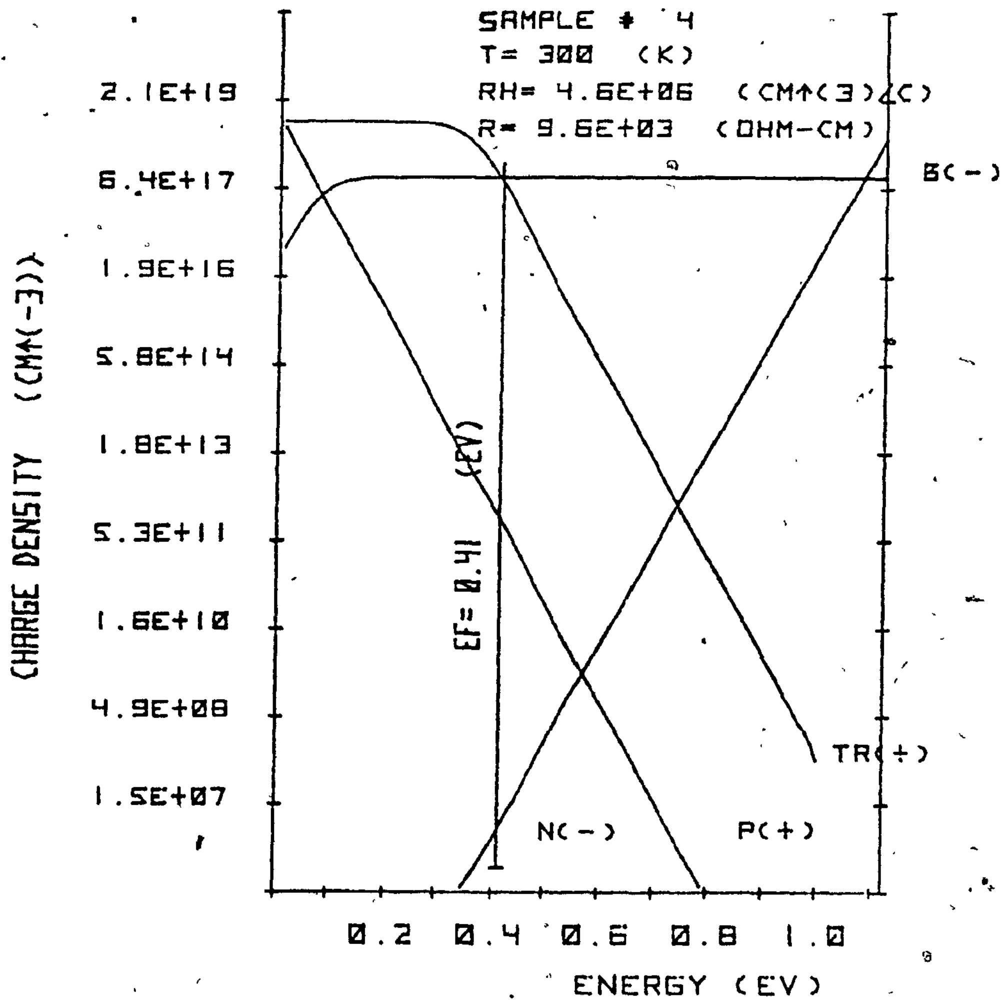


Fig. 11: The calculated position of the Fermi level ($E_f$-0.41eV) of sample #4 with the charge densities as in fig. 8. At the Fermi level the concentrations in ($cm^{-3}$) are: $n(-)=5.5\times10^{6}$, $p(+)=1.4\times10^{12}$, $B(-)=1.0\times10^{18}$, $TR(+)=8.7\times10^{17}$.

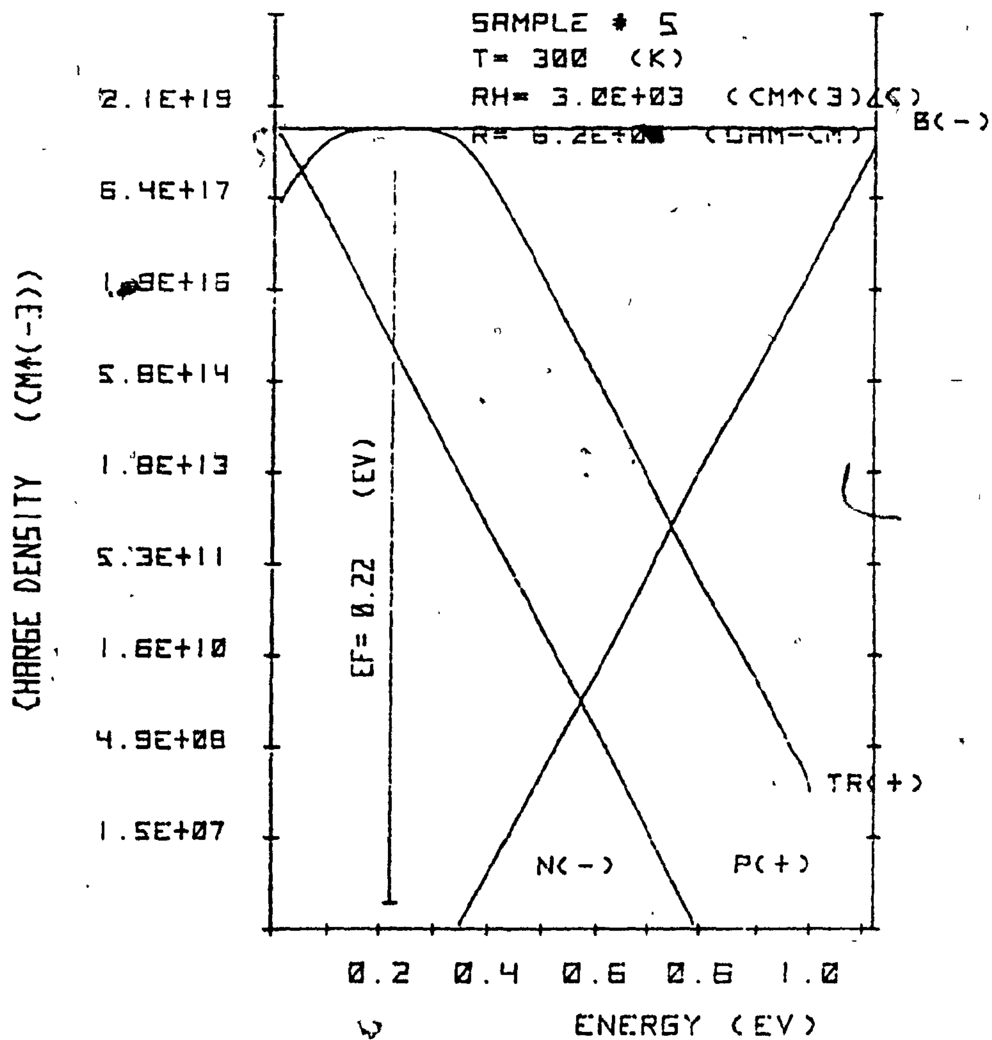


Fig. 12: The calculated position of the Fermi level ($E_f$=0.22eV) of sample #5 with the charge densities as in fig. 8. At the Fermi level the concentrations in ($cm^{-3}$) are: n(-)=$3.6\times10^{3}$, p(+)=$2.1\times10^{15}$, B(-)=$9\times10^{18}$, TR(+)=$8.9\times10^{18}$.

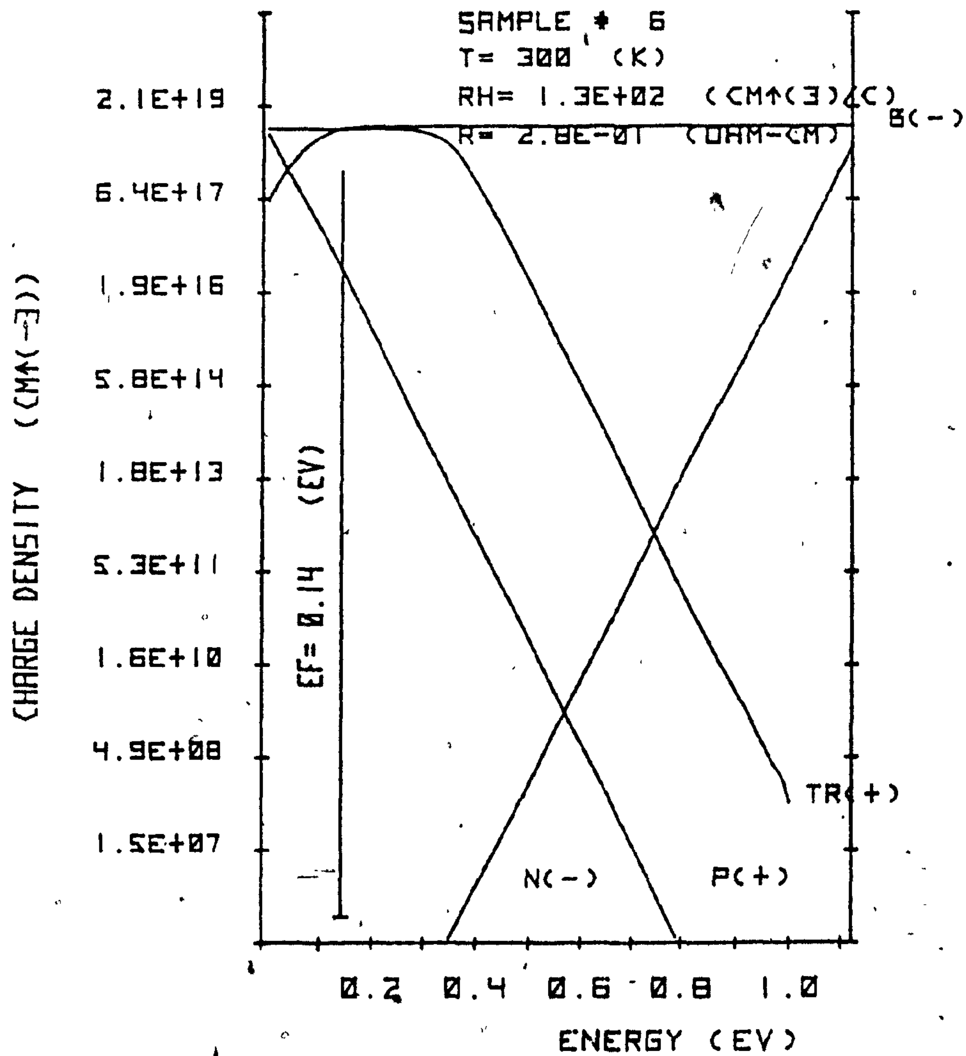


Fig. 13: The calculated position of the Fermi level ($E_f$=0.14eV) of sample #6 with the charge densities as in fig. 8. At the Fermi level the concentration in ($cm^{-3}$) are: n(-)=$1.6\times10^2$, p(+)=$4.7\times10^{16}$, B(-)=$9.1\times10^{18}$, TR(+)=$9.0\times10^{18}$.

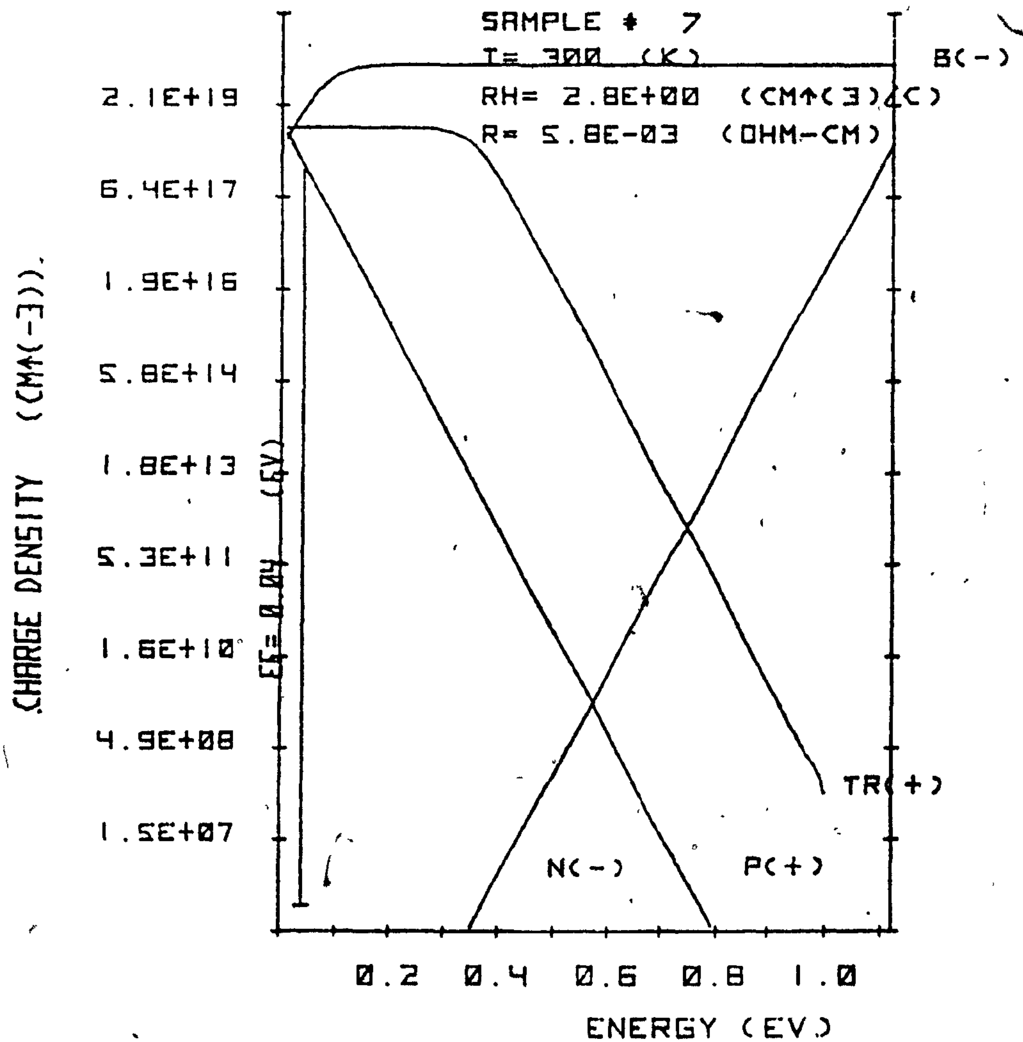


Fig. 14: The calculated position of the Fermi level ($E_f$=0.04eV) of sample #7 with the charge densities as in fig. 8. At the Fermi level the concentration in ($cm^{-3}$) are: $n(-)=3.4\times10^{0}$, $p(+)=2.2\times10^{18}$, $B(-)=1.7\times10^{19}$, $TR(+)=9.0\times10^{18}$.

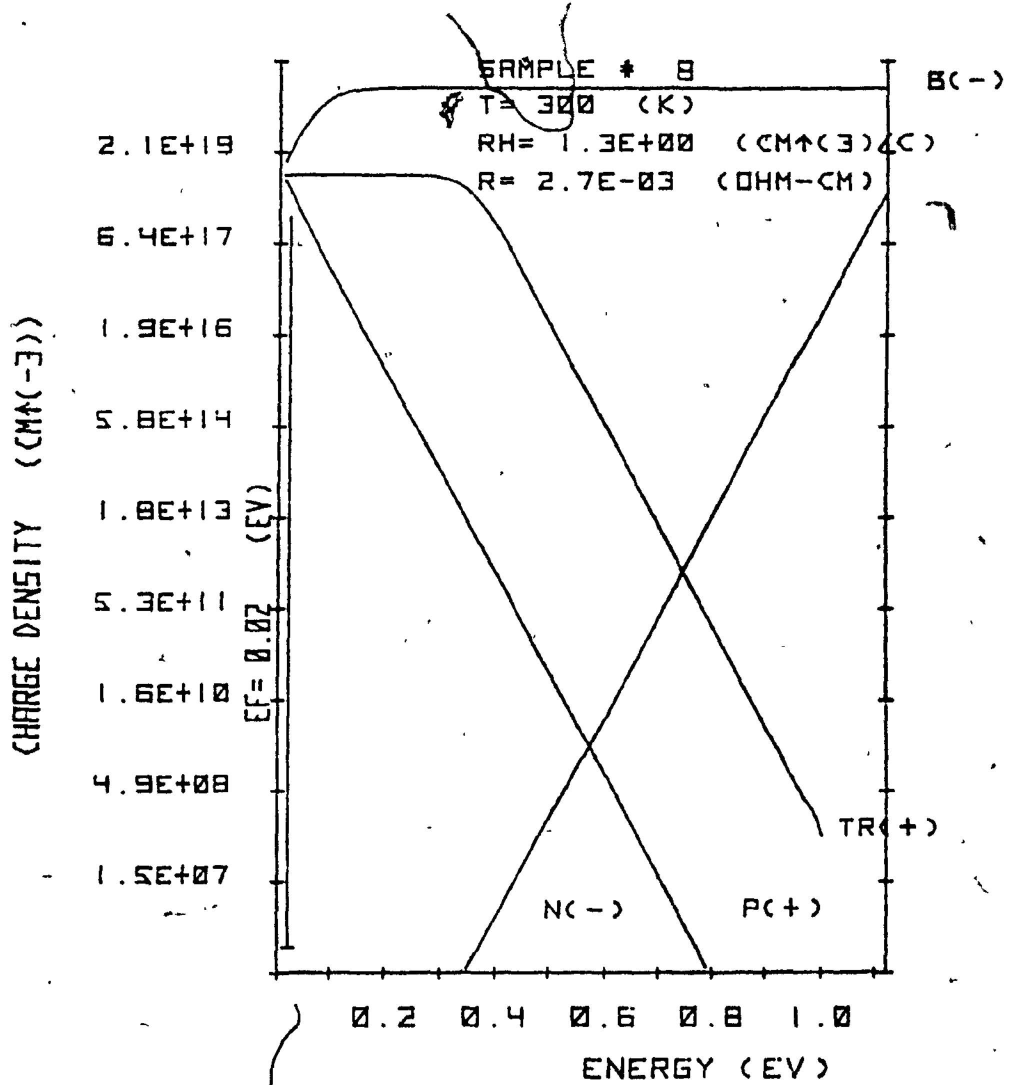


**Fig. 15:** The calculated position of the Fermi level ($E_f$=0.02eV) of sample #8 with the charge densities as in fig. 8. At the Fermi level the concentrations in ($cm^{-3}$) are: $n(-)=1.6\times10^{0}$, $p(+)=4.8\times10^{18}$, $B(-)=2.2\times10^{19}$, $TR(+)=9.0\times10^{18}$.

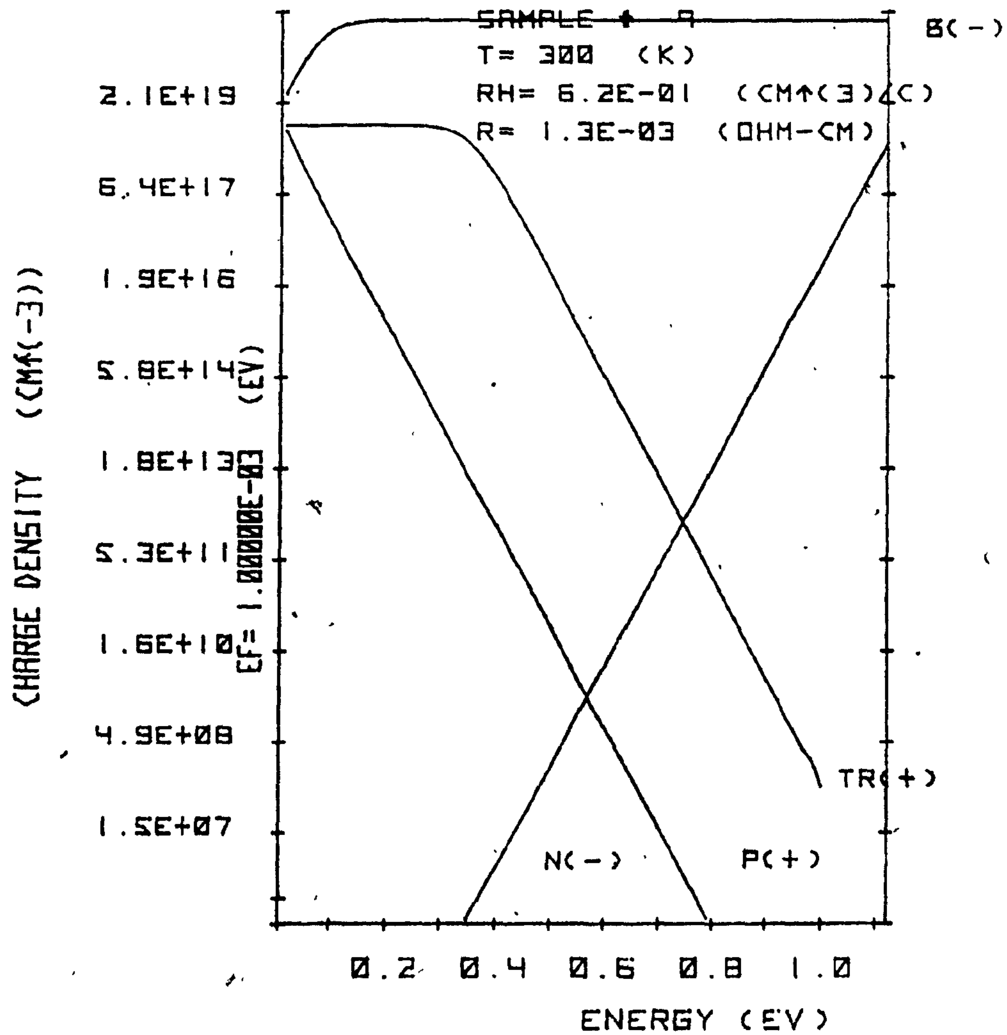


Fig. 16: The calculated position of the Fermi level ($E_f$=0.001eV) of sample #9 with the charge densities as in fig. 8. At the Fermi level the concentrations in ($cm^{-3}$) are: $n(-)=7.5\times10^{-1}$, $p(+)=1.0\times10^{19}$, $B(-)=2.2\times10^{19}$, $TR(+)=9.0\times10^{18}$.